

**FLUID TRANSPORT THROUGH A VARIABLY
SATURATED ROCK PILE HILLSLOPE SYSTEM**

by

Heather Renee Shannon

Advisor: Dr. Jan Hendrickx

Submitted in partial fulfillment of the requirement for the
Degree of Master of Science in Hydrology

Department of Earth and Environmental Sciences
New Mexico Institute of Mining and Technology
Socorro, New Mexico

August 2006

ABSTRACT

An extensive field sampling and characterization program was conducted at the Questa molybdenum mine in Questa, New Mexico to understand the mechanical and geochemical stability of the Goathill North rock pile. Analysis and interpretation of bulk density measurements, tension infiltrometer and guelph permeameter measurements, tensiometer measurements, and particle size data was completed to develop a conceptual model for a generic rock pile hillslope system to be used in numerical studies of the rock pile.

Field measurements of bulk density indicated that the mean bulk density of the rock pile material ranged between 1.60 g/cm^3 and 2.21 g/cm^3 for six mapped soil regions within the Goathill North rock pile. The mean and median saturated hydraulic conductivity (K_s) of the rock pile material estimated from tension infiltrometer measurements were $8.32\text{E-}03 \text{ cm/s}$ and $9.07\text{E-}04 \text{ cm/s}$, respectively. Guelph permeameter measurements estimates for the mean and median saturated hydraulic conductivity were $2.32\text{E-}02 \text{ cm/s}$ and $7.31\text{E-}03 \text{ cm/s}$, respectively, significantly higher than the tension infiltrometer estimates. Field measurements of matric suction using hand-held tensiometers indicated that the rock pile was relatively moist with a mean suction value of -61 cm between early September 2004 and early October 2004. Records from nested tensiometers also indicated a wet regime between June 2004 and August 2004, ranging between -80 cm and saturation.

The data collected in the field at the Goathill North rock pile was used to characterize the hillslope system and develop a conceptual model for numerical

studies. A numerical sensitivity analysis was performed to address two objectives – (1) to determine the spatiotemporal moisture distribution within a generic rock pile modeled after the Goathill North (GHN) rock pile and (2) to test the importance of soil hydraulic properties, bedrock permeability, and climate to the pressure head and moisture distribution within the generic rock pile.

The results from this study showed that the moisture distribution within the generic rock pile containing soils without rocks was relatively homogeneous. However, the moisture distribution within the generic rock pile containing soils with rocks was quite different in that the moisture contents within the different regions were lower, because the saturated moisture content of the regions decreased due to the presence of rocks within the rock pile.

In addition, the results from this research indicate that storage of water in soil, which is directly related to the soil porosity and other soil properties, is the most significant parameter explaining the moisture distribution within the pile. In addition, the investigation shows that the rocky soils respond most quickly to rainfall events, and lead to wetter-moisture conditions due to the low porosity and therefore low water storage capacity of these soils.

The results from this study are valuable to the Weathering study by providing information about the spatiotemporal moisture and pressure head distribution within the pile. The wetter-moisture conditions within the rocky soils would potentially lead to increased pyrite oxidation due to the availability of water for reactions. While the increased moisture regime also would decrease the internal friction angle a component of the shear strength of the soils. A decrease in the internal friction angle

has been shown to coincide with a slight increase in the degree of weathering of a sample (Gutierrez, 2006). Therefore, it is crucial to understand the spatial distribution of moisture in order to predict which regions of the rock pile will be of importance in future modeling efforts.

ACKNOWLEDGEMENTS

This research was funded by Molycorp Incorporated under a subcontract to the New Mexico Bureau of Geology and Mineral Resources (NMBGMR) through the University of Utah. A team of researchers from New Mexico Tech (NMT), NMBGMR, University of Utah, University of British Columbia, Weber State, University of Nevada-Reno, University of California-Berkley, the Minnesota DNR, and various consultants are part of an ongoing 4-year collaborative study to investigate the mechanical and geochemical stability of the Goathill North rock pile at the Questa molybdenum mine in Questa, New Mexico, which is owned and operated by Molycorp Incorporated.

I am also grateful to the Socorro chapter of WAAIME who provided me with a generous scholarship/loan during my time at New Mexico Tech.

I am grateful to the NMT field team and other collaborating team members who spent countless hours collecting field samples at the Questa mine. Particular persons from NMT and other collaborating universities who assisted in field and laboratory work used in this study include: Virginia T. McLemore, John Sigda, Patrick Walsh, Luiza Guterrez, Jan Hendrickx, Joesph Marcoline, Samuel Tachie-Menson, Kelly Donahue, Richard Lynn, Patty Jackson Paul, John Purcell, Alex Thamm, Remke van Dam, Karin Wagner, Donald Wenner, Nate Wenner, Sean Wentworth, and G. Ward Wilson.

I am grateful to the employees of Molycorp Inc. who have spent numerous hours helping us understand the mine history which led to the development of the mine rock piles, and assisted us in our understanding of mine safety procedures.

Particular persons from Molycorp Inc. who provided assistance include: Bruce Walker, Anne Wagner, David Jacobs, and the safety “guru” Jim Vaughn.

I am especially grateful to the members of my committee Dr. Jan Hendrickx, Dr. John Wilson, and Dr. Virginia McLemore. Dr. John Wilson has provided me with many valuable suggestions to help to improve numerical simulations. Dr. Virginia McLemore has provided me with knowledge of the complex geology of the Questa mine region. Finally, it has been a pleasure to work with my advisor, Dr. Jan Hendrickx, who has provided me with guidance through my journey at NMT.

I am very grateful for the friendships that I have made during my time at NMT.

I am also very grateful for the love and support that was provided to me by my family and Craig Altare.

TABLE OF CONTENTS

ACKNOWLEDGEMENTS	ii
TABLE OF CONTENTS	iv
LIST OF FIGURES	vi
LIST OF TABLES	xii
LIST OF APPENDICES FIGURES	xiv
LIST OF APPENDICES TABLES	xxiii
INTRODUCTION	1
The Questa Mine Site	8
Goathill North Rock Pile	11
Climate	18
Regional Geology	19
Hydrogeology	20
METHODS AND MATERIALS	26
Soil Tests	26
Bulk Density	26
Water Replacement or Excavation Method	27
Sand Replacement	29
Sand Cone	30
Nuclear Radiation	32
Hydraulic Conductivity	34
Tension Infiltrometer	34
Guelph Permeameter	39
Matric Suction	39
“Quick Draw” Soil Moisture Probe and Standard Tensiometers	39
Nested Tensiometers	41
Particle size analysis	42
Conceptual Model	45
Governing Equations and Numerical Methods	50
Soil Hydraulic Parameters	51
Boundary Conditions	60
Initial Conditions	63
Simulations	64
Sensitivity Analysis	64
RESULTS AND DISCUSSION	68
Bulk Density	68
Hydraulic Conductivity	72
Matric Suction or Negative Pressure Head	74
Particle Size Analysis	76
Constant Flux Simulations	81
Moisture Content	81
Velocity Vectors	84
Pressure Head	86
WR1, WR2, and WR3	86
Traffic Zone	88

Rubble Zone.....	89
Colluvium	90
Bedrock.....	92
Time Series Simulations	93
Atmospheric Input File	93
Moisture Content	94
Velocity Vectors	96
Pressure Heads.....	96
WR1, WR2, and WR3	97
Traffic Zone	100
Rubble Zone.....	101
Colluvium	104
Bedrock.....	107
CONCLUSIONS.....	109
Future Work or Other Considerations.....	112
REFERENCES	114
Appendix A. Evaporation Rates.	124
Appendix B. Comparison Analysis of Calculated PET from Weather Station Data in northern New Mexico.	128
Methods.....	132
Results.....	134
Discussion.....	143
Conclusions.....	145
Appendix C. Field Measurements of Bulk Density.....	167
Appendix D. Results of Tension Infiltrometer Measurements, June 2004.....	177
Summary	178
Objective.....	178
Background.....	178
Measurement locations	179
Methods.....	179
Results.....	180
Appendix E. Final Results of Tension Infiltrometer Measurements.	191
Appendix F. “Quick Draw” Moisture Probe and Standard Tensiometer Measurements.	197
Appendix G. One-Day Record of Tensiometer Data from Data Logger.....	201
Appendix H. Particle Size Distributions.....	203
Appendix I. Constant Flux Simulations.....	209
Appendix J. Atmospheric File	238
Appendix K. “Wet Year” Simulations.....	252

LIST OF FIGURES

Figure 1. Map of the Red River mining district, New Mexico. 1 = Red River mining district; 2 = Elizabethtown-Baldy mining district; 3 = Twinning district; and 4 = Molycorp Questa mine.	8
Figure 2. Aerial photograph of Molycorp’s Questa mine site located west of Red River, New Mexico. The nine rock piles are labeled in the photograph, but it should be noted that the Goathill North and South rock piles are labeled together as the Goathill Rock piles.	10
Figure 3. A typical representation of the bedrock below the Goathill North rock pile and the Capulin rock pile (from Norwest, 2003). The data used to construct these sketches was derived from observations on core from diamond drill-holes in the bedrock.	13
Figure 4. Trench LFG-004 looking west towards the front of the.....	14
Figure 5. The north wall benches of trench LFG-008. The face of the rock pile is to the left outside of the frame of the picture.	14
Figure 6. Map showing trench locations on the Goathill North rock pile. Red lines indicate the trench walls, circles indicate the surveyed trench corner points, and the black lines show elevation contours. Each trench consisted of approximately four north trench walls and four south trench walls.	16
Figure 7. Sketch of a typical trench for the GHN rock pile.....	17
Figure 8. Precipitation record from the wettest year on record at the Red River weather station (NCDC, 2005).	18

Figure 9. Simplified geologic map of Questa and surrounding study region west of the Questa Mine (from Vail, 1987). The Questa Mine is located just off the map in the eastward direction.	22
Figure 10. Aerial photograph of the GHN rock pile indicating locations of boreholes. The figure shows piezometers marked by red and blue circles; slope inclinometers marked in yellow; and elevation contours marked with blue lines. The stable portion (south) and unstable portion (north) of the rock pile are divided by the bright green line (from Tachie-Menson, 2006). Additional monitoring wells are located farther southwest and southeast of the extents of the figure.	24
Figure 11. Sand cone apparatus (ASTM D1556-00, 1996)	31
Figure 12. Nuclear Densometer (from Instruction Manual, CPN International, 1999).	33
Figure 13. Tension infiltrometer (adapted from Holt et al., 2002).	35
Figure 14. Standard Tensiometer instrument diagram.....	40
Figure 15. Advanced Tensiometer design (from Hubbell and Sisson, 1998).....	41
Figure 16. Depiction of a tensiometer field application (from Hubbell and Sisson, 1998).....	42
Figure 17. Aerial photograph of the Goathill North rock pile, overlain by a GIS shapefile designating the stable portion of the GHN rock pile. The cross-section A-A' indicated by the purple line, shows the spatial coordinates from which the elevations for the conceptual model were	

obtained. Red, purple, and green lines indicate the trenches that were cut into the rock pile.	46
Figure 18. The conceptual model zones of the Goathill North rock pile. WR1 is the region with the finest material where the majority of trenches were excavated. WR2 is the intermediate zone in which one trench was excavated. WR3 is the region with the coarsest material where little data was collected. The traffic zone is a shallow compacted region at the top of the rock pile. The rubble zone is the basal region of the rock pile, which has coarse angular cobbles and boulders. The colluvium is a unit that was deposited before the rock pile by natural weathering processes.....	47
Figure 19. Estimated daily PET (cm) for four consecutive years and the average daily PET (cm) of these four years (data from Golder Associates, 2005 a).	62
Figure 20. The moisture retention curve for base case simulation 1, for K_{low} and soils without rocks.....	77
Figure 21. The moisture retention curve for base case simulation 3, for K_{low} and rocky soils.	78
Figure 22. Schematic diagram of the simulations completed in HYDRUS 2D. Simulations were completed at four constant flux levels of 0.50, 0.35, 0.20, and 0.03 cm/day for each of the four base case simulations described. Transient state simulations were completed by using the steady state pressure head conditions from the 0.35 cm/day constant flux level simulations as the initial pressure head conditions.	80

Figure 23. The final moisture distribution within simulation 3, with low bedrock permeability and soils with rocks at the constant flux rate of 0.35 cm/day.....	82
Figure 24. The final velocity vectors within simulation 1 at the 0.35 cm/day time step. The scale ranges between 0 and 1.8 cm/day. The magnitude of the vectors have been exaggerated by five times.....	85
Figure 25. The mean pressure head (cm) within the WR1 region at each constant flux rate for the four base case simulations.	87
Figure 26. The minimum pressure head (cm) within the traffic zone at each constant flux rate for the four base case simulations.	88
Figure 27. The maximum pressure head (cm) within the rubble zone at constant flux rates for the four base case simulations.....	89
Figure 28. The minimum pressure head (cm) within the rubble zone at constant flux rates for the four base case simulations.....	90
Figure 29. The maximum pressure heads (cm) within the colluvium for the steady state conditions of the constant flux simulations.	91
Figure 30. The minimum pressure heads (cm) within the colluvium for the steady state conditions of the constant flux simulations.	91
Figure 31. The maximum pressure heads (cm) within the bedrock for the steady state conditions of the constant flux simulations.	92
Figure 32. The precipitation record for the “wet year” used in the transient simulations which took place in 1994.....	93

Figure 33. The moisture distribution within the rock-pile hillslope system for base case simulation 3 (K_{low} , soils with rocks) at 116.8 days.	95
Figure 34. The maximum pressure head (cm) within the WR1 region of the rock pile for the “wet year” simulations 1 through 4.....	98
Figure 35. The maximum pressure head distribution within the WR3 region of the pile in each of the four “wet year” transient simulations.	99
Figure 36. The maximum pressure head distribution within the traffic zone of the pile in each of the four “wet year” transient simulations.	101
Figure 37. The minimum pressure head distribution within the rubble zone for each of the four “wet year” transient simulations.	102
Figure 38. The maximum pressure heads (cm) within the rubble zone for the four “wet year” simulations.	103
Figure 39. The mean pressure head distribution within the rubble zone for the four “wet year” transient simulations.....	104
Figure 40. The minimum pressure head distribution within the colluvium region for each of the four “wet year” transient simulations. Simulations 1 and 3 exhibit similar minimum pressure heads over time, while simulations 2 and 4 also exhibit similar minimum pressure heads over time.	105
Figure 41. The mean pressure head distribution within the colluvium region for each of the four “wet year” transient simulations.	106
Figure 42. The median pressure head distribution within the colluvium region for each of the four “wet year” transient simulations.	107

Figure 43. The maximum pressure head distribution within the bedrock for
each of the four “wet year” transient simulations. 108

LIST OF TABLES

Table 1. The weight percent of gravel, sand, silt, and clay are reported for the WR1, WR2, WR3, traffic zone, rubble zone, and colluvium regions within the pile. The mean, standard deviation (std dev), and coefficient of variation (cv) for each region are presented. In addition, the mean, standard deviation, and coefficient of variation of the dry bulk density of the WR1, WR2, WR3, traffic zone, rubble zone, and colluvium are presented. 52

Table 2. The volume of rocks within the WR1, WR2, WR3, and rubble zone regions of the rock pile. The minimum volume fraction of fines and pores for the WR1, WR2, WR3, rubble zone, colluvium, and traffic zone are presented. In addition, the maximum volume fraction of gravel and rocks within the WR1, WR2, WR3, rubble zone, colluvium, and traffic zone are presented. 57

Table 3. The residual moisture content (θ_r), saturated moisture content (θ_s), van Genuchten alpha (α), van Genuchten n , saturated hydraulic conductivity (K_s) and I for the WR1, WR2, WR3, rubble zone, colluvium, traffic zone, and bedrock regions within the pile are presented above. In addition, two sets of parameters, one for fines and one for fines and rocks are presented for the WR1, WR2, WR3, rubble zone, colluvium, and traffic zone regions within the rock pile. 59

Table 4. The design matrix for the 2^3 factorial design sensitivity analysis. 65

Table 5. Constant flux (cm/day), the corresponding total annual precipitation (cm), and the maximum and minimum total annual precipitation (cm) from the Red River weather station. 66

Table 6. The four base case simulations for the sensitivity analysis. Four different constant flux levels were run for each of the four base case simulations, yielding 16 total constant flux simulations. The four base cases were also used in the time series analyses conducted for the sensitivity analysis. 67

Table 7. The calculated mean dry bulk densities from four different test methods within the WR1, WR2, WR3, rubble zone, and traffic zone regions of the rock pile are presented. The dry bulk density calculated by using the porosity of the soils estimated in HYDRUS 2D neural network is presented as well. 69

LIST OF APPENDICES FIGURES

Figure B- 1. The approximate locations of the meteorological stations are shown in the aerial photograph of the Molycorp property.....	131
Figure B- 2. ET_O vs. PET (consultants' values) for station TP-5.	136
Figure B- 3. PET vs. PET (consultants' values) for station TP-5.....	136
Figure B- 4. Calculated ET_O , PET, and PET from consultants between January 1, 2000 and December 31, 2002 using data from meteorological station TP-5.....	137
Figure B- 5. ET_O vs. PET (consultants' values) for station TP-4.	138
Figure B- 6. PET vs. PET (consultants' values) for station TP-4.....	138
Figure B- 7. Calculated ET_O , PET, and PET from consultants for the meteorological data for station TP-4.....	139
Figure B- 8. ET_O vs. PET (consultants' values) for station TP-6/7.....	140
Figure B- 9. PET vs. PET (consultants' values) for station TP-6/7.....	140
Figure B- 10. Calculated ET_O , PET, and PET from consultants for the meteorological data for station TP-6/7.....	141
Figure B- 11. Calculated PET using Priestly-Taylor methods for station TP-5 data.....	142
Figure B- 12. Calculated PET using Priestly-Taylor methods for station TP-4.	142
Figure B- 13. Calculated PET using Priestly-Taylor method for station TP-6/7.....	143
Figure B- 14. The results from station TP-5, where T_{dew} was calculated using the relative humidity (equation 12).....	152
Figure B- 15. The results from the first year of data at station TP-5.....	153

Figure B- 16. The results from the second year of data at station TP-5.	154
Figure B- 17. The results from the third year of data at station TP-5.....	155
Figure B- 18. The results from the fourth year of data at station TP-5.....	156
Figure B- 19. The results from station TP-4, where T_{dew} was calculated using the relative humidity (equation 12).....	157
Figure B- 20. The results from the first year of data at station TP-4.....	158
Figure B- 21. The results from the second year of data at station TP-4.	159
Figure B- 22. The results from the third year of data at station TP-4.....	160
Figure B- 23. The results from the fourth year of data at station TP-4.....	161
Figure B- 24. The results from TP-6/7, where T_{dew} was calculated using the relative humidity (equation 12).....	162
Figure B- 25. The results from the first year at station TP-6/7.....	163
Figure B- 26. The results from the second year of data at station TP-6/7.	164
Figure B- 27. The results from the third year of data at station TP-6/7.....	165
Figure B- 28. The results from the fourth year of data at station TP-6/7.	166
Figure D- 1. Tensiometer temperature readings and Red River meteorological data from 6/28 to 6/29/04. 6/28 = 180th day of the year 2004. a) Tensiometer temperature sensor voltages. b) Tensiometer temperature values. c) Maximum, mean, and minimum daily temperatures and daily precipitation values for Red River NWS station.....	183
Figure D- 2. Tensiometer temperature and matric potential readings and Red River meteorological data from 6/28 to 6/29/04. 6/28 = 180th day of the year 2004. a) Tensiometer matric potential sensor voltages and TEN1W	

temperature. b) Tensiometer temperature and TEN1SE matric potential values. c) Maximum, mean, and minimum daily temperatures and daily precipitation values for Red River NWS 184

Figure D- 3. Tensiometer temperature readings and Red River meteorological data from 8/16/04 to 9/11/04. a) Tensiometer temperature sensor voltages. b) Tensiometer temperature values. c) Maximum, mean, and minimum daily temperatures and precipitation values for Red River NWS station. 185

Figure D- 4. Tensiometer matric potential readings and Red River meteorological data from 8/16 to 9/11/04. a) Tensiometer matric potential sensor voltages. b) Tensiometer matric potential values. c) Maximum, mean, and minimum daily temperatures and daily precipitation values for Red River NWS station..... 186

Figure D- 5. Near-surface tensiometer temperature readings and Red River meteorological data from 6/1 to 9/11/04. Temperatures for near-surface tensiometers TEN1NE and TEN2E are indicated by violet and bright green lines, respectively. Maximum, mean, and minimum daily temperatures for Red River NWS station are shown by lines with symbols, and daily precipitation values are shown as bar charts..... 187

Figure D- 6. Matric potential and temperature data at station TEN1 from 8/16/04 to 9/11/04. a) Matric potential b) Temperature..... 188

Figure D- 7. Matric potential and temperature data at station TEN2 from 8/16/04 to 9/11/04. a) Matric potential. b) Temperature. Data from station TEN1 tensiometers at similar depths are shown for comparison.....	189
Figure I- 1. The maximum pressure head within the WR1 region of the model domain for four subsequent constant flux levels.	210
Figure I- 2. The mean pressure head distribution within the WR1 region of the model domain for four subsequent constant flux levels.	211
Figure I- 3. The median pressure head within the WR1 region of the model domain for four subsequent constant flux levels.	212
Figure I- 4. The minimum pressure head within the WR1 region of the model domain for four subsequent constant flux levels.	213
Figure I- 5. The maximum pressure head within the WR2 region of the model domain for four subsequent constant flux levels.	214
Figure I- 6. The mean pressure head within the WR2 region of the model domain for four subsequent constant flux levels.	215
Figure I- 7. The median pressure head within the WR2 region of the model domain for four subsequent constant flux levels.	216
Figure I- 8. The minimum pressure head within the WR2 region of the model domain for four subsequent constant flux levels.	217
Figure I- 9. The maximum pressure head within the WR3 region of the model domain for four subsequent constant flux levels.	218

Figure I- 10. The mean pressure head within the WR3 region of the model domain for four subsequent constant flux levels.	219
Figure I- 11. The median pressure head within the WR3 region of the model domain for four subsequent constant flux levels.	220
Figure I- 12. The minimum pressure head within the WR3 region of the model domain for four subsequent constant flux levels.	221
Figure I- 13. The maximum pressure head within the rubble zone in the model domain for four subsequent constant flux levels.	222
Figure I- 14. The mean pressure head within the rubble zone region of the model domain for four subsequent constant flux levels.	223
Figure I- 15. The median pressure head within the rubble zone region of the model domain for four subsequent constant flux levels.	224
Figure I- 16. The minimum pressure head within the rubble zone region of the model domain for four subsequent constant flux levels.	225
Figure I- 17. The maximum pressure head within the colluvium region of the model domain for four subsequent constant flux levels.	226
Figure I- 18. The mean pressure head within the colluvium region of the model domain for four subsequent constant flux levels.	227
Figure I- 19. The median pressure head within the colluvium region of the model domain for four subsequent constant flux levels.	228
Figure I- 20. The minimum pressure head within the colluvium region of the model domain for four subsequent constant flux levels.	229

Figure I- 21. The maximum pressure head within the traffic zone region of the model domain for four subsequent constant flux levels.	230
Figure I- 22. The mean pressure head within the traffic zone region of the model domain for four subsequent constant flux levels.	231
Figure I- 23. The median pressure head within the traffic zone region of the model domain for four subsequent constant flux levels.	232
Figure I- 24. The minimum pressure head within the traffic zone region of the model domain for four subsequent constant flux levels.	233
Figure I- 25. The maximum pressure head within the bedrock region of the model domain for four subsequent constant flux levels.	234
Figure I- 26. The mean pressure head within the bedrock region of the model domain for four subsequent constant flux levels.	235
Figure I- 27. The median pressure head within the bedrock region of the model domain for four subsequent constant flux levels.	236
Figure I- 28. The minimum pressure head within the bedrock region of the model domain for four subsequent constant flux levels.	237
Figure J- 1. The maximum pressure head within the WR1 region of the model domain for the four “wet year” simulations.....	253
Figure J- 2. The mean pressure head within the WR1 region of the model domain for the four “wet year” simulations.....	254
Figure J- 3. The median pressure head within the WR1 region of the model domain for the four “wet year” simulations.....	255

Figure J- 4. The minimum pressure head within the WR1 region of the model domain for the four “wet year” simulations.....	256
Figure J- 5. The maximum pressure head within the WR2 region of the model domain for the four “wet year” simulations.....	257
Figure J- 6. The mean pressure head within the WR2 region of the model domain for the four “wet year” simulations.....	258
Figure J- 7. The median pressure heads within the WR2 region of the model domain for the four “wet year” simulations.....	259
Figure J- 8. The minimum pressure heads within the WR2 region of the model domain for the four “wet year” simulations.....	260
Figure J- 9. The maximum pressure head within the WR3 region of the model domain for the four “wet year” simulations.....	261
Figure J- 10. The mean pressure head within the WR3 region of the model domain for the four “wet year” simulations.....	262
Figure J- 11. The median pressure head within the WR3 region of the model domain for the four “wet year” simulations.....	263
Figure J- 12. The minimum pressure head within the WR33 region of the model domain for the four “wet year” simulations.....	264
Figure J- 13. The maximum pressure head within the rubble zone region of the model domain for the four “wet year” simulations.....	265
Figure J- 14. The mean pressure head within the rubble zone region of the model domain for the four “wet year” simulations.....	266

Figure J- 15. The median pressure head within the rubble zone of the domain for the four “wet year” simulations.....	267
Figure J-16. The minimum pressure head within the rubble zone region of the model domain for the four “wet year” simulations.....	268
Figure J-17. The maximum pressure head within the colluvium region of the model domain for the four “wet year” simulations.....	269
Figure J- 18. The mean pressure heads within the colluvium region of the model domain for the “wet year” simulations.	270
Figure J- 19. The median pressure head within the colluvium region of the model domain for the four “wet year” simulations.....	271
Figure J- 20. The minimum pressure head within the colluvium region of the model domain for the four “wet year” simulations.....	272
Figure J- 21. The maximum pressure head within the traffic zone region of the model domain for the four “wet year” simulations.....	273
Figure J- 22. The mean pressure head within the traffic zone region of the model domain for the four “wet year” simulations.....	274
Figure J- 23. The median pressure head within the traffic zone region of the model domain for the four “wet year” simulations.....	275
Figure J- 24. The minimum pressure head within the traffic zone region of the model domain for the four “wet year” simulations.....	276
Figure J- 25. The maximum pressure head within the bedrock region of the model domain for the four “wet year” simulations.....	277

Figure J- 26. The mean pressure heads within the bedrock region of the model domain for the four “wet year” simulations.....	278
Figure J- 27. The median pressure heads within the bedrock region of the model domain for the four “wet year” simulations.....	279
Figure J- 28. The minimum pressure heads within the bedrock region of the model domain for the four “wet year” simulations.....	280

LIST OF APPENDICES TABLES

Table A- 1. The results from the 1 st Year Modeling Report, Water Balance Study For Mine Rock Piles, Questa Mine, New Mexico, Report No. 052015/2. AET represents the actual evapotranspiration in inches.	126
Table B- 1. Assumptions of values for Penman-Monteith Calculation	133
Table C- 1. The test number, field ID, hole pit ID, test method, and dry bulk density from the measurements made within the WR1 region of the GHN rock pile are presented.	168
Table C- 2. The test number, field ID, hole pit ID, test method, and dry bulk density from the measurements made within the WR2 region of the GHN rock pile are presented.	173
Table C- 3. The test number, field ID, hole pit ID, test method, and dry bulk density from the measurements made within the rubble zone region of the GHN rock pile are presented.....	175
Table C- 4. The test number, field ID, hole pit ID, test method, and dry bulk density from the measurements made within the rubble zone region of the GHN rock pile are presented.....	176
Table D- 1: Measurement locations.....	179
Table D- 2: Flux rates	180
Table D- 3. Calculated hydraulic conductivity	181

Table E- 1. Comparison of tension infiltrometer and guelph permeameter measurements.....	193
Table E- 2. Results from all of the tension infiltrometer measurements.	194
Table E- 3. Results from all of the guelph permeameter measurements.	195
Table G- 1. Matric suction measurements made within the trenches in the stable portion of the GHN rock pile using standard tensiometers and Quick Draw tensiometers.....	198
Table G- 2. One day record of matric suction and temperature recorded at TEN1NE by the data logger at the nested tensiometers station.....	202
Table H- 1. The gravel, sand, silt, and clay weight percentages from grain size analyses conducted on samples from the WR1 region of the GHN rock pile.....	204
Table H- 2. The gravel, sand, silt, and clay weight percentages from grain size analyses conducted on samples from the WR2 region of the GHN rock pile.....	205
Table H- 3. The gravel, sand, silt, and clay weight percentages from grain size analyses conducted on samples from the rubble zone region of the GHN rock pile.	206

Table H- 4. The gravel, sand, silt, and clay weight percentages from grain size analyses conducted on samples from the colluvium region of the GHN rock pile. 207

Table H- 5. The gravel, sand, silt, and clay weight percentages from grain size analyses conducted on samples from the traffic zone region of the GHN rock pile. 208

INTRODUCTION

Slope stability is a common concern at mines because rock piles and tailings piles can become gravitationally unstable, which in some cases has led to property damage, loss of life, or both (Bowman and Gilchrist, 1978; Okagbue, 1987; Richards et al., 1981; Speck et al. 1993; Ulusay et al., 1995). Numerous studies related to mine closure and risk assessment have been completed at different mine sites worldwide to investigate the geotechnical stability and remediation techniques of rock piles and tailings piles (Donovan and Karfakis, 2003; Hancock and Turley, 2006; Tesarik and McKibbin, 1999; US EPA Report, 2003; Willgoose and Riley, 1998; Williams and Curry, 2002). However, tailings piles and rock piles are much different and should not be confused. Tailing piles consist of finely ground, well sorted waste material remaining after the economic ore has gone through a milling process, while rock pile material consists of poorly sorted uneconomic mineralized rock of larger grain size and varying grain size distribution than material that has gone through any processing (Van Zyl et al., 2002). In 2003 Molycorp, Inc. initiated a study (the Weathering study) by selecting a team of independent collaborative researchers to evaluate the effect of weathering on the long-term (20-100 years and > 100 years) gravitational stability of rock piles at the Questa Molybdenum mine in northern New Mexico. The team selected the Goathill North (GHN) rock pile to study and model in detail for this study.

Weathering of rocks results from two processes: chemical, which results in compositional and mineralogical changes in the original material, or physical, which

results in physical changes that can breakdown the original material or both. The weathering processes that occur within the rock piles at the mine site involve the dynamic interaction of the rock pile material with water, air, sulfur, and microbes. Such processes can lead to a reduction in rock strength by grain size reduction or increased strength by cementation of material (Gutierrez, 2006). Donovan and Karfakis (2003) state:

“Saturation of the slopes and weathering of the slope material are the main reasons the slopes failed, and both are directly due to the presence of water.”

Thus understanding how fluids, especially water are transported in the rock-pile hillslope system is critical to reaching the goal of the Weathering study. In order to understand water transport through a rock pile, it is important to look at the fundamental concepts and factors that control fluid transport in a hillslope system.

Several questions formulated after considering how to approach the problem. (1) How does the presence of rocks impact the moisture distribution within the rock pile? (2) How does the bedrock permeability impact the moisture distribution within the pile? (3) How quickly do the rock pile soils respond to precipitation events? (4) Which regions of the rock pile become the wettest? These questions led to the development of the two main objectives of this thesis. The first objective is to determine the spatiotemporal moisture distribution within a generic rock pile modeled after the Goathill North (GHN) rock pile. The second objective is to test the importance of soil hydraulic properties, bedrock permeability, and climate to the pressure head and moisture distribution within the generic rock pile.

The importance of water to slope stability has been identified in a number of studies. Slope instability can be caused by a number of different factors including gravity sorting of waste material during construction of piles, increased overpressure due to increased soil wetness, increased slope angle from soil erosion, loss of material strength due to weathering, and promoted by precipitation or snowmelt events (Tesarik and McKibben, 1999). Slope failures reported on mine sites are often associated with a build up of positive pore pressures within the system due to heavy rainfall events (Donovan and Karfakis, 2003; Kasmer et al., 2006; and Tesarik and McKibben, 1999). Donovan and Karfakis (2003) reported that all of the eleven slope failures detected over a twelve-year period in the coal waste rock piles of their study region in southwest Virginia occurred in years of above average rainfall. In a study of spoil pile instabilities at a coal mine in Turkey, Kasmer et al. (2006) concluded that slope failure occurred approximately one month after rainfall. These studies done by Donovan and Karfakis (2003) and Kasmer et al. (2006) suggest that a lagged response of the soils to rainfall events can still lead to development of sufficient pore pressures to induce failure.

Natural analogues such as landslides of natural hillslopes and debris flows are useful for understanding failures in rock piles and mine tailing piles. Landslides of natural hillslopes and debris flows are also an environmental and safety concern due to their unpredictable nature (Basile et al., 2003; Hengxing et al., 2003; Larsen et al., 2000; Orense et al., 2004). Rainfall is an important factor which often is said to trigger landslide events, but the actual physical processes leading to landsliding are less clear (Hengxing, et al., 2003; Iverson, 2000; Orense et al., 2004). Iverson (2000)

investigated these physical processes with a numerical model that solved a reduced form of the Richards equation. The results from his study indicated that slope failure and landslide motion are impacted by groundwater pressure heads that change in response to rainfall infiltration.

Borga et al. (2002) assessed shallow landslides in the Eastern Alps of Italy and concluded that rainstorms and periods of snowmelt reduced the shear strength of soils by increasing the pore-water pressure, which in effect triggered the failures. The increase in pore-water pressure was either due to percolation of water from rainfall or saturation from below by the groundwater table, which can be locally perched (Borga et al., 2002).

Orense et al. (2004) conducted a series of laboratory tests to determine the initiation process of rainfall-induced slope failures. In the laboratory tests, artificial rainfall was dropped on the top of the sandy slope model or water was introduced from the side upslope in order to induce failure. The tests monitored the pore-water pressure, soil-moisture content, and ground deformation within the model slope. The results of this study indicated that the initiation of slope failure was due to near saturation of soils at the toe of the slope. Following slope failure, small slope displacements occurred upslope suggesting that initial failure at the base could lead to additional failures upslope.

Hengxing et al. (2003) conducted a rainfall-induced landslide stability analysis using GIS technology to investigate transient pore pressure responses to short, intense rainfall events. They made a general observation that the pore pressure response time to rainfall events is a function of several factors including rainfall

intensity, time, soil permeability, and soil depth. In addition, they concluded that shallow failure was induced by an increase of positive pore pressure in response to rainfall and often occurred on slopes with low permeability soils. However, slopes with high permeability soils remained stable, due to the need for more rainfall (longer duration and/or intensity) in order to affect the soils at depth.

Weiler and McDonnell (2004) described some of the primary factors that affect moisture distribution in a hillslope as rainfall intensity, slope angles, soil properties, and surface/bedrock topography. They identified the secondary effects on water transport as soil depth, porosity, conductivity distributions, and slope geometry.

Several studies have corroborated the claim that bedrock surface topography affects water transport within hillslopes (Guan, H., 2005; McDonnell, 1990; McDonnell et al., 1996; McGlynn et al., 2002; Mosley, 1979; Peters et al., 1995; Uchinda et al., 2003). Peters et al. (1995) found that a significant fraction of rainfall-event water moved vertically downward through preferential pathways to the bedrock surface and then laterally over the bedrock surface. Similarly, McGlynn et al. (2002) concluded that when matrix hydraulic conductivities exceed maximum rainfall intensity, water will move preferentially downward into the hillslope until reaching the soil-bedrock interface or a low permeability soil layer and then move laterally along the impeding layer.

Variability in the soil hydraulic properties (hydraulic conductivity, porosity, etc.) is a factor in controlling the transport of water through the hillslope system. Park and van de Giesen (2004) described the reasons for difficulties in obtaining accurate field measurements of the properties, which are costly to obtain. By using a

soil-landscape delineation procedure, they were able to conclude that the soils along with the surface curvature, upslope contributing area, and slope aspect could effectively explain the moisture variations within the hillslope approximately 73% of the time.

Changes in the moisture distributions within a hillslope system, such as the GHN rock pile could directly impact chemical weathering processes, such as pyrite oxidation. The oxidation of iron sulfide minerals, such as pyrite and pyrrhotite can be responsible for acid production in mine soils (Stumm, W. and J. J. Morgan, 1989). However, the oxidation reaction is dependant on water and oxygen and thus would be controlled spatially by the availability of them both. Therefore, a better understanding of the spatial moisture distribution will improve the conceptual models developed for geochemical reaction models, another aspect of the Weathering study.

In a recent study of the acid generation potential of the GHN rock pile material (also described as soil, which is an unconsolidated sediment), Tachie-Menson (2005, 2006) concluded that the rock pile material includes a number of acid-consuming minerals, namely silicates and carbonates. However, acid generation has been and is expected to continue within the rock pile. Therefore, the rock types that are present in the pile have an influence on acid generation potential of the GHN rock pile. Thus, a strong understanding of spatial distribution of minerals within the rock pile will also contribute in developing the geochemical reaction models. These models will be used to determine if weathering of the rock pile material could change the shear strength of the soils, leading to either less stable or more stable conditions within the rock pile.

Finally, the shear strength of the GHN rock pile soils has been under investigation (Gutierrez, L. A. F., 2006; Norwest, 2004; and Robertson Geoconsultants, 2000). The internal friction angle (ϕ), a shear strength parameter which relates the shear stress (τ) to the total stress (σ) by the following equation (Das, 1983; Holtz and Kovacs, 2003; Terzaghi et al., 1996),

$$\tau = c + \sigma \tan \phi \quad (1)$$

ranged between 40° and 47° (Gutierrez, 2006). She concluded that these values were higher than values reported for internal friction angles for saturated conditions ($\phi = 31^\circ$ and 36°) in previous studies conducted on the GHN rock pile material (Norwest, 2004 and Robertson Geoconsultants, 2000). Gutierrez (2006) concluded that a decrease in the internal friction angle of the rock pile material corresponded to a slight increase in the degree of weathering. Therefore, her study implies the importance of understanding the moisture distribution within the rock pile.

The Questa Mine Site

The Questa molybdenum mine is located in the Sangre de Cristo Mountains in northern New Mexico, just north of State Highway 38 in Taos County (Figure 1).

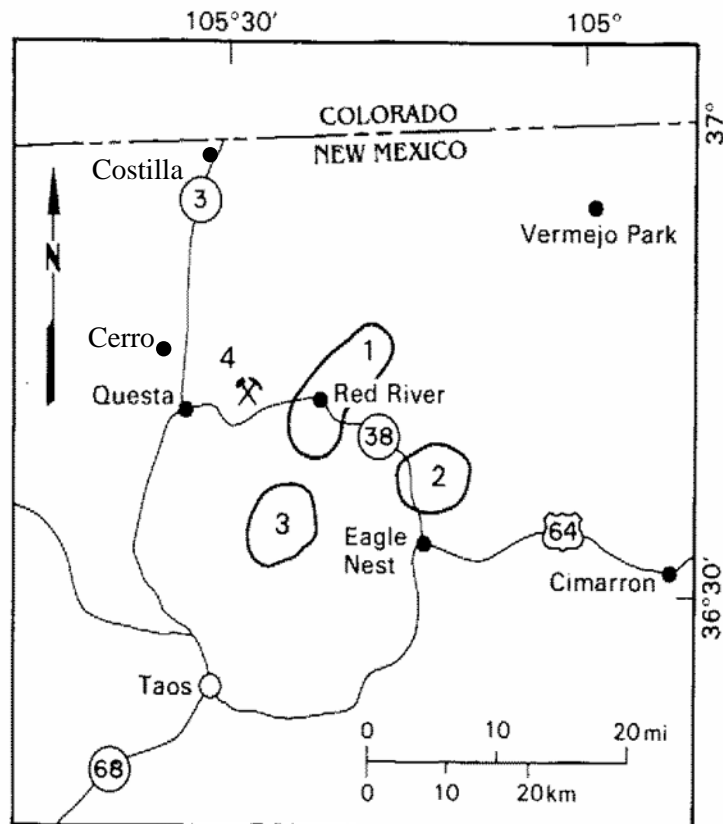


Figure 1. Map of the Red River mining district, New Mexico. 1 = Red River mining district; 2 = Elizabethtown-Baldy mining district; 3 = Twining district; and 4 = Molycorp Questa mine.

The Questa molybdenum mine began operations in the summer of 1918 as an underground mine under the ownership of R & S Molybdenum Mining Company, after geologic prospecting indicated the presence of ferrimolybdenite and

molybdenite veins exposed on canyon walls (Carpenter, 1968). In the summer of 1920, the mine was acquired by Molybdenum Corporation of America, which later became Molycorp, Inc.. Open pit mining operations began in 1964 with the removal of uneconomic overburden rock. Ore production from the open-pit occurred between 1965 and 1982. Over this period of time approximately 73.5 million metric tons of ore were processed and 317.5 million metric tons of overburden rock was stripped and deposited on the surrounding mountain slopes to create nine rock piles (Figure 2).

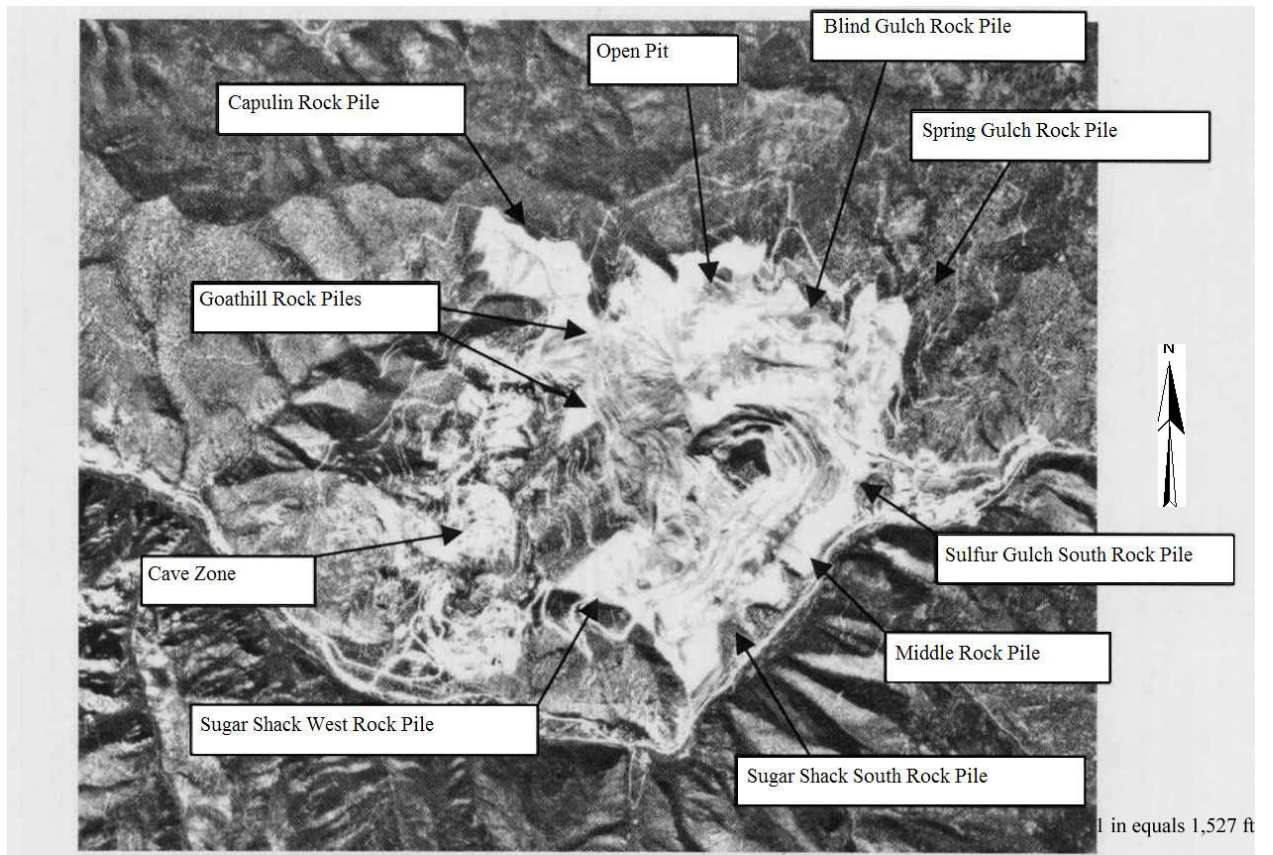


Figure 2. Aerial photograph of MolyCorp's Questa mine site located west of Red River, New Mexico. The nine rock piles are labeled in the photograph, but it should be noted that the Goathill North and South rock piles are labeled together as the Goathill Rock piles.

Goathill North Rock Pile

The GHN rock pile is located in the northwestern region of the mine property and is situated on the western side of a ridge separating the pile from the open pit (Figure 2). Prior to re-grading, the GHN rock pile consisted of stable and unstable parts. The unstable portion of the rock pile was deposited on unconsolidated sediment of colluvial and landslide material containing pyritic rock and clay rich hydrothermally altered rocks from hydrothermal alteration scars (Meyer and Leonardson, 1990; Norwest, 2000; Robertson Geoconsultants, 2000). During the dumping of material that formed the GHN rock pile between 1969 and 1972, additional weight on the colluvial material caused movement of the rock pile. The creep of the rock pile has continued continuously for more than 30 years after its initiation (Norwest, 2003) and re-grading for stabilization in 2005. The underlying material of the GHN rock pile resulted in the pile becoming separated into stable and unstable portions. Based on the findings of an extensive study of the GHN rock pile (Norwest, 2003), a four-phase mitigation plan was designed to stop the movement of the rock pile. The plan included regrading the GHN rock pile to reduce its slope angle as well as move material from the upper portion of the pile to the bottom to serve as a buttress against further movement. The gravitationally stable part of the Goathill North rock pile (GHN) provides the field basis for this study.

At the Questa mine, the overburden rock that is contained in the nine rock piles was deposited on the mountain slopes by using end-dumping techniques. The end-dumping technique is the process in which the overburden rock is dumped and or

pushed over the edge of a slope and allowed to roll down the slope (Carson, 1961). As the material moves downslope, separation of larger rock fragments from the smaller rock fragments occurs, producing particle-size segregation within the rock pile (Carson, 1961). The Goathill North (GHN) rock pile is one of nine rock piles that were created from the overburden removed during open-pit mining. The GHN rock pile contains approximately 10.6 million metric tons of rock material; and prior to re-grading it had slopes similar to the original, pre-mine topography with an approximate angle of repose between 35° and 40° (Norwest, 2003).

The stable portion of GHN was deposited directly on bedrock. The bedrock below both the stable and unstable parts of the GHN rock pile consists of Amalia Tuff, coarse andesite flow breccia and andesite porphyry (Norwest, 2003; see lithologic atlas, McLemore, 2005). The Amalia Tuff in the region is a welded, ash flow tuff that has a structural dip angle between 60° and vertical (Norwest, 2003). The andesite in the region is part of the Latir volcanic sequences and is dominated by coarse andesite flow breccia, but also consists of porphyritic to finely porphyritic andesite and volcanoclastics (Norwest, 2003; see lithologic atlas, McLemore, 2005). The structural geology below the GHN rock pile consists of fault zones, which dip approximately 30° to the northwest and separate the Amalia tuff bedrock from the andesitic bedrock (Norwest, 2003). A composite sketch of the bedrock lithology and structure underlying the Goathill North and Capulin rock piles is shown in Figure 3 below.

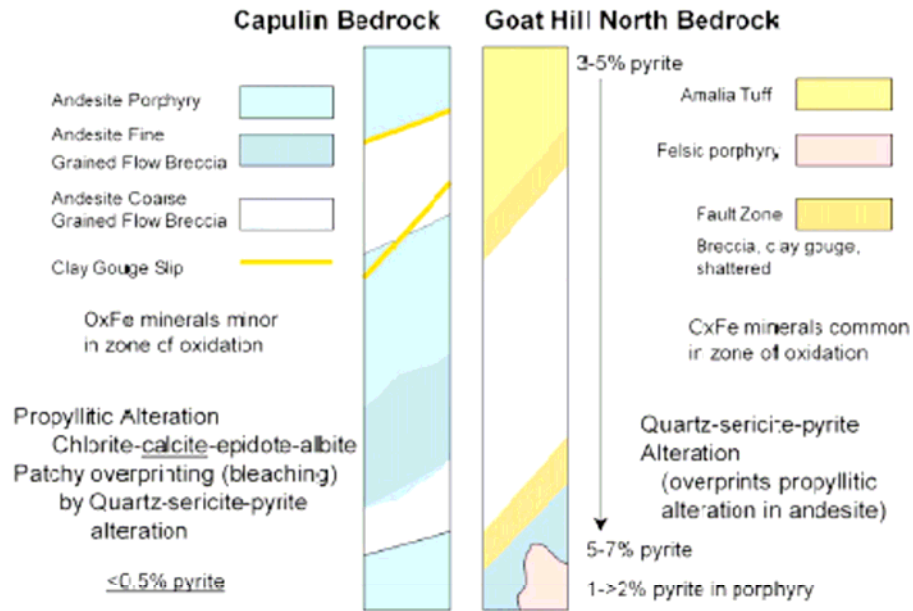


Figure 3. A typical representation of the bedrock below the Goathill North rock pile and the Capulin rock pile (from Norwest, 2003). The data used to construct these sketches was derived from observations on core from diamond drill-holes in the bedrock.

The mitigation project outlined to re-grade the GHN rock pile provided a unique opportunity to examine the inside of the rock pile, and a set of trenches were excavated in the rock pile in the fall of 2004 and winter of 2004-2005 (Figure 4 and Figure 5).



Figure 4. Trench LFG-004 looking west towards the front of the rock pile, hillslope face.



Figure 5. The north wall benches of trench LFG-008. The face of the rock pile is to the left outside of the frame of the picture.

In each trench, field samples, measurements, and observations were made to physically and geochemically characterize the rock pile. Although trenches were cut in both the stable and unstable portions of the rock pile as shown as cross-section lines in Figure 6 in red, the data presented in this study was collected from the stable portion of the pile.

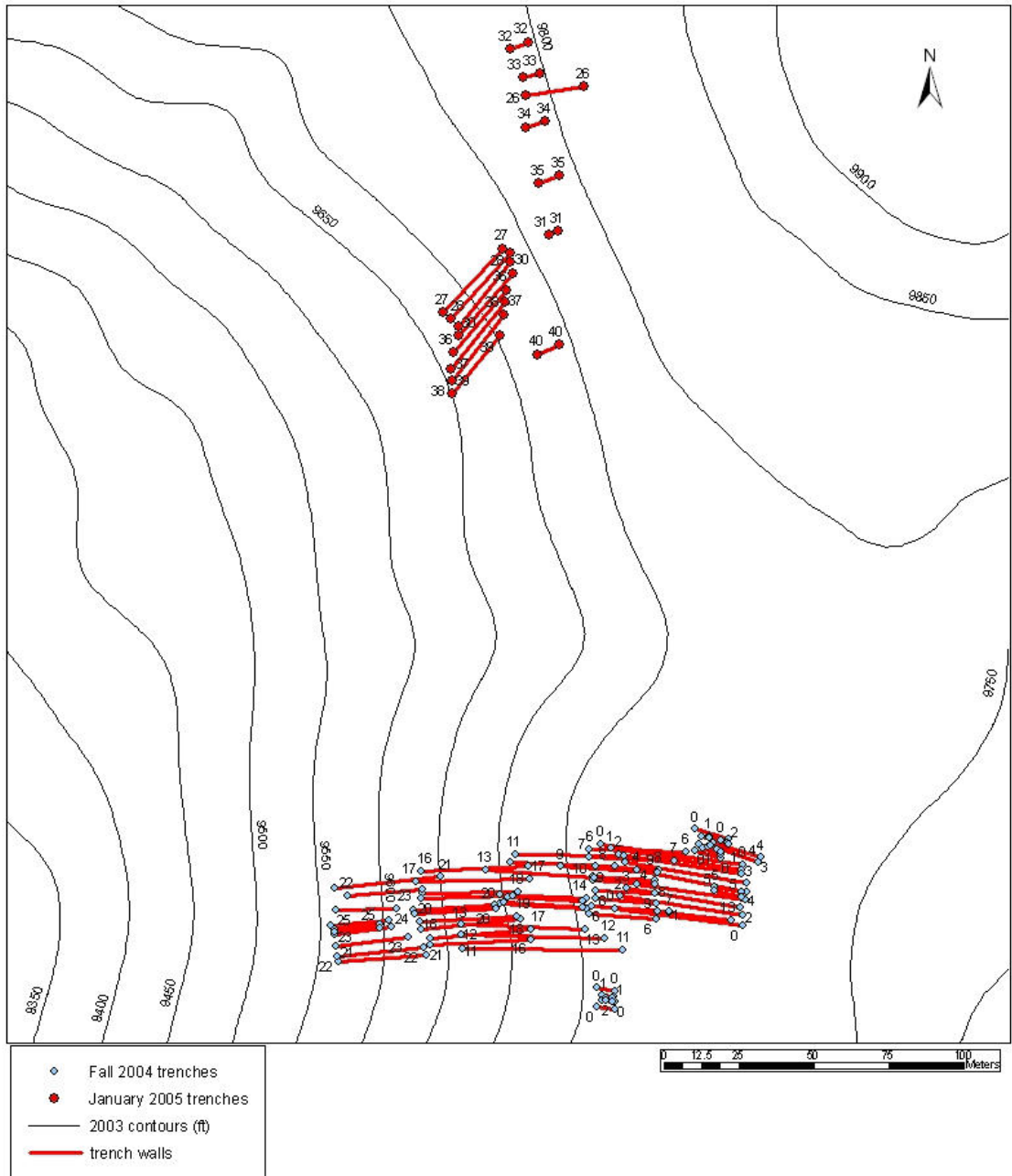


Figure 6. Map showing trench locations on the Goathill North rock pile. Red lines indicate the trench walls, circles indicate the surveyed trench corner points, and the black lines show elevation contours. Each trench consisted of approximately four north trench walls and four south trench walls.

The trenches on the stable portion of GHN were numbered sequentially starting with LFG-002 and finishing with LFG-009. The trenches were typically cut with four benches, which were approximately 37 ft (11.3 m) wide and approximately 4 ft high (1.2 m). Figure 7 illustrates a cross-cut of the general shape of the trenches.

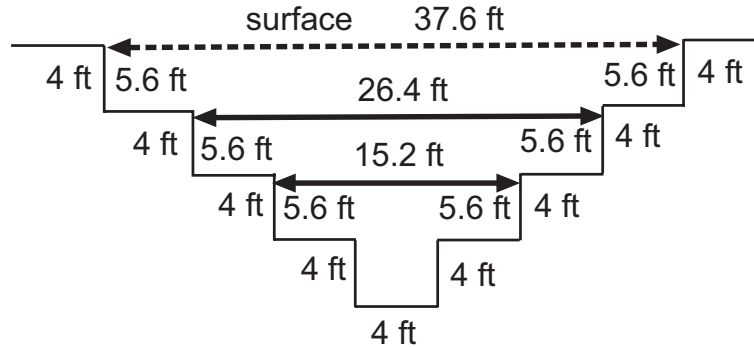


Figure 7. Sketch of a typical trench for the GHN rock pile

The trenches extended different lengths, ranging between less than 20 ft (approximately 6 m) in trenches cut into the back wall of the rock pile to 164 ft (approximately 50 m) long trenches with five benches (LFG-005). Field geologists mapped the trenches and were able to correlate units downward through a series of five excavated trenches. A total of eighteen units were distinguished within the rock piles and described by field geologists (McLemore et al., 2006). The subsurface units were differentiated based upon grain size, color, stratigraphic position, texture, and other physical properties observed in the field (McLemore et al., 2006).

Climate

The Questa molybdenum mine is located in a semi-arid climate in the Sangre de Cristo Mountains of northern New Mexico. The climate is characterized by winters with high snowfall and summer monsoonal storms, showing an increase in the precipitation in the late summer months (see Figure 8, NCDC, 2005).

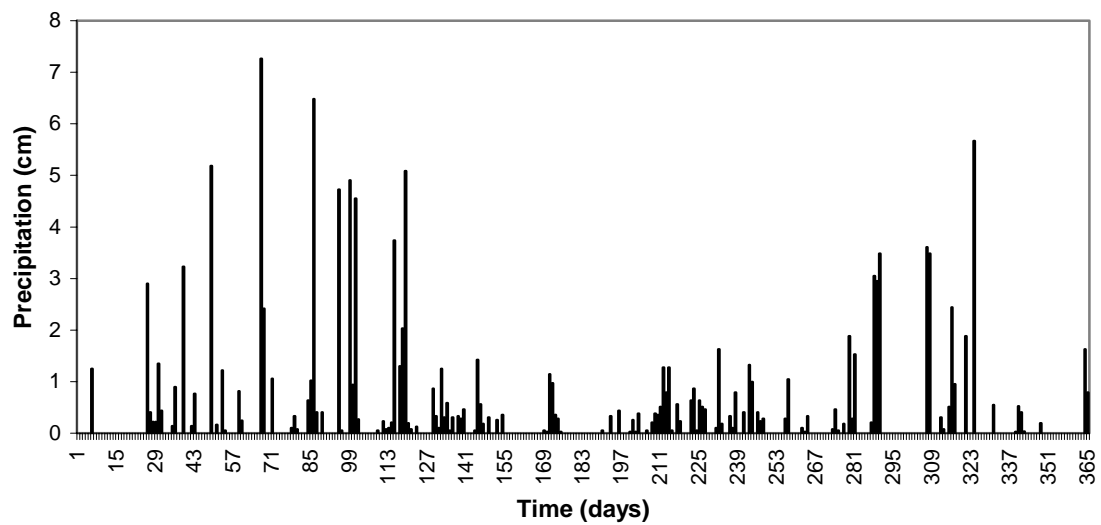


Figure 8. Precipitation record from the wettest year on record at the Red River weather station (NCDC, 2005).

There are several weather stations located on the mine site shown in Figure 1, which have been collecting climatological data for approximately 5 years, but do not have the capability to collect and accurately measure snow in the winter (Golder Associates, 2005 a, b and Robertson Geoconsultants, 2000;). The average annual precipitation (as rainfall) from these stations ranged between 32 cm and 40 cm. The average annual precipitation from the Red River station during the same period was

approximately 94 cm (55.5 cm as rainfall and 38.5 cm as snow water equivalent). The temperature recorded at the mine stations ranged between -22.1 C and 31.4 C. During approximately the same period of time the temperature recorded at the Red River weather station ranged between -25.0 C and 30.6 C. The temperatures in the region vary both seasonally and diurnally (Shannon et al., 2005).

Historical climate data was collected from the National Climate Data Center (NCDC) to determine the long-term climate at the surrounding climate stations, including Red River, Eagle Nest, Cerro, and Taos (shown in Figure 1). The average annual precipitation from the two closest stations ranges between approximately 17 inches at Cerro and 34 inches at Red River. This annual precipitation includes the total rainfall plus the snow water equivalent. The historical record from the Red River station was selected as the most appropriate record to use for the Questa mine site study because the station is nestled in the same valley as the mine site, which would likely lead both stations to experience similar climate conditions and trends, although it is at an elevation approximately 300 meters below the Questa mine station (Golder Associates, 2005). The mean maximum temperature and the mean minimum temperature as measured between 1950 and 2003 at the Red River station were 13.23 C and -4.84 C. The mean temperature over the same period was 4.35 C.

Regional Geology

The Questa mine is located on the southern edge of the Questa caldera within Latir volcanic field in a geologically complex region that has been described by Carpenter (1968), Clark (1968), Lipman and Reed (1989), Meyer and Leonardson

(1990), Czamanske et al. (1990), Roberts et al. (1990), Meyer (1991), Meyer and Foland (1991), and others. The Questa – Red River region has experienced five periods of tectonism: the Proterozoic, the Paleozoic, the Laramide orogeny, Rio Grande rift volcanism, and the Rio Grande rift fill. During the Proterozoic period, basement rocks, including fractured, metamorphosed sedimentary, volcanics, and volcaniclastics were intruded during four tectonic events by plutonic rocks ranging in composition from mafic to felsic (Karlstrom and Bowring, 1988, 1993; Karlstrom et al., 1990, 2004; Adams and Keller, 1994, 1996; Karlstrom and Humphreys, 1998; Pittenger et al., 1994; Barnes et al., 1999; Shannon et al., 1997). During the Paleozoic period, basin formation and uplift resulted in the Uncompahgre-San Luis highlands and Sangre de Cristo uplift which are part of the Tusas and Sangre de Cristo Mountains (Lipman and Reed, 1989; Baltz and Myers, 1999; Bauer and Kelson, 2004). The Laramide orogeny resulted in thrust and high angle reverse faults (Baltz and Myers, 1999; Chapin and Cather, 1994). The rocks from the Rio Grande rift are fractured volcanic rocks including rocks from the Latir volcanic field, extrusive basaltic, andesitic, and quartz-latic flows as well as welded ash-flow Amalia Tuff from the Questa caldera. These volcanic rock assemblages are associated with granitic intrusions as well as other mafic to felsic volcanic intrusions (Lipman and Reed, 1989; Czamanske et al., 1990).

Hydrogeology

The regional hydrogeology in Taos County near the Questa mine site has been investigated by numerous state agencies and private concerns (Abshire, 1998; Dames

and Moore, 1987; LoVetere et al., 2004; Robertson Geoconsultants, 1997; Souder Miller & Associates, 2000; SRK, 2004; URS, 2001; Winograd, 1959 and others). The investigations have focused on the Questa mine tailings site and the hydrogeology local to that region (RGC Inc., 1997), the southeastern region of the Questa mine site along the front rock piles (Abshire, 1998 and LoVetere et al., 2004), and on the Goathill Gulch region (SRK, 2004). There is a general understanding of the regional groundwater aquifer system within this region, but because of the complex geology (volcanism, intrusions, fractures, and faults) and local underground block cave mining, and the local groundwater tables are more difficult to predict.

The regional alluvial aquifer in the vicinity of the town of Cerro and southward towards Questa (see Figure 1) is situated between the Sangre de Cristo Mountains to the east and the volcanic Guadalupe Mountains to the west (Figure 9). Winograd (1959) describe its water table as being between 60 and 160 feet below the ground surface. He also states that an additional aquifer made up of volcanic rock (volcanic aquifer) is several hundred feet below the ground surface in the region near the Guadalupe Mountains (Figure 9). There is also the presence of shallow alluvial sediments which act as aquifers in these mountains; the hydraulic heads in these alluvial sediments appear to be tens of feet greater than the underlying volcanic aquifer, but the downward flow of groundwater is retarded by the intersection of silt or clay layers (Winograd, 1959). Winograd (1959) also notes other perched conditions exist as a result of alluvial sediments overlaying low permeability clay lenses, but they are not important on the regional scale. Robertson Geoconsultants developed a regional groundwater flow model based upon studies from Winograd

(1959) and Dames and Moore (1987). The regional groundwater system is described by an alluvial aquifer east of the Guadalupe Mountains and a deep volcanic aquifer underneath and west of the Guadalupe Mountains (RGC Inc., 1997) (Figure 9).

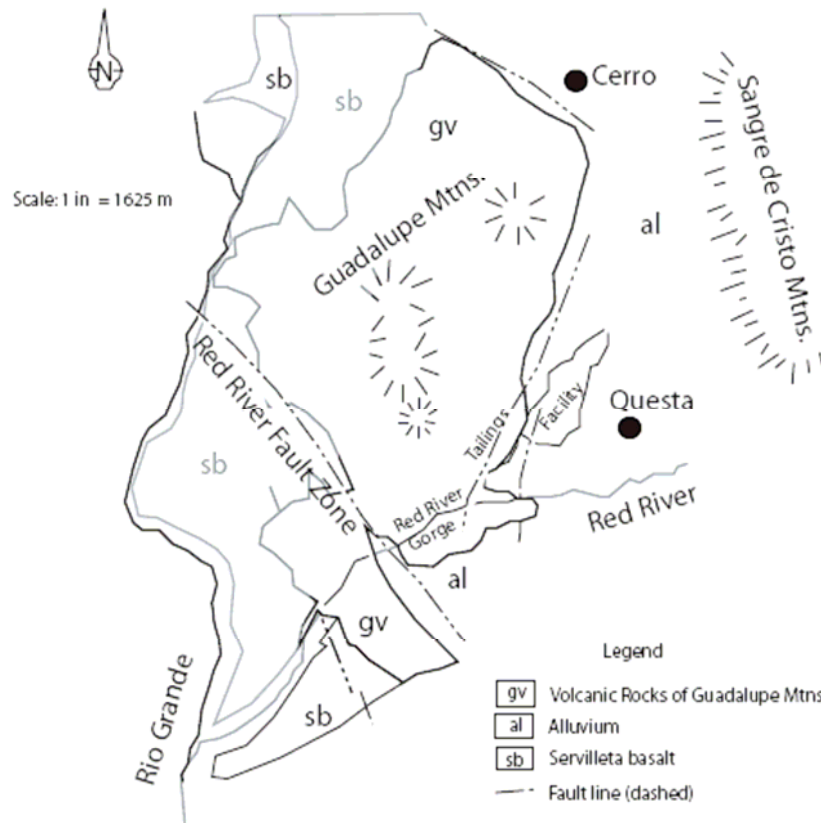


Figure 9. Simplified geologic map of Questa and surrounding study region west of the Questa Mine (from Vail, 1987). The Questa Mine is located just off the map in the eastward direction.

The regional groundwater flow is characterized as generally flowing to the west within the alluvial aquifer, and flowing to the southwest within the volcanic aquifer (Robertson Geoconsultants, 1997). The western region of the Sangre de Cristo

Mountains is characterized as the area of regional recharge to the groundwater system, while the Red River Canyon and Rio Grande Canyon represent discharge points from the aquifer (Robertson Geoconsultants, 1997).

The US EPA conducted a study of the hydrogeology in this region and measured the groundwater table in monitoring wells, located between 400 and 700 ft (122 to 213 m) north of the Red River on the Questa mine property as between 60 and 120 ft below the surface (Abshire, 1998). Twelve monitoring wells in total were used to investigate the aquifer properties, groundwater gradient, and groundwater quality in this region and were installed between July and August of 1994 (Abshire, 1998). Several of the wells indicate the presence of a cone of depression in the region, possibly due to dewatering of the open pit and underground mine workings. However, all of the monitoring wells are south of the open pit and not located near the GHN. The mine area is described as having two aquifers: a valley fill aquifer and an underlying shallow fractured bedrock aquifer (Abshire, 1998). The well tests from the area show that there is weak hydraulic separation between the two units, possible clay lenses in some areas, and although they may appear to act as one aquifer during periods of low recharge, the valley fill has a greater horizontal hydraulic conductivity than the bedrock unit (Abshire, 1998). Thus, periods of high recharge could result in the aquifers acting as two distinct aquifer systems.

SRK Consultants performed an extensive study of the subsidence zone in Goathill Gulch on the Molycorp mine property (SRK, 2004). The results from this study indicate that in general, fractures in the bedrock within the Goathill Gulch region do not act as pathways to drain the bedrock (SRK, 2004). These conclusions

were based upon the presence of alteration clay minerals in drill holes, which were crosscut by fractures in the bedrock. The study indicates that the fractures are filled with the clay minerals (SRK, 2004). Also, this investigation found evidence of a possible drained condition in an exploration hole located approximately 150 meters west of the toe of GHN, suggesting a cone of depression extending at least as far north as the hole (Figure 10).



Figure 10. Aerial photograph of the GHN rock pile indicating locations of boreholes. The figure shows piezometers marked by red and blue circles; slope inclinometers marked in yellow; and elevation contours marked with blue lines. The stable portion (south) and unstable portion (north) of the rock pile are divided by the bright green line (from Tachie-Menson, 2006).

Additional monitoring wells are located farther southwest and southeast of the extents of the figure.

This would be further evidence of a cone of depression that was noted in monitoring wells on the southern part of the property just north of the Red River (Abshire, 1998). However, the drill holes closest to exploration hole No. 527250 (No. 504137 and No. 527339/A), which are located just west of the region shown in Figure 10, do not appear to be drained, and have water elevations approximately 369 ft and 848 ft higher, which suggests that there is great anisotropy in the fractured bedrock system (SRK, 2004). Preliminary results from this study indicate that the system drains into the underground mine workings, southwest of the region shown in Figure 10. The data from the wells also suggest that there is a groundwater divide between the underground mine workings and the Red River (SRK, 2004). Finally, it was noted that recent studies by Norwest Corporation (Norwest Corporation, 2003) on the GHN rock pile concluded that the Goathill spring, which discharges just above the base of the GHN rock pile, and is thought to be water from local recharge that was discharged from the pile as result of being perched above clayey material (SRK, 2004).

It is evident from these studies that the groundwater table within the region local to the mine site is highly variable in the complex geologic system. The regional water table below the GHN rock pile ranges from 10's to 100's of meters deep. However, the perched condition near the toe of the GHN rock pile manifested by local discharge and the perched condition noted near the top of the pile at the rock pile bedrock interface (personal communication with Virginia McLemore, 2006) is not well understood. Therefore, the conceptual model of the system will be impacted by our lack of understanding of the groundwater depth below the GHN rock pile.

METHODS AND MATERIALS

Soil Tests

Samples of material from the Goathill North rock pile were collected in the field according to standard methods. The following analyses were performed.

Bulk Density

The bulk densities of the Goathill North rock pile materials were estimated from data collected in the field using several methods. Bulk density is of interest when estimating the hydraulic properties because it provides an indication of how moisture may be distributed in a system. The variability in the bulk density of the rock pile system is attributed to the variable proportion of rocks, which have a higher density and lower porosity than soils, within the material samples. The bulk density of a soil can be related to the porosity (n) of the material as,

$$n = \left(1 - \frac{\rho_b}{\rho_s} \right) \quad (2)$$

where ρ_s is the specific particle density (M/L^3) (Hillel, 1998). The porosity of the rock pile material is synonymous with the saturated volumetric water content, which is an important parameter in understanding fluid storage and transport within the system.

Water Replacement or Excavation Method

The field tests were conducted on horizontal surfaces. Loose rocks in the designated area were tossed aside to ensure a level surface. The masses of a collection bucket, lid, and plastic sheet were measured. A hole was then excavated at the designated location. The hole was estimated to be approximately 30 times larger in volume than the largest rock present in the hole in order to gather a representative sample. The excavated material was recovered and placed in the collection bucket and carefully mixed to homogenize the sample. A small soil sample was removed from the recovered material, placed in a pre-weighed tin (approximately 190 cm³ or 250 cm³), the mass of the tin with sample was recorded, and then the tin was sealed with tape to prevent moisture loss. The soil sample was then covered with a plastic sheet and the bucket was covered with the lid. Finally, the mass of the bucket with the sample, plastic sheet, and lid was measured and recorded. The excavated hole was lined with a plastic sheet and filled with water until it was flush with the ground surface. The volume of water added to the hole was recorded and subsequently represented the volume of the excavated hole. The excavated material in the bucket was air- and then oven-dried at approximately 105° C. The sample in the tin was oven-dried to determine its contribution to the dry soil-mass and its gravimetric moisture content. The dry bulk density of the solid was then calculated as:

$$\rho_b = \frac{M_{dry_solid}}{V_{total}} \quad (3)$$

where ρ_b is the dry bulk density [$M L^{-3}$], M_{dry_solid} is the mass of the dry solid sample [M], and V_{total} is the volume of the excavated hole [L^3] which is equivalent to the volume of water added to the hole. The gravimetric (w) and volumetric (θ) water contents of the rock pile sample were then calculated from the tin sample as:

$$w = \frac{(M_{wet_solid} - M_{dry_solid})}{M_{dry_solid}} = \frac{M_{water}}{M_{dry_solid}} \quad (4)$$

$$\theta = w \left(\frac{\rho_b}{\rho_w} \right) \quad (5)$$

where w is the gravimetric moisture content [$M M^{-1}$], ρ_w is the density of water at 25°C [$M L^{-3}$], and M_{wet_solid} is the in situ mass of the solid sample [M]. The water replacement method was adapted from the American Society of Testing and Materials method D 5030-89 (ASTM, 1989).

An additional calculation was made to estimate the effect of rocks on the bulk density of the samples collected from the water replacement method. For this determination, all of the large rocks were separated out from these two samples and they were weighed, air-dried, and re-weighed. The approximate adjusted bulk density of the soil eliminating the effects of the rocks in the sample was estimated by a method described by Curtis and Post (1964). The initial steps in the method described by Curtis and Post (1964) are sieving the sample to separate out the coarse fragments (> 2 mm) from the sample, drying the sample, and then determining the average specific gravity of the rock materials. The mass of the coarse material (g)

and the specific density (g/cm^3) were utilized in equation 5 below to adjust the bulk density (g/cm^3 , kg/m^3 , and g/cm^3):

$$\text{Bulk Density} = \frac{\text{Total dry wt soil core (g)} - \text{mass coarse fragments (g)}}{\text{Total volume soil core (cm}^3\text{)} - \frac{\text{mass coarse fragments (g)}}{\text{specific density (g cm}^{-3}\text{)}}} \quad (6)$$

In this study the adjusted bulk density estimate was made by separating out the largest rocks in the sample and treating them as the coarse fragments instead of sieving out all of the rocks larger than 2 mm in diameter as Curtis and Post (1964) suggest. Also, an estimated specific density for the rocks of 2.5 g/cm^3 was used instead of measured values.

Sand Replacement

The sand replacement method follows the same type of excavation method as the water replacement method. A pre-weighed bucket was filled with excavated material that was then homogenized. A pre-weighed tin was filled with excavated material from the bucket for gravimetric water content. The sand replacement field procedure differed from the water replacement method because the plastic lined hole was filled with a dry, free flowing sand of known bulk density instead of water. After filling the plastic lined hole flush with horizontal, the full plastic bag was carefully removed from the hole and the mass of the bag was measured. The volume of the test hole was estimated using the relationship below:

$$V_{hole} = \frac{(M_{sand} - M_{empty\ bag})}{\rho_{sand}} \quad (7)$$

where V_{hole} = volume of the test hole, cm³, M_{sand} = bulk mass of the sand used to fill the test hole, grams, M_{bag} = mass of the empty bag, grams, and ρ_{sand} = bulk density of the sand, 1.54 g/cm³. The bag of sand was emptied and the procedure was repeated for a total of three volume measurements. The volume was considered acceptable when the three measurements varied by less than 10%. The variability in the calculated bulk density values as a result of the different estimates of volume ranged between 1 % and 7 %. As a final check, the sand from the final test was placed in the excavated hole without the bag each time the test was conducted. This step was not necessary, but it was conducted in order to give confidence that the volume of sand was equal to the volume of the test hole. The bulk density of the excavated rock pile material was estimated using equation (3). The gravimetric water content and volumetric water content of these samples were estimated using equations (4) and (5). The method used was adapted from the American Society of Testing and Materials method D 4914-89 (ASTM, 1989).

Sand Cone

Sand cone tests were performed on flat horizontal surfaces. The sand cone apparatus is illustrated in Figure 11 below.

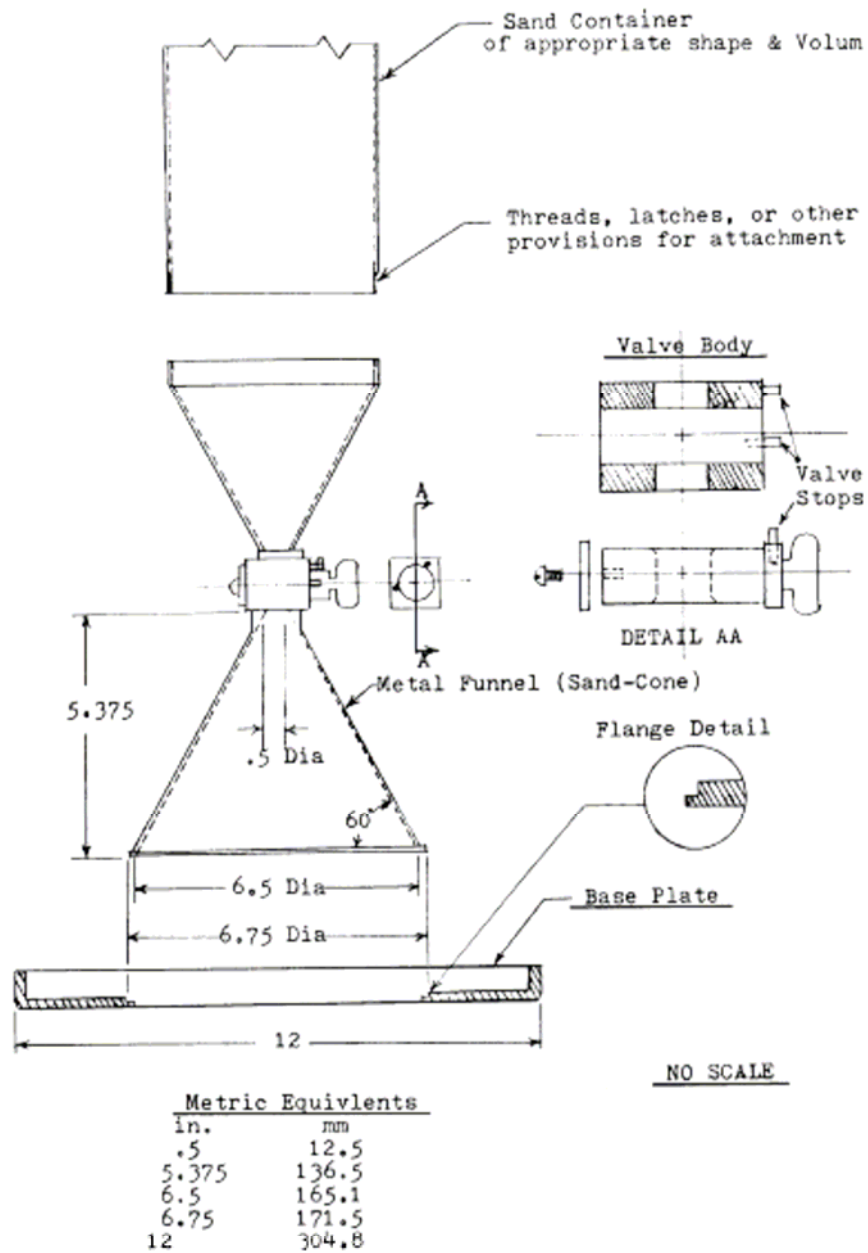


Figure 11. Sand cone apparatus (ASTM D1556-00, 1996)

The base plate of the sand cone apparatus was secured on the ground with stakes over the designated area to be excavated. The masses of a bucket and matching lid were measured and recorded. The mass of the sand cone apparatus containing sand was

recorded. A test hole was then excavated from the center hole of the base plate, attempting to cause minimal disturbance of the surrounding soil. The excavated material was dumped in a bucket and the mass was recorded. A sample was collected from the bucket after homogenization for gravimetric moisture content.

The sand cone apparatus was then inverted and seated on the base plate. Sand of a known density was allowed to fill the hole and cone of the apparatus. The mass of the apparatus with the remaining sand was recorded. The mass of sand used to fill the hole was calculated as the difference in the mass of the apparatus before and after the test. The volume of the hole was calculated in the same manner as the sand replacement method, but an additional term was needed to account for the volume of sand used to fill the cone in the apparatus. The volume of the hole was estimated using the equation below.

$$V_{total} = V_{hole} + V_{cone} = \frac{M_{sand}}{\rho_{sand}} \quad (8)$$

$$V_{hole} = V_{total} - V_{cone} \quad (9)$$

The bulk density of the rock pile material was then calculated using equation (3), the gravimetric water content of the sample was estimated using equation (4), and the volumetric water content of the sample was estimated using equation (5). The sand cone method was adapted from the ASTM D1556 – 00 (2000).

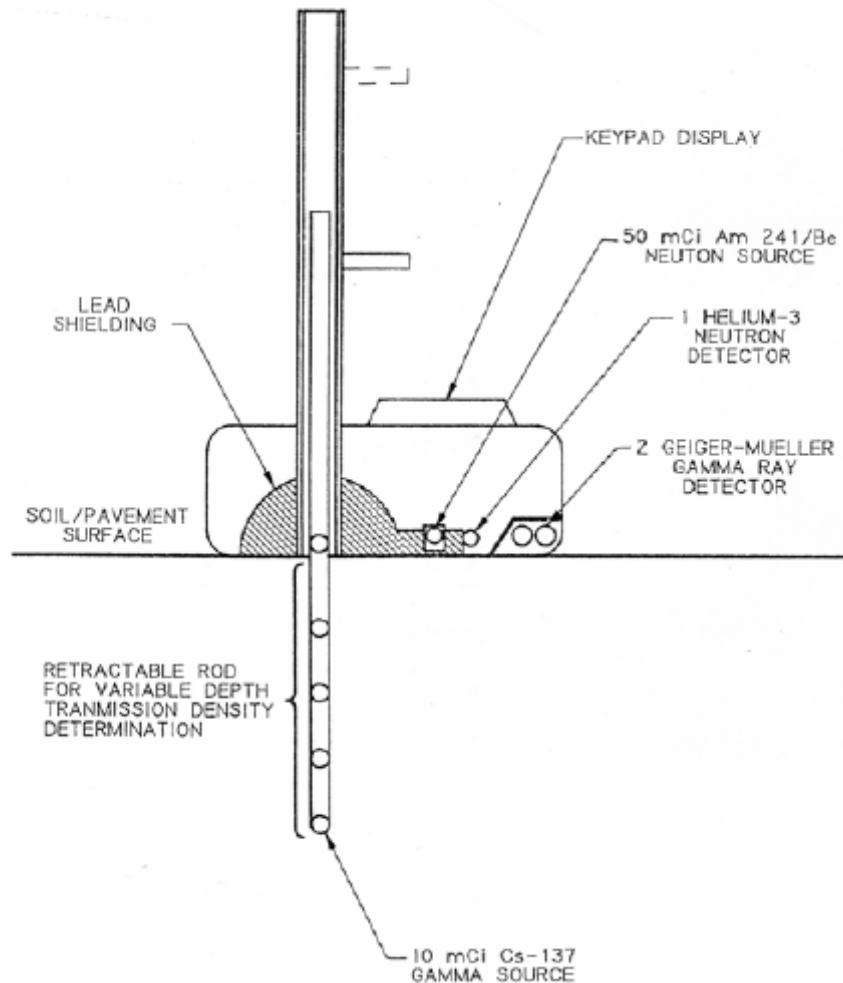
Nuclear Radiation

A nuclear densometer was used to measure dry bulk density and gravimetric moisture content of the soils in many locations across the field site. The nuclear densometer consists of a gamma and neutron source. The gamma source is used to

measure the density and the neutron source is used to measure the moisture content.

A diagram of the nuclear densometer from the instruction manual is illustrated in

Figure 12.



CPN MODEL MC PORTAPROBE

Figure 12. Nuclear Densometer (from Instruction Manual, CPN International, 1999).

A certified professional consultant used the nuclear densometer in direct transmission mode, which involved inserting the source rod into the soil profile. The average density of the soil was measured from the surface to the source end of the rod and was read from the nuclear densometer gauge. A neutron source was used with a backscatter technique to measure the average moisture content of approximately the top 10 cm of material below the gauge. These measurements were conducted following ASTM standards for moisture content and density by nuclear gauge method (D2922-96 and D3017-96).

Hydraulic Conductivity

The unsaturated hydraulic conductivities and the saturated hydraulic conductivities of the rock pile were measured using two different techniques. The tension infiltrometer was used to directly measure the unsaturated hydraulic conductivity as a function of matric suction and indirectly used to estimate the saturated hydraulic conductivity using the Reynolds and Elrick method (1991). The guelph permeameter was used to measure the saturated hydraulic conductivity.

Tension Infiltrimeter

The tension infiltrometer was used to measure the unsaturated hydraulic conductivity as a function of matric suction at various locations on the surface of the rock pile and within trenches during the deconstruction phase of the Goathill North rock pile.

Prior to taking field measurements, I checked and calibrated the instruments in the laboratory. The Mariotte bottle and water column were checked for leaks according to manufacturer's directions, by submerging them in a bath of water. The instrument was then calibrated to set the matric suctions (Figure 13) applied to the porous media according to the instrument manual. The pressure transducers to be used in monitoring the matric suctions were calibrated according to the manufacturer's directions. Finally, the nylon mesh, used to cover the membrane on the disc was checked for holes or tears and replaced if necessary.

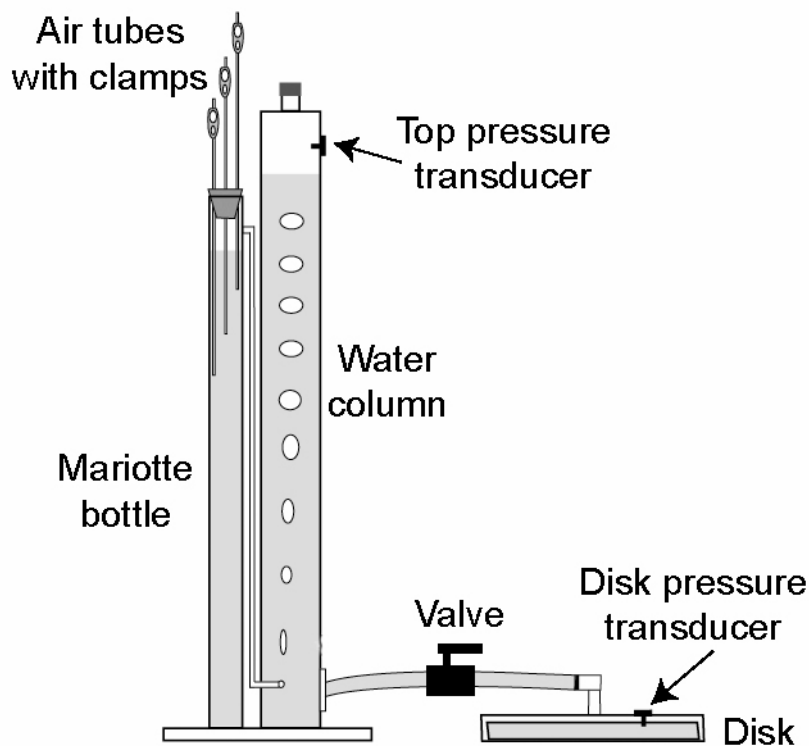


Figure 13. Tension infiltrometer (adapted from Holt et al., 2002).

The tension infiltrometer measurements were made on level surfaces on the Goathill North rock pile. A small soil sample was collected for the gravimetric water

content near the designated infiltrometer location. The nylon mesh was placed in a bucket of clean water. The damp mesh was then secured over the clean disc with an o-ring, making sure to remove wrinkles in the membrane. Excess membrane was trimmed to within approximately 1.5 cm from the edge of the disc, without setting the disc down while the membrane is intact. The disc was then left to soak for approximately 15 minutes while the infiltrometer location was being prepared. A ring collar from Soil Measurement Systems or brace of equivalent diameter was placed on the surface designated for the disc. The ring collar was secured in a level position and then filled with a thin layer (≥ 1 cm) of Weldron 510 sand. A station for the infiltrometer tower was prepared less than approximately 30 cm away from the ring collar position, and was also level to the elevation of the sand surface. If the two stations were not completely level, the changes in elevations were recorded in a field notebook. The clamps and outlet hose valve on the infiltrometer were closed and then the main water reservoir of the infiltrometer was filled to approximately 5 cm below the top of the reservoir. The Mariotte bottle or the bubbling tower of the infiltrometer was then opened and filled with water to approximately 7 cm below the top. The bubbling tower was then closed and the air tube(s) or tension stick(s) were adjusted to the desired level(s) marked on the bottle during calibration. The infiltrometer tower was set upon a covered bucket, next to the bucket containing the disc. The transducers were then inserted into the top of the water column and in the disc, being careful to keep the bottom of the disc below the water surface at all times. The identification number of the transducers, and the associated data logger channels were noted in a field notebook. After attaching the transducer to the disc, air bubbles were removed through the top outlet of the disc by

gentle tapping. When the disc was free of bubbles larger than dime size, all of the valves on the infiltrometer were closed and clamped shut, and the disc was attached to the infiltrometer tower, while remaining submerged in water. The outlet valve on the infiltrometer was opened to remove new bubbles in the tubing by gently rocking the infiltrometer tower and was then closed again. The sand location designated for the disc was moistened with a spray bottle to ensure good hydraulic contact between the disc and surface. A paper towel was placed over the sand to provide extra protection for the mesh membrane in some of the first tests. However, this often resulted in poor contact between the disc and soil surface and was abandoned for the remaining tests. The disc was then carefully removed from the bucket and the infiltrometer and disc were moved to the prepared site. The disc was placed on top of the moistened sand and the infiltrometer towers were placed on the designated station. The disc was inspected to ensure that complete hydraulic contact was made between the sand and the membrane on the disc. The water level in the water column and the distance to the bottom of the air entry tube within the Mariotte bottle was recorded. The data logger program was initiated to begin collecting matric potential measurements from the two transducers once the system was in place. The difference between the operator's watch and the data logger's internal clock was noted in a field notebook.

Measurements were made by starting with the most negative matric potential, measuring the infiltration rate until it reached steady-state and then changing the applied matric potential to a more positive value. The valve to the disk and the clamp to the air entry tube were opened as quickly as possible after placing the disk on the sand surface.

The clamp to the air entry tube for the most negative matric potential value was opened; the value was typically between -15 to -30 cm. After bubbles were observed in the water reservoir, the water level in the Mariotte bottle, the bottom level of the air entry tube, and the level of water in the water reservoir were recorded. The tension in the tower was calculated as $\text{tension} = \text{air entry tube level} - \text{water level in Mariotte bottle} - \text{correction factor}$ (determined from calibration). The time and water level in the water reservoir were recorded at regular intervals after tower started to bubble. A steady state was distinguished by a consistent change in the water level within the water tower. Once the infiltration rate reached a steady state, the water level was recorded at the steady state for approximately 10 to 15 minutes. The clamp to the air entry tube was closed after the steady-state period and the air entry tube with the next applied matric suction was opened. The same procedure was followed for the remaining three matric suctions applied to the soil. When using an infiltrometer with one air entry tube, the level of the tube was moved to the calibrated marks in the Mariotte bottle. The water reservoir was refilled between tension settings when necessary, but it was not necessary to refill the Mariotte bottle. Following the measurements, all of the data was downloaded from the data logger to a PDA or computer. The data was analyzed and used to calculate the unsaturated hydraulic conductivity as a function of matric suction based upon the Wooding solution (1968) as described in the Soil Measurement Systems (2001) manual. The saturated hydraulic conductivity was estimated using the Reynolds and Elrick method (1991).

Guelph Permeameter

I assisted in using the guelph permeameter to measure the saturated hydraulic conductivity by applying a constant pressure within a shallow hole excavated in the Goathill North rock pile. The guelph permeameter, which can be described as an in-hole Mariotte bottle, was used to apply a constant head and allow water to infiltrate into the rock pile material. When a steady infiltration rate was achieved, a saturated hydraulic conductivity, K_s , was then calculated using the steady-state rate, Q (L^3/T) and the constant depth of water, H (L) in an uncased cylindrical hole of radius, a (m) (Reynolds et al., 1985).

Matric Suction

The *in situ* matric suction was measured within trenches using a “Quick Draw” moisture probe and standard tensiometers (Soilmoisture Equipment Corp., 2000). The matric suction of a small region on the top of the stable portion of the Goathill North rock pile was monitored for approximately 2 months during the monsoon season using nested tensiometers.

“Quick Draw” Soil Moisture Probe and Standard Tensiometers

The “Quick Draw” soil moisture probe and standard tensiometers were used in the field during the trench activities to measure the matric suction in the different mapped units of the GHN pile. The Quick Draw moisture probe and standard tensiometers were prepared according to the manufacturer’s instructions. In

preparation for fieldwork, field crew-members including myself, left the instruments to soak in a bucket of water to ensure that the porous cups were fully saturated. The tensiometers were inserted into pre-made holes created by carefully hammering a metal rod into the rock pile. The tensiometers were left for 5 to 15 minutes to allow equilibrium with the system and then a measurement was taken by reading the value in kilopascals directly from the gauge. The instrument is illustrated in Figure 14 below.

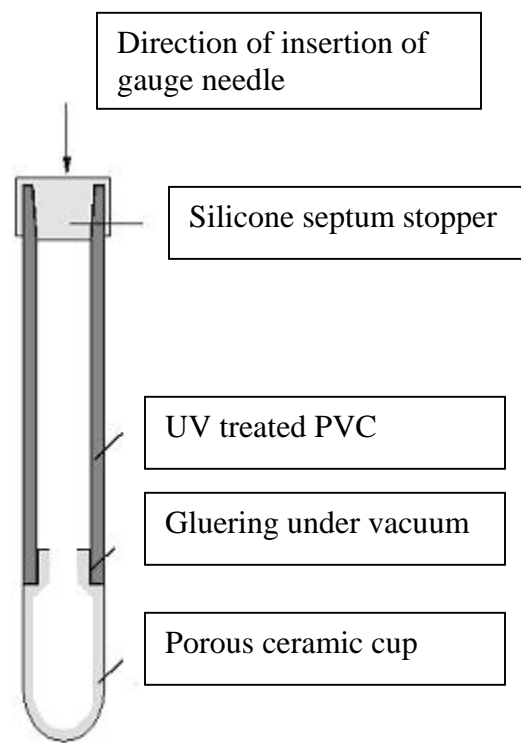


Figure 14. Standard Tensiometer instrument diagram.

Nested Tensiometers

The nested tensiometers were installed in the rock pile during the summer prior to excavation of the trenches and gradation of the slope. I assisted in collecting data from the data loggers as well as removing the tensiometers at the end of the summer. The tensiometers design is illustrated in Figure 15 (Hubbell and Sisson, 1996, 1998, and 2003) and a depiction of the typical tensiometer set up in the field is illustrated in Figure 16 (Hubbell and Sisson, 1998).

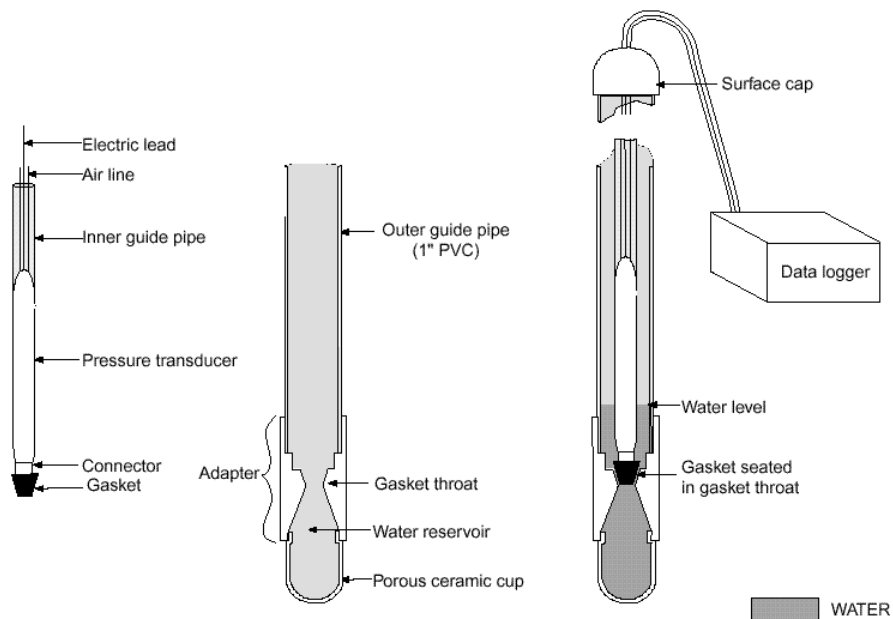


Figure 15. Advanced Tensiometer design (from Hubbell and Sisson, 1998).

As is shown in Figure 15, a tensiometer consists of a sealed tube filled with water, a porous cup on one end of the tube, and a pressure sensor (read by the data logger) connected to the water chamber. During installation, the porous cup was placed in the excavated hole in the soil (Figure 16). Special care was taken by the field crew

when installing the tensiometers to ensure good hydraulic contact between the water in the tensiometer and moisture in the soil surrounding the porous cup.

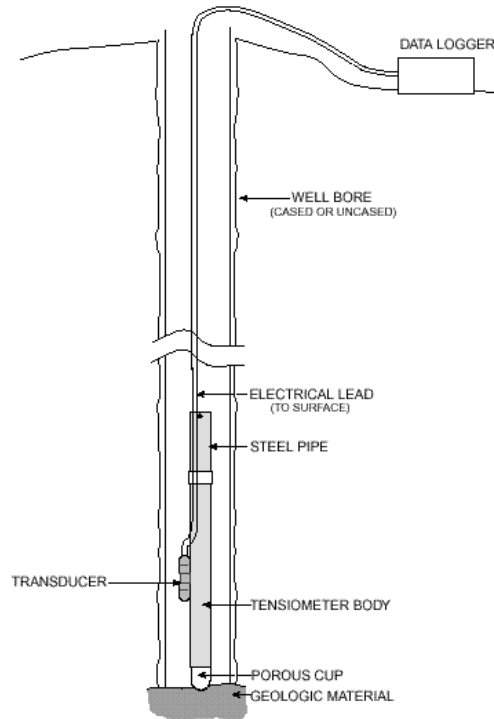


Figure 16. Depiction of a tensiometer field application (from Hubbell and Sisson, 1998).

The data produced from the pressure sensors in the tensiometers was collected on a Campbell Scientific CR21X Micrologger. Myself and other field assistants downloaded the data from the micrologger directly to a laptop computer or a palm pilot.

Particle size analysis

Lab assistants and graduate students working on this stability/weathering study conducted particle size analyses on samples collected in five-gallon buckets

from the trenches on the Goathill North rock pile according to ASTM D421 (ASTM, 2002).

After the dry sieving process, the fraction passing the No. 200 sieve was used for hydrometer tests to determine the percentages of silt and clay in the remaining soil. I conducted hydrometer tests on the dry sieved samples in the summer of 2005, but was relinquished of this duty when a new graduate student arrived. The hydrometer tests were conducted according to ASTM D422-63 (ASTM, 2002) using the 152H hydrometer. The soil sample passing the No. 200 sieve was poured in a large pan where it was mixed to homogenize the sample. Approximately 100g of soil sample was placed in a bowl, the exact mass was recorded and then the sample was placed in the oven (at 105° C) to dry over night. The mass of the sample was measured the next day. The hygroscopic moisture correction factor was then determined to be the ratio of the oven-dry mass to the air-dry mass of the sample. This correction factor was used in calculations that will be discussed below. The dry sample was placed in a bowl and 125 mL of a dispersion agent (40 g/L sodium Calgon™ solution) was added. The contents of the bowl were mixed together and then left to soak for at least 16 hours.

After soaking, the soil in solution was transferred to a dispersion cup and placed on a stirring apparatus and stirred for one minute. The soil-water slurry was carefully dumped into a 1000 mL sedimentation cylinder immediately after using the stirring apparatus. Distilled water was added to the cylinder to bring the total volume in the cylinder to 1000 mL. A small piece of Parafilm™ was used to seal the top of the cylinder, and then the cylinder was turned upside down and back for a period of

one minute. After the one minute was up, the cylinder was placed on the laboratory counter and allowed to settle for one minute. Approximately 30 seconds after placing the cylinder on the counter, the hydrometer was inserted into the cylinder. At the end of one minute of the cylinder being placed on the counter, the hydrometer level was measured and recorded as well as the temperature read from a thermometer inserted into the cylinder. After the hydrometer reading was made, the cylinder was covered with Parafilm™ again, and the process was repeated. If the hydrometer reading was the same the second time, then the cylinder was left on the counter and additional readings were taken after 2, 4, 8, 15, 30, 60, 120, 240, 960, and 1440 minutes. The temperature of the slurry was measured and recorded at the same time the hydrometer readings were made. If the hydrometer reading was not the same the second time, the mixing process was repeated again a third time. I never needed to repeat this mixing process more than three times when I was running the experiments.

After the last reading was made, the slurry was poured into a No. 200 sieve and washed with tap water until the water was clear. The soil remaining in the sieve was then transferred into a metal dish and placed into a drying oven, at approximately 105° C, to dry. When the sample was completely dry, the total mass was measured and recorded. Finally, the material was poured into a set of sieves, starting with the coarsest on top (No. 16, sieve opening = 1.18 mm or 0.047 in) and the finest on the bottom (No. 200, sieve opening = 0.075 mm or 0.0029 in) seated in a catch pan. The set of sieves and catch pan were then covered, placed on a shaking device and set to shake for approximately 20 minutes. The mass of soil in each sieve was then

measured and used to determine the total percentage passing each sieve. The details of the calculations done after the test are outlined in ASTM D422-63 (ASTM, 2002).

Conceptual Model

This section describes how the conceptual model of fluid transport in the GHN hillslope system was developed and how it was implemented in HYDRUS 2D, a two-dimensional finite element code for unsaturated soils. I describe how the geometry of the pile was developed and from which region within the pile the 2D cross-section was obtained. Then I describe how the model domain was segregated into different zones, based upon field observations and knowledge of deposition of material by the end-dumping technique (Carson, 1961). The boundary conditions and initial conditions for the conceptual model are presented next, followed by the governing equations of fluid transport in the variably saturated system. After introducing the governing equations I present how the soil hydraulic properties of the different zones were developed. The remainder of the chapter discusses the numerical simulations and the approach used to perform sensitivity analyses.

The conceptual model of the GHN hillslope system was developed from a synthesis of field observations, soil samples, field measurements, topographic data, and general knowledge of the end-dumping deposition of the rock pile, which commenced in 1964 and was completed in 1974 (URS, 2001). The topographic information from pre-mine topography (1962) and 2003 digital elevation model (DEM) was used to designate the geometry of the hillslope along a designated cross-section in the center of the rock pile domain (Figure 17).

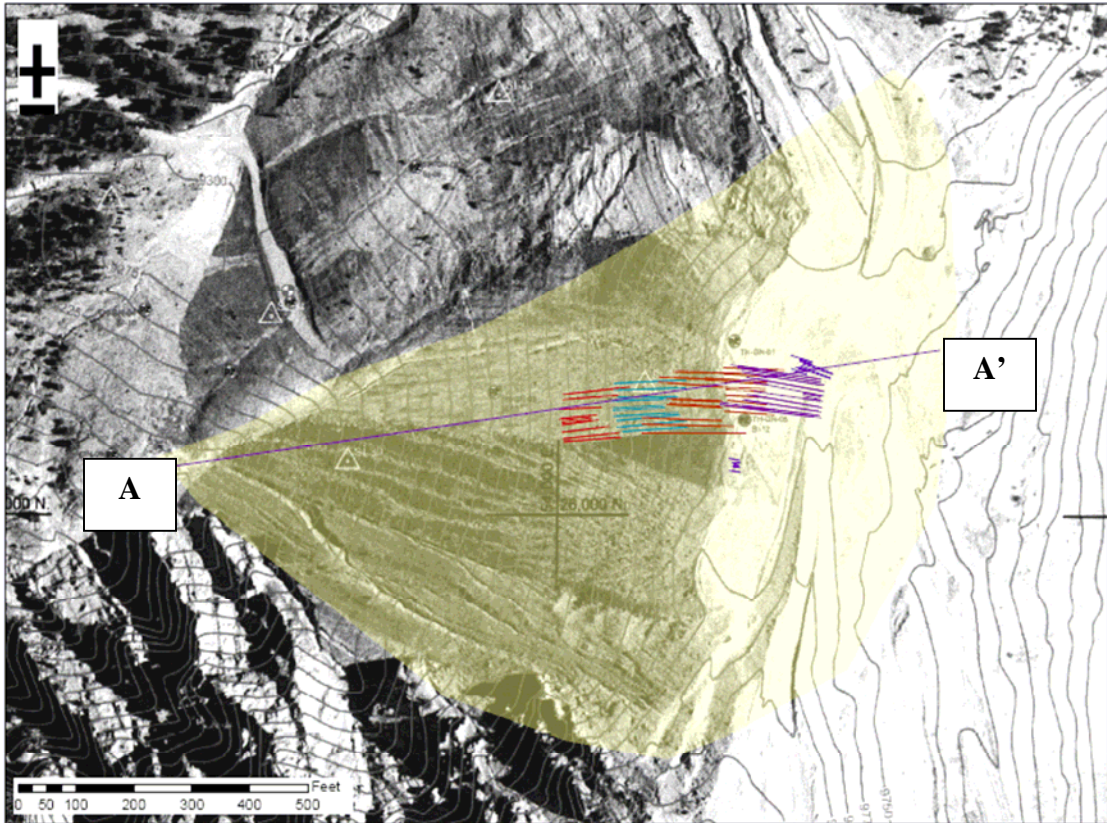


Figure 17. Aerial photograph of the Goathill North rock pile, overlain by a GIS shapefile designating the stable portion of the GHN rock pile. The cross-section A-A' indicated by the purple line, shows the spatial coordinates from which the elevations for the conceptual model were obtained. Red, purple, and green lines indicate the trenches that were cut into the rock pile.

Based upon observations made in the field, a generalized conceptual model of the GHN rock pile was developed with five different zones of rock pile material and two underlying materials (Figure 18).

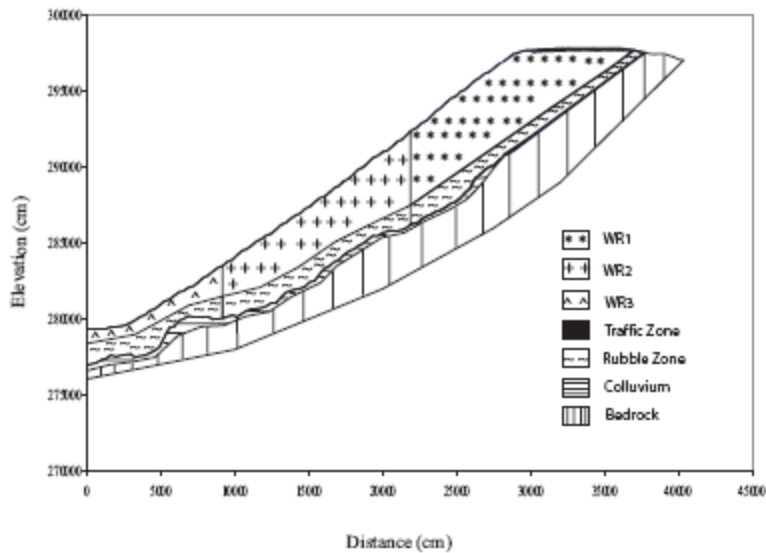


Figure 18. The conceptual model zones of the Goathill North rock pile. WR1 is the region with the finest material where the majority of trenches were excavated. WR2 is the intermediate zone in which one trench was excavated. WR3 is the region with the coarsest material where little data was collected. The traffic zone is a shallow compacted region at the top of the rock pile. The rubble zone is the basal region of the rock pile, which has coarse angular cobbles and boulders. The colluvium is a unit that was deposited before the rock pile by natural weathering processes.

Of the eighteen units mapped in the trenches, two of them were used directly to describe the lower foundation of the pile, while the remainder of the subsurface units were used to describe the materials in the traffic zone, and zones WR1 and WR2. The uppermost zone exposed at the top of the hillslope was designated as the traffic zone. This zone was characterized as being compacted by haulage traffic and ranged between 1 and 5 feet (approximately between 0.3 and 1.5 meters) in thickness. WR1 (Figure 18) is the region in which most of the trenches were excavated and was characterized as having finer material than the units down slope. Fifteen of the subsurface units in trenches LFG-003 through LFG-008 could be used to characterize

the material in WR1. The majority of the units in this region were described as matrix supported, poorly sorted, sandy-gravel with some cobbles and boulders. Experienced field geologists estimated the maximum volume percentage of rocks larger than gravel (cobbles and boulders, 64 mm in diameter and greater) within this region of the rock pile to be about 30 % (personal communication with Virginia T. McLemore, Kelly Donohue, Erin Phillips, and Rick Lynn). The soil samples collected from trench LFG-009 were used to characterize WR2. In general, WR2 was described as an intermediate zone of cobble-supported, well-graded, poorly sorted material. Field geologists estimated that the maximum volume percentage of rocks within this region was greater than in WR1 and was approximately 40 % (personal communication with Virginia T. McLemore, Kelly Donohue, Erin Phillips, and Rick Lynn). The lowest portion of the pile near the toe, WR3 was characterized based upon field observations by geologists, and was described as having the largest maximum volume percentage of rocks within the pile, approximately 60 % and was cobble-supported (personal communication with Virginia T. McLemore, Kelly Donohue, Erin Phillips, and Rick Lynn). There was little, or no data collected about the soil hydraulic properties of WR3 within the stability/weathering study. The general observation was that the material within WR3 was similar to the material within the rubble zone, but that it contained a larger volume fraction of rocks (personal communication with Virginia T. McLemore, Kelly Donohue, Erin Phillips, and Rick Lynn). The rubble zone was defined as the basal region of the rock pile (McLemore, 2006). The region was described as a cobble-supported coarse unit, containing large angular cobbles (64 to 256 mm in diameter) and boulders (256 mm

in diameter and larger), with little sand and clay matrix material, that reached 2 m (approximately 7 ft) in thickness in the upper portion of the pile, and lay unconformably on top of weathered bedrock and colluvium material. However, based upon observations by other consultants, geologists suggested that it would become coarser towards the toe of the pile (personal communication with Virginia McLemore).

In addition to the five units from the GHN rock pile described above, the GHN hillslope system also included the underlying foundation material, colluvium and bedrock. The colluvium, which we have described within the rock pile, is believed to be the same material as was discussed previously in the description of the GHN rock pile, a secondary material that developed from rockfalls of over-steepend scars (Meyer and Leonardson, 1990). The colluvium observed in the trenches was a matrix-supported yellowish-orange sandy clayey material that was approximately 0.3 to 0.9 m (1 to 3 ft) thick in the trenches where it was observed. However, following the trench activities geologists interpreted drill cores collected from several drill holes on GHN and were able to estimate that the colluvium reached a local thickness of nearly 15 ft (4.5 m) within the pile (personal communication with Mike Smith, Rick Lynn, and Virginia T. McLemore). Therefore, the thickness of the colluvium in the conceptual model was increased to take into account the drill hole data. Finally, an arbitrary bedrock thickness was assigned to investigate the interaction between the rock pile and the bedrock. The bedrock under the GHN rock pile was previously described in the *Field Site* section. It was simplified in the conceptual model and treated as one type of volcanic rock, instead of two different rocks intersected by a

fault. This simplification to the system may not accurately represent the conditions at the GHN rock pile, but the exact orientation of the fault and bedrock thickness below the model domain in the stable portion of the pile are not known. Therefore, the bedrock was treated as a continuous unit. However, the presence of a fault in the bedrock could act as a preferential pathway, which could lead to a different soil moisture distribution in the overlying soil units.

Governing Equations and Numerical Methods

The numerical simulations of the GHN rock pile were completed using the HYDRUS 2D variably saturated flow model (Simunek et al., 2001). The HYDRUS 2D model uses the Richards equation as the governing equation to describe Darcy-type fluid flow in a variably saturated porous media. HYDRUS 2D solves the governing equations numerically using Galerkin-type linear finite element schemes. The Richards equation can be expressed as:

$$\frac{\partial \theta_w}{\partial t} = \frac{\partial}{\partial x_i} \left[K_{ij}(\psi) \left(\frac{\partial \psi}{\partial x_j} + \frac{\partial z}{\partial x_j} \right) \right] - S \quad (10)$$

where θ_w is the volumetric water content [$L^3 L^{-3}$], ψ is the pressure head [L], S is the sink term [T^{-1}], x_i ($i = 1,2$) are spatial 2D Cartesian coordinates [L], t is time [T], and $K_{ij}(\psi)$ are the directional components of the unsaturated hydraulic conductivity function [$L T^{-1}$].

The van Genuchten equations relate the volumetric water content to the pressure head and are used to develop the water retention or soil water characteristic curves. The equations can be written as:

$$\theta_e = \frac{\theta_w - \theta_r}{\theta_s - \theta_r} = \left[\frac{1}{1 + (\alpha\psi)^n} \right]^m \quad (11)$$

$$K(\theta_e) = K_s \theta_e^l \left[1 - (1 - \theta_e^{1/m})^m \right]^2 \quad (12)$$

where θ_e is the effective water saturation [$L^3 L^{-3}$], θ_s is the saturated water content (approximately equal to the porosity), θ_r is the residual water content, α , m , n are the van Genuchten (1980) parameters ($m = 1 - 1/n$), $K(\theta_e)$ is the saturation dependent hydraulic conductivity [$L T^{-1}$], K_s is the saturated hydraulic conductivity [$L T^{-1}$] and l is a parameter that represents pore connectivity.

Soil Hydraulic Parameters

The soil hydraulic parameters implemented in the HYDRUS2D simulations were estimated using the Rosetta Lite v.1.0 (February 1999) Neural Network Prediction tool in HYDRUS2D (Schaap, 1999). Bulk density and grain size distributions were calculated from measurements and samples collected in the field for each region in the conceptual model and were described in the *Methods and Materials* section. The summary statistics from the grain size distributions for each region are shown in Table 1 below.

Table 1. The weight percent of gravel, sand, silt, and clay are reported for the WR1, WR2, WR3, traffic zone, rubble zone, and colluvium regions within the pile. The mean, standard deviation (std dev), and coefficient of variation (cv) for each region are presented. In addition, the mean, standard deviation, and coefficient of variation of the dry bulk density of the WR1, WR2, WR3, traffic zone, rubble zone, and colluvium are presented.

	Gravel	Sand	Silt	Clay	Dry Density (g/cm³)
WR1					
Mean	53.1	35.7	7.0	4.1	1.85
Std Dev	17.4	10.6	3.6	4.4	0.13
CV	0.3	0.3	0.5	1.1	0.07
WR2					
Mean	54.8	36.5	6.6	2.1	1.76
Std Dev	11.0	7.7	1.9	0.8	0.15
CV	0.2	0.2	0.3	0.4	0.08
WR3					
Mean	75.0	18.4	5.8	0.9	1.69
Std Dev	5.1	2.8	2.2	0.1	0.01
CV	0.2	0.5	1.1	0.3	0.03
Traffic Zone					
Mean	49.4	36.1	8.9	5.6	1.94
Std Dev	NA	NA	NA	NA	0.02
CV	NA	NA	NA	NA	0.06
Rubble Zone					
Mean	75.0	18.4	5.8	0.9	1.69
Std Dev	5.1	2.8	2.2	0.1	0.01
CV	0.2	0.5	1.1	0.3	0.03
Colluvium					
	8.3	67.3	17.0	7.4	1.75

The summary statistics of density for WR1 were calculated from 219 density measurements made in the field: 213 measurements from the nuclear gauge, 2 measurements from the sand replacement method, and 4 measurements from the sand cone method. The statistics summarized for the grain size distribution in WR1 were

based upon laboratory measurements from 36 samples. The summary statistics of density for WR2 were calculated from 47 density measurements made in the field: 43 measurements from the nuclear gauge, 2 measurements from the sand replacement method, and 2 measurements from the sand cone method. The statistics summarized for the grain size distribution in WR2 were based upon laboratory measurements from 6 samples. The summary statistics of density for the rubble zone were calculated from 6 measurements made using the nuclear gauge. The statistics summarized for the grain size distribution of the rubble zone were based upon laboratory measurements from 3 samples. No direct measurements were made in the WR3 region of the rock pile. However, based upon observations and the advice of field geologists, the rubble zone was considered to be the most similar to WR3, thus the summary statistics from the rubble zone were used to represent WR3. One sample was collected in the colluvium and analyzed to determine the grain size distribution of this region. The summary statistics of density for the traffic zone were calculated from 6 measurements made using the nuclear gauge. The grain size distribution for the traffic zone was based upon the analysis of one sample collected in the field.

The mean values of gravel, sand, silt, and clay presented in Table 1 represent the mass percent or the weight percent of the soil sample. In order to use the Neural Network Prediction tool, the weight percent of the fines (sand, silt, and clay) in each region was determined. Therefore, for each region, the following calculations were made.

$$\sum_{fines} = W_{sand} + W_{silt} + W_{clay} \quad (12)$$

$$W \%_{sand} = \frac{W_{sand}}{\sum_{fines}} \quad (13)$$

$$W \%_{silt} = \frac{W_{silt}}{\sum_{fines}} \quad (14)$$

$$W \%_{clay} = \frac{W_{clay}}{\sum_{fines}} \quad (15)$$

where W_{sand} = weight percent sand of the total sample; W_{silt} = weight percent silt of the total sample; and W_{clay} = weight percent clay of the total sample.

The weight percentages of sand, silt, and clay were inserted into the Neural Network to predict the van Genuchten parameters for the fines. The predicted van Genuchten parameters include estimates of the saturated volumetric water content, $\theta_s = n =$ porosity; the residual water content, θ_r ; the saturated water content, K_s ; and the van Genuchten fitting parameters, α and n . These predicted parameters were only useful to represent the behavior of the different regions with fine soil material. Therefore, additional calculations were needed to correct the water retention curves, unsaturated hydraulic conductivity curves, and thus the van Genuchten parameters for the prescience of gravels and rocks in the different regions. A volume-based correction method was adapted from the Bouwer and Rice method (1984), to modify the unsaturated hydraulic conductivity function and the water retention functions for the volume fraction of gravel and rocks present in the soils (Hendrickx et al., 1991).

In order to determine the volume of the fines and pores, it was necessary to determine the bulk density of the fines. The Neural Network Prediction tool provided

an estimate of the porosity of the fines in each sample, and the specific density of the fines was estimated to be to be 2650 kg/m³ (Koorevaar et al., 1983). The relationship between the bulk density of the fines and the specific density of the fines is expressed as,

$$\rho_{b \text{ fines}} = (1 - n)\rho_{s \text{ fines}} \quad (16)$$

where $\rho_{b \text{ fines}}$ = bulk density of the fines and $\rho_{s \text{ fines}}$ = specific density of the fines.

The volume of the fines and the pores and the volume of the gravel in the soil sample were then calculated as follows,

$$V_{\text{gravel}} = M_{\text{gravel}} / \rho_s \quad (17)$$

$$V_{\text{fines + pores}} = M_{\text{fines + pores}} / \rho_{b \text{ fines}} \quad (18)$$

$$V_{\text{total}} = V_{\text{gravel}} + V_{\text{fines + pores}} \quad (19)$$

where $\rho_s = 2770 \text{ kg/m}^3$ for the andesitic gravel (value for basalt, Goodman. R. E., 1989)

Therefore the volume fraction of the gravel and the volume fraction of fines and pores were calculated as,

$$F_{\text{gravel}} = V_{\text{gravel}} / V_{\text{total}} \quad (20)$$

$$F_{\text{fines + pores}} = V_{\text{fines}} / V_{\text{total}} \quad (21)$$

Finally, the volume fraction of the gravel and rock was calculated for WR1, WR2, WR3, and the rubble zone. The total volume of the region and the different volume fractions can be represented by equations 21 through 25 below.

$$V^*_{total} = V_{rocks} + V_{gravel} + V_{fines+pores} \quad (22)$$

$$F^*_{gravel+fines+pores} = 1 - F^*_{rocks} \quad (23)$$

$$F^*_{gravel} = (1 - F^*_{rocks})F_{gravel} \quad (24)$$

$$F^*_{fine+pores} = (1 - F^*_{rocks})F_{fines+pores} \quad (25)$$

$$F^*_{rocks+gravel} = F^*_{rocks} + F^*_{gravel} \quad (26)$$

where V^*_{total} = total volume of soil material in a region [L^3], V_{rocks} = volume of rocks in a region, cobbles and boulders [L^3], V_{gravel} = volume of gravel in a region [L^3], $V_{fines+pores}$ = volume of fines plus the pore space [L^3], $F^*_{gravel+fines+pores}$ = fraction of the volume represented by gravel, fines, and pores, F^*_{gravel} = fraction of the volume represented by gravel, $F^*_{fines+pores}$ = fraction of the volume represented by fines and pores, and $F^*_{rocks+gravel}$ = fraction of the volume represented by gravel, cobbles, and boulders. Field geologists (personal communication with Virginia T. McLemore, Kelly Donahue, Rick Lynn, and Erin Phillips) estimated the maximum volume of rocks (cobbles and boulders) within the WR1, WR2, WR3, and rubble zone regions and are presented in Table 2 below. In addition, equations 22 through 26 were used to calculate the total maximum volume of rocks (gravel, cobbles, and boulders) and minimum volume of fines within each region of the pile. The calculated values for each of the regions are presented in Table 2 below.

Table 2. The volume of rocks within the WR1, WR2, WR3, and rubble zone regions of the rock pile. The minimum volume fraction of fines and pores for the WR1, WR2, WR3, rubble zone, colluvium, and traffic zone are presented. In addition, the maximum volume fraction of gravel and rocks within the WR1, WR2, WR3, rubble zone, colluvium, and traffic zone are presented.

Region	Volume Rocks (cobbles and boulders)	Minimum Volume Fraction of Fines and Pores *	Maximum Volume Fraction of Gravel and Rocks*
WR1	30	53	47
WR2	40	35	65
WR3	60	15	85
Rubble Zone	40	22	78
Colluvium	NA	95	5
Traffic Zone	NA	63	37

The final step in the procedure to correct for the volume of gravels and rocks present in the soil is to modify the water retention and unsaturated hydraulic conductivity curves using a modified version of the Bouwer and Rice method (1984). The functions were modified for the fraction of gravels and rocks larger than 2 mm in diameter and written as

$$K^*(h) = K(h)(1 - F^*_{rocks+gravel}) \quad (27)$$

$$\theta^*(h) = \theta(h)(1 - F^*_{rocks+gravel}) \quad (28)$$

where $K^*(h)$ and $\theta^*(h)$ are the unsaturated hydraulic conductivity and volumetric water content functions for the rocky soils, and $K(h)$ and $\theta(h)$ are the unsaturated hydraulic conductivity and volumetric water content functions for the fine soil matrix.

The Bouwer and Rice (1984) method (volume-based) and the Gardner (1986) method (mass-based) have both been examined for use in studies where the hydraulic properties of soils containing stones have been difficult to measure (Hendrickx et al., 1991 and Khaleel and Relyea, 1997). Hendrickx et al. (1991) used the Bouwer and Rice (1984) method to estimate the water retention and hydraulic conductivity curves for stony soils in Pakistan. This study concluded that the travel time of recharge water to the groundwater was less sensitive to the soil physical characteristics than to differences in the annual infiltration rates, and thus the estimation method for determining the soil hydraulic properties was appropriate. Khaleel and Relyea (1997) concluded from their study that the two methods work rather well to predict the water retention and hydraulic conductivity data under relatively high moisture conditions (between saturation and –1500 cm), which is a range that was observed during field work on the GHN rock pile. However, they concluded that more work needs to be done to investigate the correction procedure for the low-moisture ranges (Khaleel and Reylea, 1997).

The final region in the conceptual model that was characterized was the bedrock. A limited number of studies have been done to estimate the van Genuchten parameters of bedrock (Stauffer and Stone, 2005; Katsura et al., 2005; Vesselinov et al., 2002; Or et al., 2005; and Flint, 2003). The soil hydraulic parameters or the van Genuchten parameters of the andesite/tuff bedrock in this system were estimated based upon literature values reported for types of volcanic bedrock (Stauffer and Stone, 2005; Vesselinov et al., 2002). The same set of van Genuchten parameters, but different saturated hydraulic conductivity values were used to represent the maximum

and minimum values for the bedrock conductivity and are listed in Table 3 below.

The parameters for the high bedrock conductivity were directly obtained from

Vesselinov et al. (2002).

Table 3. The residual moisture content (θ_r), saturated moisture content (θ_s), van Genuchten alpha (α), van Genuchten n , saturated hydraulic conductivity (K_s) and I for the WR1, WR2, WR3, rubble zone, colluvium, traffic zone, and bedrock regions within the pile are presented above. In addition, two sets of parameters, one for fines and one for fines and rocks are presented for the WR1, WR2, WR3, rubble zone, colluvium, and traffic zone regions within the rock pile.

	θ_r	θ_s	Alpha	n	Ks	I
WR1						
Fines	0.0433	0.383	0.0377	1.53	64.22	0.5
Fines & Rocks	0.0231	0.2041	0.0377	1.53	34.22	0.5
WR2						
Fines	0.039	0.3867	0.0422	1.74	106.05	0.5
Fines & Rocks	0.0137	0.1355	0.0422	1.74	37.17	0.5
WR3						
Fines	0.0319	0.3933	0.0436	1.51	75.68	0.5
Fines & Rocks	0.0047	0.0574	0.0436	1.51	11.05	0.5
Rubble Zone						
Fines	0.0319	0.3933	0.0436	1.51	75.68	0.5
Fines & Rocks	0.0070	0.0862	0.0436	1.51	16.58	0.5
Colluvium						
Fines	0.0403	0.3853	0.0381	1.48	56.98	0.5
Fines & Rocks	0.0383	0.3659	0.0381	1.48	54.11	0.5
Traffic						
Fines	0.0452	0.383	0.0348	1.43	45.18	0.5
Fines & Rocks	0.0287	0.2428	0.0348	1.43	28.65	0.5
Bedrock (low)	0.066	0.300	0.001	2	2.86	0.5
Bedrock (high)	0.066	0.300	0.001	2	28.65	0.5

The “high” and “low” variants of the bedrock conductivity were selected to fall within the range of bedrock conductivity values (between 1.1E-04 cm/sec and 9.7E-05 cm/sec) measured in the stable portion of the GHN rock pile from drill hole TH-GN-08S (Norwest, 2003).

Boundary Conditions

The upper boundary of the conceptual model represented the surface of the rock pile, which was exposed to atmospheric conditions. Therefore, for the purposes of this study, a long-term historical record of the climate in the region was evaluated to determine the maximum total precipitation (including precipitation in the form of rainfall and snowfall) and the maximum precipitation event ever recorded.

Meteorological stations were present on the mine site property, but had only been in operation for approximately 5 years (Golder Associates, 2005). However, the weather station in Red River, New Mexico located approximately 6 miles east of the Questa mine site in the Sangre de Cristo Mountains had a lengthy climate record (approximately 100 years, 1906 to present) and was located in the same valley within the mountainous region (NCDC, 2005; Golder Associates, 2005 a, b). Therefore, the climate data from the Red River weather station collected from the National Climate Data Center (NCDC, 2005) was used for the model simulations because it gave us a better idea of the extreme climate conditions in the region.

The climate data from the Red River weather station indicated that the wettest year on record was 1994. During this year the total annual precipitation, which is the total rainfall plus the snow water equivalent was equal to 1350 mm. The maximum precipitation experienced within a 24-hour period during this year was approximately 7.3 cm. On this day, March 8, 1994, 2.5 cm of rain fell in addition to 43 cm of snow. The snow water equivalent was estimated by multiplying the daily snow accumulation by the average ratio of the snow density to the water density, 0.11 (Dingman, 2002; Garska, 1964). However, the estimate of the snow density to water

density ratio may not properly characterize the conditions at the top of the GHN rock pile because high wind speeds at the top of the rock pile leads to redistribution of the snowpack. High wind speeds have been shown to lead to a denser snowpack, which may better represent the conditions that would be represented on the rock pile (McKay, 1970). Consequently, modification of the ratio of snow density to water density would further increase the total annual precipitation.

Estimates of evaporation and transpiration within the region were missing from the Red River data set, but numerous studies were conducted on the mine site to estimate ET both daily and annually. The annual evaporation rates (little or no vegetation to transpire) were estimated using pan evaporation techniques, lysimeter data, and meteorological data (Wels et al., 2001a, 2001b; Robertson Geoconsultants, 2000, 2001, 2003). The estimated values of evaporation ranged between approximately 380 mm/yr, actual evapotranspiration (AET) of the land surface as predicted by the computer model WREVAP (RGC, 2000), to over 1400 mm/yr, estimated from pan evaporation data on site (RGC, 2001). A summary of the studies that were conducted on the mine site is presented in Appendix A. In addition, consultants working on the mine site estimated daily potential evapotranspiration (PET) using data collected at the weather stations by the Penman and Priestly Taylor methods (Golder, 2005). In order to best represent the climate at the mine site, we employed estimates of the daily PET as inputs for the Hydrus simulations. Therefore, daily PET values from the four-year record were used to calculate an average PET for each julian day. The averaging of PET can lead to overestimates of the true PET on any given day during rainstorms and/or cloudy conditions, which will decrease the

evapotranspiration rates (Kearns and Hendrickx, 1998). The average PET values are plotted with the non-averaged values of PET from the four-year record in Figure 19 below.

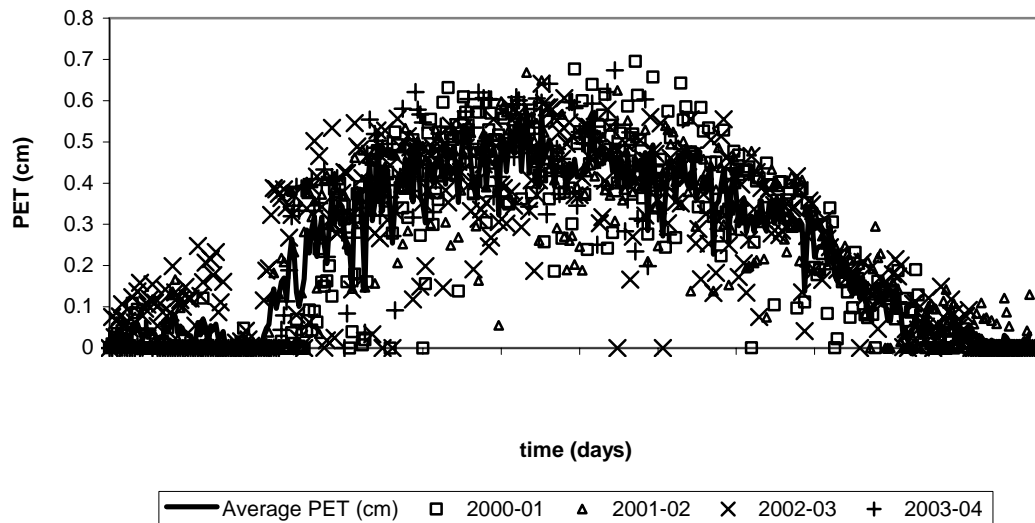


Figure 19. Estimated daily PET (cm) for four consecutive years and the average daily PET (cm) of these four years (data from Golder Associates, 2005 a).

The estimated PET values show some variability between the different years, but there is a clear trend, illustrated in Figure 20, that justifies the use of this data.

Calculations were made to try to verify estimates of the PET using the Penman-Monteith method. However, the results were inconclusive because the variability between the ET calculated in my analysis and the PET calculated by consultants did not reveal a clear systematic error. The PET estimated by the consultants using the Penmn-Monteith method were closest to the reference ET (ET_0) calculated in the verification analysis, but the exact reason for discrepancies could not be determined with the information provided. Additional calculations were made using the Priestly-

Taylor method, which revealed that the discrepancy between the calculations made in my analysis and the calculations made by the consultants may be due to the slope of saturated vapor pressure-temperature curve, psychometric constant, net radiation, and/or the soil heat flux parameters. The final results from this analysis are presented in Appendix B. However, in order to keep consistency within the collaborative study, the calculated PET values from the consultants were used for the numerical models.

The lower boundary along the bottom of the bedrock was treated as a free drainage boundary, which is simulated by a unit vertical hydraulic gradient. This type of boundary is applicable to field studies where water is draining or becoming redistributed in the unsaturated zone (Sisson, 1987; McCord, 1991). The free drainage boundary condition is pertinent to problems where the groundwater table is deep below the domain of investigation (McCord, 1991).

Finally, a seepage face was used to represent the vertical face at the toe of the rock pile. The Hydrus 2D code assumes that the pressure head along seepage face boundary is always equal to zero (Simunek, 2001). Thus, in order for water to leave the system, the pressure head inside the rock pile adjoining with the seepage face has to become positive.

Initial Conditions

The initial pressure head distribution assigned to the rock pile was selected by using the field measurements of matric suction as a guide for the first set of steady-state simulations with the base case scenarios (discussed in the *Simulations* section

below). The pressure head distribution was assumed to be uniform within the system. The details of how the initial pressure head distributions were selected for the remaining steady-state simulations, and transient simulations, are presented in the *Simulations* section below.

Simulations

Sensitivity Analysis

A sensitivity analysis was performed using the conceptual model that was described in the previous section. The sensitivity analysis was designed to test the objectives by testing the importance of soil hydraulic properties, bedrock permeability, and climate to the pressure head distribution and moisture distribution. The analysis was adapted from the 2^k factorial design, where each parameter to be tested was given “high” and “low” variants (Law and Kelton, 1999).

The three parameters selected for the sensitivity analysis were climate, volume fraction of rocks in the soils, and bedrock permeability. The response variables to be investigated were pore pressure, moisture distribution, and storage within the pile. The pore pressure and moisture distribution were selected to illustrate the regions within the pile that become most saturated or experience the lowest tensions (or the pressure heads closest to zero). The storage of the materials was also selected as a response variable to better understand how the overlying soil responds to changes in moisture. The design matrix for this sensitivity analysis is shown in Table 4 below.

Table 4. The design matrix for the 2³ factorial design sensitivity analysis.

<u>Design Point</u>	<u>Climate</u>	<u>Volume Rocks</u>	<u>Bedrock Permeability</u>
1	-	-	-
2	+	-	-
3	-	+	-
4	+	+	+
5	-	+	+
6	+	-	+
7	-	-	+
8	+	+	+

Climate: + = wet year and - = dry year

Volume Rocks: + = maximum and - = minimum

Bedrock Permeability: + = maximum and - = minimum

Preliminary simulations were conducted before starting the simulations described in Table 4 to establish initial conditions under different climate regimes. The first step involved understanding how the system would change under different climate regimes, and then looking at how the system would respond to changes in daily precipitation. In order to simplify the problem numerically for the preliminary simulations, a constant flux rate was applied to the upper boundary of the system, which is exposed to the atmosphere. This type of boundary condition was used instead of an atmospheric boundary condition because it typically runs more smoothly than atmospheric files and allowed the establishment of steady state conditions for each climate regime. In order to understand how the system would respond to different climates, four constant flux levels were selected. These levels were based upon the historical climate data available from the nearby Red River weather station. The different rates and the corresponding total annual precipitation are presented in Table 5 below.

Table 5. Constant flux (cm/day), the corresponding total annual precipitation (cm), and the maximum and minimum total annual precipitation (cm) from the Red River weather station.

Level	Constant Flux Conditions (cm/day)	Total Annual Precipitation (cm)	Red River Weather Station Annual Precipitation Extremes (cm)
1	0.5	183	
2	0.35	128	135 – Maximum Annual Amount
3	0.2	73	
4	0.03	11	34 – Minimum Annual Amount

The maximum constant flux level corresponds to significantly more precipitation than the maximum annual precipitation recorded at the Red River weather station (approximately 40 % more), but was selected to provide additional information about the system if a climate change were to occur in the future. In order to minimize the run-time needed to finish running the models, the simulations were started under rather wet conditions (water pressures equivalent to -30 cm) and stepped down to drier conditions. This type of “step” procedure allows the program to run more smoothly and is more time efficient than progressing in the opposite direction, from dry to wet. The simulations were run until the system reached an approximate steady state, designated as the condition when the pressure heads at observation nodes and the volume of water in each region reached an approximate constant value.

Two of the factors in the sensitivity analysis are represented in the base descriptions, thus 2² base cases were tested at constant flux levels. The descriptions of the base cases are presented in Table 6.

Table 6. The four base case simulations for the sensitivity analysis. Four different constant flux levels were run for each of the four base case simulations, yielding 16 total constant flux simulations. The four base cases were also used in the time series analyses conducted for the sensitivity analysis.

Description ID	Description
1	Low Permeability Bedrock with Soils without Rocks and Gravels
2	High Permeability Bedrock with Soils without Rocks and Gravels
3	Low Permeability Bedrock with Rocky Soils
4	High Permeability Bedrock with Rocky Soils

After each simulation reached a steady-state for the first level, the final pressure head distribution represented from the final time step, was applied as the initial condition of the pressure head distribution for the second level. The remainder of the simulations for each subsequent constant flux level followed the same procedure. The results from the final time step for each level are presented in the Results and Discussion section.

Once the simulations were complete, the 2² factorial design was implemented by setting up simulations with each of the four base cases presented in Table 6 and applying an atmospheric boundary condition to replace the constant flux condition. A “high” variant was applied to this condition in the form of a wet year. The wettest year from the historical record was repeated five times in a Microsoft Excel file to create a time series to be tested with the four base cases described in Table 6. The “high” variant simulations used the steady-state condition of the pressure head distribution from given constant flux simulations as an initial condition for the moisture distribution within the rock pile. Due to our interest in the understanding the rock pile under wet regimes, a “low” variant for the time series analyses was not tested.

RESULTS AND DISCUSSION

This section first briefly discusses the results from field tests conducted to determine bulk density, hydraulic conductivity, matric suction (negative pore pressures), and particle size analyses. The results from the numerical model simulations performed using HYDRUS 2D follow.

Bulk Density

Several methods were used to determine the bulk density of the soils on the GHN rock pile as described in the methods section. All of the results from the bulk density tests are presented in Appendix C. Due to the fact that the nuclear gauge test could be performed very quickly, it was the most frequently used test method at the field site, with 213 measurements in WR1, 43 measurements in WR2, 6 measurements in the rubble zone, and 6 measurements in the traffic zone. The water replacement method was used in 2 tests within the WR1 region and the sand replacement method was used in 2 tests within the WR2 region. Finally, the sand cone method was used for 4 measurements in WR1 and 2 measurements in WR2. Any tests conducted in the excavated trenches within the unstable portion of the GHN rock pile (see Figure 10) are not presented here because that area is not part of this thesis investigation.

The results from the tests performed in the stable part of the GHN rock pile, are presented in Table 7 below.

Table 7. The calculated mean dry bulk densities from four different test methods within the WR1, WR2, WR3, rubble zone, and traffic zone regions of the rock pile are presented. The dry bulk density calculated by using the porosity of the soils estimated in HYDRUS 2D neural network is presented as well.

Region	Test Method	Mean Dry Bulk Density from Test Method(g/cm³)	Dry Bulk Density calculated using HYDRUS 2D data (g/cm³)
WR1	Nuclear Gauge	1.86	1.64
	Water Replacement	2.21	
	Sand Cone	1.72	
WR2	Nuclear Gauge	1.77	1.63
	Sand Replacement	1.60	
	Sand Cone	1.68	
WR3	NA	NA	1.61
Rubble Zone	Nuclear Gauge	1.69	1.61
Colluvium	NA	NA	1.63
Traffic Zone	Nuclear Gauge	1.94	1.64

The results indicate that the sand cone method produced bulk density values between 5 and 7% less than those measured using the nuclear gauge. The water replacement method produced the highest bulk densities and the sand replacement method produced the lowest bulk densities.

The results from the water replacement method in the WR1 region produced higher mean bulk densities than the nuclear gauge method and the sand cone method

(see Table 7 above). The two water replacement measurements were made within one of the mapped unit in the trenches within the WR1 region. The first and second water replacement tests interrogated total volumes of 16500 cm³ and 13500 cm³ respectively. The procedure for the water replacement method stated that the soil sample collected should be approximately 30 times larger in volume than the largest rock within the soil sample. This stipulation is to ensure that the soil is accurately represented in the test. Therefore, the main advantage of the water replacement method is that it is a simple test that can be used to interrogate large volumes of material. However, the main disadvantages of the method are the transport of water to fill the excavated hole and the necessity for a flat surface. The flat surface is necessary so that the water can be filled up to the top of the hole in order to determine the volume of the excavated region.

In contrast to the water replacement tests, the four sand cone tests interrogated smaller volumes of soil ranging between 4322 cm³ and 5994 cm³ and had a mean bulk density nearly 0.5 g/cm³ less than was calculated by the water replacement method. The soil volume for the tests was constrained by the size of the sand cone apparatus, which had an opening in the base plate approximately 171.5 mm in diameter. The holes for the sand cone tests were excavated to between 80 mm and 200 mm depth. In order to make a good measurement, without disturbing the ground around the base plate of the sand cone apparatus, the hole cannot be excavated much deeper, limiting the total volume that can be interrogated. Therefore, the main disadvantages associated with the sand cone method were the limited size that can be interrogated

by the instrument, the transport of the sand cone apparatus, and extra sand to be used in the test.

The nuclear densometer or nuclear gauge measurements interrogated a region along the length of the source rod from the surface to the depth of penetration. The mean bulk density calculated from the 213 measurements in WR1 was approximately 0.4 g/cm^3 less than the calculated values from the water replacement method. The main disadvantage associated with measurements obtained using the nuclear densometer is that results can be highly variable in heterogeneous materials due to the averaging of the measurements across the length of the source rod. The source rod may be inserted between 5 cm and 30 cm into the ground. Therefore, the volume of rocks present in the region of interrogation could bias the results from this test. However, the advantage of this method is the speed of data collection, which was critical due to the very limited time that was available to make measurements on the rock pile.

The discrepancy between the calculated values from the water replacement, sand cone, and nuclear gauge measurements could be due to the volume of material tested. The greater rock to soil ratio in the excavated material collected from the water replacement measurements resulted in a greater mass to volume ratio. However, the variability between the calculated values from the different test methods could also be due to the heterogeneity of the material within the rock pile.

The bulk density of the soils from the water replacement measurements were adjusted for rocks, as is described in the *Methods and Materials* section. The mean estimate of the adjusted bulk density of the soils from the water replacement method

was 0.95 g/cm^3 . The results from this estimate of adjusted bulk density stand alone, because none of the other samples collected from the field tests were adjusted for the effects of rocks. These results also indicate that the matrix material between the rocks within the soil sample was well-sorted, whereas a poorly-sorted soil would be more likely to have a higher bulk density of 1.5 g/cm^3 (Koorevaar et al., 1983).

In addition to the field measurements, estimates of the bulk density were calculated when determining the soil hydraulic properties for each region of the pile for use in the numerical model. The bulk densities were estimated using equation (2) (see Chapter 2, Methods and Materials, *Bulk Density*). The values for porosity, n , were predicted by entering grain size distributions into the neural network in HYDRUS 2D (Simunek, 2001). The estimated bulk densities of the different regions within the pile are presented in Table 7 above. The estimated dry bulk densities were between 3% and 26 % less than the results from the field measurements, with the exception of one measurement in the WR2 region, which was 2 % greater than the dry bulk densities measured in the field. The final bulk densities used in the numerical model were those calculated by equation (2) using the porosity values from HYDRUS 2D. These values were used in order to be consistent by estimating all of the parameters for the numerical model using information from the neural network in HYDRUS 2D.

Hydraulic Conductivity

The results from 21 tension infiltrometer measurements are presented in Appendices D and E. The estimated values of saturated hydraulic conductivity

predicted from the tension infiltrometer measurements ranged between $1.31\text{E-}05$ cm/s and $1.10\text{E-}01$ cm/s with a mean K_s of $8.32\text{E-}03$ cm/s and a median K_s of $9.07\text{E-}04$ cm/s.

The tension infiltrometer was sensitive to changes within the disc and along the contact between the disc and the sand. Therefore, extra attention was focused on eliminating bubbles within the disc prior to beginning measurements. In addition, time was spent to ensure contact between the disc and the sand. All of the measurements made were completed only if satisfactory hydraulic contact was made between the disc and sand. In addition to bubbles in the disc and hydraulic contact between the soil and the disc, a thick sand layer on top of the rock pile material could have influenced the results from the tests. For example, if a thick sand layer were packed on top of the soil, the water would first need to infiltrate through the sand before making contact with the soil of interest. This could influence the results from early-time readings to reflect the infiltration rate of the sand.

The results from 51 Guelph permeameter measurements are presented in Appendix E. The mean saturated hydraulic conductivity of the rock pile material measured from the Guelph permeameter was $2.32\text{E-}02$ cm/s and the median K_s was $7.31\text{E-}03$ cm/s. Colleagues at the University of British Columbia (UBC) made the majority of the Guelph permeameter measurements and all of the calculations of K_s from those measurements.

Estimated K_s values for each domain were also predicted from the porosity by entering the grain size distributions into the neural network within HYDRUS 2D. The mean K_s predicted for the regions with fine soils was $7.01\text{E-}04$ cm/s and the

median was $7.43\text{E-}04$ cm/s. The mean value is nearly two orders of magnitude less than the mean K_s value calculated from the Guelph permeameter measurements and approximately one order of magnitude less than the mean calculated value from the tension infiltrometer measurements. However, the median predicted K_s value in HYDRUS 2D was $7.43\text{E-}04$ cm/s, which is approximately 20% less than the mean value of K_s predicted from the tension infiltrometer measurements and almost an order of magnitude less than the median K_s value calculated from the Guelph permeameter measurement. The predicted mean K_s for the regions with rocky soils was $3.05\text{E-}04$ cm/s and the median was $3.32\text{E-}04$ cm/s. Therefore, the estimates of K_s in the HYDRUS 2D simulations for the fine soils agree well with the results of estimated K_s from the field measurements using the tension infiltrometer. The estimates of K_s in the HYDRUS 2D simulations for the rocky soils were approximately half an order of magnitude less than the results from the field measurements of K_s using the tension infiltrometer.

The K_s values predicted using HYDRUS 2D were used in the numerical simulations in order to be consistent with the other parameters used within the model.

Matric Suction or Negative Pressure Head

The *in situ* matric suction within the trenches was measured with Quick Draw and standard tensiometers. The results from the 108 measurements made in the stable portion of the GHN rock pile are presented in Appendix F. The mean matric suction measured in the trenches in the stable portion of the pile between early September

2004 and late October 2004 was approximately -61 cm. During the four-week period in which the measurements were made, a saturated condition was encountered once and a minimum value of -214 cm was recorded. The tensiometers were inserted into the rock pile and left for the period of in situ testing, and were believed to have reached an equilibrium state. In order to reach equilibrium, the atmospheric pressure within the tensiometers must decrease to a sub-atmospheric pressure. Therefore, to reach equilibrium water moves through the porous cup of the tensiometer and into the soil until the sub-atmospheric pressure within the soil is equal to the sub-atmospheric pressure within the tensiometers (Hillel, 1998).

The results from the nested tensiometer data revealed that the soils in the upper portion of the GHN rock pile responded well to precipitation events, but the magnitude of the response decreased with depth. In addition, the matric suction recorded from the shallowest tensiometer (82 cm depth) in the uncompacted tensiometer nest near the rim of the GHN rock pile responded more slowly to precipitation events than the shallowest tensiometer (63 cm depth) in the compacted tensiometer nest. In a similar response, the next-shallowest tensiometer at the uncompacted nest (146 cm depth) responded approximately one week after the tensiometer in the compacted nest (147 cm depth) responded to a precipitation event.

Overall, the matric suction values recorded in the time period between August and September ranged between -80 cm and near saturation. Although the soils may not have reached full saturation, the matric suction of -80 cm can still be considered relatively moist. A full report regarding the nested tensiometers is presented in

Appendix D. An example file of the data collected from the data loggers at the tensiometer station is presented in Appendix G.

Particle Size Analysis

The results from the particle size analyses for samples collected within the stable portion of the GHN rock pile are presented in Appendix I. The mean particle size distributions from each region of the rock pile domain are presented in Table 1 in the *Soil Hydraulic Properties* section.

The soil hydraulic properties for each of the materials within the conceptual model were determined from the particle size analyses using the Rosetta Neural Network (Simunek, 2001) in HYDRUS 2D, as described in the *Soil Hydraulic Properties* section. The moisture retention curves for each of the four base case simulations (Table 6) illustrates the behavior of the moisture content (θ) as a function of the negative pressure head (h). The moisture retention curves for base cases 1 and 2 were the same, and the curves for base cases 3 and 4 were the same because the hydraulic conductivity was the only parameter that was varied between the high permeability and low permeability bedrock simulations. The moisture retention curves for base cases 1 and 3 are illustrated in Figure 20 and Figure 21.

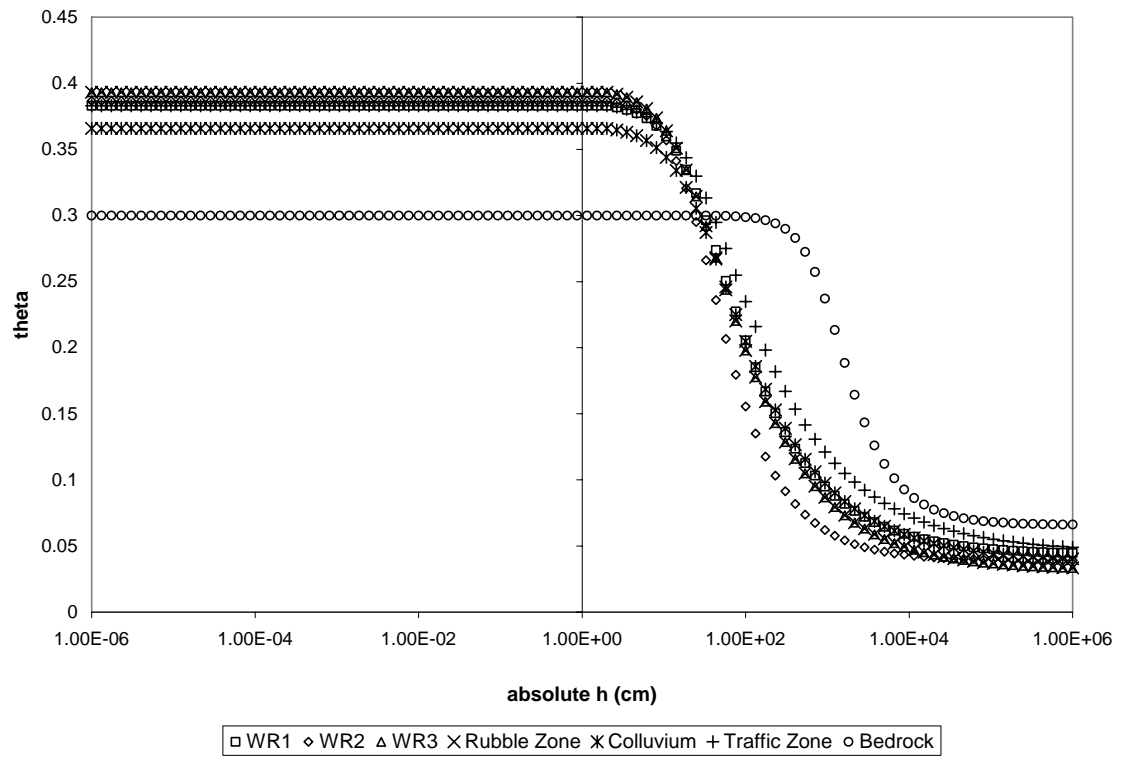


Figure 20. The moisture retention curve for base case simulation 1, for K_{low} and soils without rocks.

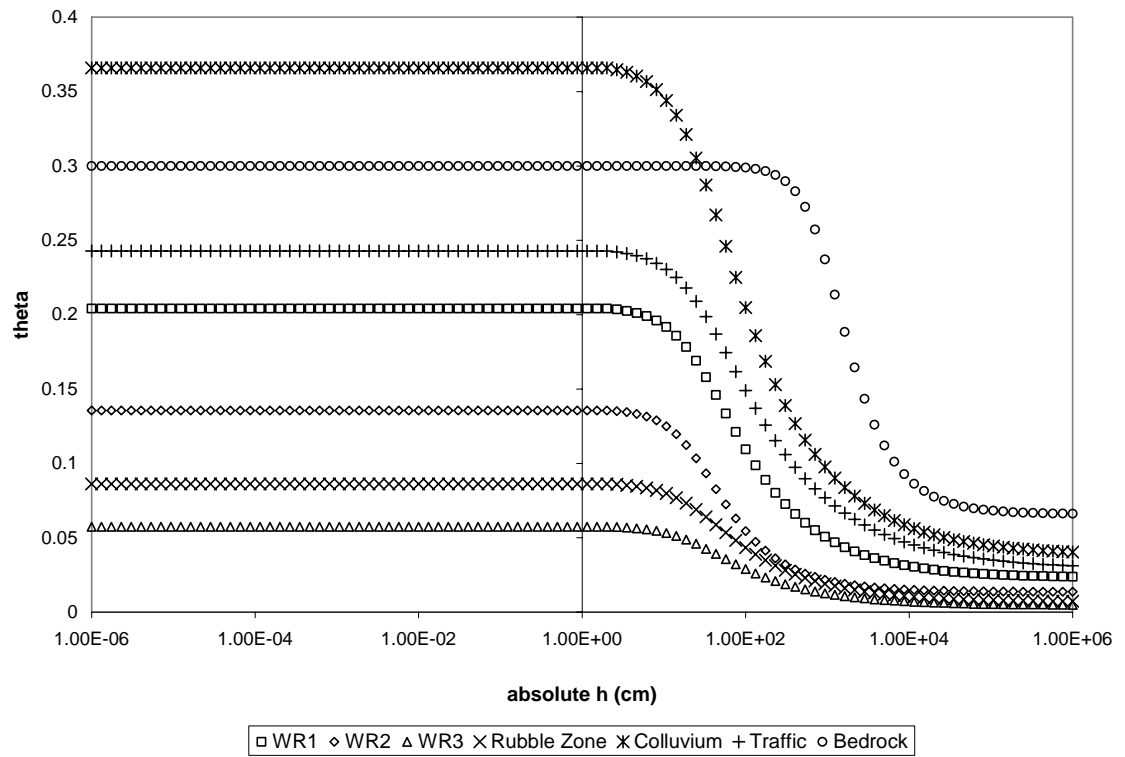


Figure 21. The moisture retention curve for base case simulation 3, for K_{low} and rocky soils.

The moisture retention curves for each of the four base cases illustrated that the bedrock used in the study remained wet after the soils had already reached an inflection point where the moisture content decreased steadily or rapidly. In simulations 1 and 2 (without rocks), all of the units in the rock pile above the colluvium and bedrock have approximately the same moisture retention curves. The approximate inflection point of these units within the rock pile is at -2.66 cm and the inflection point for the bedrock is approximately at -100 cm. Therefore, the moisture content of the respective material decreases after the inflection point as pressure head becomes more negative. In simulations 3 and 4 (with rocks), all of the units in the rock pile have very different moisture retention curves. The approximate inflection point of all of the soil units above the bedrock, is at -2.01 cm, while the inflection point for the bedrock is approximately -100 cm.

Hydrus 2D Simulations

The Hydrus 2D simulations were set up with four base cases for the sensitivity analysis presented in Table 6 in the Methods and Materials section. The modified 2^k factorial design sensitivity analysis was focused on testing the importance of soil hydraulic properties, bedrock permeability, and the climate to the pressure head distribution and moisture distribution within the generic rock pile modeled after the GHN rock pile. The simulations were carried out in the order that is illustrated in Figure 22.

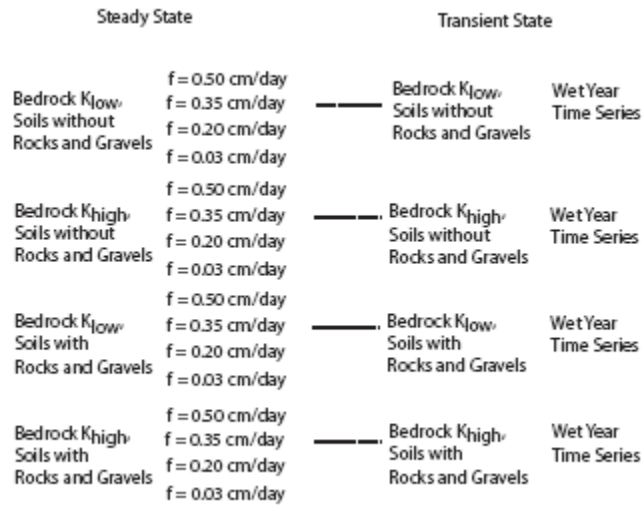


Figure 22. Schematic diagram of the simulations completed in HYDRUS 2D. Simulations were completed at four constant flux levels of 0.50, 0.35, 0.20, and 0.03 cm/day for each of the four base case simulations described. Transient state simulations were completed by using the steady state pressure head conditions from the 0.35 cm/day constant flux level simulations as the initial pressure head conditions.

The simulations completed in HYDRUS 2D are illustrated in the schematic diagram above, and progressed from left to right, with the steady state simulations first and the transient state simulations last. As mentioned previously in the Methods and Materials section, the steady-state pressure head conditions from the 0.35 cm/day constant flux level simulations were used as the initial conditions for the transient state simulations for each subsequent base case.

Constant Flux Simulations

Simulations were completed in HYDRUS 2D by applying a constant flux boundary along the entire upper boundary representing the surface of the rock pile (Figure 18) described in the Methods and Materials section. Simulations were completed for four different base cases, by applying four different constant flux rates (Figure 22).

Moisture Content

The resultant moisture distribution within the rock pile hillslope-system was dependant upon the moisture retention curves for each of the regions within the model domain (illustrated in Figure 20 and Figure 21). Therefore, the moisture distribution of the rock pile material, illustrated in Figure 23 below was controlled by the negative pressure head distribution within the pile.

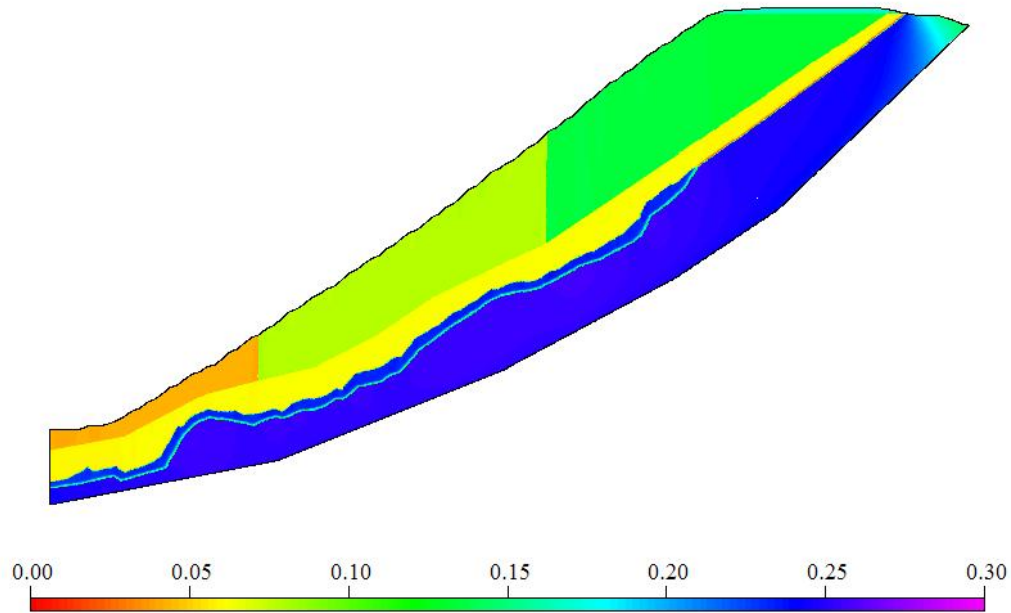


Figure 23. The final moisture distribution within simulation 3, with low bedrock permeability and soils with rocks at the constant flux rate of 0.35 cm/day.

Figure 23 illustrates the final moisture distribution within base case simulation 3 (with rocks, K_{low}). The figure illustrates that the bedrock was the wettest region within the model domain. The colluvium was the region within the rock pile with the highest moisture content, but the saturated moisture content of this region was also the highest out of all of the soils within the pile, leading to approximately 64 % saturation. The moisture content within the WR3 region is the lowest, but the ratio of the moisture content to the saturated moisture content is the closest to saturation (approximate moisture content of 0.043 with a saturated moisture content of 0.057, thus 75 % saturated). The remaining soil units in descending order from most

saturated to least saturated are as follows: rubble zone, traffic zone, WR1, colluvium, and WR2.

The moisture distribution within base case simulation 1, K_{low} without rocks, showed that the bedrock within the model domain once again had the highest moisture content and was the most saturated region of the hillslope-system. However, the traffic zone was the region with the highest moisture content and saturation within the soils of the rock pile. The remaining soil units in descending order from the most saturated to the least saturated are as follows: colluvium, WR1, rubble zone, WR3, and WR2. The results indicate that the pressure head within all of the regions of the rock pile (except for the traffic zone) were less than -30 cm, because this is approximately where the moisture retention curve of the bedrock intersects the moisture retention curve of the soils (Figure 20). The subtle difference in the moisture content within the WR1 region and the WR3 regions resulted in the moisture content fingering downward into the soils.

The final moisture distribution within the base case simulation 2 (without rocks, K_{high}), showed that the bedrock had a lower moisture content than all of the soils within the pile for this simulation. However, the saturated moisture content of the bedrock is lower than those of the soils, leading the bedrock to be the second most saturated unit within the rock pile hillslope system. The traffic zone was the wettest zone. The WR1 region had the next highest moisture content and subsequently percent saturation. The remaining soils in descending order from wettest to driest are as follows: colluvium, rubble zone, WR3, and then WR2. Subtle differences in the

moisture content were illustrated in the WR1 and WR3 regions of the pile, by showing that the water infiltrates downward in a finger-like appearance.

Finally, the final moisture distribution within base case simulation 4 (with rocks, K_{high}) showed that the traffic zone was the wettest region within the model domain. WR1, WR3, the rubble zone, and the colluvium all had similar moisture contents, but the saturated moisture contents for each of the four regions were slightly different. Thus, WR1 was the most saturated region, followed by the colluvium, the rubble zone, and the WR3 region, which was the driest.

Velocity Vectors

Velocity vectors within the rock pile hillslope-system illustrate that the fluid is being transported into the bedrock. Water flowed into the bedrock with ease, due to the soil hydraulic properties selected for the bedrock. This indicates that the soil hydraulic properties of the bedrock within the system should be well understood in order to properly constrain this important lower boundary. A less porous and less permeable rock would most likely have led to the fluids being transported parallel to the slope instead of vertically. The behavior illustrated in each of the simulations is represented in Figure 24 below.

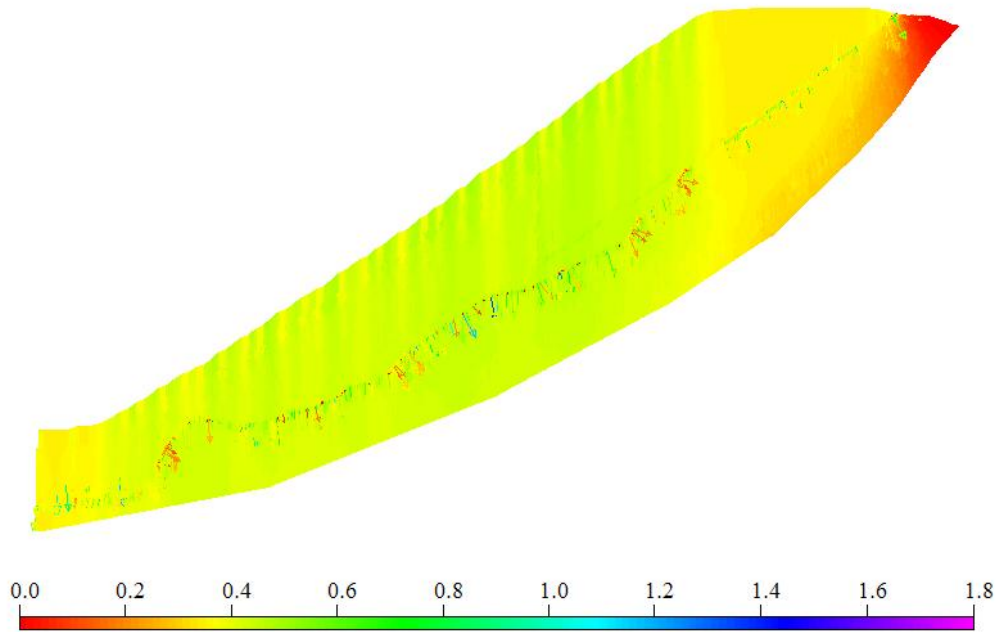


Figure 24. The final velocity vectors within simulation 1 at the 0.35 cm/day time step. The scale ranges between 0 and 1.8 cm/day. The magnitude of the vectors have been exaggerated by five times.

One additional observation from the illustrations of the velocity vectors is the magnitude and direction of the vectors at the bedrock boundary. The direction of the velocity vectors appears to be controlled by the bedrock surface topography. Once again, this illustrates the importance of understanding the characteristics of the underlying bedrock.

Pressure Head

The results from the final time step of the constant flux simulations at the respective flux levels are presented as pressure heads in Appendix J. The figures within Appendix I, illustrate the mean, maximum, minimum, and median values of pressure head at individual nodal locations within the rock pile. The results discussed in this section were taken from the final time step of the constant flux simulations, which represents the steady-state condition under the climate regime defined by the flux level.

WR1, WR2, and WR3

The three large-area upper units exposed to the atmosphere (WR1, WR2, and WR3) are impacted most by the soil hydraulic properties within the regions because within each of the three regions the pressure head distribution is the same for simulations 1 and 2, which have soils without rocks and gravel, and for simulations 3 and 4, which have rocky soils.

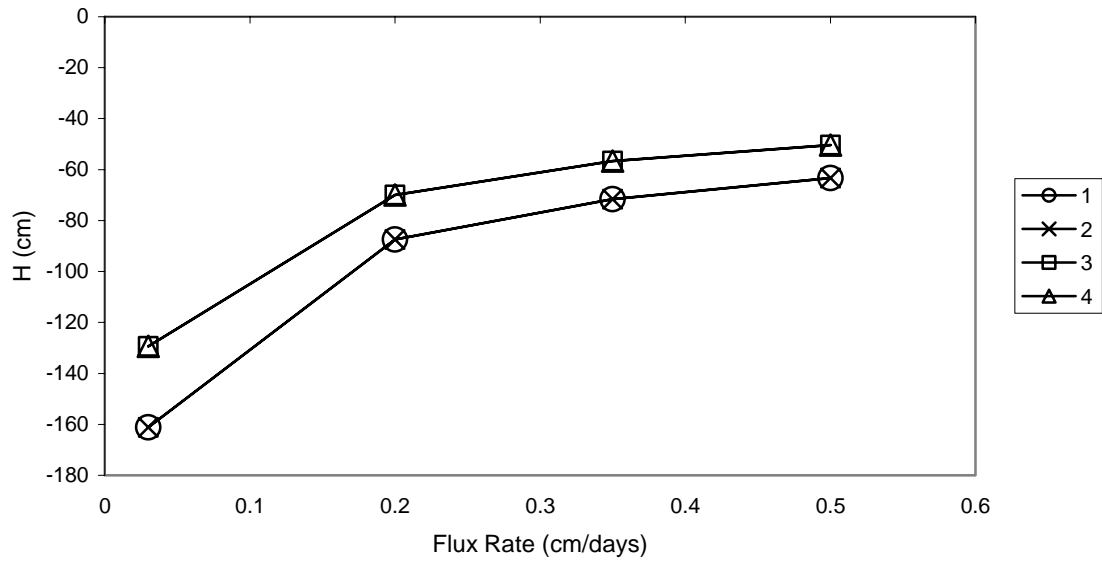


Figure 25. The mean pressure head (cm) within the WR1 region at each constant flux rate for the four base case simulations.

Figure 25 illustrates this behavior in plot of the mean pressure head within the WR1 region of the pile at each of the subsequent constant flux levels. Figure 25 (in addition to the remaining figures illustrate the same behavior and are presented in Appendix I) shows that the soils do not appear to be affected by the bedrock permeability, because the simulations with the same soil type, but different bedrock permeability still have the same approximate pressure head values. Therefore, for each of the constant flux levels, the pressure heads in simulations 1 and 2 are the same and the pressure heads in 3 and 4 are the same because simulations 1 and 2 contain the same soils and simulations 3 and 4 contain the same soils (Figure 25).

Traffic Zone

All of the pressure heads within the traffic zone indicate the same patterns, which were observed in the WR1, WR2, and WR3 regions of the pile, except for the minimum pressure heads.

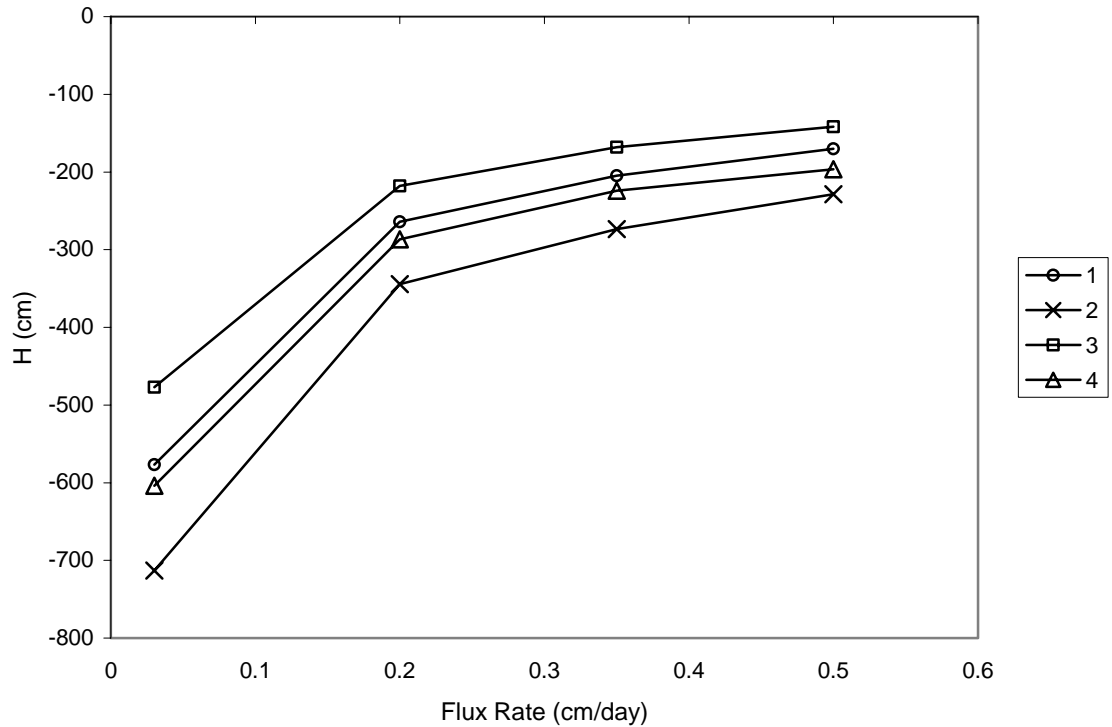


Figure 26. The minimum pressure head (cm) within the traffic zone at each constant flux rate for the four base case simulations.

The minimum pressure heads within the traffic zone (Figure 26) exhibit that both the bedrock permeability and the soil hydraulic properties are more important. Figure 26 illustrates that simulations with low bedrock permeability have higher minimum pressure heads than those simulations with high bedrock permeability. Also, the simulations with rocks (3 and 4) have higher pressure heads than their counterparts without rocks (1 and 2).

Rubble Zone

The maximum pressure heads within the rubble zone for simulations 1 and 2 (soils without rocks) are approximately equal, as well as for simulations 3 and 4 (soils with rocks) (Figure 27). Thus indicating that the soil hydraulic properties of the overlying soils are more important in controlling infiltration and the subsequent pressure heads within the region than the underlying bedrock permeability.

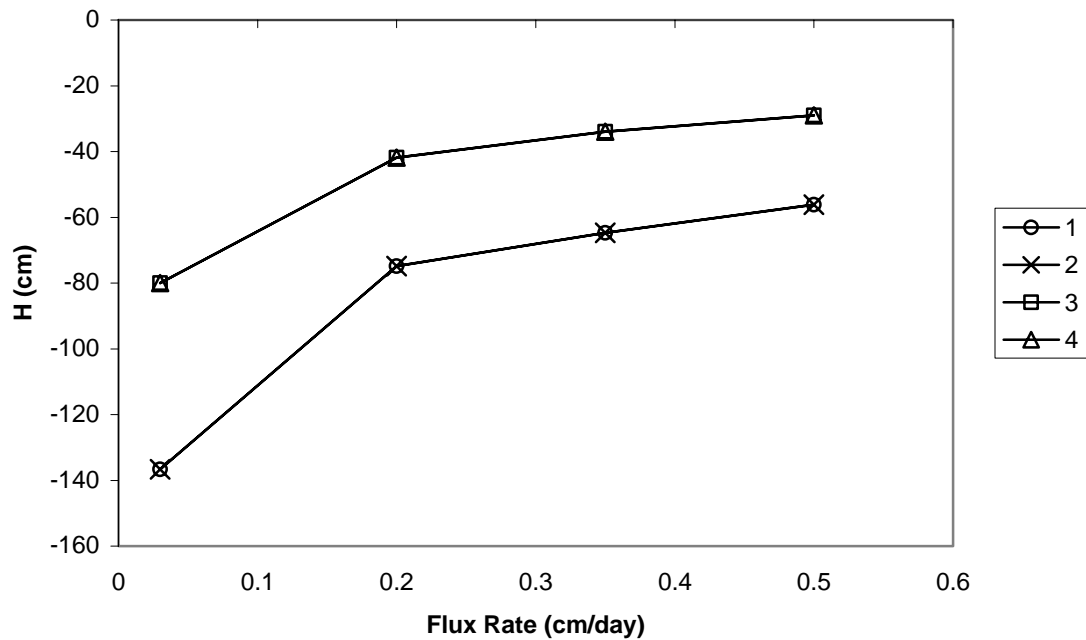


Figure 27. The maximum pressure head (cm) within the rubble zone at constant flux rates for the four base case simulations.

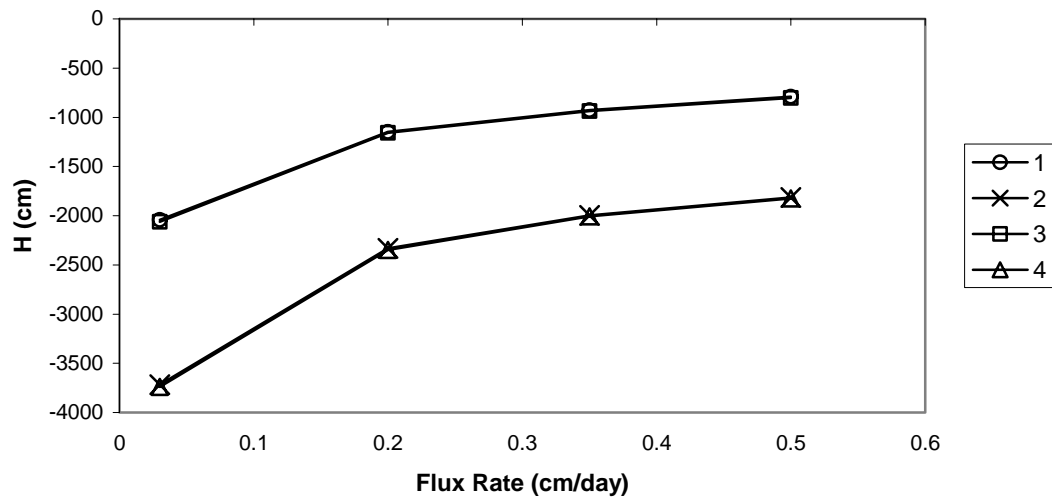


Figure 28. The minimum pressure head (cm) within the rubble zone at constant flux rates for the four base case simulations.

The minimum pressure heads within the rubble zone for simulations with low bedrock permeability (base cases 1 and 3) and high bedrock permeability (base cases 2 and 4) illustrate the control the bedrock has on the pressure head distribution within the overlying soils. Therefore, Figure 28 indicates that the minimum pressure heads within the rubble zone are controlled by the ability of the underlying bedrock to drain water from the system.

Colluvium

The maximum pressure heads within the colluvium indicate the same behavior as was observed within the rubble zone. Simulations 1 and 2 (soils without rocks) and simulations 3 and 4 (soils with rocks) have the same approximate maximum pressure heads within the colluvium (Figure 29).

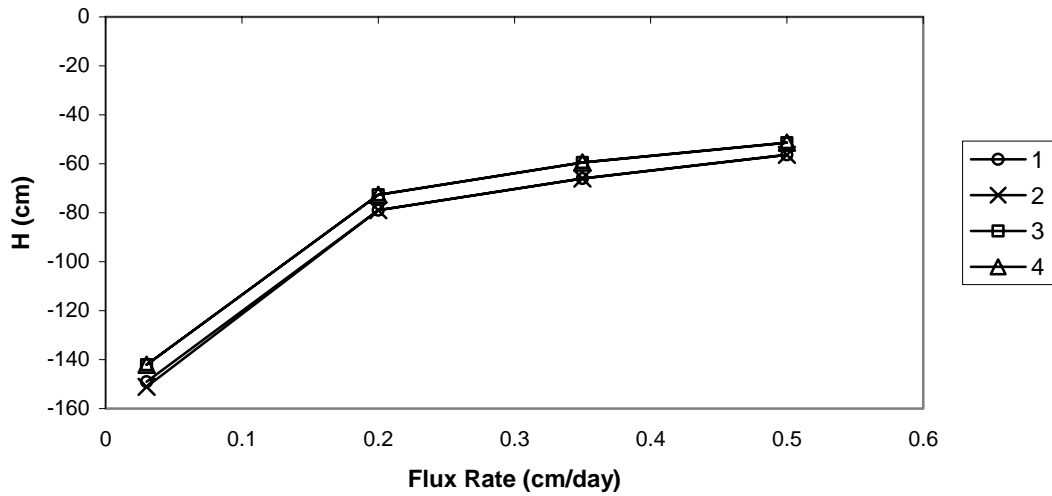


Figure 29. The maximum pressure heads (cm) within the colluvium for the steady state conditions of the constant flux simulations.

The minimum pressure heads within the colluvium (Figure 30) also exhibit the same behavior as is observed in the rubble zone, they are more impacted by the underlying bedrock permeability than the overlying soil hydraulic properties.

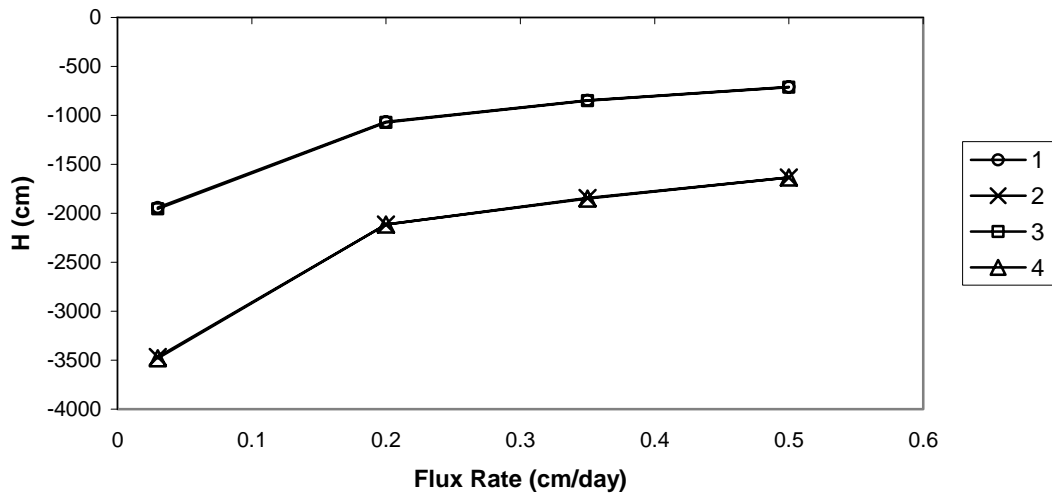


Figure 30. The minimum pressure heads (cm) within the colluvium for the steady state conditions of the constant flux simulations.

Bedrock

The mean, median, maximum, and minimum pressure heads within the bedrock are approximately the same for simulations where bedrock permeability is low (base cases 1 and 3) and high (base cases 2 and 4) (Figure 31).

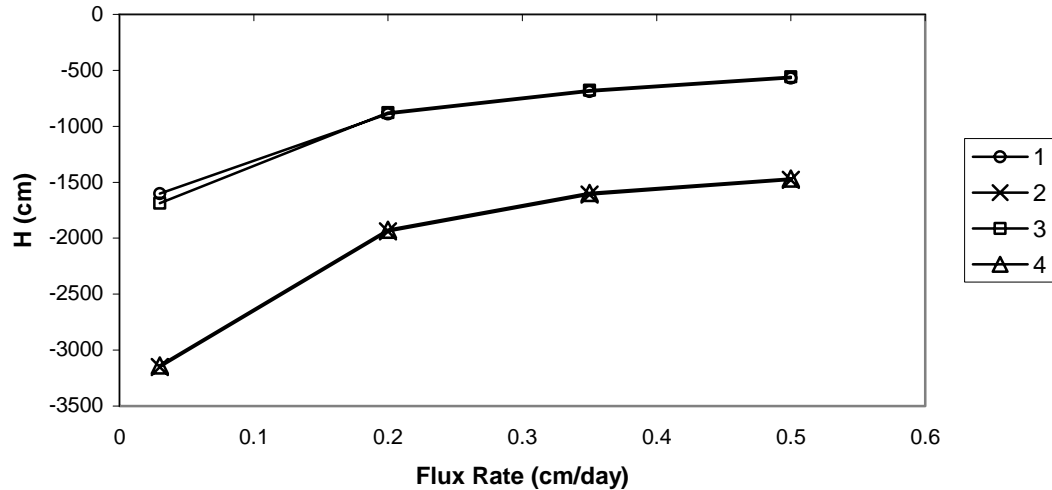


Figure 31. The maximum pressure heads (cm) within the bedrock for the steady state conditions of the constant flux simulations.

The results from the final set of constant flux simulations indicate that the presence of rocks within the pile affects the soil moisture regime. In general, simulations with fine soils were drier than simulations with rocky soils (fine soil, gravel, plus cobbles and boulders). However, the colluvium had the same soil properties for the simulations with fine soils and with rocky soils. This implies that changes in the pressure head distribution within the colluvium region is a direct result of changes observed in the overlying soils and underlying bedrock.

Time Series Simulations

A set of time series simulations were completed by using the initial set-up conditions from the four base case scenarios (Table 6) and using an input atmospheric file for the upper boundary condition which extends along the entire surface of the rock pile (Appendix J).

Atmospheric Input File

The results and discussion below discuss the outcome of the simulations for the wettest year in the climate record from the Red River weather station and refer to the base case simulation numbers presented in Table 6. The annual record of precipitation used in the “wet year” simulations is illustrated in Figure 32.

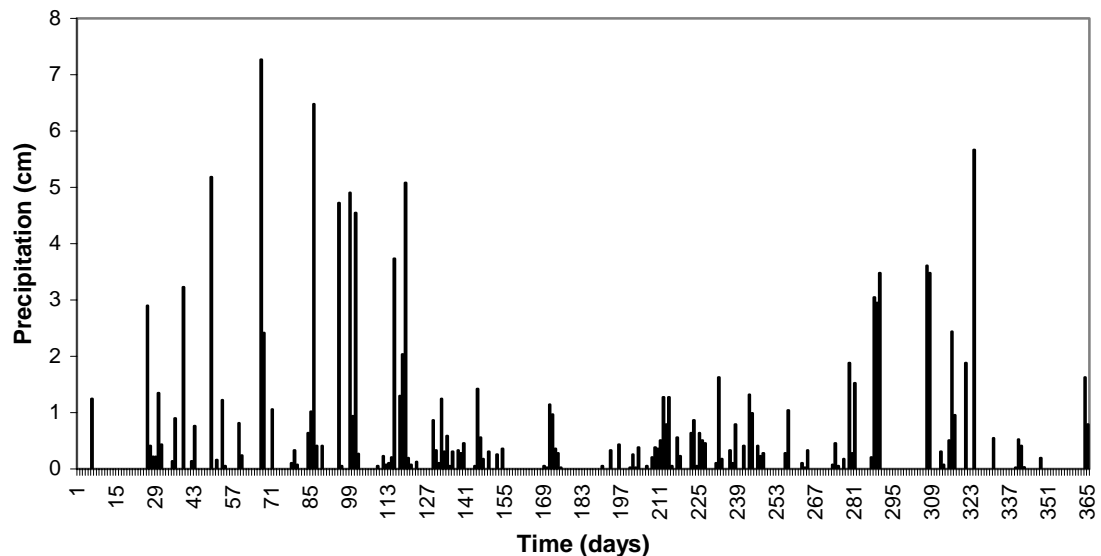


Figure 32. The precipitation record for the “wet year” used in the transient simulations which took place in 1994.

The annual record of PET (Figure 19) was input into the atmospheric file as transpiration. Although there is no vegetation on the rock pile surface, we know that exothermic reactions can lead to evaporation within the pile (McLemore et al., 2006). Therefore, the PET was input in this manner so that evaporation could occur within the pile as opposed to simply occurring at the nodes along the upper surface of the model domain.

Moisture Content

Once again, the resultant moisture distribution was dependant upon the moisture retention curves for each of the regions within the model domain (illustrated in Figure 20 and Figure 21) and was controlled by the negative pressure head distribution within the pile. Figure 33 illustrates the moisture distribution within the rock pile hillslope system at 116.8 days in base case simulation 3 (Table 6, K_{low} , soils with rocks). The moisture contents within the WR3 region and rubble zone at this time step were very near the saturated conditions for these materials. The maximum moisture content within the WR3 region shown in pale orange near the boundary with the WR2 region is approximately 0.0549, which is approximately 96 % saturated ($\theta_s = 0.0574$) (Figure 33). The maximum moisture content within the rubble zone, shown in a light green patch near the toe of the pile close to the interface with the WR3 region, is approximately 0.079, which is approximately 92 % saturated ($\theta_s = 0.0862$) (Figure 33). Although other regions within the pile at this time step have higher moisture contents, the percent saturation of the WR3 region is the highest,

followed by the rubble zone. This behavior is exhibited throughout most of the time period.

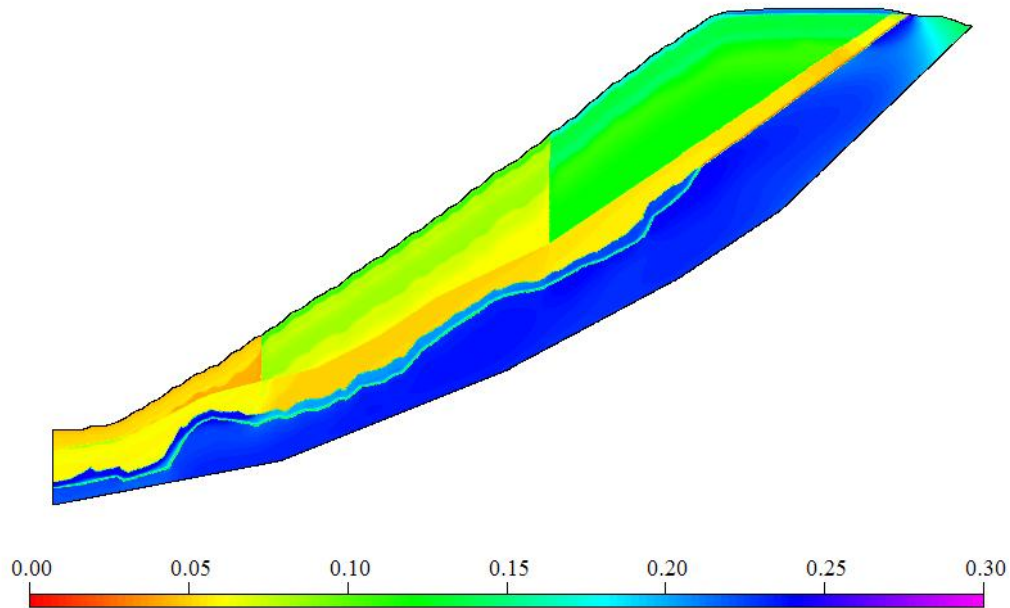


Figure 33. The moisture distribution within the rock-pile hillslope system for base case simulation 3 (K_{low} , soils with rocks) at 116.8 days.

There are two areas within the WR3 region that are typically the wettest, the first is shown in Figure 33 in pale orange yellow, near the dark orange area closest to the WR2 boundary. The second area within the WR3 region that is typically the wettest is shown in dark orange in Figure 33 near the boundary with the WR2 region of the pile. The wettest region within the rubble zone is typically located near the boundary with the WR3 region as shown in Figure 33, or it is deeper near the colluvium boundary near the toe of the pile.

The moisture distribution within base case simulation 4 (Table 6, K_{high} , soils with rocks) is very similar to that shown in Figure 33. The main difference is that the system in simulation 4 is slightly drier, and the response of the soils to rainfall is lagged (approximately the same response occurred 11 days after the response was observed in simulation 3).

The moisture distributions within base case simulations 1 and 2 (Table 6, soils without rocks) illustrate more homogenous conditions. The maximum percent saturation of the regions within the pile for these simulations was between approximately 50 and 66, except for the traffic zone which was had a maximum saturation of about 73 percent. The results from these simulations indicate that a rock pile consisting of soils without rocks would become less saturated than a rock pile consisting of soils containing a large rock volume fraction.

Velocity Vectors

Velocity vectors within the rock pile hillslope-system once again illustrated that the water was infiltrated vertically into the pile and flowed directly into the bedrock. Therefore, it is clear that the soil hydraulic properties selected for the bedrock influence the flow regime within the rock pile.

Pressure Heads

The results from all of the transient simulations are presented as pressure heads in Appendix K. The figures within Appendix K, illustrate the mean, maximum,

minimum, and median values of pressure head at individual nodal locations within the rock pile.

WR1, WR2, and WR3

The results from the transient simulations indicate that the bedrock permeability did not significantly affect the pressure head distribution within the upper regions of the hillslope system for simulations 1 and 2. The regions WR1, WR2, and WR3 are all exposed to atmospheric conditions, and the median, mean, maximum, and minimum pressure heads do not appear to have been influenced by the bedrock permeability. Instead, the two base case simulations with fine soils (see Table 6 above), simulations 1 and 2, produced approximately the same pressure head distributions at the respective time steps as those illustrated in Figure 34 (the remaining figures are located in Appendix K).

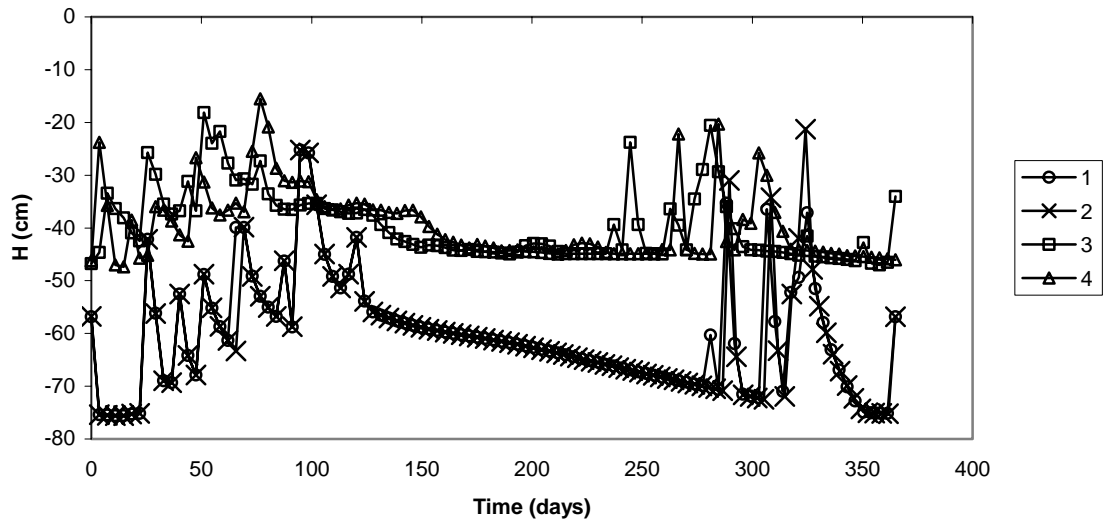


Figure 34. The maximum pressure head (cm) within the WR1 region of the rock pile for the “wet year” simulations 1 through 4.

However, the two base case simulations with rocky soils, simulations 3 and 4, produce approximately the same pressure head distributions at lagged time steps (Figure 34). This indicates that the bedrock permeability is influencing the moisture regime in the upper units of the pile when the soils have a rocky texture. The lagged response observed in simulation 4 is not observed for simulation 2, which also has high bedrock permeability, but has fine soils. This could be due to the fact that the fine soils are between 15 % and 63% more conductive than the rocky soils, with the exception of the colluvium, which is the same for both soils. This increase in the conductance of the fine soils indicates that they have higher water storage capacity. The response of the fine soils to rainfall events can be expected to lead to drier conditions in simulations 1 and 2 than in simulations 3 and 4. The response also indicates that the soil hydraulic properties are more important in controlling the flow regime in simulations 1 and 2.

The region at the toe of the pile, WR3 reached maximum pressure head values that were near saturation at time steps in the months of February, August, September, and November. These maximum pressure heads appear to be in response to precipitation events (Figure 35).

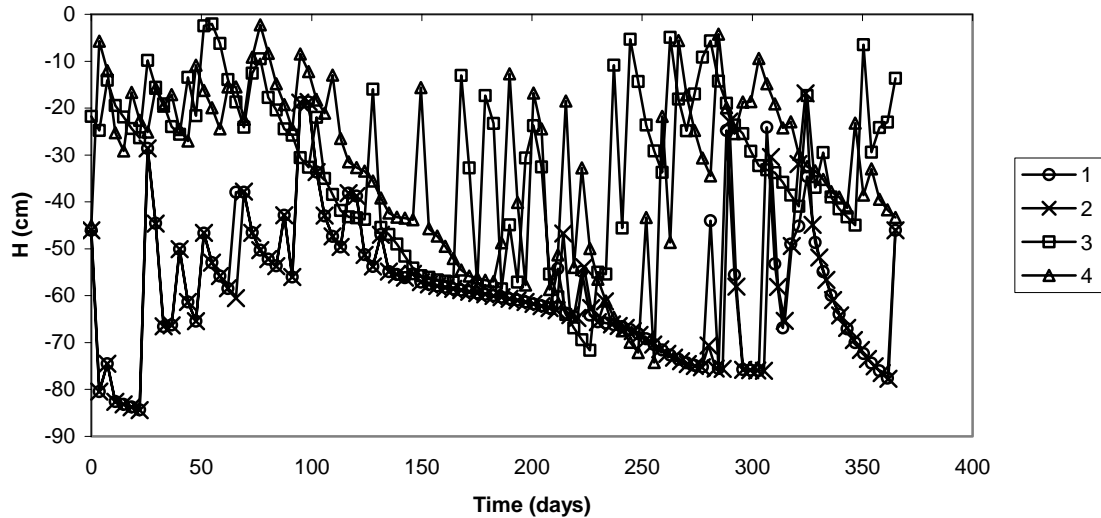


Figure 35. The maximum pressure head distribution within the WR3 region of the pile in each of the four “wet year” transient simulations.

It is possible that additional peak maximum pressure heads were not recorded due to the fact that pressure heads were only reported every 3.65 days. The maximum pressure heads within the WR3 region generally occurred at nodes near the seepage face or near the boundary with the WR2 region. Subsequently, additional nodes with pressure head values very close to the maximum values observed often surround these nodes. We can conclude that the WR3 region within the hillslope exhibits higher maximum pressure head values than within the other regions of the pile, which may be due to the redistribution of water as a result of gravity driven flow. The results of the moisture distribution within the pile also showed that for

rocky soils, the WR3 region of the pile came closest to saturation in response to rainfall events. This increased wetness near the toe of the pile has been a recognized phenomenon in previous hillslope studies (Mosley, 1979; Sklash et al., 1986; McGlynn et al., 2002) and has been shown to induce slope failure (Orense et al., 2004). Therefore, it appears that under the conditions imposed in the model, the WR3 region within the pile would be of the greatest interest when investigating potential instabilities in the system.

Traffic Zone

The median, mean, maximum, and minimum pressure heads within the traffic zone did not appear to show an influence from the bedrock permeability. The traffic zone exhibited the same behavior observed in the WR1, WR2, and WR3 regions of the pile. Base case simulations 1 and 2 (soils without rocks) (Table 6) produced approximately the same pressure head distributions at the respective time steps (Figure 36). Simulation 4 showed approximately the same pressure head response as simulation 3, but it was lagged.

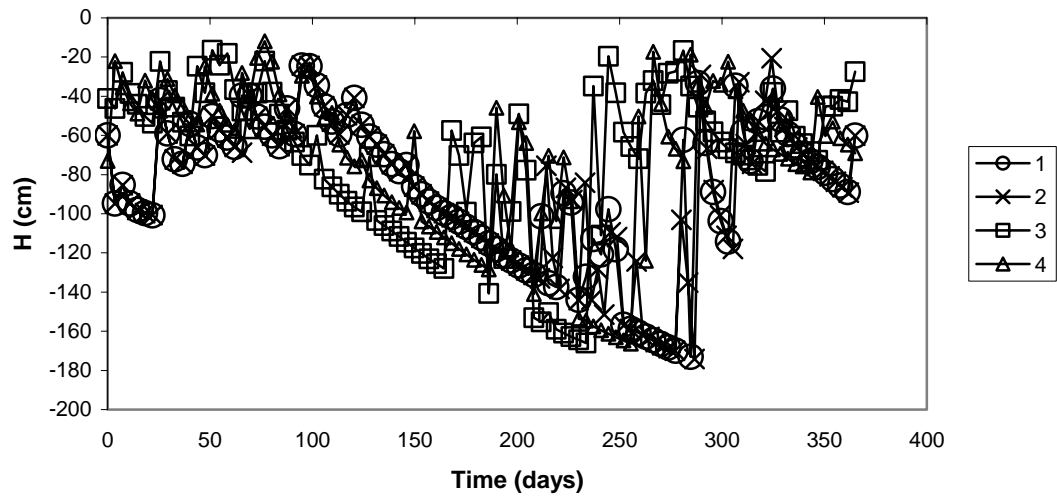


Figure 36. The maximum pressure head distribution within the traffic zone of the pile in each of the four “wet year” transient simulations.

Rubble Zone

The minimum pressure head conditions in the rubble zone exhibit drier conditions within simulation 2 than those from simulation 1 (Figure 37). Similarly, simulation 4 exhibits drier minimum pressure head conditions in the rubble zone than those in simulation 3.

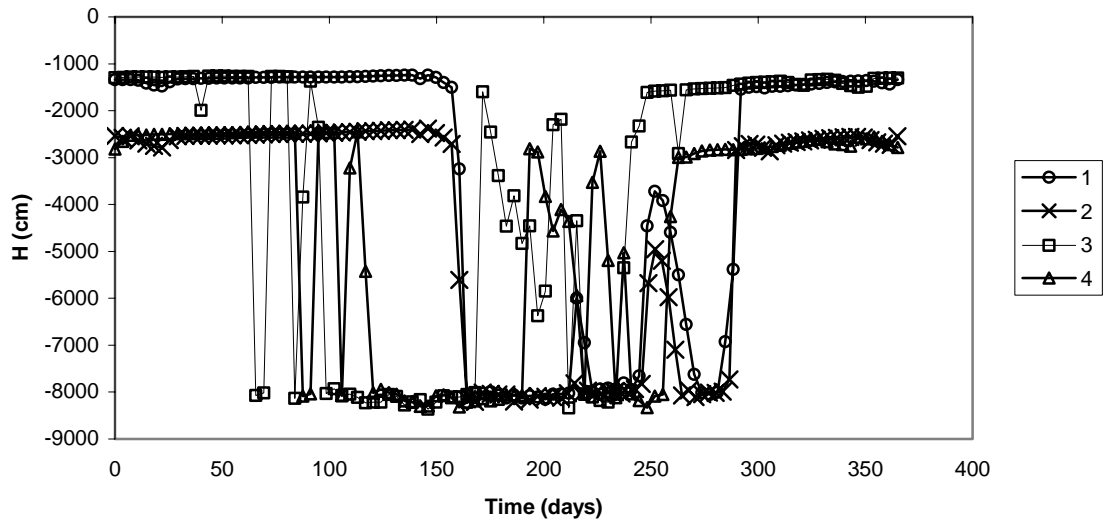


Figure 37. The minimum pressure head distribution within the rubble zone for each of the four “wet year” transient simulations.

The wetter conditions exhibited in simulations 1 and 3 are most likely due to the fact that the low permeability bedrock has less storage capacity than the high permeability bedrock, and thus wicks water more quickly in the unsaturated system, while the high permeability bedrock drains water out of the system more quickly. In addition to being drier, the pressure head response in simulation 4 is lagged behind the response in simulation 3. As mentioned previously, this lagged response, also observed in the maximum pressure head distributions, can be attributed to the higher bedrock permeability in simulation 4 than in simulation 3. The rocky soils therefore display the effects of precipitation and bedrock permeability more easily. The shapes of the pressure head distribution curves over time are approximately the same between simulations 1 and 2 and between simulations 3 and 4 as illustrated in Figure 37.

The maximum pressure heads within the rubble zone in simulations 1 and 2 are approximately equal for the given time steps. Note that the maximum pressure heads within the rubble zone consist of the second highest maximum pressure heads observed out of all of the seven regions of the hillslope system shown in Figure 38.

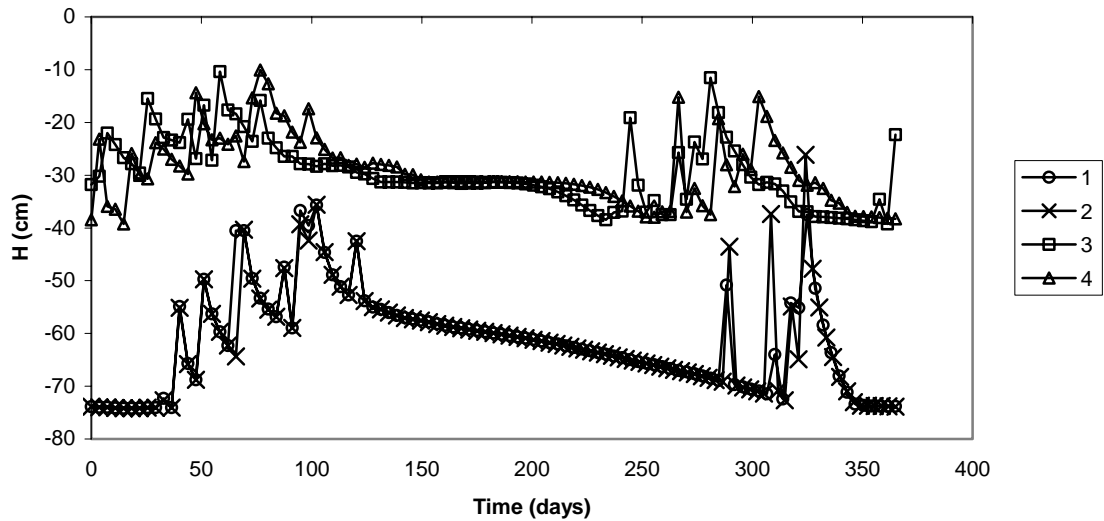


Figure 38. The maximum pressure heads (cm) within the rubble zone for the four “wet year” simulations.

Also note that the maximum pressure head response within the rubble zone in simulation 4 shows the lagged response behind simulation 3 as is observed in the other units within the rock pile.

The mean pressure heads from simulations 1 and 2 reflect the variability in the minimum pressure heads in addition to any other fluctuations in the pressure heads not exhibited in the statistics. The results indicate that this deviation between simulations 1 and 2 is consistently approximately equal to 10 cm of head (Figure 39).

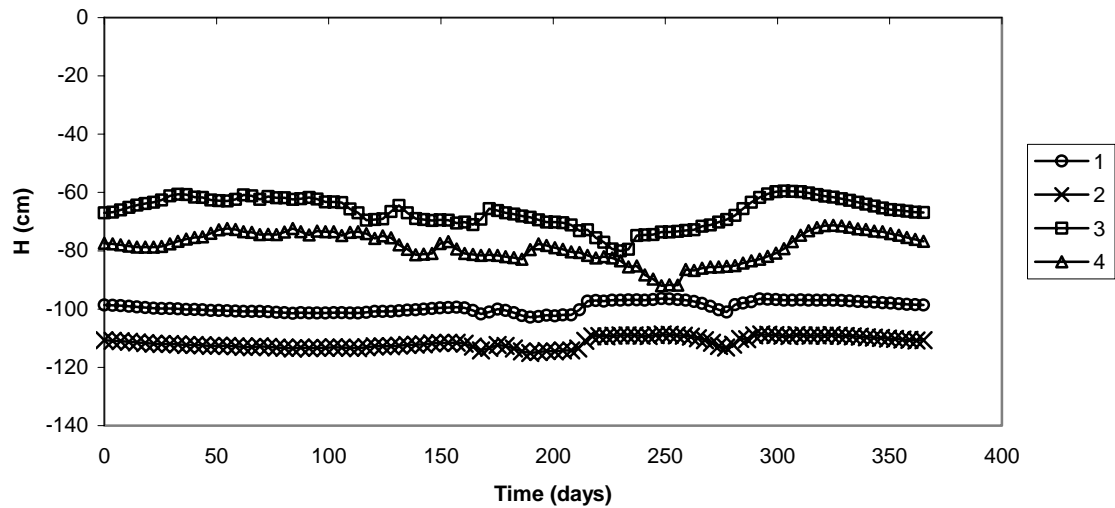


Figure 39. The mean pressure head distribution within the rubble zone for the four “wet year” transient simulations.

The difference in the mean pressure head between simulations 3 and 4 could also equal 10 cm of head if the lag in simulation 4 was removed and the pressure heads were in phase.

Colluvium

The minimum and mean pressure heads recorded within the colluvium region of the pile exhibit clear differences between the high and low permeability simulations (Figure 40 and Figure 41). This change in the pressure head response of the colluvium can be attributed directly to the change in the bedrock permeability because the soil properties of the colluvium did not change between the simulations for fine soils or rocky soils. The pressure head response can also be attributed to the soil properties of the overlying soil. This is illustrated by the similarity in the shape

of the minimum pressure head values over time in simulations 1 and 2 and in simulations 3 and 4. The shapes of the curves are directly related to the soil type within the simulations.

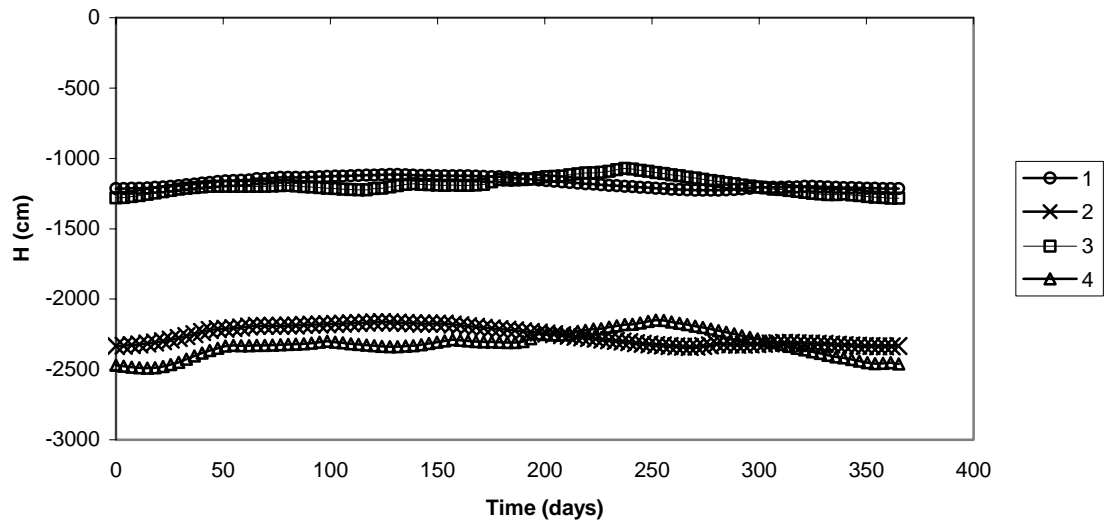


Figure 40. The minimum pressure head distribution within the colluvium region for each of the four “wet year” transient simulations. Simulations 1 and 3 exhibit similar minimum pressure heads over time, while simulations 2 and 4 also exhibit similar minimum pressure heads over time.

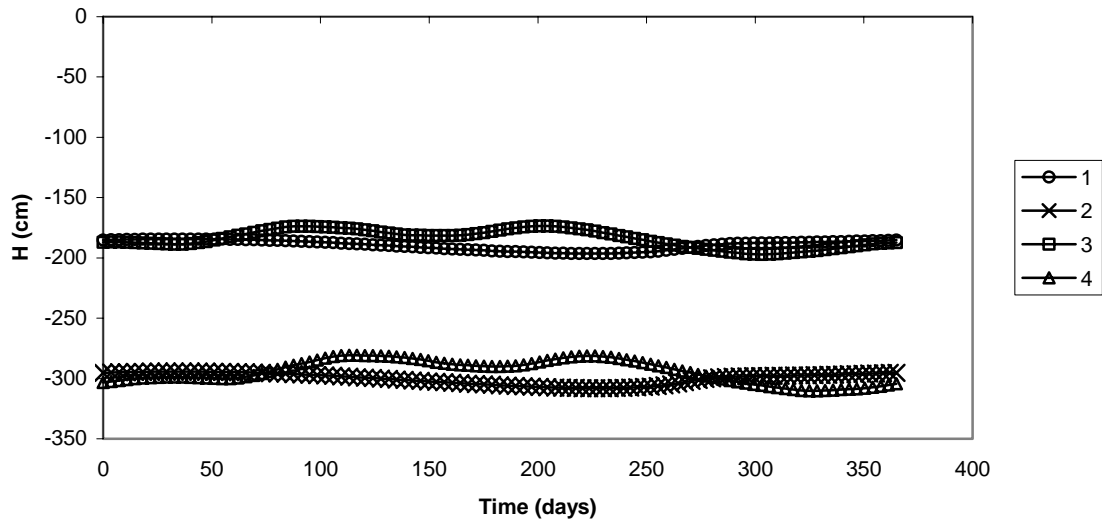


Figure 41. The mean pressure head distribution within the colluvium region for each of the four “wet year” transient simulations.

The minimum and mean pressure head responses over time within the colluvium also show the lagged response of simulation 4 behind simulation 3.

The median pressure heads within the colluvium region in simulations 3 and 4 respond slowly to precipitation events. Conversely, the median pressure heads within the colluvium in simulations 1 and 2 respond quickly to rainfall events. In simulations 3 and 4, the colluvium reacts more slowly to the rainfall. This was not expected because the properties of the soils in simulations 3 and 4 have less storage capacity and would be expected to respond more quickly to precipitation events. However, the colluvium is a deeper layer along the bedrock interface, and water from precipitation events must first infiltrate through the upper, more conductive regions (WR1, WR2, and WR3) before reaching the colluvium region. Therefore, the delayed response of the soils in the colluvium can be attributed to the storage capacity of the overlying regions (Figure 42).

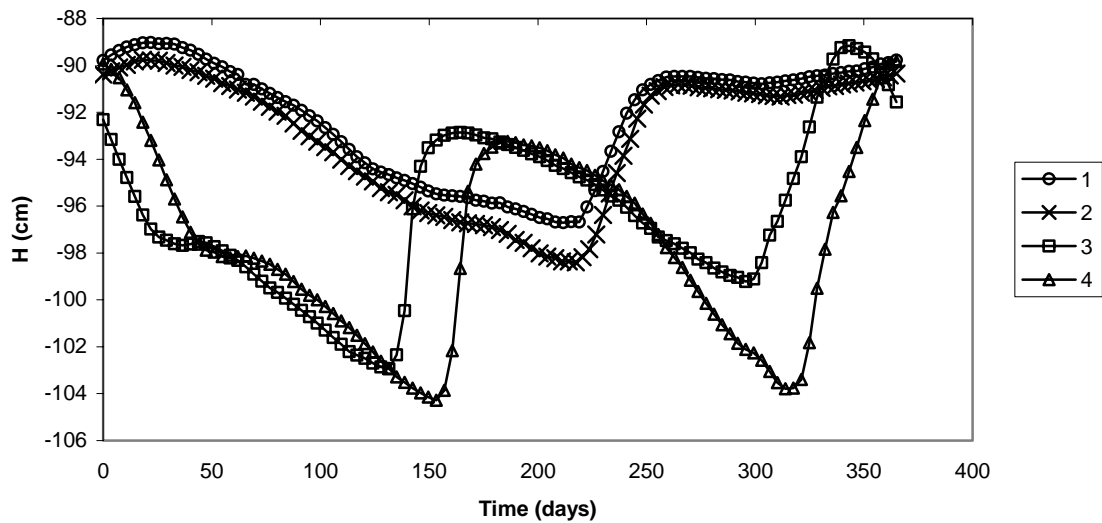


Figure 42. The median pressure head distribution within the colluvium region for each of the four “wet year” transient simulations.

The lag of simulation 4 behind simulation 3 is clearly observed in the median pressure head within the colluvium over time.

Bedrock

Finally, the results from the simulations show that the soil hydraulic properties of the overlying soils impact the shape of the pressure head response within the bedrock, but not the magnitude of the pressure head. As would be expected, the two base cases with high bedrock permeability (simulations 2 and 4) are similar in the magnitude of their mean, median, maximum, and minimum pressure head values, and this is also true for the simulations with low bedrock permeability (simulations 1 and 3). However, the shape of the response is based upon the type of overlying soil that is

present in the simulation. The difference between the simulations with fine soils and the simulations with rocky soils, indicate that the hillslopes containing rocky soils become wetter than those with fine soils (Figure 43).

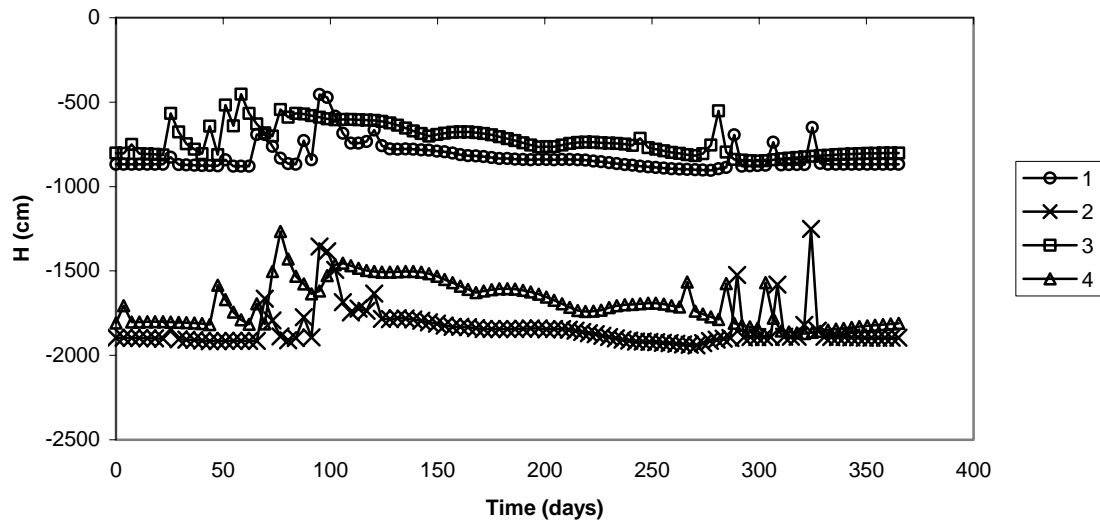


Figure 43. The maximum pressure head distribution within the bedrock for each of the four “wet year” transient simulations.

The wetness of the simulations with rocky soils can be attributed to the estimated soil hydraulic properties, which indicate that these soils are less porous due to finer material filling pore spaces. This is in contrast to the fine soils, which primarily consist of sand. The poor sorting of the rocky system creates an environment that becomes more easily wetted. The “response time” of the system to precipitation events is quicker in rocky soils, which is consistent with findings in a study by Hengxing et al. (2003). Hengxing et al. (2003) found that lower permeability soils have a quicker response time to rainfall events, while higher permeability soils have a slower response time because they have a higher storage capacity and thus a longer time is needed to observe the response to rainfall.

CONCLUSIONS

The bulk densities of the rock pile materials measured in the field were greater in magnitude than the bulk densities estimated using the porosities calculated by the Neural Network in HYDRUS 2D. The presence of rocks within the soils affected the bulk densities calculated for the soil material at the mine site.

The saturated hydraulic conductivity estimated using the tension infiltrometer on the GHN rock pile ranged between $1.31\text{E-}05$ cm/s and $1.10\text{E-}01$ cm/s. The median K_s was $9.07\text{E-}04$ cm/s, which agreed well with the K_s values predicted in the neural network of HYDRUS 2D for simulations with fine soils. However, the median K_s estimated from guelph permeameter measurements was $7.31\text{E-}03$ cm/s which is an order of magnitude greater than the median K_s for the fine soils in the HYDRUS 2D simulations. The estimated saturated hydraulic conductivity for the measurements made in the field and estimates made using HYDRUS 2D indicate that the GHN rock pile has rather permeable soils and relate more strongly to the fine soils investigated in the sensitivity analysis.

The mean matric suction or pressure head (negative) measured within the rock pile soils during trenches between early September and early October was approximately -61 cm. The matric suction measured from nested tensiometers in the summer prior to trench activities ranged between -80 cm and near saturation. The matric suction response of the soils to precipitation events was illustrated in the record from the nested tensiometers. A lag between the precipitation events and the

response of the matric suction within the soils is shown by the nested tensiometer data.

The results from the numerical modeling study indicate that understanding the soil hydraulic properties of the rock pile material and the bedrock hydraulic properties are crucial to properly characterizing and constraining numerical models to describe a hillslope system. The results from this study showed that the presence of rocks within the soils led to wet conditions within the rock pile. In some cases, areas within the soil regions came close to saturation (WR3 was 96 % saturated while the rubble zone was 92 % saturated, near the toe of the pile). One caveat in associating the results of this research with the GHN rock pile is that model assumes that even the rockiest regions of the pile are matrix supported. However, observations have indicated that in WR2 and WR3 near the toe of the pile the rocks were not matrix supported, which would lead to a breakdown in the model to capture the behavior of the rock pile near the toe. This once again shows how important it is to have a strong conceptual model based upon field data.

The soil properties and thus the regional storage appear to play a more dominant role in controlling the moisture distribution within the model domain. The soil hydraulic properties were the dominant factor controlling the pressure heads and moisture distribution within the WR1, WR2, WR3 and traffic zone regions within the pile. The soil hydraulic properties were also more important in controlling the maximum pressure heads within the rubble zone and colluvium than the bedrock permeability.

The effect of the bedrock permeability on the moisture distribution within the soils is more evident in the simulations with rocky soils (lower conductivity) than those with fines (higher conductivity). The bedrock permeability was most important in controlling the minimum pressure heads within the rubble zone and colluvium. The porosity and permeability of the bedrock was also important in controlling the flow regime (velocity vectors) within the rock pile. A less porous and less permeable bedrock would be expected to result in more interfacial flow.

The results from the transient simulations showed that the soils responded quickly to rain events. The shallower soils with rocks responded most quickly to precipitation events. The results from this study indicate that the WR3 region and rubble zone region of the generic rock pile with rocky soils would be the regions most likely to undergo chemical weathering due to the increased percent saturation. This information can be used to assist in setting up conditions for geochemical reaction models.

Finally, the increased moisture content (near saturation in some cases) within the WR3 region and rubble zone could lead to an increase in the degree of weathering, which could lead to a decrease in the internal friction angle (Gutierrez, 2006). Therefore, the increased moisture content following infiltration events could lead to a decrease in the internal friction angle and mechanical weathering of the rock pile materials.

Future Work or Other Considerations

In order to fully understand the rock pile hillslope system, a fully coupled model of heat, vapor, and fluid transport should be attempted. However, a better understanding of the groundwater levels below the rock pile should be developed first. Smith and Chapman (1983) indicated that it is important to understand the groundwater table in order to predict the heat flux background levels by a numerical model.

Borga et al. (2002) discussed the concept of saturation from above (percolation) or saturation from below (perched groundwater table), which may possibly play an important role in understanding the flow processes at the GHN rock pile. Saturation from below may be a factor at the rock pile due to evidence of perched water at the bedrock-rock pile interface encountered by field geologists (personal communication with Virginia T. McLemore, 2006). However, without a firm understanding of the groundwater table in the immediate vicinity of the GHN rock pile (i.e., not a wealth of piezometer wells within the actual rock pile) it would be difficult to add the groundwater table as an input to the model. However, future work may be to put in a fictional groundwater table to see what affects it may have on the moisture distribution (i.e. could it lead to saturation).

In addition to developing a better understanding of the groundwater table below the GHN rock pile, it would be useful to collect samples of the bedrock to determine their hydraulic properties. A better understanding of the moisture retention

characteristics of the bedrock could lead to constraining future models more appropriately.

For future investigations on different rock piles it would also be useful to collect a long-term record of matric suction within the rock pile that could be used to calibrate the numerical model predictions. I would suggest installing nested tensiometers at greater depths than the nested tensiometers that were discussed within this thesis. By installing nested tensiometers at greater depths it would lead to a better understanding of how the numerical models are predicting the changes in the matric suction distribution near the surface of the rock pile/atmosphere interface. I would also suggest keeping the nested tensiometers installed for a greater length of time if possible (6 months to 1 year), in order to allow the tensiometers to become equilibrated and record data from more than one season during the year. As mentioned, it would no longer be possible to install tensiometers on the GHN rock pile, but should be considered for rock piles under investigation in the future.

Finally, the presence of vegetation on a rock pile surface could potentially improve the stability of the hillslope by the presence of roots, which would suck up some of the moisture. Future numerical studies could be conducted using the more detailed conceptual model in an effort to determine whether the presence of trees on the GHN rock pile would assist in stabilizing the hillslope system by decreasing the net infiltration and increasing support on the slope by root networks.

REFERENCES

- Abshire, D. 1998. Report on Hydrological Connection Associated with Molycorp Mining Activity, Questa, New Mexico. Prepared for USEPA, Region 6 NPDES Permits Branch (6WQ-P).
- Adams, D. C., and G. R., Keller, 1994. Possible extension of the Midcontinent Rift in west Texas and eastern New Mexico. *Canadian Journal of Earth Science*. 31 (709-720).
- Adams, D. C., and G. R., Keller, 1996. Precambrian basement geology of the Permian Basin region of West Texas and eastern New Mexico: A geophysical perspective. *American Association of Petroleum Geologists, Bulletin*. 80 (410-431).
- ASTM D 2922-96 Density of Soil and Soil-Aggregate in Place by Nuclear Methods. American Society for Testing Materials, Annual Book of ASTM Standards, 1996, Soil and Rock Building Stones, Philadelphia, PN.
- ASTM D 3017-96 Moisture Content of Soil and Soil-Aggregate in Place by Nuclear Methods. American Society for Testing Materials, Annual Book of ASTM Standards, 1996, Soil and Rock Building Stones, Philadelphia, PN.
- ASTM D 4914-99 Standard Test Methods for Density of Soil and Rock in Place by the Sand Replacement Method in a Test Pit. American Society for Testing Materials, Annual Book of ASTM Standards, 1999, Soil and Rock Building Stones, Philadelphia, PN.
- ASTM D 1556 – 00 Standard Test Method for Density and Unit Weight of Soil in Place by the Sand-Cone Method. American Society for Testing Materials, Annual Book of ASTM Standards, 2000, Soil and Rock Building Stones, Philadelphia, PN.
- ASTM D422-63 Standard Test Method for Particle-Size Analysis of Soils. American Society for Testing Materials, Annual Book of ASTM Standards, Reapproved 2002, Soil and Rock, Philadelphia, PN.
- Baltz, E. H., and D. A., Myers, 1999. Stratigraphic framework of upper Paleozoic rocks, southeastern Sangre de Cristo Mountains, New Mexico. *New Mexico Bureau of Mines and Mineral Resources. Memoir 48*. p. 269.
- Barnes, M. A., Rohs, C. R., Anthony, E. Y., van Schmus, W. R., and R. E., Denison, 1999. Isotopic and elemental chemistry of subsurface Precambrian igneous

- rocks, west Texas and eastern New Mexico. *Rocky Mountain Geology*. 34 (245-262).
- Basile, A., Mele, G., and F. Terribile, 2003. Soil hydraulic behavior of a selected benchmark soil involved in the landslide of Sarno 1998. *Geoderma*. 117, 331-346.
- Bauer, P. W., and K. I., Kelson, 2004. Cenozoic structural development of the Taos area, New Mexico. *New Mexico Geological Society Guidebook*. 55 (129-146).
- Borga, M., Fontana, F. D., Gregoretti, C., and L. Marchi, 2002. Assessment of shallow landsliding by using a physically based model of hillslope stability. *Hydrological Processes*. 16, 2833-2851.
- Bouwer, H. and R.C., Rice, 1983. Effect of stones on hydraulic properties of vadose zones. *ASAE Winter Meeting*, New Orleans, LA. Paper No. 84-2515, 11 pp.
- Bowman, P. M., and H. G. Gilchrist, 1979. Waste Dump Instability and Its Operational Impact for a Canadian Plains Lignite Mine. *Stability in coal mining; Proceedings of the First International Symposium on Stability in Coal Mining*, Vancouver, British Columbia, Canada. 381-394.
- Carpenter, R. H., 1968. Geology and ore deposits of the Questa molybdenum mine area, Taos County, New Mexico: in *Ore deposits of the United States, 1933-1967*. Graton-Sales. J. D., Ridge, ed. AIME. p. 1328-1350.
- Carson, A. B., 1961. *General Excavation Methods*. New York. F. W. Dodge Corps.
- Chapin, C. E. and S. M., Cather, 1994. Tectonic setting of the axial basins of the northern and central Rio Grande rift. In: Keller, G.R. and S.M. Cather, eds. *Basins of the Rio Grande rift: Structure, Stratigraphy, and Tectonic Setting*. Geological Society of America, Special Paper 291, p. 39-58.
- Clark, K.F., 1968. Structural controls in the Red River District, New Mexico. *Economic Geology*. 63 (553-566).
- CPN International, *Nuclear Densometer Instruction Manual*. 1999.
- Curtis, R. O., and B. W. Post, 1964. Estimating bulk density from organic matter content in some Vermont forest soils. *Soil Sci. Soc. Am. Proc.* 28, 285-286.
- Czamanske, G.K., Foland, K.A., Hubacher, F.A. and J.C., Allen, 1990. The ⁴⁰Ar/³⁹Ar Chronology of Caldera Formation, Intrusive Activity and Mo-ore Deposition near Questa, New Mexico. *New Mexico Geological Society*

Guidebook. 41 (355-358).

- Dames and Moore, 1987. Hydrogeologic and Chemical Analyses for the Proposed Guadalupe Mountain Tailings Disposal Site Ground-Water Discharge Plan, Taos County, New Mexico. Report prepared for Molycorp, Inc., July 1987.
- Das, B.M., 1983. Advanced Soil Mechanics. New York, McGraw-Hill Book Company, 511 pp.
- Dingman, S. L., 2002. Physical Hydrology. Upper Saddle River, New Jersey. Prentice Hall.
- Donovan, J. G. and M. G. Karfakis, 2003. Assessment of Hillside Coal Waste Embankment Failures Using Qualitative Analysis. International Journal of Surface Mining, Reclamation and Environment. 17(4), 234-245.
- Gardner, W.H., 1986. Water Content, In: *Methods of Soil Analysis Part 1. Physical and Mineralogical Methods*, Agronomy Monograph no. 9, Soil Science Society of America, Madison, WI, USA, p. 493-509.
- Garstka, W. U., 1964. Snow and snow survey, Section 10 In: V. T. Chow (ed.) *Handbook of Applied Hydrology*. New York, NY. McGraw-Hill.
- Goodman, R. E., 1989. Introduction to Rock Mechanics. New York. John Wiley and Sons.
- Golder and Associates, 2005a. Fourth Monitoring and Modelling Report For Infiltration Test Plot Study, Questa Mine, New Mexico. Submitted to Molycorp, Inc. April 5, 2005.
- Golder and Associates, 2005b. Mine Rock Water Balance Study, Questa Mine, New Mexico. Submitted to Molycorp, Inc. June 3, 2005.
- Grossman, R.B. and R.G., Reinsch. 2002. Chapter 2. The solid phase. 2.1 Bulk density and linear extensibility. In: J.H. Dane and G.C. Topp (eds.) *Methods of soil analysis. Part 4. Physical Methods*. Soil Science Society of America, Madison, Wisconsin. pp. 201-228.
- Guan, H. 2005. Water Above the Mountain Front- Assessing Mountain-Block Recharge in Semiarid Regions. Ph. D Thesis, New Mexico Institute of Mining and Technology.
- Gutierrez, L. A. F., 2006. The Influence of Mineralogy, Chemistry, and Physical Engineering Properties on Shear Strength Parameters of the Goathill North Rock Pile Material, Questa Molybdenum Mine, New Mexico. M. S. Thesis, New Mexico Institute of Mining and Technology.

- Hancock, G. R. and E. Turley, 2006. Evaluation of proposed waste rock dump designs using the SIBERIA erosion model. *Environmental Geology*. 49, 765-779, doi:10.1007/s00254-005-0127-7.
- Hendrickx, J.M.H., 1990. Determination of hydraulic soil properties. In: M.G. Anderson and T.P. Burt (eds.), *Process studies in hillslope hydrology, chapter 3*. John Wiley and Sons. pp. 42-93.
- Hendrickx, J.M.H. and L.W., Dekker, 2002. Section 6.1.2 Measurement of solute content using soil extraction. In: J.H. Dane and G.C. Topp (eds.) *Methods of soil analysis. Part 4. Physical Methods*. Soil Science Society of America, Madison, Wisconsin. pp. 1255-1261.
- Hendrickx, J.M.H., S. Khan, M.H. Bannink, D. Birch, and C., Kidd, 1991. Numerical analysis of groundwater recharge through stony soils using limited data. *Journal of Hydrology* 127:173-192.
- Hengxing, L., Chenghu, Z., Lee, C. F., Sjing, W., and W., Faquan, 2003. Rainfall-induced landslide stability analysis in response to transient pore pressure, A case study of natural terrain landslide in Hong Kong. *Science in China*. 46, 52-68.
- Hillel, D, 1998. *Environmental Soil Physics*. San Diego. Academic Press.
- Holt, R. M., Wilson, J. L., and R. J. Glass, 2002. Spatial bias in field-estimated unsaturated hydraulic properties. *Water Resources Research*. 38 (12), 1311, doi:10.1029/2002WR001336.
- Holtz, R.D. and Kovacs, W.D., 2003. *An Introduction to Geotechnical Engineering*. Civil Engineering and Engineering Mechanics Series. Pearson Education Taiwan Ltd., 733 pp.
- Hubbell, J. M. and J. B. Sisson, 1998. Advanced tensiometer for shallow or deep soil water potential measurements. *Soil Science*. 163, 271–277.
- Iverson, R. M., 2000. Landslide triggering by rain infiltration. *Water Resources Research*. 36 (7), 1897-1910.
- Jury, W.A., W.R. Gardner, and W.H. Gardner, 1991, *Soil Physics*, John Wiley and Sons, New York, p. 45.
- Karlstrom, K. E., Amato, J. M., Williams, M. L., Heizler, M., Shaw, C. A., Read, A. S. and P. Bauer, 2004. Proterozoic tectonic evolution of the New Mexico region: a synthesis: New Mexico Geological Society, Special Publication 11,

p. 1-34.

- Karlstrom, K. E., and S. A. Bowring, 1988. Early Proterozoic assembly of tectonostratigraphic terranes in southwestern North America. *Journal of Geology*, 96, 561-576.
- Karlstrom, K. E., and S. A. Bowring, 1993. Proterozoic orogenic history of Arizona. In: Reed, J. C., Jr., Bickford, M. E., Houston, R. S., Link, P. K., Rankin, D. W., Sims, P. K. and W. R., van Schmus, (eds.) *Precambrian: Conterminous U. S.*: Geological Society of America, *The Geology of North America*. C-2 188-211.
- Karlstrom, K. E., Doe, M. F., Wessels, R. L., Bowring, S. A., Donn, J. C., and M. L. Williams, 1990. Juxtaposition of Proterozoic crustal blocks: 1.65-1.60 Ga Mazatzal orogeny: Arizona Geological Survey, Special Paper 7, p. 114-123.
- Karlstrom, K. E. and E. D. Humphreys, 1998, Persistent influence of Proterozoic accretionary boundaries in the tectonic evolution of southwestern North America: Interaction of cratonic grain and mantle modification events. *Rocky Mountain Geology*. 33 (161-179).
- Kasmer, O., Ulusay, R., and C. Gokceoglu, 2006. Spoil pile instabilities with reference to a strip coal mine in Turkey: mechanisms and assessment of deformations. *Environmental Geology*. 49, 570-585.
- Khaleel, R., and J. F. Relyea, 1997. Correcting laboratory-measured moisture retention data for gravels. *Water Resources Research*. 33 (8), 1875-1878.
- Kearns, A. K. and J. M. H. Hendrickx. 1998. Temporal Variability of Diffuse Groundwater Recharge in New Mexico. New Mexico Water Resources Research Institute Technical Completion Report No. 309, New Mexico State University, Las Cruces, NM, 50 pp.
- Koorevaar, P., Menelik, G., and C. Dirksen, 1983. *Elements of Soil Physics*. Elsevier Science.
- Law, A. M. and W. D., Kelton, 2000. *Simulation Modeling and Analysis*. San Francisco. McGraw Hill.
- Lefebvre, R., Lamontagne, A., Wels, C., and Robertson, A., 2002. ARD Production And Water Vapor Transport at the Questa Mine, Tailings and Mine Waste '02: Proceedings of the Tailings & Mine Waste '02 Conference, January 27-30: Fort Collins, A.A.Balkema, p. 479-488.
- Lipman, P. W. and J. C. Jr. Reed, 1989. Geologic map of the Latir volcanic field and

adjacent areas, northern New Mexico: U. S. Geological Survey, Miscellaneous Investigations Map I-1907, scale 1:48,000.

- LoVetere, S. H., Nordstrom, D. K., Maest, A. S., and C. A. Naus, 2004, Questa baseline and pre-mining ground-water quality investigation. 3. Historical ground-water quality for the Red River valley, New Mexico: U. S. Geological Survey, Water Investigations Report 03-4186, 238 p.
- McCord, J. T., Stephens, D. B. and J. L. Wilson, 1991. Hysteresis and State-Dependent Anisotropy in Modeling Unsaturated Hillslope Hydrologic Processes. *Water Resources Research*. 27 (7), 1501-1518.
- McDonnell, J. J., 1990. A rationale for old water discharge through macropores in a steep, humid catchment. *Water Resources Research*. 26 (11), 2821-2832.
- McDonnell, J. J., Freer, J., Hooper, R., Kendall, C., Burns, D., Beven, K., and J. Peters, 1996. New method developed for studying flow in hillslopes. *EOS*, 77 (47), 465.
- McGlynn, B. L., McDonnell, J. J., and D. D. Brammer, 2002. A review of the evolving perceptual model of hillslope flowpaths at the Maimai catchments, New Zealand. *Journal of Hydrology*. 257, 1-26.
- McKay, G. A., 1970. Precipitation, In: D. M. Gray, ed. *Handbook on the Principles of Hydrology*. Port Washington, NY. Water Information Center, Inc.
- McLemore, V. T., Donahue, K. M., Phillips, E., Dunbar, N., Walsh, P., Gutierrez, L. A. F., Tachie-Menson, S., Shannon, H. R., Lueth, V. W., Campbell, A. R., Wilson, G. W., and B. M. Walker, 2006. Characterization of Goathill North Mine Rock Pile, Questa Molybdenum Mine, Questa, New Mexico. ICARD/SME 2006.
- Meyer, J. W.. 1991. Volcanic, plutonic, tectonic and hydrothermal history of the southern Questa Caldera, New Mexico: University Microfilms, Ph.D. dissertation, 348 p.
- Meyer, J. and K.A. Foland, 1991. Magmatic-tectonic interaction during early Rio Grande rift extension at Questa, New Mexico. *Geological Society of America Bulletin*. 103, 993-1006.
- Meyer, J. W., and R. W. Leonardson, 1990. Tectonic, hydrothermal and geomorphic controls on alteration scar formation near Questa, New Mexico: *New Mexico Geological Society, Guidebook 41*, p. 417-422.
- Mosley, M. P., 1979. Streamflow generation in a forested watershed, New Zealand. *Water Resources Research*. 15, 795-806.

- National Climate Data Center (NCDC). Online resource. 2005.
- Norwest Corporation. 2003. Goathill North Slide Investigation, Evaluation and Mitigation Report. Prepared for Molycorp, Inc.
- Okagbue, C. O., 1987. Stability of Waste Spoils in an Area Strip Mine – Geological and Geotechnical Considerations. *Earth Surface Processes and Landforms*. 12, 289-300.
- Orense, R. P., Shimoma, S., Maeda, K., and I. Towhata, 2004. Instrumented Model Slope Failure due to Water Seepage. *Journal of Natural Disaster Science*. 26 (1), 15-26.
- Park, S. J., and N. van de Giesen, 2004. Soil-landscape delineation to define spatial sampling domains for hillslope hydrology. *Journal of Hydrology*. 295, 28-46.
- Peters, D. L., Buttle, J. M., Taylor, C. H., and B. D. LaZerte, 1995. Runoff production in a shallow soil Canadian Shield basin. *Water Resources Research*. 31 (5), 1291-1304.
- Pittenger, M. A., Marsaglia, K. M., and M. E. Bickford, 1994. Depositional history of the middle Proterozoic Castner Marble and basal Mundy Breccia, Franklin Mountains, West Texas. *Journal of Sedimentary Research*. 64B (282-297).
- Reynolds, W.D. and D.E. Elrick. 1991. Determination of hydraulic conductivity using a tension infiltrometer. *Soil Science Society of America Journal*. 55:633-639.
- Richards, B. G., Couthard, M. A., and C. T. Toh, 1981. Analysis of slope stability at Goonyella Mine. *Canadian Geotechnical Journal*. 18, 179-194.
- Roberts, T. T., Parkison, G. A., and V. T. McLemore, 1990. Geology of the Red River district, Taos County, New Mexico: New Mexico Geological Society, Guidebook 41, p. 375-380.
- Robertson Geoconsultants, Inc., 1997. Report to Molycorp Inc., Study of potential seepage proposed Guadalupe Mountain tailings area. Prepared for Molycorp, Inc. Report No. 52002/1.
- Robertson GeoConsultants Inc., 2000. Interim Mine Site Characterization Study, Questa Mine, New Mexico, RGC Report 052008/10 prepared for Molycorp Inc., November 2000.
- Robertson GeoConsultants Inc., 2001. Initial Soil Atmosphere Modeling For Mine Rock Piles, Questa Mine, New Mexico, RGC Report 052008/14 prepared for Molycorp Inc., January 2001.

- Robertson GeoConsultants Inc., 2003. 1st Year Modeling Report Water Balance Study For Mine Rock Piles, Questa Mine, New Mexico, RGC Report 052015/2 prepared for Molycorp Inc., March 2003.
- Schapp, M., 1999. Predicting Soil Hydraulic Parameters from Basic Soil Data. Rosetta Lite Version 1.0, U. S. Salinity Laboratory, Riverside, CA.
- Shannon, H.R., Sigda, J.M., Van Dam, R.L., Hendrickx, J.M.H., and V.T. McLemore, 2005. Thermal Camera Imaging of Rock Piles At The Questa Molybdenum Mine, Questa, New Mexico. *American Society for Mining Reclamation (ASMR)*, June 18-23, 2005, Breckenridge, CO.
- Shannon, W. M., Barnes, C. G., and M. E. Bickford, 1997. Grenville magmatism in west Texas: Petrology and geochemistry of the Red Bluff granitic suite. *Journal of Petrology*. 38, 1279-1305.
- Simunek, J., M. Sejna, and T. van Genuchten, 1999. The HYDRUS-2D software Package for simulating the two-dimensional movement of water, heat, and multiple solutes in variably saturated media, Version 2.0, U.S. Salinity Laboratory, agricultural research Service, U.S. Dept. of Agriculture, Riverside, CA, USA, April, 1999.
- Sklash, M. G., Stewart, M. K., and A. J. Pierce, 1986. Storm runoff generation in humid headwater catchments 2. A case study of hillslope and low-order stream response. *Water Resources Research*. 22, 1273-1282.
- Smith, L. and D. S. Chapman, 1983. On the thermal effects of groundwater flow 1. Regional scale systems. *J. of Geophysical Research*. 88 (B1), 593-608.
- Soil Measurement Systems, 2001. Tension Infiltrometer Users Manual. Tucson, AZ.
- Soilmisture Equipment Corporation, 2000. Operating Instructions Model 2900F1 "Quick Draw" Soilmoisture Probe. Santa Barbara, CA.
- Souder Miller and Associates. 2000. 1999 Hydrogeologic investigation, Questa, New Mexico. Prepared for Molycorp Inc.
- Speck, R. C., Huang, S. L., and E. B. Kroeger, 1993. Large-scale slope movements and their affect on spoil-pile stability in Interior Alaska. *International Journal of Surface Mining and Reclamation*. 7 (4), 161-166.
- SRK, 2004, Hydrogeologic characterization of the caving induced subsidence areas: SRK project Number 009216.00, 184 p.

- Stauffer, P. H., and W. J. Stone, 2005. Surface Water-Groundwater Connection at the Los Alamos Canyon Weir Site: Part 2. Modeling of Tracer Test Results. *Vadose Zone Journal*. 4, 718-728.
- Stumm, W., and Morgan, J. J., 1981. *Aquatic Chemistry - An Introduction Emphasizing Chemical Equilibria in Natural Waters*. John Wiley & Sons, Inc., 470 p.
- Tachie-Menson, S., 2005. Characterization of Acid Drainage Potential from the Goathill North Rock Pile of the Questa Molybdenum Mine, Questa, New Mexico - Initial Results. *Geological Society of America Abstracts with Programs*, 37(7): 349.
- Tachie-Menson, S., 2006. Characterization of Acid-Producing Potential and Investigation of Its Effect on Weathering of the Goathill North Rock Pile at the Questa Molybdenum Mine, Questa, New Mexico. M. S. Thesis, New Mexico Institute of Mining and Technology.
- Terzaghi, K., Peck, R.B. and G.M Mesri, 1996. *Soil Mechanics in Engineering Practice*. John Wiley and Sons, Inc., New York, 549 pp.
- Tesarik, D. R. and R. W. McKibbin, 1999. Material Properties Affecting The Stability of a 50-Year-Old Rock Dump in an Active Mine. Report of Investigation, U. S. Department of Health and Human Services.
- Uchinda, t., Asano, Y., Ohte, N., and T. Mizuyama, 2003. Seepage area and rate of bedrock groundwater discharge at a granitic unchanneled hillslope. *Water Resources Research*. 39 (1), 1018, doi: 10.1029/2002WR001298.
- URS Corporation. 2001. Molycorp Questa Mine site-wide comprehensive hydrologic characterization report. Prepared for Molycorp Inc.
- US EPA Report, Conceptual Model and RI/FS SOW, Callhan Mining Superfund Site, Brookville, Maine. Contract No. 68-W6-0042.
- Vail S. G., 1987. Geological Evaluation of the Guadalupe Mountain Area, Taos County, New Mexico, Report to Molycorp Inc., Questa Division, March 16, 1987, 9 pages.
- Van Dam, J.C., J.M.H. Hendrickx, H.C. van Ommen, M.H. Bannink, M.Th. van Genuchten, and L.W. Dekker. 1990. Water and solute movement in a coarse-textured water-repellent field soil. *Journal of Hydrology*, 120, 359-379.
- Van Zyl, D., Sassoon, M., Digby, C., Fleury, A. M., and Kyeyune, S., 2002. Mining For the Future: Appendix A, Large Volume Waste Working Paper:

International Institute for Environment and Development, 31.

- Vesselinov, V. V., Keating, E. H., and G. A. Zyvoloski, 2002. Analysis of model sensitivity and predictive uncertainty of capture zones in the Espanola Basin regional aquifer, Northern New Mexico. LA-UR-02. Los Alamos National Laboratory, Los Alamos, NM.
- Weiler, M., and J. McDonnell, 2004. Virtual experiments: a new approach for improving process conceptualization in hillslope hydrology. *Journal of Hydrology*. 285, 3-18.
- Wels, C., O'Kane, M., and S. Fortin, 2001. Storage Cover Test Plot Study for Questa Tailings Facility, New Mexico. Paper accepted to the 18th Annual National Meeting, American Society for Surface Mining and Reclamation, June 3-7, 2001, Albuquerque, New Mexico.
- Wels, C., O'Kane, M., Fortin, S., and D. Christensen, 2001. Infiltration Test Plot Study for Waste Rock at Questa Mine, New Mexico. Paper accepted to the 18th Annual National Meeting, American Society for Surface Mining and Reclamation, June 3-7, 2001, Albuquerque, New Mexico.
- Winograd, I. J., 1959. Ground-Water Conditions and Geology of Sunshine Valley and Western Taos County, New Mexico. United States Geological Survey, Technical Report No. 12., 70 pp.
- Willgoose, G. and S. Riley, 1998. The Long-Term Stability of Engineered Landforms of The Ranger Uranium Mine, Northern Territory Australia: Application of a Catchment Evolution Model. *Earth Surface Processes and Landforms*. 23, 237-259.
- Williams, D. J. and N. A. Curry, 2002. Engineering Closure of an Open Pit Gold Operation in a Semi-Arid Climate. *International Journal of Surface Mining, Reclamation and Environment*. 16 (4), 270-288.
- Wooding, R. A., 1968. Steady infiltration from a shallow circular pond. *Water Resources Research*. 4, 1259-1273.

APPENDIX A. EVAPORATION RATES.

The following appendix is a literature review of evaporation rates at the Questa mine site and was presented as a report to Molycorp Inc. on July 15, 2004 for the completion of Task 1.11.2.2.

From: Heather Shannon

To: Virginia McLemore, team leader, Bureau of Geology

RE: Literature Review for Evaporation Rates at the Questa Mine Facilities, Questa, New Mexico

(1) Storage Cover Test Plot Study for Questa Tailings Facility, New Mexico.

This report includes information in the site description indicating that the estimated annual pan evaporation for the region near the tailings facility is approximately 65-70 inches. After installing a meteorological station, the cumulative potential evapotranspiration was estimated to be 14.04 inches from Aug. 9, 2000 to Jan. 6, 2001 for stations TP 1,2, and 3.

(2) Infiltration Test Plot Study For Mine Rock Piles At Questa Mine, New Mexico.

This report includes estimates of lake evaporation (large free-water surface) and actual evapotranspiration (land surface evaporation and transpiration from vegetation) for the mine site at ~1000 mm and 400 mm (this value was reported in Report No. 052008/10). The cumulative potential evaporation was calculated using the Penman method for three test plot meteorological stations, based on daily average values in the three different microclimates. TP-4, located on the upper bench of the Sugar Shack South rock pile, at 2820 m elevation had 401.3 mm of cumulative potential evaporation. TP-5, located on the top of the Capulin rock pile, at 2990 m elevation had 317.5 mm of cumulative potential evaporation. Finally, TP-6/TP-7, both located on the lower bench of the Sugar Shack South rock pile had ~356.8 mm of cumulative potential evaporation.

(3) Interim Mine Site Characterization Study, Questa Mine, New Mexico, Report No. 052008/10.

This report includes two estimates of evaporation on the mine site. One site refers to evaporation over a large free-water surface and the other site refers to a vegetated land surface (this calculation includes transpiration from vegetation). The evaporation rates were estimated/calculated using the WREVAP computer model by providing humidity, air temperature, and global solar radiation as inputs. The average annual lake evaporation was estimated to be 40 inches. The average annual evapotranspiration was estimated to be 15 inches on the land surface.

(4) Initial Soil Atmosphere Modeling For Mine Rock Piles, Questa Mine, New Mexico, Report No. 052008/14.

Evaporation was estimated at the Questa mill site climate station by using the Penman equation. The calculation required daily average air temperature, humidity, wind movement and solar radiation. This estimation technique involves making numerous calculations and a program developed by the EPA called WDMUtil was used to assist in making the estimations. The average annual pan evaporation determined for the period between 1995-2000 at the mill site was 56 inches. Other information

regarding the validation of the WDMUtil program is available in the paper. The report also includes a summary of estimations made for a 6-month period between Aug. 8, 2000 and Jan. 8 2001. The data includes cumulative potential evaporation calculated from the average meteorological data using the Penman method. TP-5, at 9800 ft had 21.0 inches of cumulative potential evaporation. TP-4, at 9250 ft had 26.5 inches of cumulative potential evaporation. TP-6/TP-7 had 19.7 inches of cumulative potential evaporation or 23.3 inches (this value was an estimated total from interpolation of missing data).

(5) 1st Year Modeling Report, Water Balance Study For Mine Rock Piles, Questa Mine, New Mexico, Report No. 052015/2.

This report includes a summary of the four lysimeter test plots for the first year of monitoring (July 2000 – July 2001). Cumulative potential evaporation reported in inches for each station is as follows: TP-4 = 47.8, TP-5 = 36.7, TP-6/TP-7 = 45.0. The report also includes simulated water balance components from Aug. 8, 2000 – Jan. 8, 2001 with the actual evapotranspiration (in inches) estimated as follows; TP-4 = 6.54, TP-5 = 3.43, TP-6 = 4.44, and TP-7 = 4.90. The report also includes modeling results for test plots from Nov. 15, 2000 – July 23, 2001 where several model runs were made for the actual evapotranspiration (in inches) for TP-5 and TP-6. The results are presented below in Table A-1.

Table A- 1. The results from the 1st Year Modeling Report, Water Balance Study For Mine Rock Piles, Questa Mine, New Mexico, Report No. 052015/2. AET represents the actual evapotranspiration in inches.

Test Plots	Run Name	AET (in)
TP-5	Run A	8.3
	Run E	6.22
	Run M	7.01
TP-6	Run A	8.89
	Run B	6.33

REFERENCES

Wels, C., O'Kane, M., and S, Fortin, 2001. Storage Cover Test Plot Study for Questa Tailings Facility, New Mexico. Paper accepted to the 18th Annual National Meeting, American Society for Surface Mining and Reclamation, June 3-7, 2001, Albuquerque, New Mexico.

Wels, C., O'Kane, M., Fortin, S., and D, Christensen, 2001. Infiltration Test Plot Study for Waste Rock at Questa Mine, New Mexico. Paper accepted to the 18th Annual National Meeting, American Society for Surface Mining and Reclamation, June 3-7, 2001, Albuquerque, New Mexico.

Robertson GeoConsultants Inc., 2000. Interim Mine Site Characterization Study, Questa Mine, New Mexico, RGC Report 052008/10 prepared for Molycorp Inc., November, 2000.

Robertson GeoConsultants Inc., 2001. Initial Soil Atmosphere Modeling For Mine Rock Piles, Questa Mine, New Mexico, RGC Report 052008/14 prepared for Molycorp Inc., January, 2001.

Robertson GeoConsultants Inc., 2003. 1st Year Modeling Report Water Balance Study For Mine Rock Piles, Questa Mine, New Mexico, RGC Report 052015/2 prepared for Molycorp Inc., March, 2003.

**APPENDIX B. COMPARISON ANALYSIS OF CALCULATED PET FROM
WEATHER STATION DATA IN NORTHERN NEW MEXICO.**

The following appendix presents the results from a comparison study between PET values calculated by consultants and by myself. The PET estimations were based upon data collected at weather stations on the Molycorp, Inc. property

Introduction

An in-depth characterization of the Questa molybdenum mine site led to the installation of several on-site meteorological stations. The on-site meteorological stations were installed so that predictive models could be developed to most accurately portray the mine property. In order to develop a better understanding of the water balance of the system, it is important to estimate daily evapotranspiration throughout the year. A four-year record of meteorological data was obtained from three of the weather stations on-site to be used in hydrological models. Each of the data files consists of calculated values of potential evapotranspiration ET from consultants using the Penman-Monteith method and the Priestly-Taylor method. The three stations were installed in 2000 and are located on the upper bench of the Sugar Shack South rock pile (TP-4, elevation 2820 m, Figure B-1), on the top of the Capulin rock pile (TP-5, elevation 2990 m, Figure B1), and on the lower bench of the Sugar Shack South rock pile (TP-6/7, elevation 2660 m, Figure B-1). An analysis of the meteorological data was performed by re-calculating the reference evapotranspiration (ET_O) and potential evapotranspiration (PET) for each site in addition to evaluating the integrity of the weather station data. The purpose of the following analysis is to successfully apply methods from the ASCE Standardized Reference ET Equation manual (Walter, 2001) and the FAO Irrigation and Drainage Paper, No. 56, Crop Evapotranspiration (Allen et al., 1998) using the meteorological data to calculate the ET_O and PET for each of the three stations.

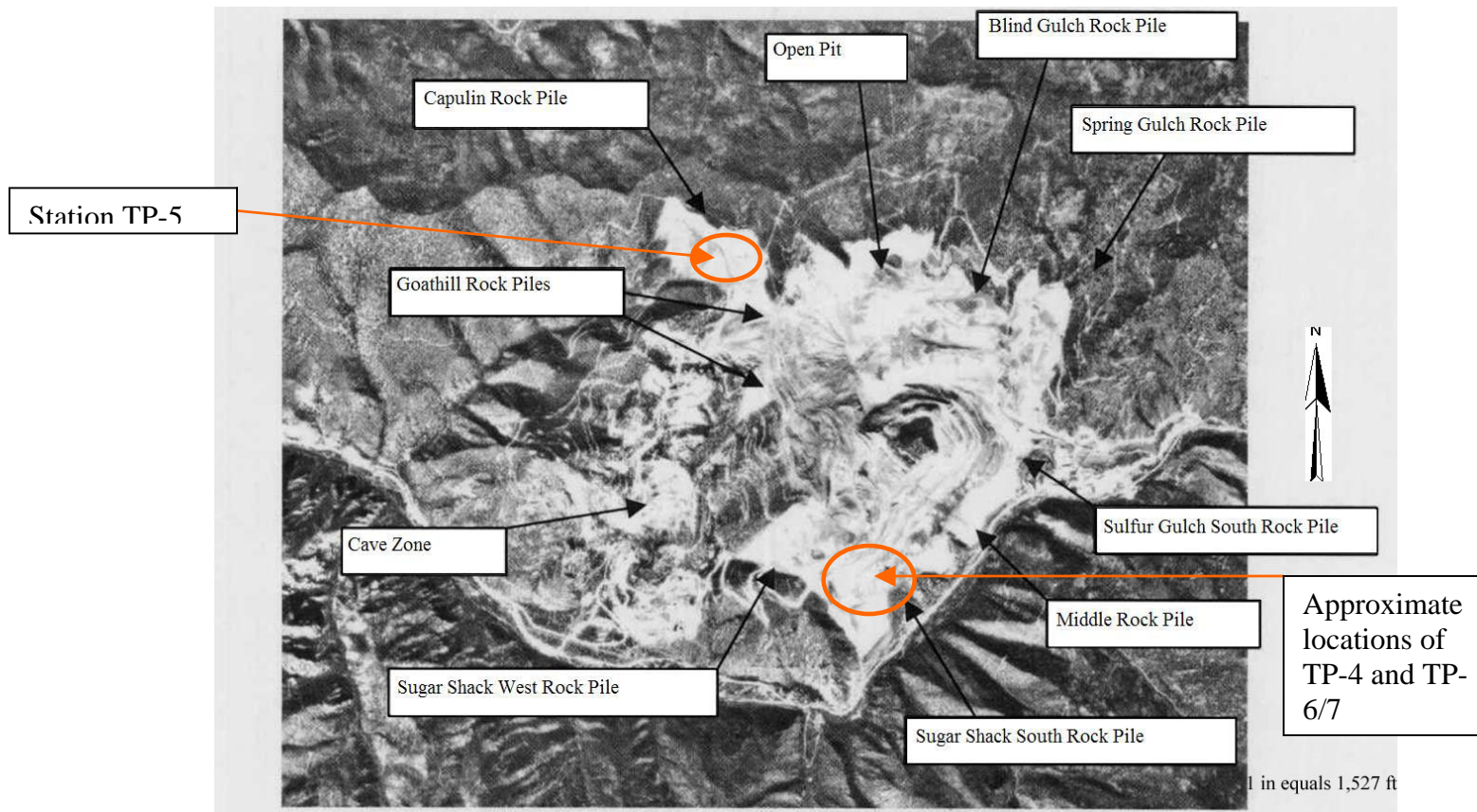


Figure B- 1. The approximate locations of the meteorological stations are shown in the aerial photograph of the Molycorp property.

Site Description

The Questa molybdenum mine is located in a region with high topographic relief. The mine ranges in elevation from approximately 7550 ft along the Red River to more than 10750 ft at a peak dividing the Red River and Cabresto Creek drainage basins. Steep sided incised valleys characterize much of the mine property with grades typically from 2:1 to 1.4:1. Valleys in the region consist of weathered, hydrothermally altered, brecciated, and erosive rocks (locally referred to as hydrothermally scars) (Robertson GeoConsultants, 2000).

The rock piles were created by end dumping excess rock material from the open pit mining over the ridges into the valleys (some of which consisted of underlying hydrothermal scars). Each rock pile is made up of material mined from the open pit, but a clear record has not been found to correlate the stratigraphic units to the rock fragments that were dumped on to each pile. However, the general stratigraphy of the open pit consisted of Amalia tuff (from rhyolitic eruptions 25.7 million years ago) and andesite (from interbedded lava flows 27 million years ago) from the top layers and aplites and granite in the lower portion (Carpenter, 1968; Czamanske et al., 1990). The average size of the blasted rock from the pit, dumped onto the rock piles varied from 1 to 5 inches in size (Robertson GeoConsultants, 2000).

Methods

The meteorological data obtained from three weather stations on the Molycorp mine property was used in this study to estimate the ET_0 and PET using methods

outlined in the ASCE Standardized Reference ET Equation manual (Walter et al., 2001) and the FAO Irrigation and Drainage Paper, No. 56, Crop Evapotranspiration (Allen et al., 1998) and to estimate the PET by the Priestly Taylor method.

In order to calculate the ET_0 using the Penman-Monteith method, a series of equations were used to calculate the mean air temperature, atmospheric pressure, psychrometric constant, slope of saturated vapor pressure-temperature curve, saturated vapor pressure, actual vapor pressure, and wind profile and are presented following the text. These calculations of the ET_0 were made by assuming that the vegetation surrounding the weather station was a short crop and by making numerous other assumptions presented in Table B-1. We know that the surfaces of the rock piles are not vegetated, but there is not sufficient public documentation, which describes the conditions surrounding each weather station. Therefore, we made the assumption by using a short reference crop in order to make the calculations using the ASCE method (Walter et al., 2001) and the FAO publication (Allen et al., 1998). In addition, there is little documentation describing the weather station set-up, including the height of air temperature measurements and relative humidity measurements (the height of wind speed measurements was obtained from personal communication with Golder Associates consultants).

Table B- 1. Assumptions of values for Penman-Monteith Calculation

Reference Vegetation Height	0.12 m
Height of air temperature or humidity	1.5 - 2.5 m
Height of windspeed measurement	1.89 m (personal communication)
Zero plane displacement height	0.08 m
Latent heat of vaporization	2.45 MJ/kg
Surface resistance, r_s daily	70 s/m

The calculations of the PET were made by assuming that $r_s=0$. This assumes that the surface is well-watered and is often referred to as the ET from a free water surface. This calculation was made using a slightly modified version of the Penman-Monteith equation (equations are presented following the text) partially outlined in the FAO Irrigation and Drainage Paper, No. 56, Crop Evapotranspiration (Allen et al., 1998).

The calculations of PET using the Priestly-Taylor method were simplified by assuming an adjustment factor alpha of 1.26. The equations used to calculate the input parameters and the PET by the Priestly-Taylor method are described in following the text.

Finally, the weather station data was briefly examined for integrity by visual and semi-quantitative inspection. The dew point temperature was calculated for the daily data using the actual vapor pressure, which was calculated using the relative humidity data (see equations B1 and B9 following the text). The dew point temperature was then plotted along with the mean air temperature, minimum air temperature and the mean relative humidity for each day (example from FAO, Annex 5, p. 254).

Results

The results of the calculations of ET_O and PET (by Penman-Monteith methods) are shown in a series of figures described below. The results from the calculations for station TP-5 indicate a strong correlation between the calculated ET_O values and the calculated PET by the consultants (correlation = 0.92, Figure B-2),

whereas the results from the PET calculated in the analysis indicate poor correlation with the calculations made by the consultants (correlation = 0.17, Figure B3). Figure B-4 shows the two calculated values from this analysis (ET_O and PET) along with the consultants' values across the first two years of meteorological data. The figure illustrates that the calculated PET is always greater than ET_O and the consultants' PET. The results from the calculations for station TP-4 have a similar pattern. The results for this station also indicate a strong correlation between ET_O and the consultants' PET (correlation = 0.87, Figure B-5) and a poor correlation between the calculated PET in this analysis and the consultants' PET (correlation = 0.20, Figure B-6). In addition, the calculated PET is greater than the ET_O and the consultants' PET (Figure B-7). The results from the third station, TP-6/7 appear to have a slightly different trend. The correlation between the ET_O and the consultants PET remains strong (correlation = 0.92, Figure B-8), but the correlation between the calculated PET and the consultants' PET is stronger (correlation = 0.67, Figure B-9) than at the other stations. The trend is also apparent in Figure B-10, which shows that the calculated PET in this study is not always greater than the ET_O and the consultants' PET.

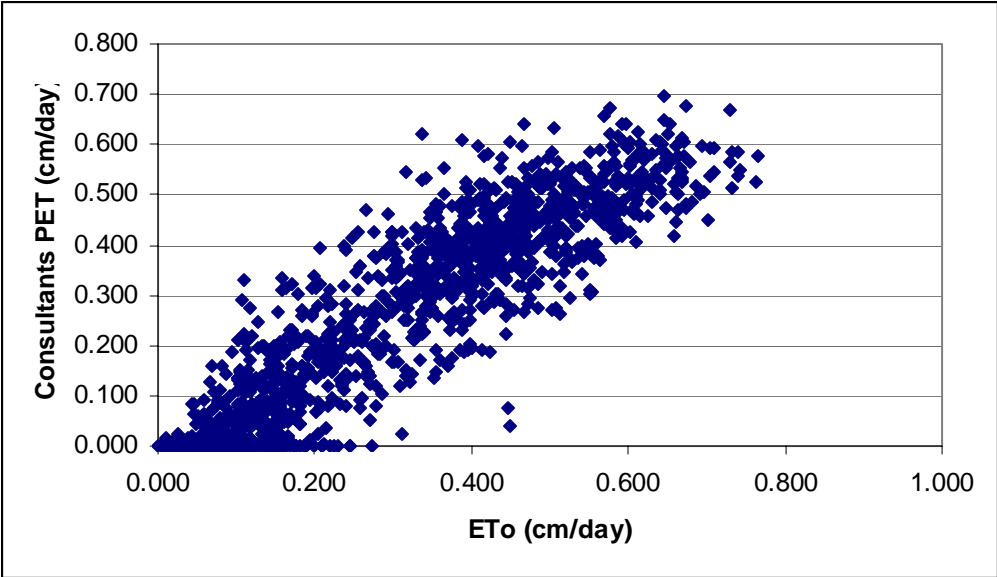


Figure B- 2. ET_0 vs. PET (consultants' values) for station TP-5.

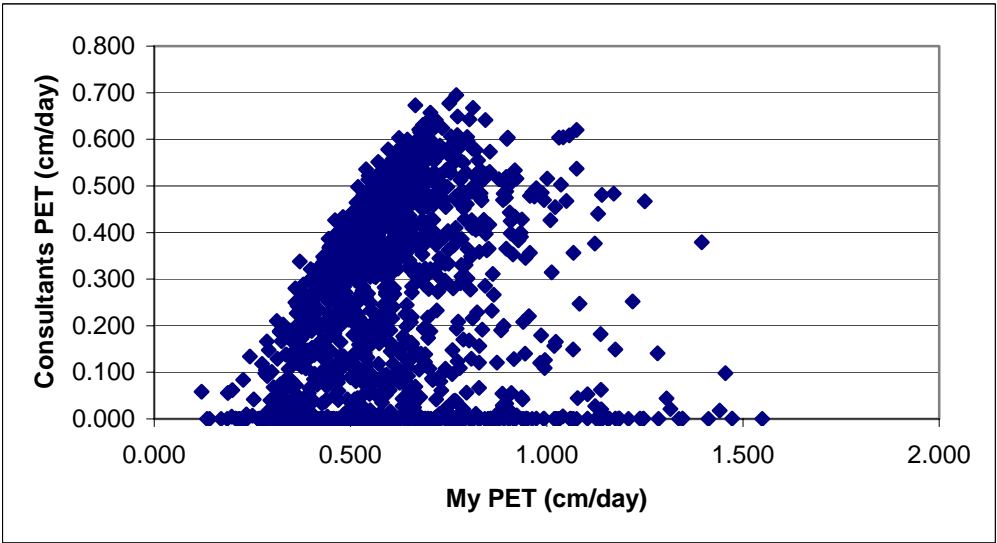


Figure B- 3. PET vs. PET (consultants' values) for station TP-5.

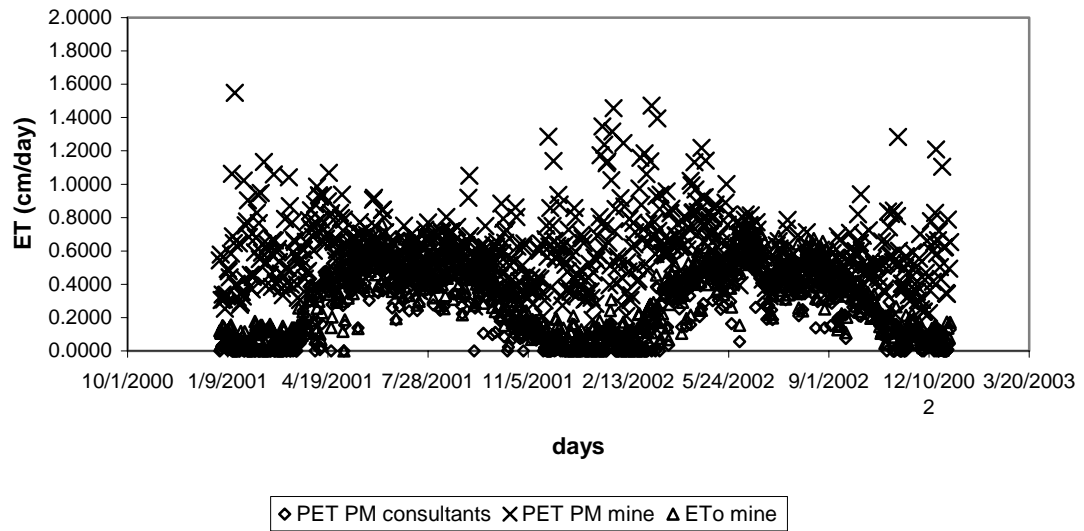


Figure B- 4. Calculated ET_0 , PET, and PET from consultants between January 1, 2000 and December 31, 2002 using data from meteorological station TP-5.

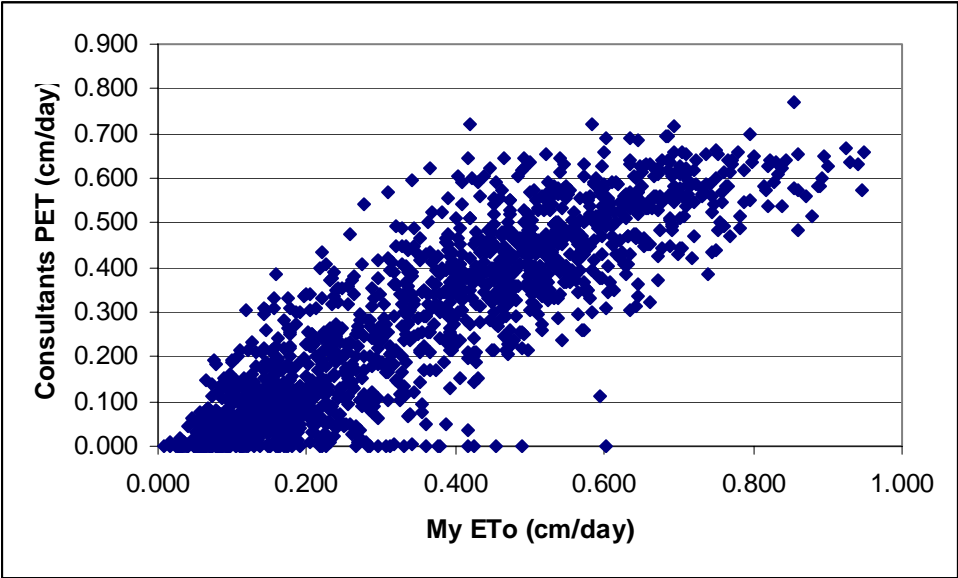


Figure B- 5. ET_0 vs. PET (consultants' values) for station TP-4.

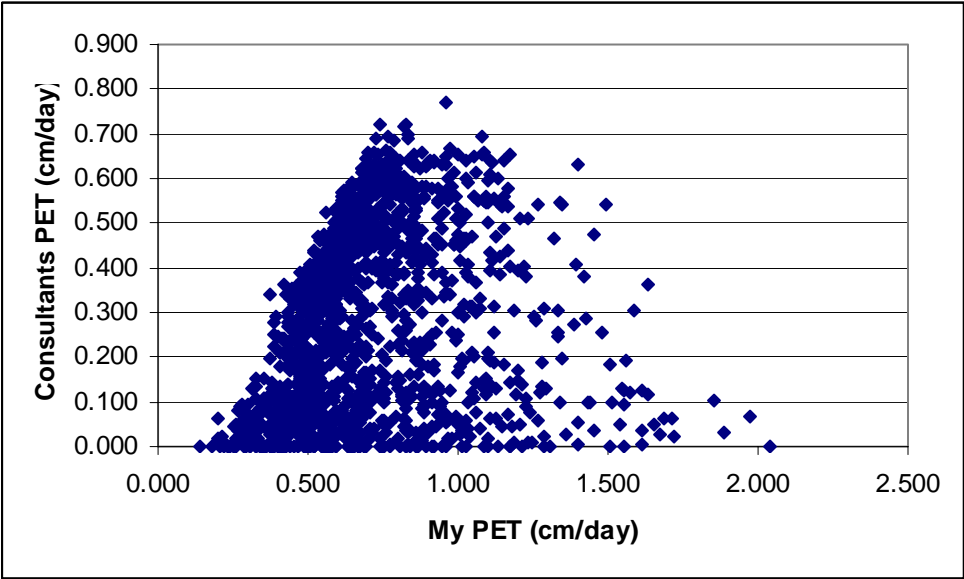


Figure B- 6. PET vs. PET (consultants' values) for station TP-4.

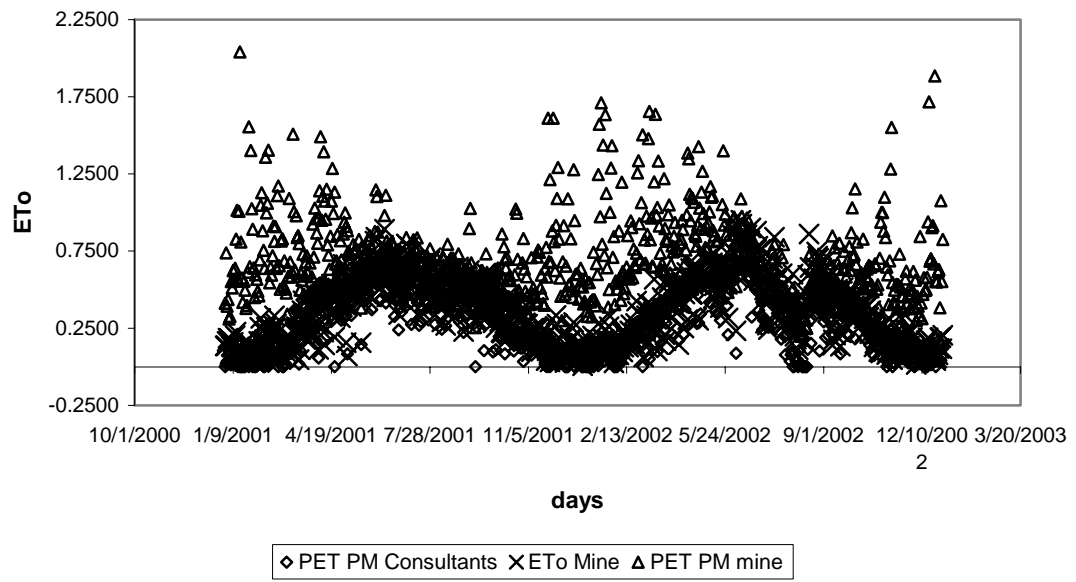


Figure B- 7. Calculated ET₀, PET, and PET from consultants for the meteorological data for station TP-4.

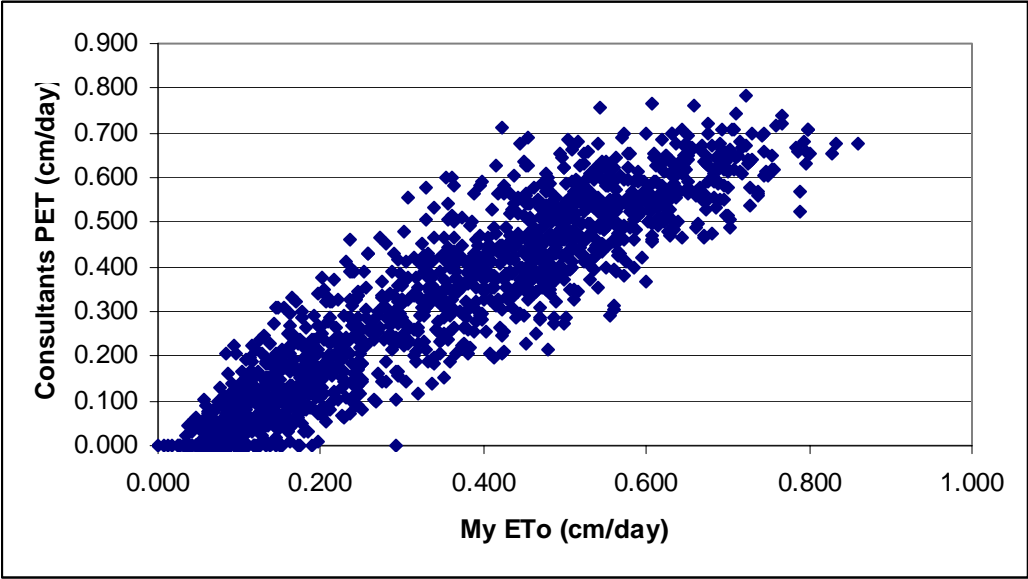


Figure B- 8. ET₀ vs. PET (consultants' values) for station TP-6/7.

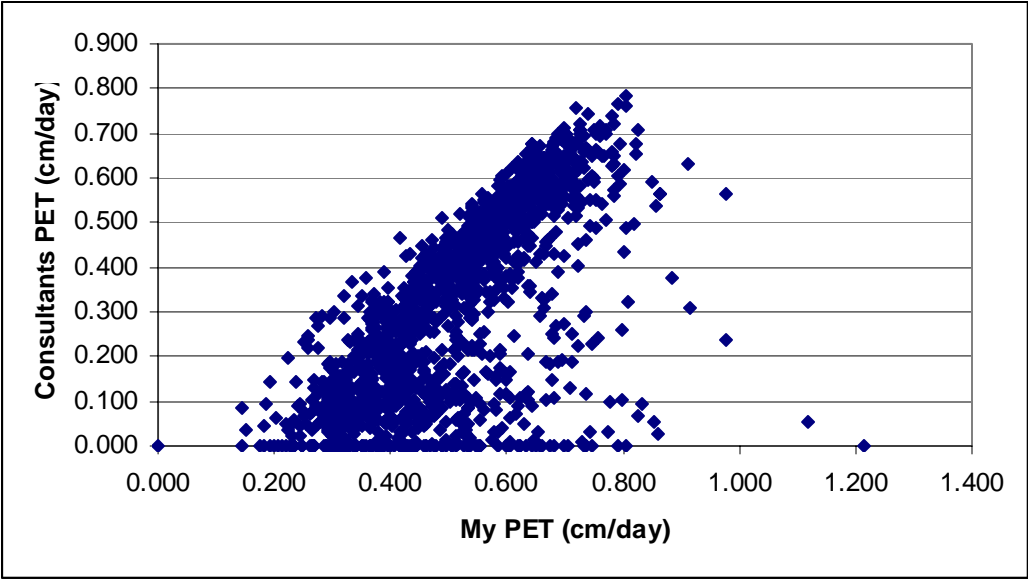


Figure B- 9. PET vs. PET (consultants' values) for station TP-6/7.

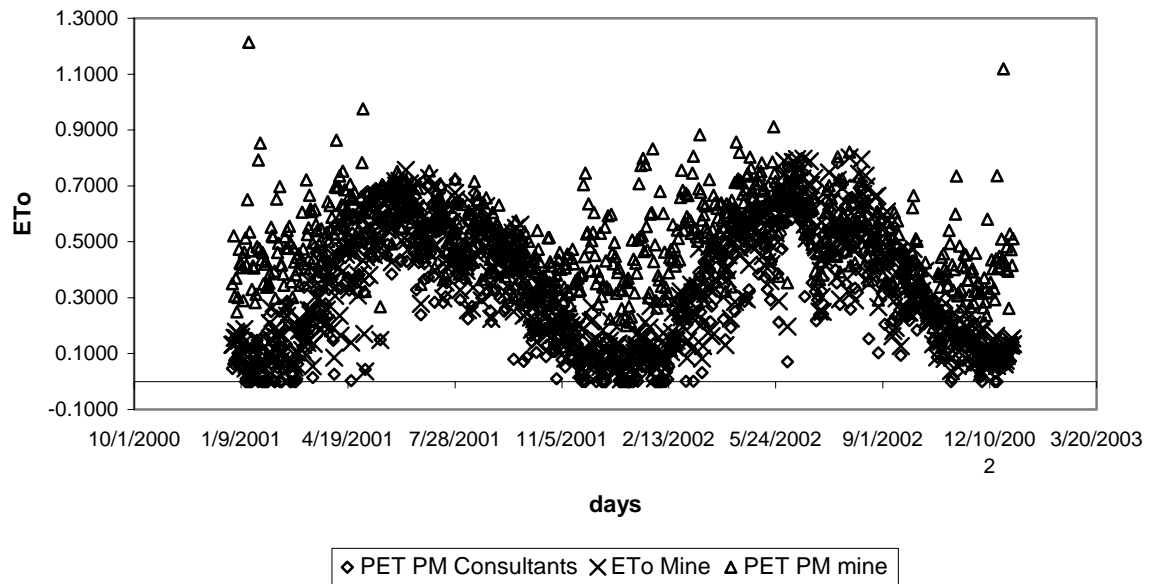


Figure B- 10. Calculated ET_0 , PET, and PET from consultants for the meteorological data for station TP-6/7.

The results from the calculations of the PET using the Priestly-Taylor method showed strong correlation with the consultants calculated PET values. The correlation between the consultants PET Priestly-Taylor and my calculated Priestly-Taylor was greater than 0.98 for each station. Figures B-11, B-12, and B-13 show the relationships between the calculated values at each station.

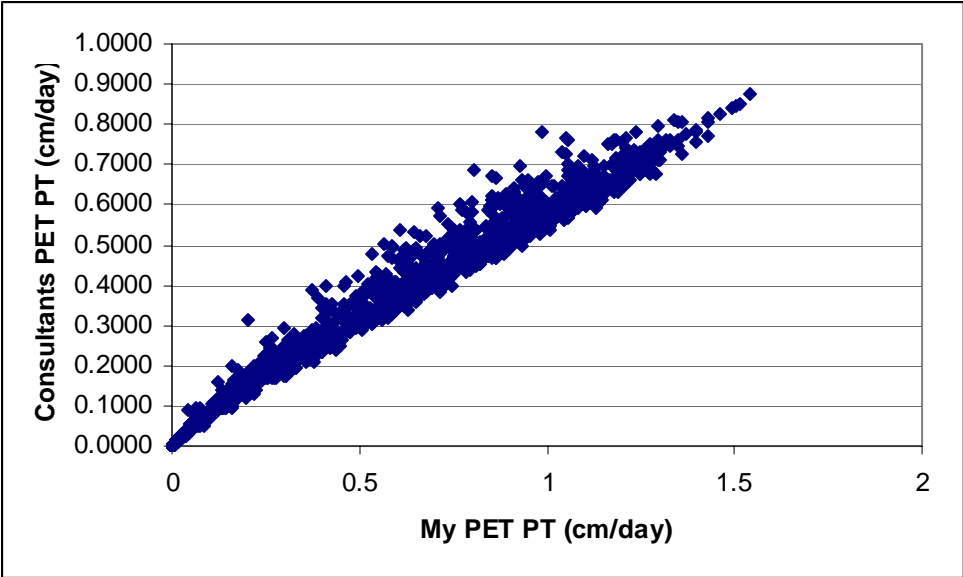


Figure B- 11. Calculated PET using Priestly-Taylor methods for station TP-5 data.

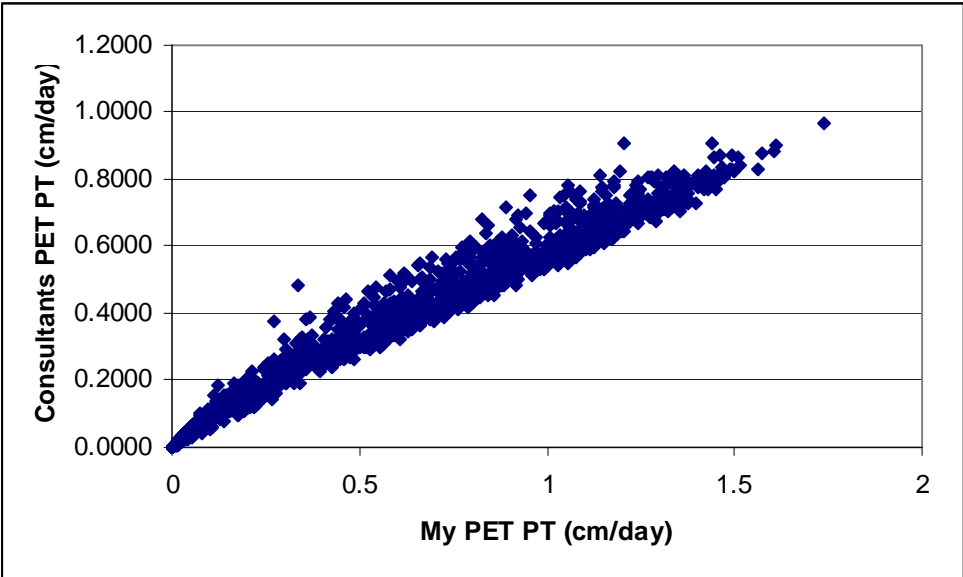


Figure B- 12. Calculated PET using Priestly-Taylor methods for station TP-4.

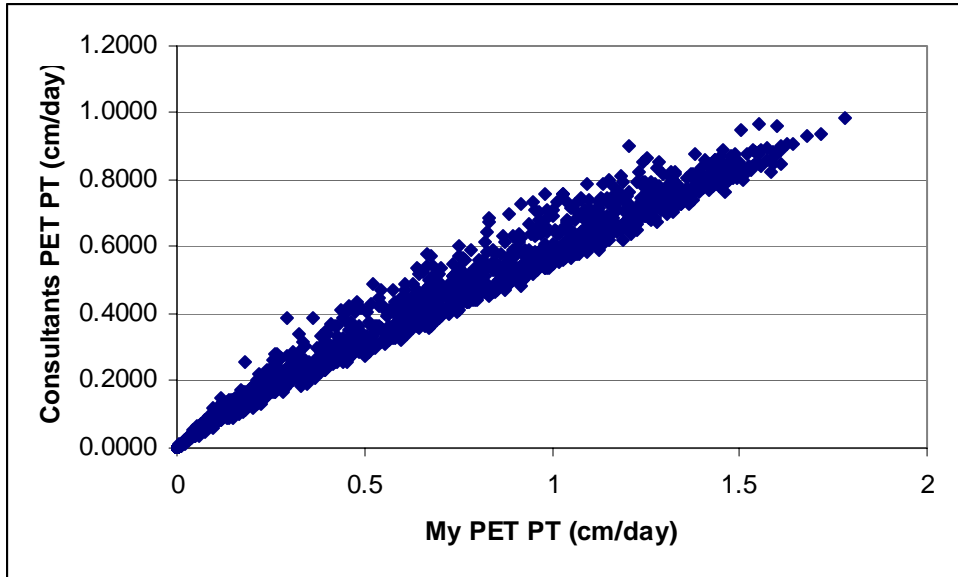


Figure B- 13. Calculated PET using Priestly-Taylor method for station TP-6/7.

The results from the analysis of the integrity of the relative humidity measurements are shown in figures following the list of equations. The results show significant fluctuations in the annual average relative humidity. Although there are great fluctuations in the relative humidity throughout each year, it does appear that in general there is a drier period which occurs between late April or early May through late June. This dry period also occurs in the month of August, but it is not as severe. These dry periods coincide with elevated mean air temperature.

Discussion

The results from the calculations of ET_0 and PET, lead to many more questions about how the calculations of PET were made by the consultants. The results presented in Figures B-2 through B-10 indicate that there is a significant

amount of scatter within the calculated values. It appears that the technique that was used to calculate the PET by the consultants leads to an estimate that is closer to the ET_O calculated in this study. However, there does not appear to be a systematic error between the calculations of the ET_O in this study and the PET calculated by the consultants, which could possibly indicate that the consultants made corrections for the height of air temperature measurements, the height of humidity measurements, and possibly the zero displacement height. However, the consultants may simply have used a different method to calculate one or more of the input variables to the Penman-Monteith equation.

The results from the calculations of PET using the Priestly-Taylor method indicate that either the slope of saturated vapor pressure-temperature curve, psychrometric constant, net radiation, and/or the soil heat flux have been estimated differently. The calculated PET values were very similar, but there was still scatter evident in the data.

The daily dew point temperatures were calculated using equation B-12 in the list of equations following the text. These calculations involved using the actual vapor pressure, which was calculated using the minimum and maximum relative humidity. The dew point temperature is expected to be very similar to the minimum air temperature that would be recorded in the morning when dew is present of the land surface (Allen, 1996). Therefore, the minimum air temperature was plotted with the dew point temperature as well as the mean air temperature and relative humidity. The dew point temperature is generally less than the minimum air temperature at all of the stations. The dew point temperature drops significantly below the minimum air

temperature (approximately 20°C) during the same periods when the relative humidity is low, between late April or early May through late June. The conclusions about the trends in the relative humidity data could possibly make sense for the region that is being studied. There is typically less rainfall in the early spring in this region, leading to less moisture in the air. However, it seems unlikely that it would be as dry as the measurements indicated (averaging approximately 20% in this spring period). Also, the weather stations are located in a mountainous region that is not as arid as some of the surrounding parts of the state of New Mexico. Due to this fact, it seems that the relative humidity measurements are relatively low for the three stations. According to Allen (1996), relative humidity sensors are often plagued with problems, so it would not be unusual if the sensors at the weather stations propagated errors in the measurements.

Conclusions

After analyzing the data by replicating the calculations of evapotranspiration using the Penman-Monteith method, the results are inconclusive. It appears that the consultants were actually calculating the reference ET (ET_0) and not the potential ET (PET) as named in the spreadsheet. Although the calculated values of ET_0 were closer to those calculated by the consultants, the values were not a perfect match and did not show a systematic error. Therefore, it is difficult to determine exactly where the discrepancies lie in the calculations using the Penman-Monteith method.

The Priestly-Taylor method was also used to calculate PET and compare results to the calculations made by consultants. After making these calculations it

seems more apparent that one of the parameters that could be leading to scatter in the calculations could be the slope of saturated vapor pressure-temperature curve, psychometric constant, net radiation, and/or the soil heat flux. The consultants refer to the net radiation as “corrected” in the weather station data file. It is unclear what this means, but it could possibly indicate that assumptions have been made in the calculations of PET that are not made obvious by the excel file. The Priestly-Taylor method served as an additional analysis tool, but led to more questions about the data.

Finally, the integrity of the weather station data was examined to identify weaknesses in the data set. The relative humidity and dew point temperatures were examined in the most detail, and they indicated that there were probably errors in the humidity measurements because the values seemed to be quite low year round for this mountainous region.

EQUATIONS

Reference Evapotranspiration (ET_O)

$$ET_O = \frac{0.408\Delta(R_n - G) + \gamma \frac{C_n}{T + 273} u_2 (e_s - e_a)}{\Delta + \gamma(1 + C_d u_2)} \quad (B1)$$

(Allen, 1996 and Allen et al., 1998)

where

- R_n = calculated net radiation at the crop surface (MJ/m²)
- G = soil heat flux density at soil surface (MJ/m²)
- T = mean daily temperature at 1.5 m height (°C)
- u_2 = mean daily wind speed at 2 m height (m/s)
- e_s = saturated vapor pressure (kPa) at 1.5 m
- e_a = mean actual vapor pressure (kPa) at 1.5 m
- Δ = slope of the saturation vapor pressure - temperature curve (kPa/°C)
- γ = psychrometric constant (kPa/°C)
- C_n = numerator constant, 900 mm/day for daily time step
- C_d = denominator constant, 0.34 MJ/m²day for daily time step
- ET_O is in mm/day

Mean Air Temperature (T)

$$T = \frac{T_{\max} + T_{\min}}{2} \quad (B2)$$

(Allen, 1996 and Allen et al., 1998)

where T is in °C

Atmospheric Pressure (P)

$$P = 101.3 \left(\frac{293 - 0.0065z}{293} \right)^{5.26} \quad (B3)$$

(Allen, 1996 and Allen et al., 1998)

where z = weather site elevation above mean sea level (m)
 P is in kPa

Psychrometric Constant (γ)

$$\gamma = 0.000665P \quad (\text{B4})$$

(Allen, 1996 and Allen et al., 1998)

where P = atmospheric pressure in kPa
 γ is in kPa/°C

Slope of Saturated Vapor Pressure-Temperature Curve (Δ)

$$\Delta = \frac{2504 \exp\left(\frac{17.27T}{T + 237.3}\right)}{(T + 237.3)^2} \quad (\text{B5})$$

(Allen, 1996 and Allen et al., 1998)

where T = daily mean air temperature (°C)
 Δ is in kPa/°C

Saturation Vapor Pressure (e_s)

$$e_s = \frac{e^\circ(T_{\max}) + e^\circ(T_{\min})}{2} \quad (\text{B6})$$

(Allen, 1996 and Allen et al., 1998)

where $e^\circ(T) = 0.6108 \exp \frac{17.27T}{T + 237.3}$
 e° is in kPa
 T is in °C

Actual Vapor Pressure (e_a)

$$e_a = \frac{e^\circ(T_{\min}) \frac{RH_{\max}}{100} + e^\circ(T_{\max}) \frac{RH_{\min}}{100}}{2} \quad (\text{B7})$$

(Allen, 1996 and Allen et al., 1998)

where RH_{\min} and RH_{\max} are percentages

Soil Heat Flux Density (G)

$$G_{\text{day}} = 0 \quad (\text{B8})$$

(Allen, 1996 and Allen et al., 1998)

For daily periods

Wind Profile (u_2)

$$u_2 = u_z \left[\frac{4.87}{\ln(67.8z_w - 5.42)} \right] \quad (\text{B9})$$

(Allen, 1996 and Allen et al., 1998)

where u_2 = windspeed at 2 m
 u_z = measured windspeed at z_w
 z_w = height of windspeed measurement above ground surface (m)

Potential Evapotranspiration (PET)

$$PET = \frac{\Delta(R_n - G) + \rho_a c_p \frac{(e_s - e_a)}{r_a}}{\Delta + \gamma \left(1 + \frac{r_s}{r_a} \right)} \quad (\text{B10})$$

(Allen, 1996 and Allen et al., 1998)

where $\rho_a = 1.205 \text{ kg/m}^3$ (at 20°C)
 $c_p = 1003 \text{ m}^2 / (\text{s}^2 \text{K})$
 $r_a = \text{aerodynamic resistance (s/m)} = 208 / u_2$
 $r_s = 0$

Potential Evapotranspiration by Priestly-Taylor method

$$E_{\text{pot}} = 1.26 \frac{\Delta(R_n - G)}{\gamma + \Delta} \quad (\text{B11})$$

(Allen, 1996 and Allen et al., 1998)

where E_{pot} is in mm/day

Dew Point Temperature (T_{dew})

$$T_{\text{dew}} = \frac{116.91 + 237.3 \ln(e_a)}{16.78 - \ln(e_a)} \quad (\text{B12})$$

(Allen, 1996 and Allen et al., 1998)

where e_a is in kPa
 T_{dew} is in °C

References

- Allen, R. G., Pereira, L. S., Raes, D., and M. Smith, 1998. FAO Irrigation and Drainage Paper, No. 56, Crop Evapotranspiration (guidelines for computing crop water requirements). FAO- Food and Agriculture Organization of the United Nations, Rome.
- Allen, R. G. 1996. Assessing Integrity of Weather Data For Reference Evapotranspiration Estimation. *Journal of Irrigation and Drainage Engineering*, ASCE, 122(2), 97-106.
- Carpenter, R. H. 1968. Geology and ore Deposits of the Questa Molybdenum Mine Area, Taos County, New Mexico. In: *Ore Deposits of the United States, 1933-1967: AIME Graton-Sales*. 2, 1328-1350.
- Czamanske, G. K., Foland, K. A., Hubacher, F. A., and J. C Allen, 1990. The $^{40}\text{AR}/^{39}\text{AR}$ Chronology of Caldera Formation, Intrusive Activity and Mo-ore Deposition near Questa, New Mexico. In: *41st Field Conference Guidebook*, New Mexico Geological Society, p. 355-358.
- Robertson GeoConsultants Inc. 2000. Interim Mine Characterization Study, Questa, New Mexico. Report No. 052008/10. Report prepared for Molycorp Inc., November 2000.
- Walter, I., Allen, R., Elliott, R., Jensen, M., Howell, T., Snyder, R., Brown, P., Echings, S., Spofford, T., and J. Wright, 2001. ASCE's Standardized Reference Evapotranspiration Equation Manual. American Society of Civil Engineers Watershed Management Conference.

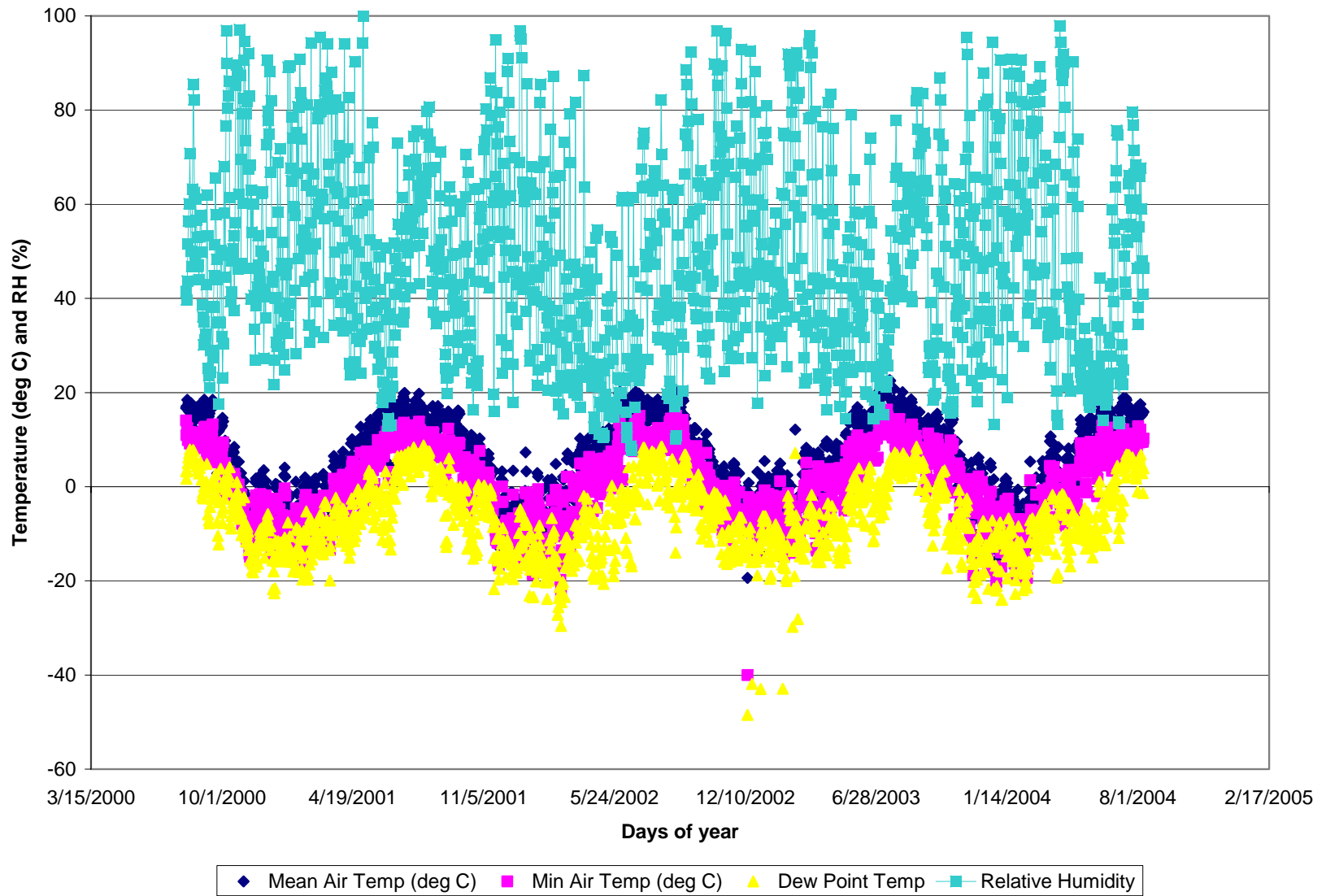


Figure B- 14.The results from station TP-5, where T_{dew} was calculated using the relative humidity (equation 12).

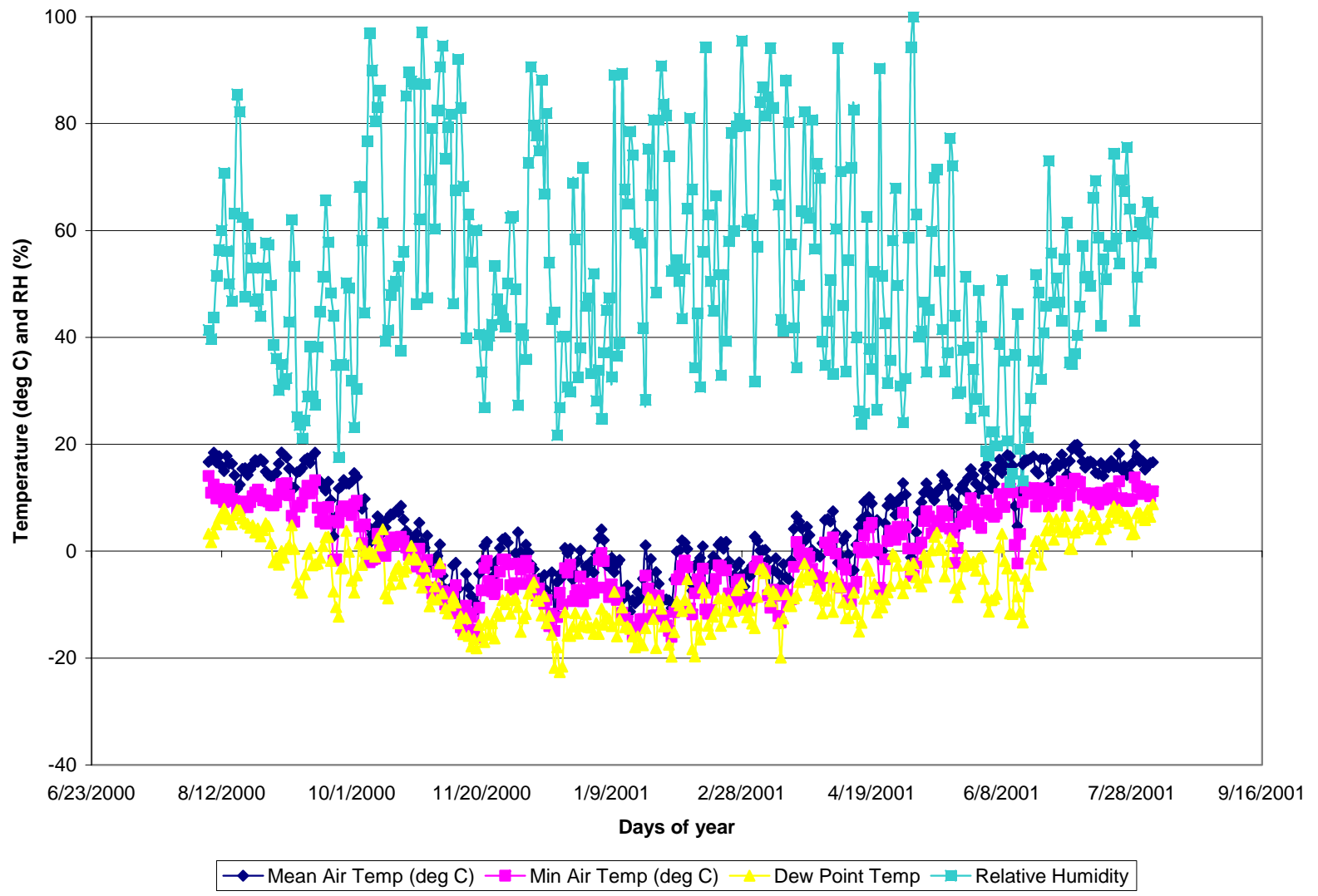


Figure B- 15. The results from the first year of data at station TP-5.

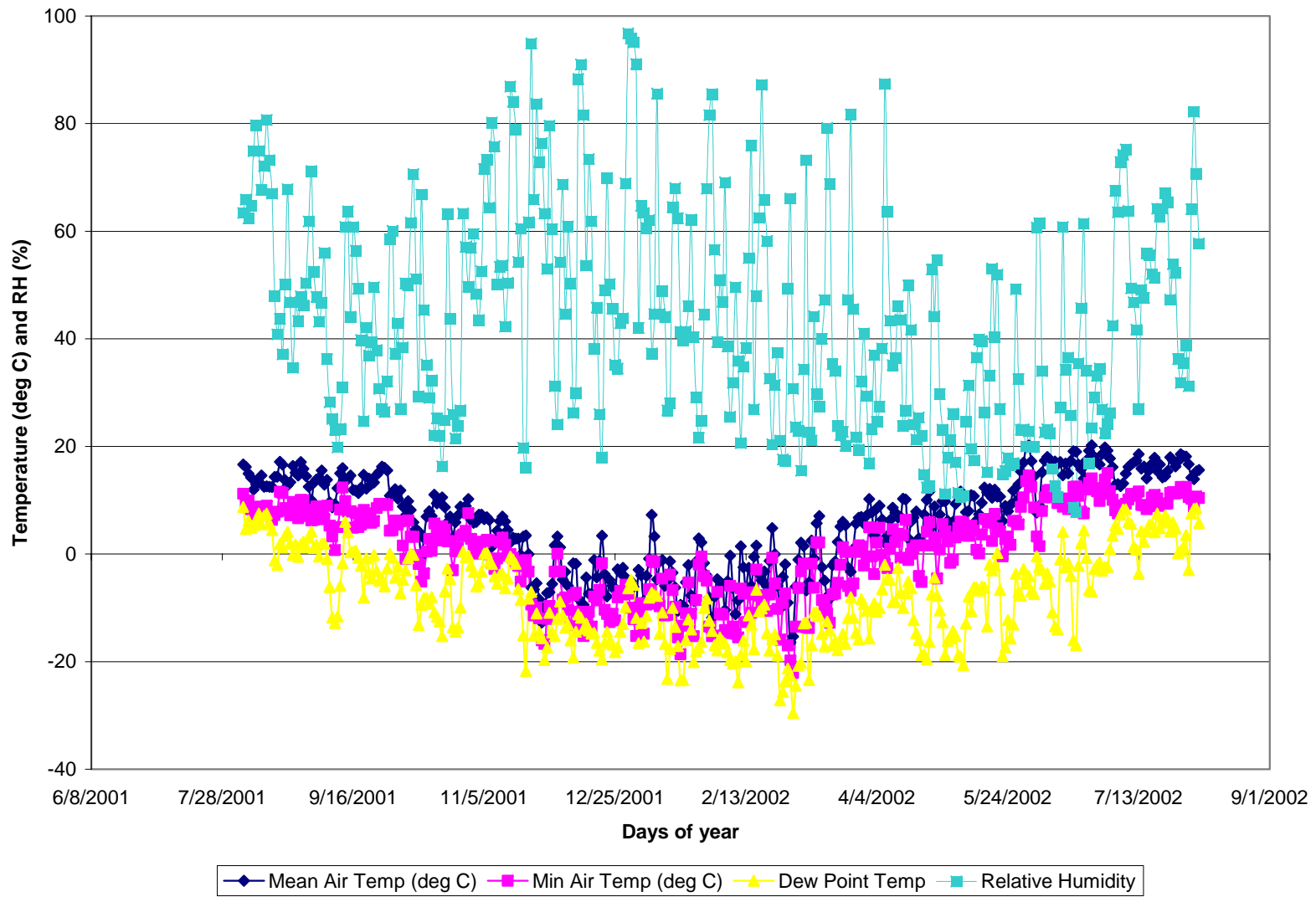


Figure B- 16. The results from the second year of data at station TP-5.

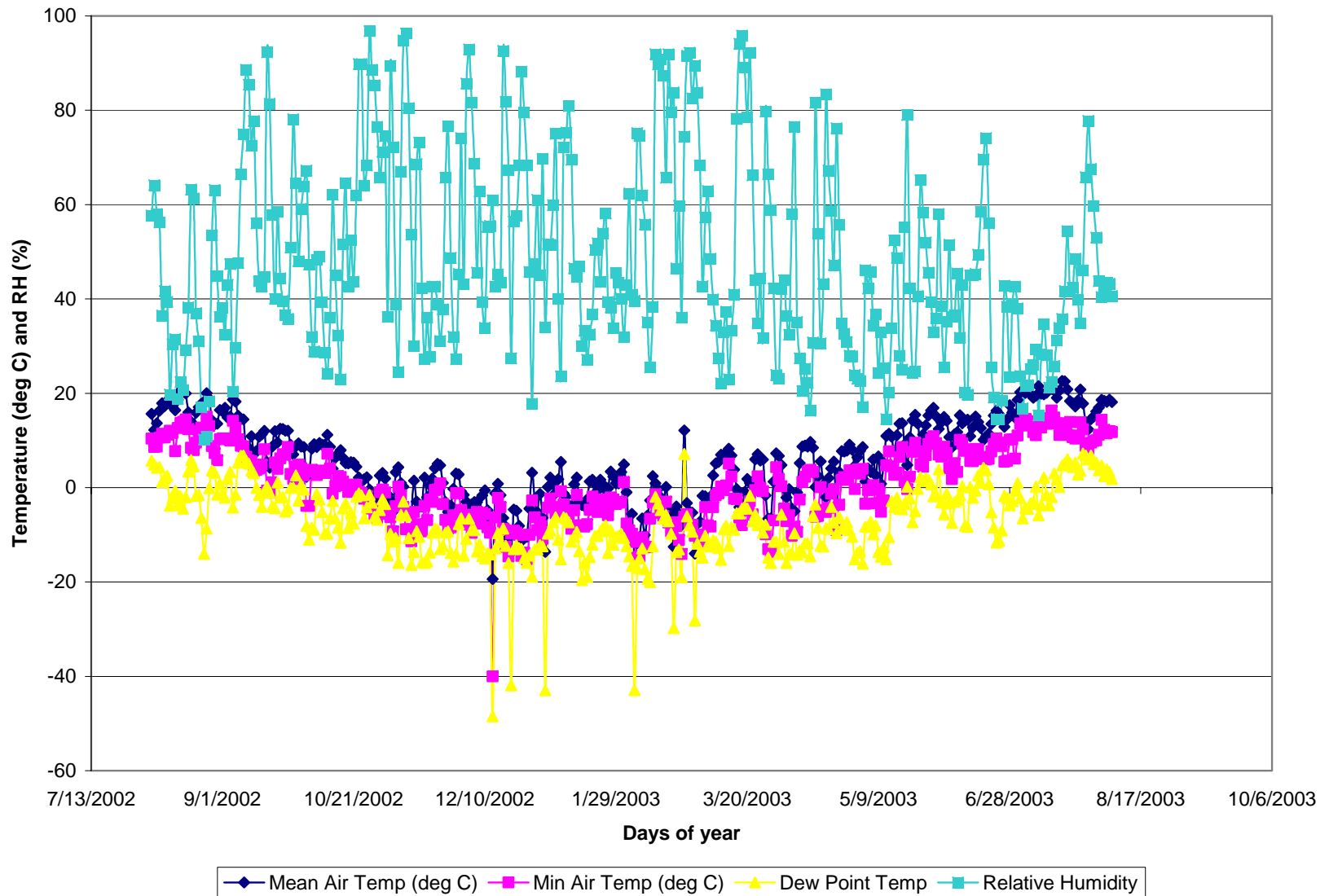


Figure B- 17. The results from the third year of data at station TP-5.

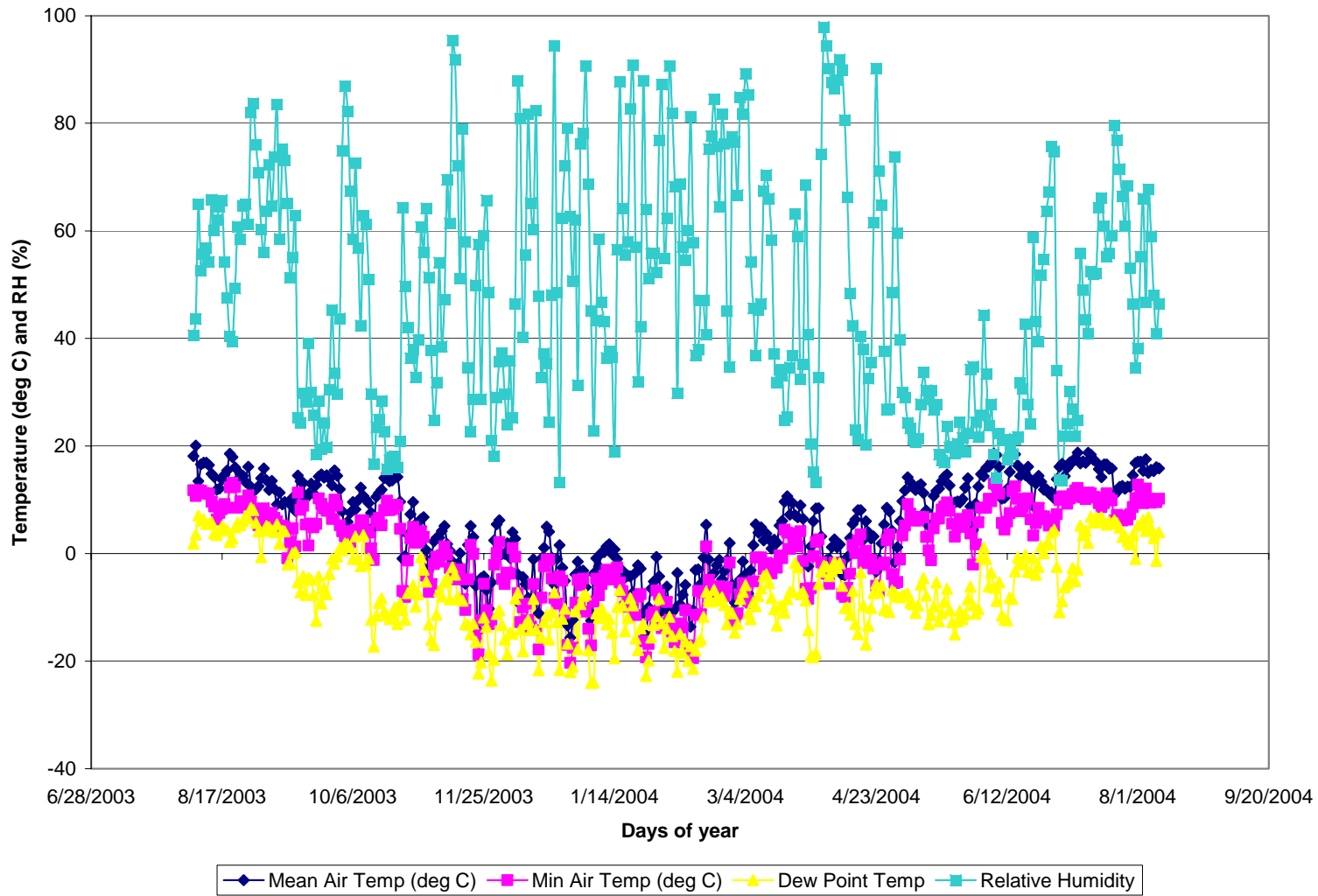


Figure B- 18. The results from the fourth year of data at station TP-5.

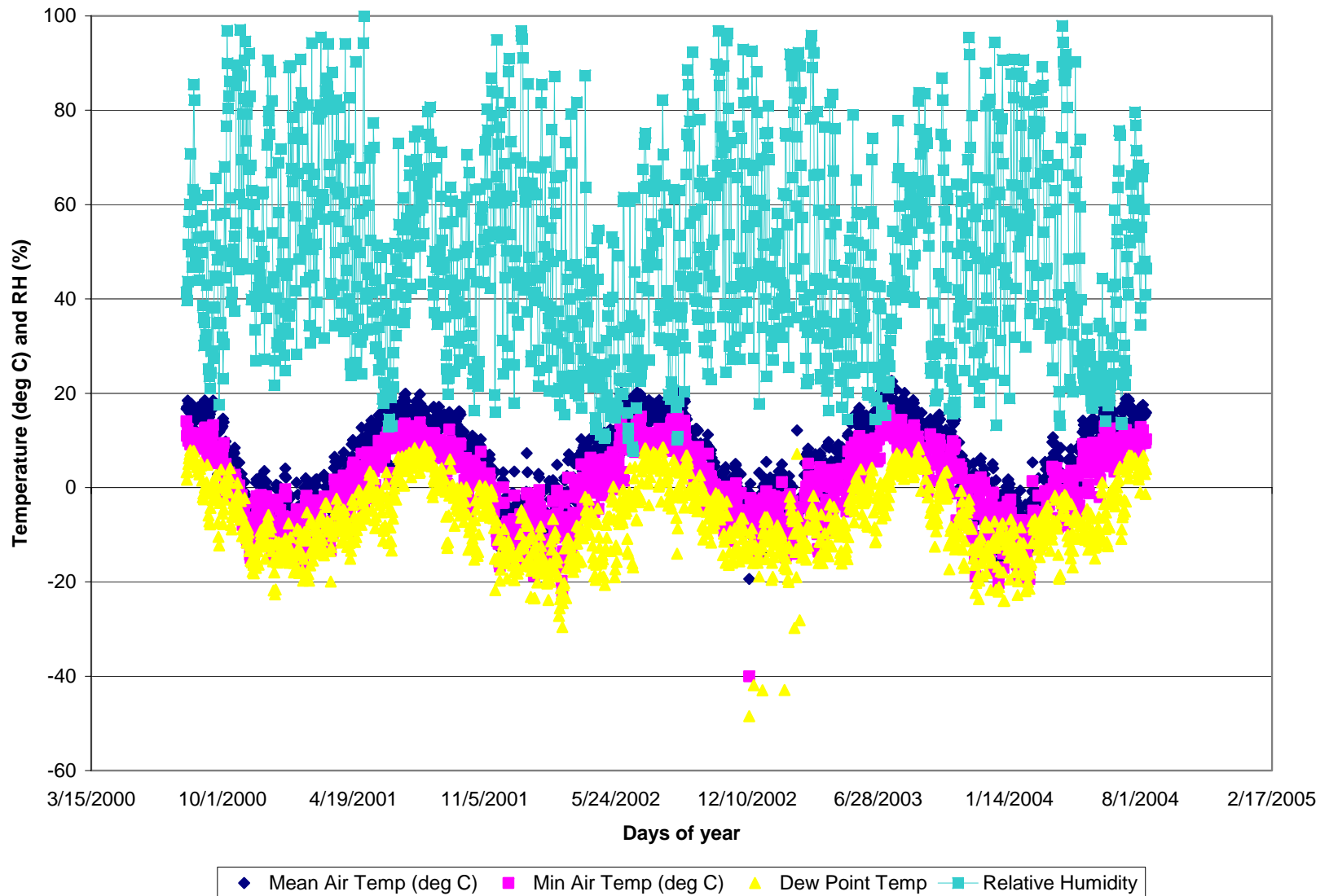


Figure B- 19. The results from station TP-4, where T_{dew} was calculated using the relative humidity (equation 12).

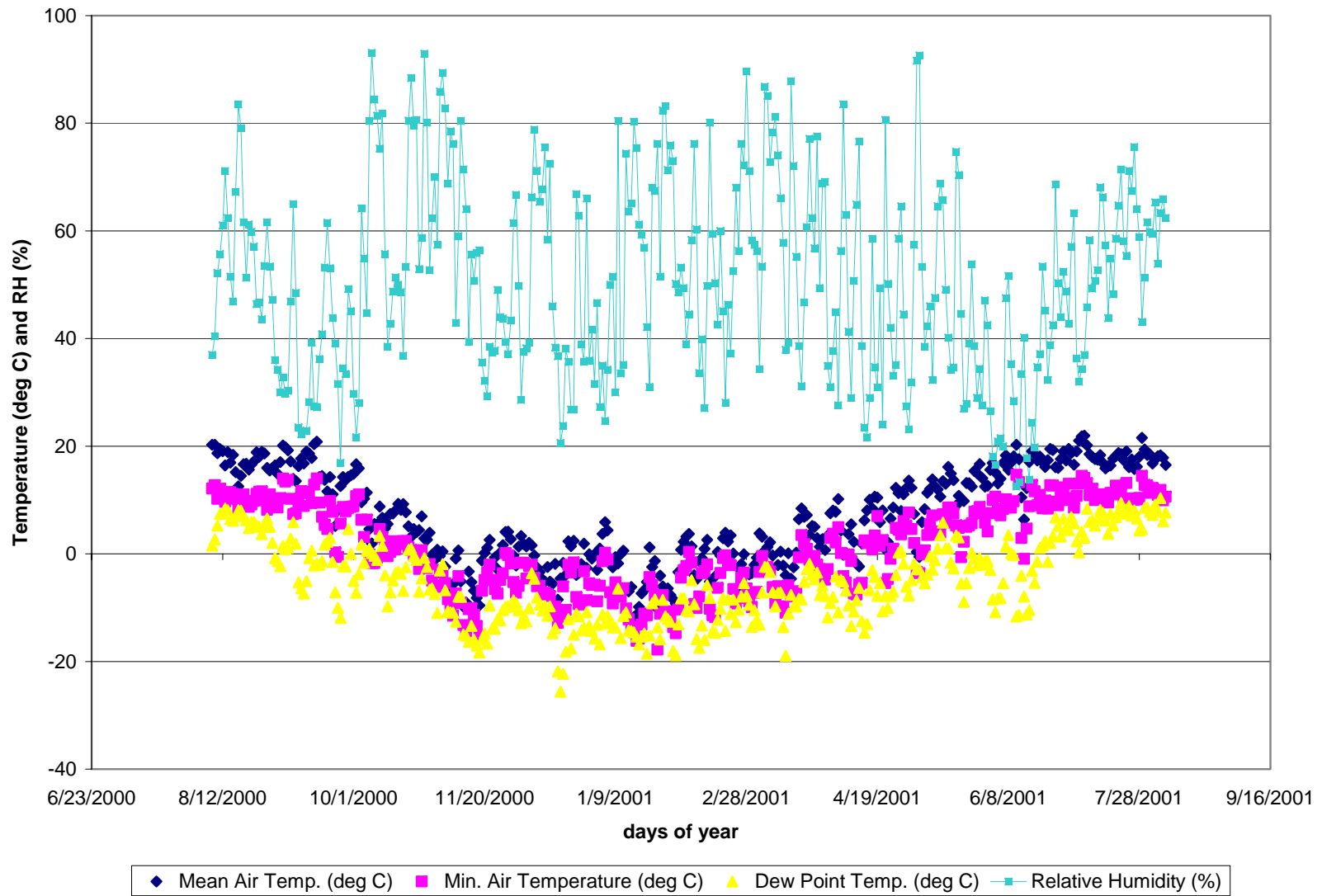


Figure B- 20. The results from the first year of data at station TP-4.

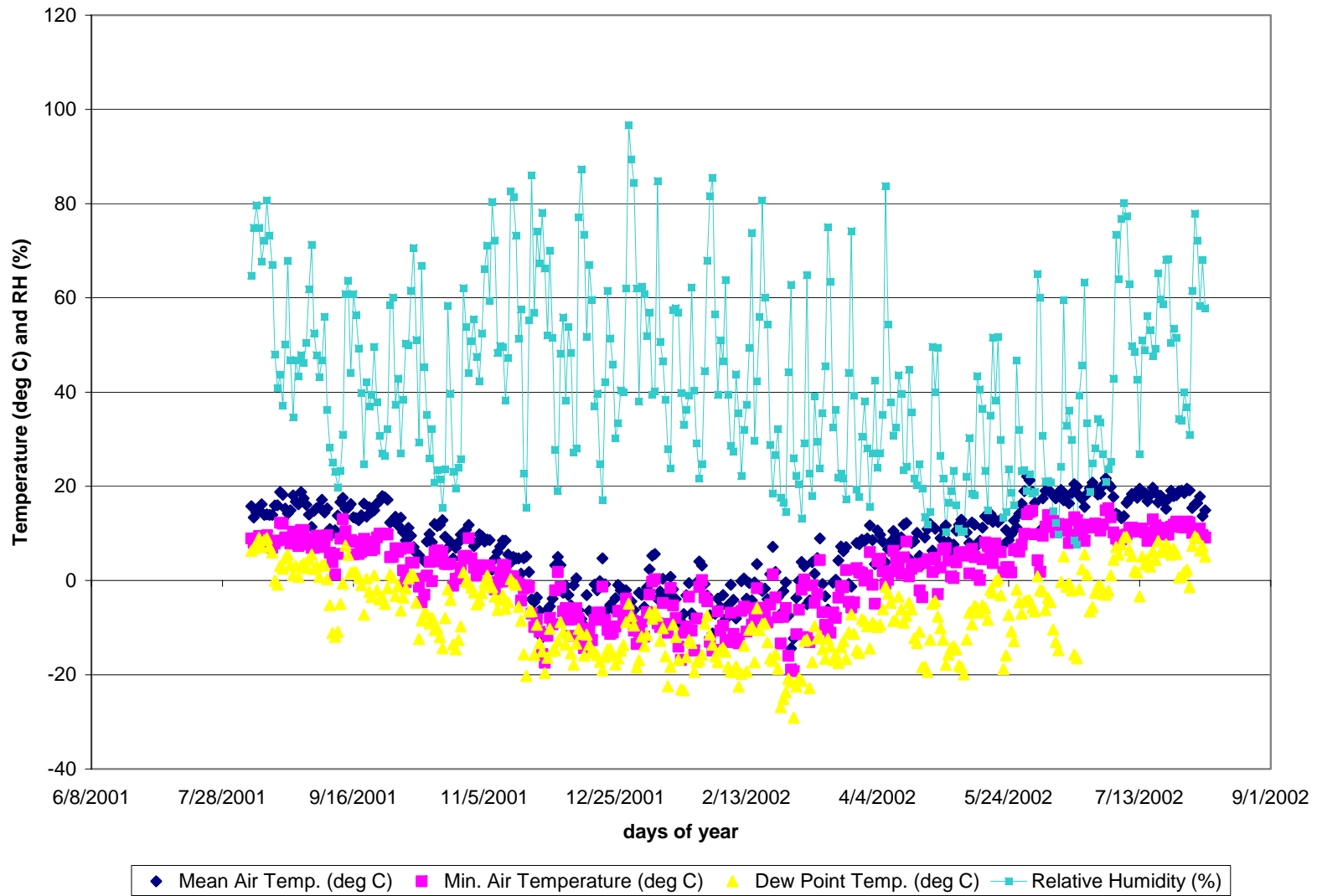


Figure B- 21. The results from the second year of data at station TP-4.

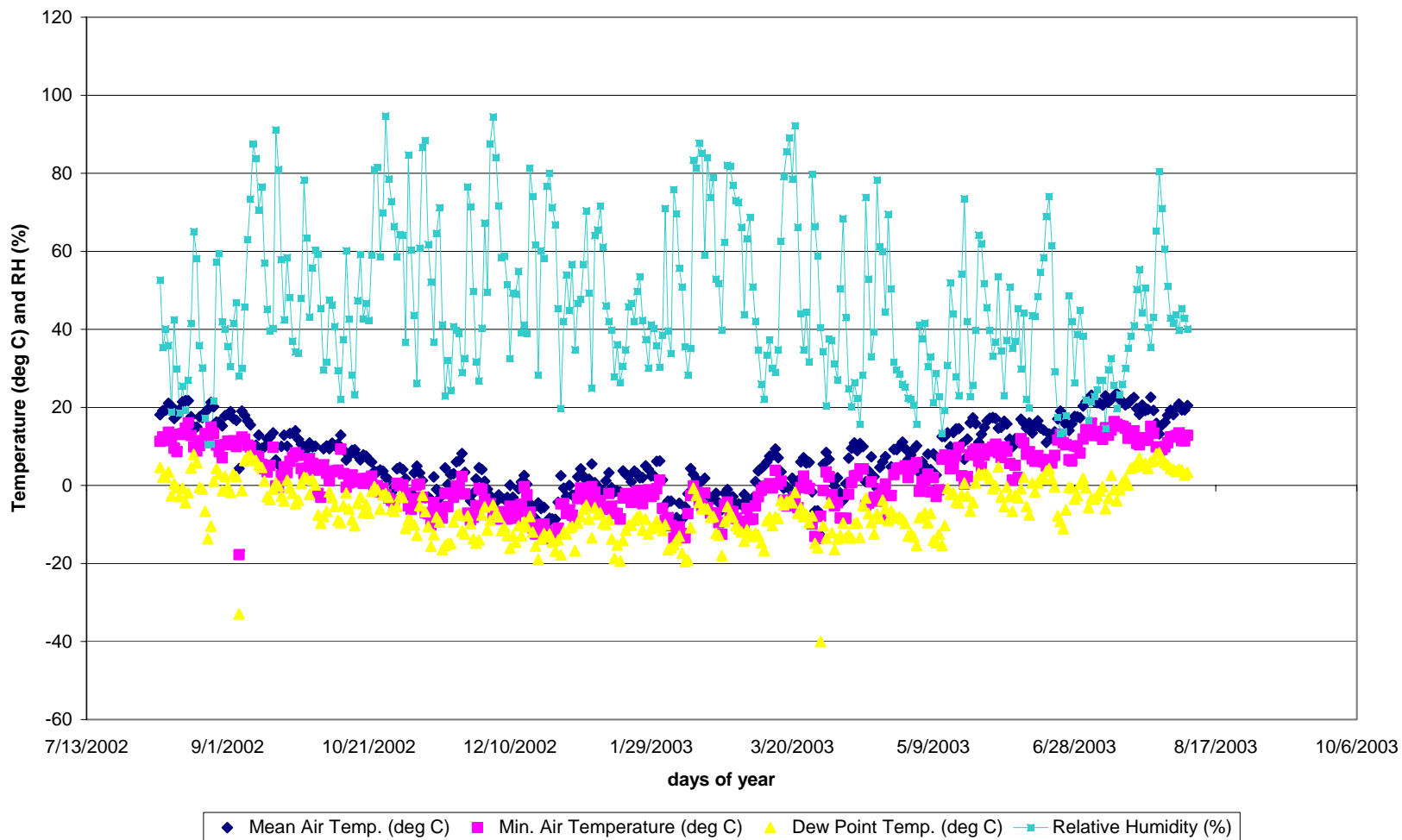


Figure B- 22. The results from the third year of data at station TP-4.

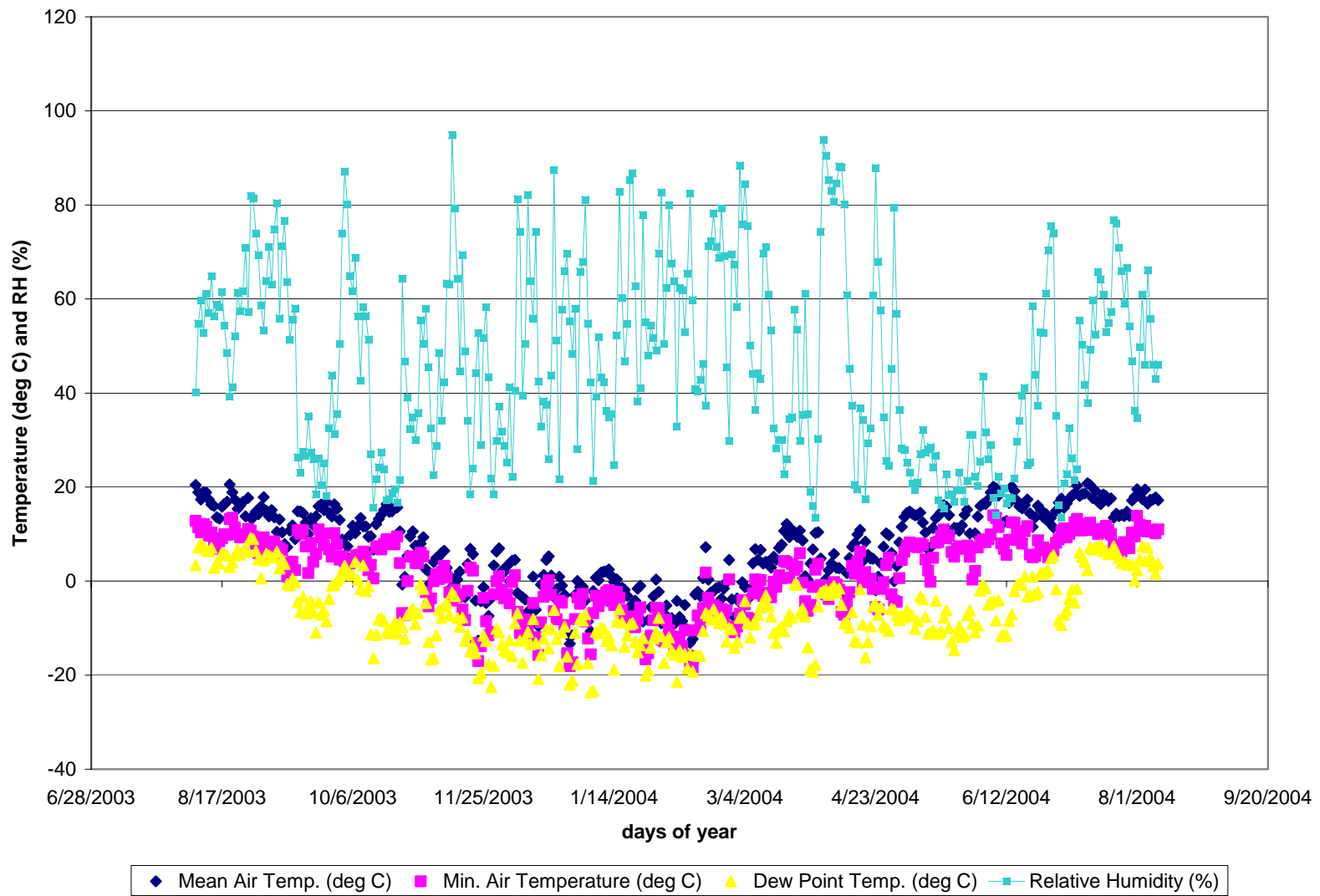


Figure B- 23. The results from the fourth year of data at station TP-4.

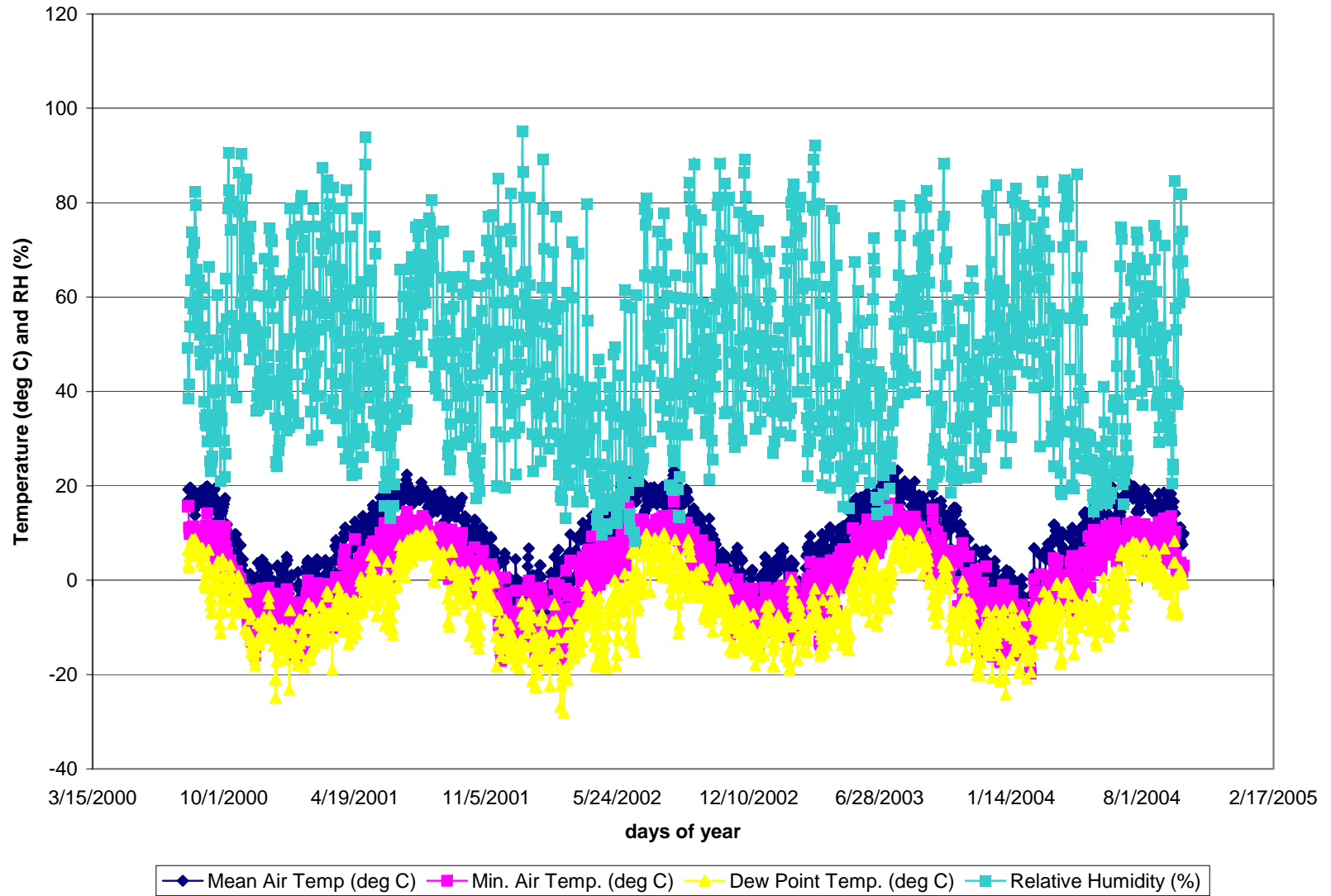


Figure B- 24. The results from TP-6/7, where T_{dew} was calculated using the relative humidity (equation 12).

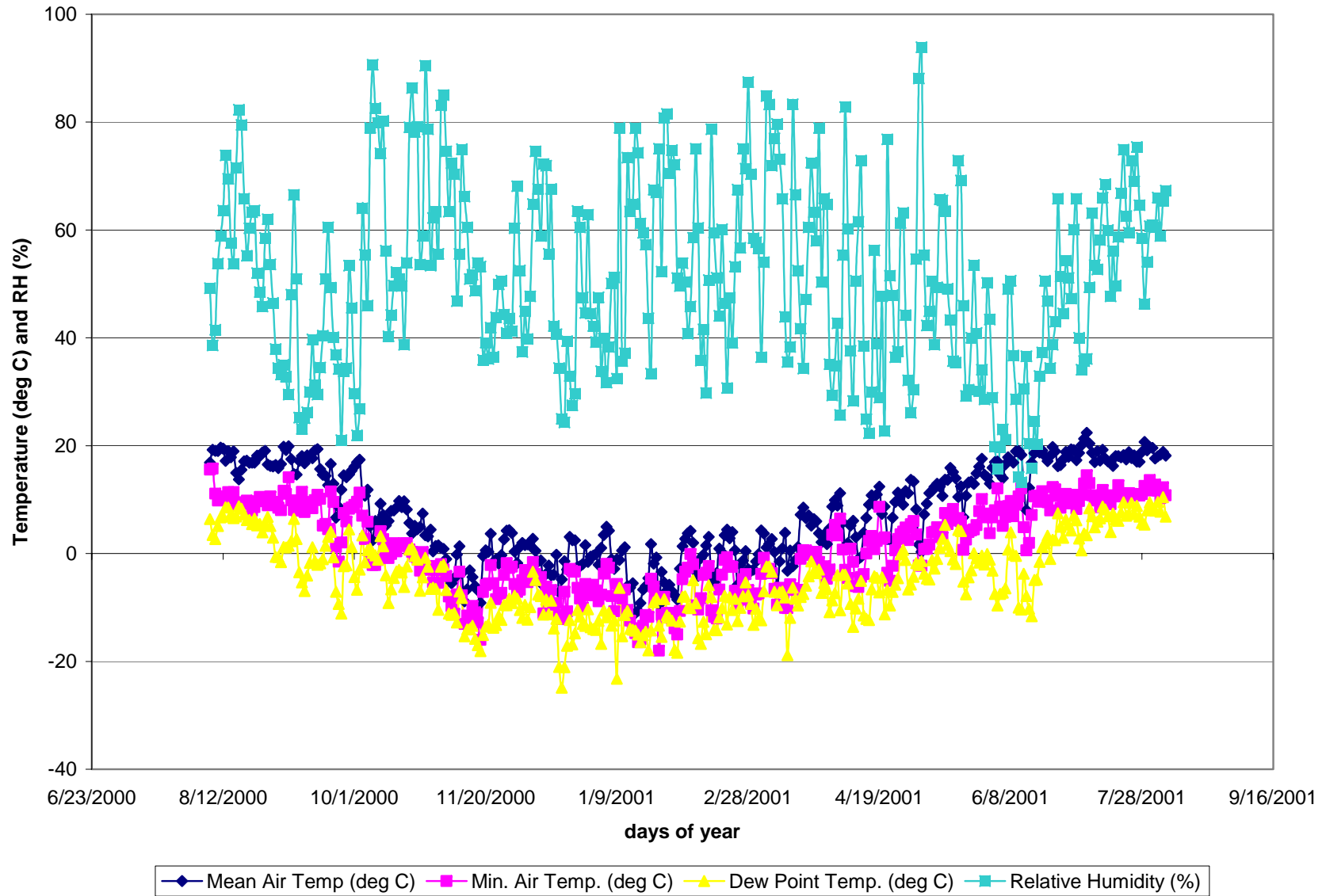


Figure B- 25. The results from the first year at station TP-6/7.

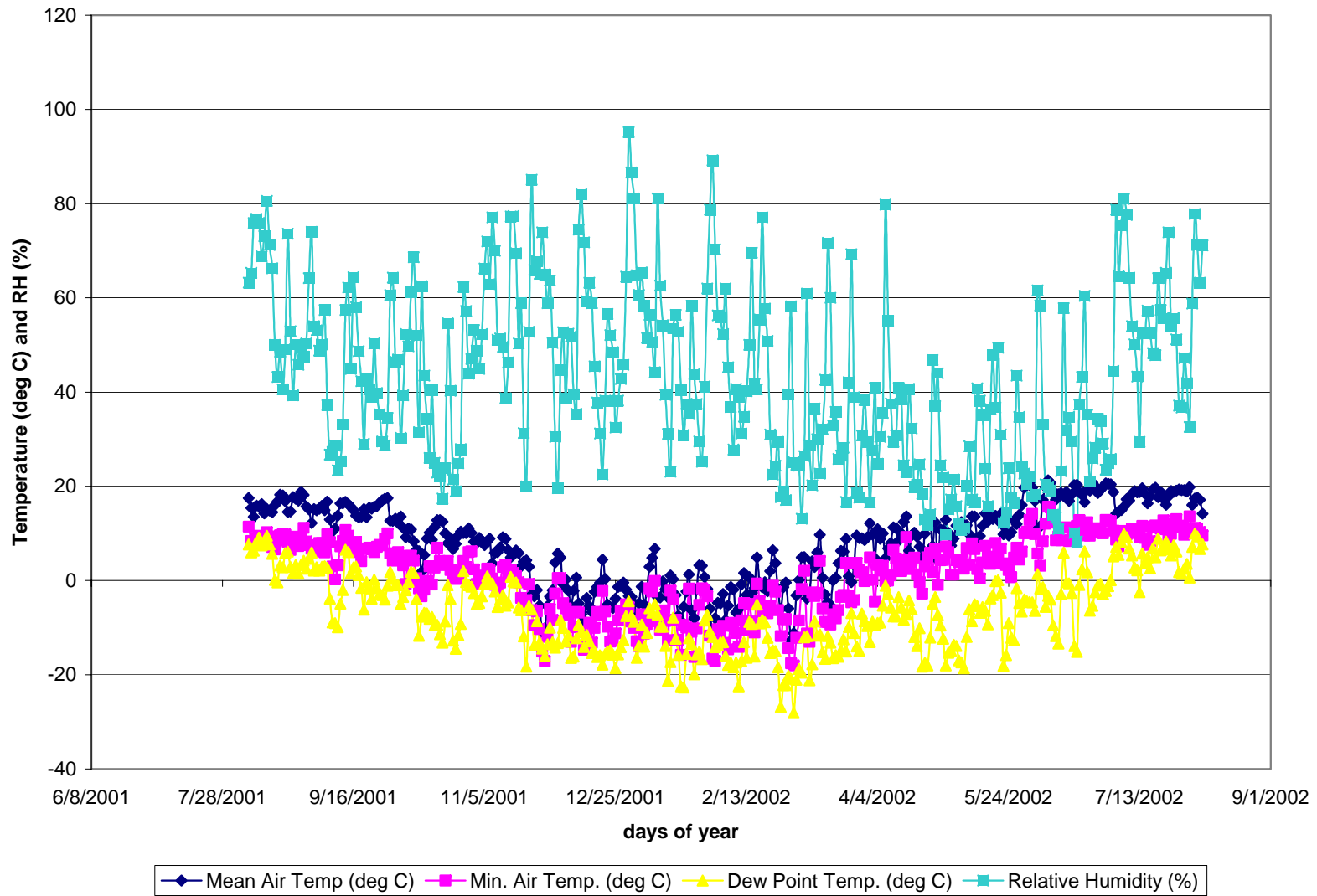


Figure B- 26. The results from the second year of data at station TP-6/7.

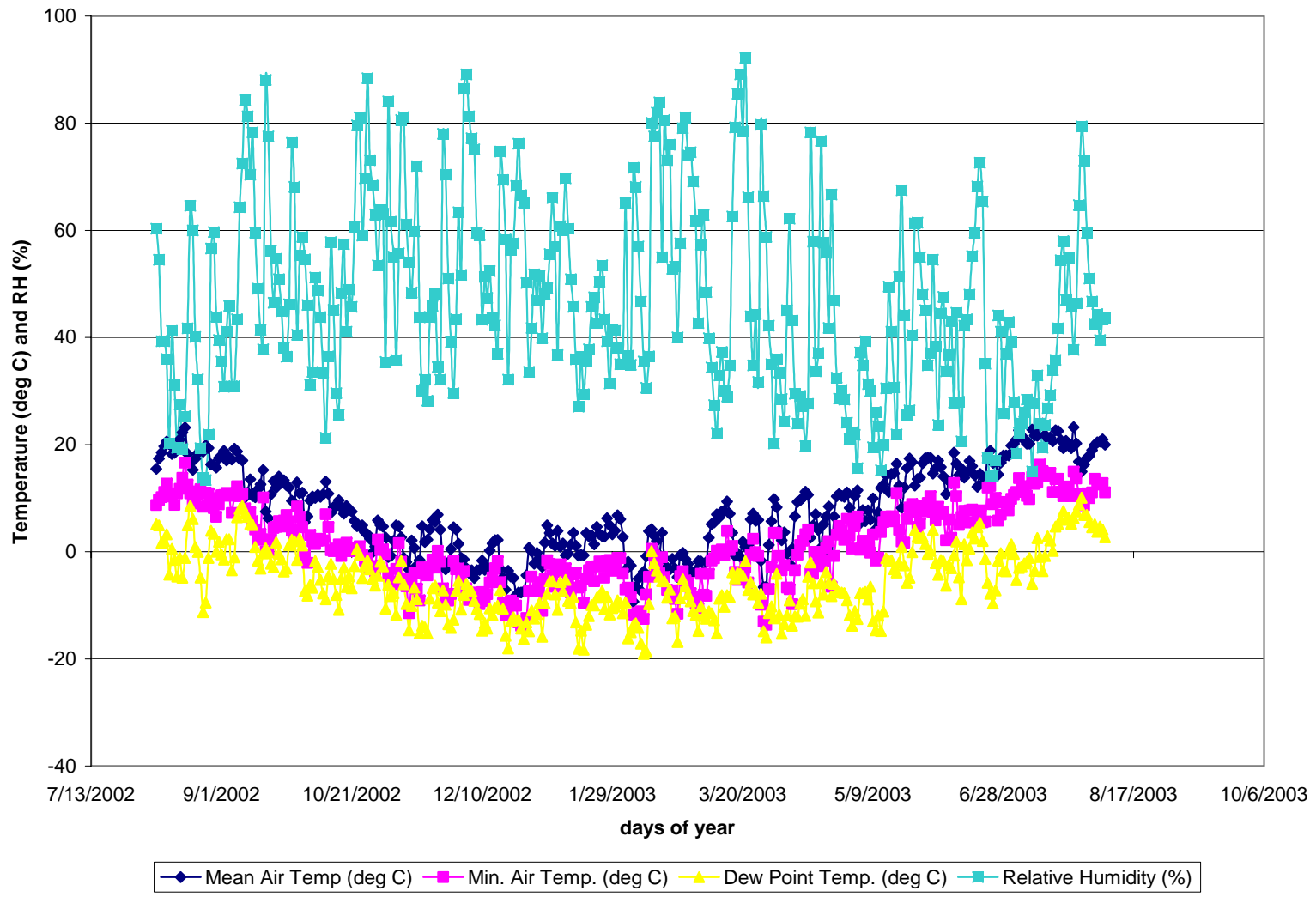


Figure B- 27. The results from the third year of data at station TP-6/7.

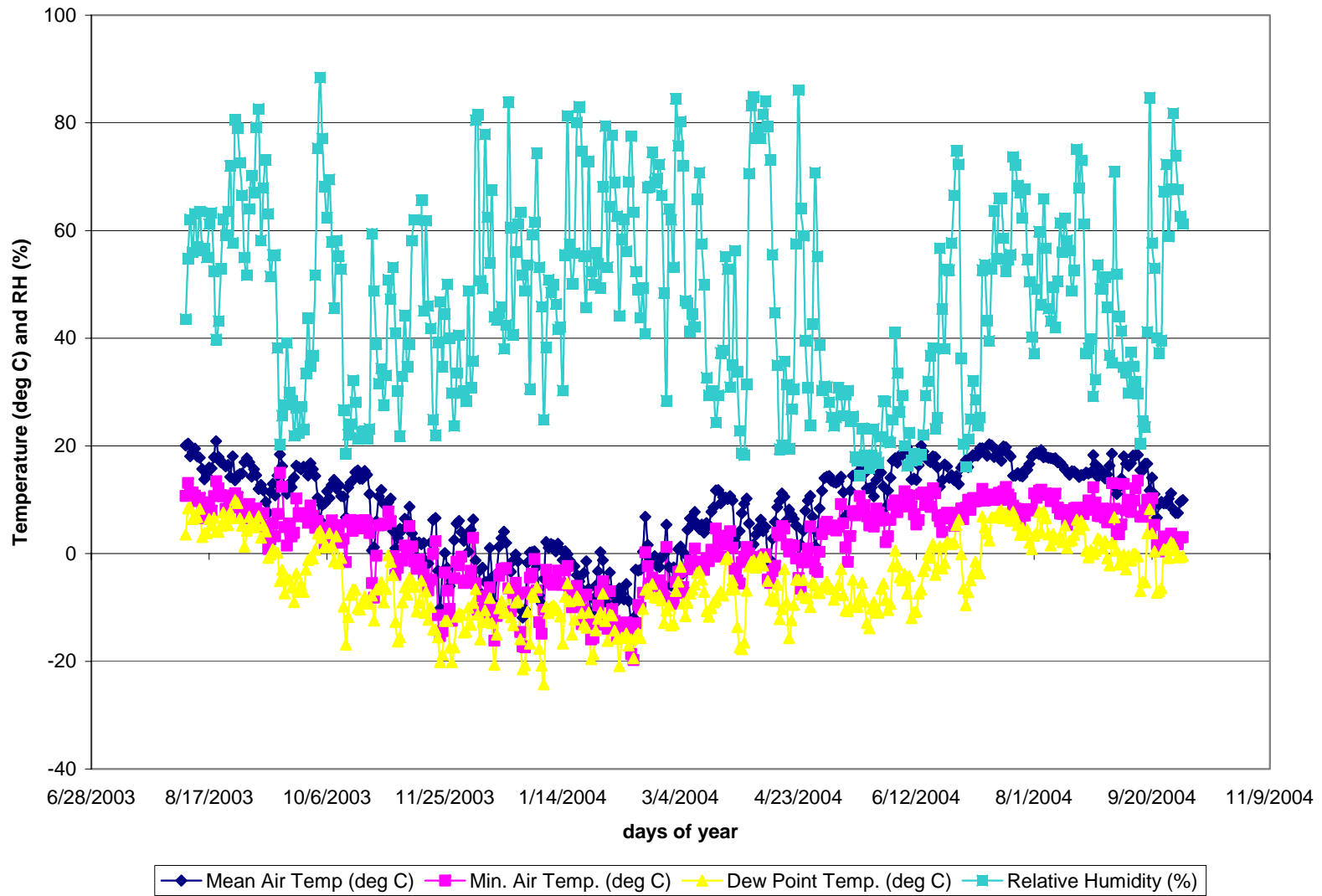


Figure B- 28. The results from the fourth year of data at station TP-6/7.

APPENDIX C. FIELD MEASUREMENTS OF BULK DENSITY.

The results of the field measurements of bulk density are presented in this appendix. The number of tests, field test number, field identification (field id), hole pit identification (hole pit id), test method, and dry bulk density are presented in the following tables.

Table C- 1. The test number, field ID, hole pit ID, test method, and dry bulk density from the measurements made within the WR1 region of the GHN rock pile are presented.

#	Test Number	Field ID	Hole Pit ID	Test Method	Dry Bulk Density (g/cm ³)
1	4b	NA	LFG-0004	Nuclear Gauge	1.79
2	3a	NA	LFG-0004	Nuclear Gauge	1.8
3	4a	NA	LFG-0004	Nuclear Gauge	1.79
4	2b	NA	LFG-0004	Nuclear Gauge	1.65
5	7b	NA	LFG-0004	Nuclear Gauge	1.93
6	5b	NA	LFG-0004	Nuclear Gauge	1.89
7	7a	NA	LFG-0004	Nuclear Gauge	1.98
8	1b	NA	LFG-0004	Nuclear Gauge	1.77
9	3b	NA	LFG-0004	Nuclear Gauge	1.64
10	5a	NA	LFG-0004	Nuclear Gauge	1.94
11	6b	NA	LFG-0004	Nuclear Gauge	1.86
12	6a	NA	LFG-0004	Nuclear Gauge	1.84
13	1a	NA	LFG-0004	Nuclear Gauge	1.79
14	2a	NA	LFG-0004	Nuclear Gauge	1.73
15	7-5-12I-E	GHN-KMD-0055	LFG-007	Nuclear Gauge	2.06
16	7-5-12I-W	GHN-KMD-0055	LFG-007	Nuclear Gauge	1.94
17	7-5-12I-S	GHN-KMD-0055	LFG-007	Nuclear Gauge	2.11
18	7-5-12I-N	GHN-KMD-0055	LFG-007	Nuclear Gauge	1.89
19	7-5-12J-N	GHN-KMD-0054	LFG-007	Nuclear Gauge	1.89
20	7-5-12J-S	GHN-KMD-0054	LFG-007	Nuclear Gauge	1.95
21	7-5-12J-W	GHN-KMD-0054	LFG-007	Nuclear Gauge	1.96
22	7-5-12J-E	GHN-KMD-0054	LFG-007	Nuclear Gauge	1.96
23	NGT-22-Js	GHN-JRM-0021	LFG-009	Nuclear Gauge	1.86
24	57-1d	GHN-LFG-0057	LFG-005	Nuclear Gauge	1.85
25	57-1e	GHN-LFG-0057	LFG-005	Nuclear Gauge	1.87
26	57-1b	GHN-LFG-0057	LFG-005	Nuclear Gauge	1.92
27	57-1a	GHN-LFG-0057	LFG-005	Nuclear Gauge	1.9
28	57-1f	GHN-LFG-0057	LFG-005	Nuclear Gauge	1.76
29	57-1c	GHN-LFG-0057	LFG-005	Nuclear Gauge	1.84
30	7W	NA	LFG-006	Nuclear Gauge	1.94
31	7N	NA	LFG-006	Nuclear Gauge	2.12
32	7S	NA	LFG-006	Nuclear Gauge	2.04
33	7Sb	NA	LFG-006	Nuclear Gauge	1.95
34	7-5-12K-N	GHN-KMD-0052	LFG-007	Nuclear Gauge	1.98
35	7Wb	NA	LFG-006	Nuclear Gauge	1.9
36	59-1a	GHN-LFG-0059	LFG-005	Nuclear Gauge	1.94
37	59-1b	GHN-LFG-0059	LFG-005	Nuclear Gauge	1.92
38	59-1c	GHN-LFG-0059	LFG-005	Nuclear Gauge	1.83
39	59-1e	GHN-LFG-0059	LFG-005	Nuclear Gauge	1.56
40	12a	NA	LFG-0003	Nuclear Gauge	1.77
41	7-3-13Sb	NA	LFG-007	Nuclear Gauge	1.8
42	59-1d	GHN-LFG-0059	LFG-005	Nuclear Gauge	1.78

43	7-3-13Wb	NA	LFG-007	Nuclear Gauge	1.7
44	7-3-13W	NA	LFG-007	Nuclear Gauge	1.95
45	7-5-12K-W	GHN-KMD-0052	LFG-007	Nuclear Gauge	1.98
46	12b	NA	LFG-0003	Nuclear Gauge	1.74
47	7E	NA	LFG-006	Nuclear Gauge	1.99
48	7-3-13S	NA	LFG-007	Nuclear Gauge	1.93
49	7-3-13Nb	NA	LFG-007	Nuclear Gauge	1.64
50	7-3-13N	NA	LFG-007	Nuclear Gauge	1.95
51	7-3-13Eb	NA	LFG-007	Nuclear Gauge	1.64
52	7-3-13E	NA	LFG-007	Nuclear Gauge	1.9
53	7-5-12K-E	GHN-KMD-0052	LFG-007	Nuclear Gauge	1.99
54	7-5-12K-S	GHN-KMD-0052	LFG-007	Nuclear Gauge	1.9
55	59-1f	GHN-LFG-0059	LFG-005	Nuclear Gauge	1.51
56	NGT17S3w	NA	LFG-008	Nuclear Gauge	1.97
57	NGT17S3s	NA	LFG-008	Nuclear Gauge	1.99
58	NGT17S3n	NA	LFG-008	Nuclear Gauge	2.02
59	NGT17S3e	NA	LFG-008	Nuclear Gauge	1.93
60	NGT17S3-6w	NA	LFG-008	Nuclear Gauge	1.89
61	NGT17S3-6s	NA	LFG-008	Nuclear Gauge	1.89
62	NGT17S3-6n	NA	LFG-008	Nuclear Gauge	1.9
63	NGT17S3-6e	NA	LFG-008	Nuclear Gauge	1.8
64	NDT002b	NA	LFG-005	Nuclear Gauge	2.01
65	NDT002c	NA	LFG-005	Nuclear Gauge	2.07
66	NDT002d	NA	LFG-005	Nuclear Gauge	2
67	NDT002e	NA	LFG-005	Nuclear Gauge	2.02
68	NDT002f	NA	LFG-005	Nuclear Gauge	1.88
69	NDT002a	NA	LFG-005	Nuclear Gauge	2.04
70	NGT18S4n	NA	LFG-008	Nuclear Gauge	1.81
71	NGT18S4e	NA	LFG-008	Nuclear Gauge	1.76
72	NGT18S4-6w	NA	LFG-008	Nuclear Gauge	1.73
73	NGT18S4s	NA	LFG-008	Nuclear Gauge	1.75
74	NGT18S4-6e	NA	LFG-008	Nuclear Gauge	1.65
75	NGT18S4w	NA	LFG-008	Nuclear Gauge	1.8
76	NGT18S4-6n	NA	LFG-008	Nuclear Gauge	1.55
77	NGT18S4-6s	NA	LFG-008	Nuclear Gauge	1.51
78	11a	NA	LFG-0003	Nuclear Gauge	1.8
79	7-5-12N-S	GHN-KMD-0053	LFG-007	Nuclear Gauge	1.85
80	7-5-12N-N	GHN-KMD-0053	LFG-007	Nuclear Gauge	1.84
81	7-5-12N-E	GHN-KMD-0053	LFG-007	Nuclear Gauge	1.79
82	NGT17N61S	NA	LFG-008	Nuclear Gauge	1.83
83	NGT17N61N	NA	LFG-008	Nuclear Gauge	1.68
84	NGT17N61E	NA	LFG-008	Nuclear Gauge	1.73
85	NGT17N12W	NA	LFG-008	Nuclear Gauge	1.72
86	NGT17N12S	NA	LFG-008	Nuclear Gauge	2.06
87	NGT17N12N	NA	LFG-008	Nuclear Gauge	2
88	NGT17N12E	NA	LFG-008	Nuclear Gauge	2.02
89	11b	NA	LFG-0003	Nuclear Gauge	1.72
90	7-5-12N-W	GHN-KMD-0053	LFG-007	Nuclear Gauge	1.74

91	NGT17N61W	NA	LFG-008	Nuclear Gauge	1.27
92	NGT17S1w	NA	LFG-008	Nuclear Gauge	1.94
93	NGT17S1-6n	NA	LFG-008	Nuclear Gauge	1.78
94	NGT17S1-6e	NA	LFG-008	Nuclear Gauge	1.82
95	NGT17S1n	NA	LFG-008	Nuclear Gauge	1.93
96	7-2-12E	NA	LFG-007	Nuclear Gauge	1.94
97	NGT17S1-6s	NA	LFG-008	Nuclear Gauge	1.78
98	KMD-75n	GHN-KMD-0075	LFG-008	Nuclear Gauge	1.93
99	NGT17S1s	NA	LFG-008	Nuclear Gauge	1.89
100	NGT17S1e	NA	LFG-008	Nuclear Gauge	1.92
101	NGT17S1-6w	NA	LFG-008	Nuclear Gauge	1.88
102	7-4-14S	NA	LFG-007	Nuclear Gauge	1.84
103	73NE	GHN-KMD-0073	LFG-008	Nuclear Gauge	1.92
104	73NN	GHN-KMD-0073	LFG-008	Nuclear Gauge	1.95
105	73NS	GHN-KMD-0073	LFG-008	Nuclear Gauge	1.84
106	73NW	GHN-KMD-0073	LFG-008	Nuclear Gauge	1.94
107	7-4-14E	NA	LFG-007	Nuclear Gauge	1.68
108	7-4-14Eb	NA	LFG-007	Nuclear Gauge	1.76
109	KMD-75w	GHN-KMD-0075	LFG-008	Nuclear Gauge	1.83
110	7-4-14Nb	NA	LFG-007	Nuclear Gauge	1.7
111	73-6NN	NA	LFG-008	Nuclear Gauge	1.8
112	7-4-14W	NA	LFG-007	Nuclear Gauge	1.94
113	7-5-12O1-E	GHN-KMD-0050	LFG-007	Nuclear Gauge	2.06
114	7-5-12O1-N	GHN-KMD-0050	LFG-007	Nuclear Gauge	2.01
115	7-5-12O1-S	GHN-KMD-0050	LFG-007	Nuclear Gauge	1.99
116	7-5-12O1-W	GHN-KMD-0050	LFG-007	Nuclear Gauge	1.97
117	7-4-14N	NA	LFG-007	Nuclear Gauge	1.72
118	7-2-12N	NA	LFG-007	Nuclear Gauge	1.95
119	6Sb	NA	LFG-006	Nuclear Gauge	1.74
120	6S	NA	LFG-006	Nuclear Gauge	1.92
121	6N	NA	LFG-006	Nuclear Gauge	1.82
122	6Eb	NA	LFG-006	Nuclear Gauge	1.81
123	6E	NA	LFG-006	Nuclear Gauge	2.07
124	61NW	GHN-KMD-0072	LFG-008	Nuclear Gauge	1.8
125	61NS	GHN-KMD-0072	LFG-008	Nuclear Gauge	1.82
126	73-6NW	NA	LFG-008	Nuclear Gauge	1.73
127	61NE	GHN-KMD-0072	LFG-008	Nuclear Gauge	1.85
128	73-6NS	NA	LFG-008	Nuclear Gauge	1.73
129	7-2-12Nb	NA	LFG-007	Nuclear Gauge	1.72
130	7-2-12S	NA	LFG-007	Nuclear Gauge	1.95
131	7-2-12Sb	NA	LFG-007	Nuclear Gauge	1.84
132	7-2-12W	NA	LFG-007	Nuclear Gauge	1.97
133	7-2-12Wb	NA	LFG-007	Nuclear Gauge	1.78
134	73-6NE	NA	LFG-008	Nuclear Gauge	1.88
135	7-5-12O2-S	GHN-KMD-0051	LFG-007	Nuclear Gauge	1.9
136	61NN	GHN-KMD-0072	LFG-008	Nuclear Gauge	1.68
137	121NS	GHN-KMD-0072	LFG-008	Nuclear Gauge	1.91
138	7-5-12O2-E	GHN-KMD-0051	LFG-007	Nuclear Gauge	1.99

139	KMD-76-6s	GHN-KMD-0076	LFG-008	Nuclear Gauge	1.69
140	KMD-76-6w	GHN-KMD-0076	LFG-008	Nuclear Gauge	1.68
141	KMD-76e	GHN-KMD-0076	LFG-008	Nuclear Gauge	1.95
142	KMD-76n	GHN-KMD-0076	LFG-008	Nuclear Gauge	1.86
143	KMD-76s	GHN-KMD-0076	LFG-008	Nuclear Gauge	1.9
144	KMD-76w	GHN-KMD-0076	LFG-008	Nuclear Gauge	1.85
145	KMD-76-6e	GHN-KMD-0076	LFG-008	Nuclear Gauge	1.64
146	7-2-12Eb	NA	LFG-007	Nuclear Gauge	1.76
147	KMD-75s	GHN-KMD-0075	LFG-008	Nuclear Gauge	1.91
148	121NN	GHN-KMD-0072	LFG-008	Nuclear Gauge	1.76
149	121NE	GHN-KMD-0072	LFG-008	Nuclear Gauge	1.92
150	NDT001a	GHN-LFG-0084	LFG-005	Nuclear Gauge	1.89
151	NDT001b	GHN-LFG-0084	LFG-005	Nuclear Gauge	1.84
152	NDT001c	GHN-LFG-0084	LFG-005	Nuclear Gauge	1.83
153	NDT001d	GHN-LFG-0084	LFG-005	Nuclear Gauge	1.82
154	NDT001e	GHN-LFG-0084	LFG-005	Nuclear Gauge	1.74
155	121NW	GHN-KMD-0072	LFG-008	Nuclear Gauge	1.87
156	7-1-11W	NA	LFG-007	Nuclear Gauge	1.94
157	NDT001f	GHN-LFG-0084	LFG-005	Nuclear Gauge	1.65
158	7-5-12O2-W	GHN-KMD-0051	LFG-007	Nuclear Gauge	1.99
159	7-1-11E	NA	LFG-007	Nuclear Gauge	1.93
160	7-1-11Eb	NA	LFG-007	Nuclear Gauge	1.77
161	7-1-11N	NA	LFG-007	Nuclear Gauge	1.99
162	7-1-11Nb	NA	LFG-007	Nuclear Gauge	1.76
163	7-1-11S	NA	LFG-007	Nuclear Gauge	1.95
164	KMD-76-6n	GHN-KMD-0076	LFG-008	Nuclear Gauge	1.65
165	7-1-11Sb	NA	LFG-007	Nuclear Gauge	1.79
166	7-5-12O2-N	GHN-KMD-0051	LFG-007	Nuclear Gauge	2.05
167	7-1-11Wb	NA	LFG-007	Nuclear Gauge	1.85
168	KMD-75-6e	GHN-KMD-0075	LFG-008	Nuclear Gauge	1.66
169	KMD-75-6n	GHN-KMD-0075	LFG-008	Nuclear Gauge	1.7
170	KMD-75-6s	GHN-KMD-0075	LFG-008	Nuclear Gauge	1.73
171	KMD-75-6w	GHN-KMD-0075	LFG-008	Nuclear Gauge	1.64
172	KMD-75e	GHN-KMD-0075	LFG-008	Nuclear Gauge	1.9
173	6W	NA	LFG-006	Nuclear Gauge	1.9
174	77-61NE	GHN-KMD-0077	LFG-008	Nuclear Gauge	1.83
175	NGT18S12W	NA	LFG-008	Nuclear Gauge	1.91
176	77-61NS	GHN-KMD-0077	LFG-008	Nuclear Gauge	1.79
177	NGT18S6W	NA	LFG-008	Nuclear Gauge	1.72
178	NGT18S12E	NA	LFG-008	Nuclear Gauge	1.87
179	NGT18S12S	NA	LFG-008	Nuclear Gauge	1.93
180	77-61NW	GHN-KMD-0077	LFG-008	Nuclear Gauge	1.73
181	77-61NN	GHN-KMD-0077	LFG-008	Nuclear Gauge	1.79
182	77-121NW	GHN-KMD-0077	LFG-008	Nuclear Gauge	1.88
183	77-121NN	GHN-KMD-0077	LFG-008	Nuclear Gauge	1.84
184	77-121NE	GHN-KMD-0077	LFG-008	Nuclear Gauge	1.92
185	NGT18S6E	NA	LFG-008	Nuclear Gauge	1.61
186	77-121NS	GHN-KMD-0077	LFG-008	Nuclear Gauge	1.9

187	NGT18S6S	NA	LFG-008	Nuclear Gauge	1.79
188	NGT18S12N	NA	LFG-008	Nuclear Gauge	1.79
189	NGT18S6N	NA	LFG-008	Nuclear Gauge	1.71
190	71-121NW	GHN-KMD-0071	LFG-008	Nuclear Gauge	1.85
191	71-121NE	GHN-KMD-0071	LFG-008	Nuclear Gauge	1.82
192	71-61NS	GHN-KMD-0071	LFG-008	Nuclear Gauge	1.72
193	71-121NN	GHN-KMD-0071	LFG-008	Nuclear Gauge	1.85
194	71-61NN	GHN-KMD-0071	LFG-008	Nuclear Gauge	1.68
195	71-61NE	GHN-KMD-0071	LFG-008	Nuclear Gauge	1.76
196	71-121NS	GHN-KMD-0071	LFG-008	Nuclear Gauge	1.83
197	71-61NW	GHN-KMD-0071	LFG-008	Nuclear Gauge	1.72
198	NGT17S2-6e	NA	LFG-008	Nuclear Gauge	1.92
199	NGT17S2n	NA	LFG-008	Nuclear Gauge	1.98
200	NGT17S2-6n	NA	LFG-008	Nuclear Gauge	1.78
201	NGT17S2e	NA	LFG-008	Nuclear Gauge	1.99
202	NGT17S2-6s	NA	LFG-008	Nuclear Gauge	1.81
203	NGT17S2s	NA	LFG-008	Nuclear Gauge	2
204	NGT17S2w	NA	LFG-008	Nuclear Gauge	2
205	NGT18S3-6e	NA	LFG-008	Nuclear Gauge	1.81
206	NGT18S3-6n	NA	LFG-008	Nuclear Gauge	1.77
207	NGT18S3-6s	NA	LFG-008	Nuclear Gauge	1.92
208	NGT18S3-6w	NA	LFG-008	Nuclear Gauge	1.8
209	NGT18S3e	NA	LFG-008	Nuclear Gauge	1.85
210	NGT18S3n	NA	LFG-008	Nuclear Gauge	1.88
211	NGT18S3s	NA	LFG-008	Nuclear Gauge	1.95
212	NGT18S3w	NA	LFG-008	Nuclear Gauge	1.86
213	NGT17S2-6w	NA	LFG-008	Nuclear Gauge	1.82
214	NA	GHN-KMD-0072	LFG-008	Water Replacement	1.94
215	NA	GHN-KMD-0072	LFG-008	Water Replacement	2.48
216	NA	GHN-KMD-0050	LFG-007	Sand Cone	1.64
217	NA	GHN-LFG-0059	LFG-005	Sand Cone	1.67
218	NA	GHN-LFG-0082	LFG-005	Sand Cone	1.73
219	NA	GHN-LFG-0084	LFG-005	Sand Cone	1.82

Table C- 2. The test number, field ID, hole pit ID, test method, and dry bulk density from the measurements made within the WR2 region of the GHN rock pile are presented.

#	Test Number	Field ID	Hole Pit ID	Test Method	Dry Bulk Density (g/cm ³)
1	NGT-22-Je6	GHN-JRM-0021	LFG-009	Nuclear Gauge	1.63
2	NGT-24Jn	NA	LFG-009	Nuclear Gauge	1.65
3	NGT-24Jw	NA	LFG-009	Nuclear Gauge	1.58
4	NGT-24Je	NA	LFG-009	Nuclear Gauge	1.64
5	NGT-22-Jn	GHN-JRM-0021	LFG-009	Nuclear Gauge	1.89
6	NGT-22-Je	GHN-JRM-0021	LFG-009	Nuclear Gauge	1.93
7	NGT-22-Js6	GHN-JRM-0021	LFG-009	Nuclear Gauge	1.54
8	NGT-22-Jw	GHN-JRM-0021	LFG-009	Nuclear Gauge	1.89
9	NGT-24Js	NA	LFG-009	Nuclear Gauge	1.52
10	NGT-22-Jw6	GHN-JRM-0021	LFG-009	Nuclear Gauge	1.59
11	NGT-22-Jn6	GHN-JRM-0021	LFG-009	Nuclear Gauge	1.61
12	NGT-22-Ne	GHN-JRM-0002	LFG-009	Nuclear Gauge	1.97
13	NGT-22-Ns6	GHN-JRM-0002	LFG-009	Nuclear Gauge	1.8
14	NGT-22-Ns	GHN-JRM-0002	LFG-009	Nuclear Gauge	2.01
15	NGT-22-Nn6	GHN-JRM-0002	LFG-009	Nuclear Gauge	1.83
16	NGT-25Nw6	NA	LFG-009	Nuclear Gauge	1.73
17	NGT-22-Ne6	GHN-JRM-0002	LFG-009	Nuclear Gauge	1.82
18	NGT-22-Nw	GHN-JRM-0002	LFG-009	Nuclear Gauge	2.03
19	NGT-22-Nw6	GHN-JRM-0002	LFG-009	Nuclear Gauge	1.93
20	NGT-22-Nn	GHN-JRM-0002	LFG-009	Nuclear Gauge	1.98
21	NGT-25Ns	NA	LFG-009	Nuclear Gauge	1.78
22	NGT-25Ne	NA	LFG-009	Nuclear Gauge	1.85
23	NGT-25Ne6	NA	LFG-009	Nuclear Gauge	1.64
24	NGT-25Nn	NA	LFG-009	Nuclear Gauge	1.82
25	NGT-25Nw	NA	LFG-009	Nuclear Gauge	1.89
26	NGT-25Nn6	NA	LFG-009	Nuclear Gauge	1.72
27	NGT-25Ns6	NA	LFG-009	Nuclear Gauge	1.58
28	NGT-24Oe	NA	LFG-009	Nuclear Gauge	1.71
29	NGT-22-Ow	GHN-JRM-0019	LFG-009	Nuclear Gauge	1.81
30	NGT-22-Os6	GHN-JRM-0019	LFG-009	Nuclear Gauge	1.74
31	NGT-24Ow6	NA	LFG-009	Nuclear Gauge	1.73
32	NGT-24Ow	NA	LFG-009	Nuclear Gauge	1.78
33	NGT-24Os6	NA	LFG-009	Nuclear Gauge	1.58
34	NGT-24Os	NA	LFG-009	Nuclear Gauge	1.66
35	NGT-24On6	NA	LFG-009	Nuclear Gauge	1.78
36	NGT-24On	NA	LFG-009	Nuclear Gauge	1.81
37	NGT-24Oe6	NA	LFG-009	Nuclear Gauge	1.5
38	NGT-22-Ow6	GHN-JRM-0019	LFG-009	Nuclear Gauge	1.81
39	NGT-22-On	GHN-JRM-0019	LFG-009	Nuclear Gauge	1.86
40	NGT-22-Oe6	GHN-JRM-0019	LFG-009	Nuclear Gauge	1.76
41	NGT-22-Os	GHN-JRM-0019	LFG-009	Nuclear Gauge	1.96
42	NGT-22-Oe	GHN-JRM-0019	LFG-009	Nuclear Gauge	1.99

43	NGT-22-On6	GHN-JRM-0019	LFG-009	Nuclear Gauge	1.68
44	NA	GHN-JRM-0030	LFG-009	Sand Replacement	1.53
45	NA	GHN-JRM-0031	LFG-009	Sand Replacement	1.66
46	NA	GHN-JRM-0028	LFG-009	Sand Cone	1.52
47	NA	GHN-JRM-0029	LFG-009	Sand Cone	1.84

Table C- 3. The test number, field ID, hole pit ID, test method, and dry bulk density from the measurements made within the rubble zone region of the GHN rock pile are presented.

#	Test Number	Field ID	Hole Pit ID	Test Method	Dry Bulk Density (g/cm³)
1	NDT003a	NA	LFG-005	Nuclear Gauge	1.75
2	NDT003b	NA	LFG-005	Nuclear Gauge	1.74
3	NDT003d	NA	LFG-005	Nuclear Gauge	1.66
4	NDT003e	NA	LFG-005	Nuclear Gauge	1.67
5	NDT003f	NA	LFG-005	Nuclear Gauge	1.64
6	NDT003c	NA	LFG-005	Nuclear Gauge	1.68

Table C- 4. The test number, field ID, hole pit ID, test method, and dry bulk density from the measurements made within the rubble zone region of the GHN rock pile are presented.

#	Test Number	Field ID	Hole Pit ID	Test Method	Dry Bulk Density (g/cm³)
1	9b	NA	LFG-0003	Nuclear Gauge	1.97
2	10a	NA	LFG-0003	Nuclear Gauge	1.82
3	9a	NA	LFG-0003	Nuclear Gauge	1.96
4	8b	NA	LFG-0003	Nuclear Gauge	2.07
5	8a	NA	LFG-0003	Nuclear Gauge	2.06
6	10b	NA	LFG-0003	Nuclear Gauge	1.76

**APPENDIX D. RESULTS OF TENSION INFILTRMETER
MEASUREMENTS, JUNE 2004.**

This appendix contains a progress report on the collection of tension
infiltrometer field measurements submitted to Molycorp Inc. on 27 August 2004.

**RESULTS OF TENSION INFILTRMETER MEASUREMENTS, JUNE,
2004
TASK 1.11.2.2**

Date: 27 August 2004

From: J. Sigda, NM Bureau of Geology, and H. Shannon, Dept. of Earth and Environmental Science, New Mexico Tech, with field assistance from V. McLemore, D. Wenner, and N. Wenner

To: Molycorp stability project team

Summary

Measurements of hydraulic conductivity as a function of matric potential were made on compacted and uncompactd surfaces on the top of the Goat Hill North rock pile. Hydraulic conductivity was higher for uncompactd than compactd materials.

Objective

Measure the hydraulic conductivity as a function of matric potential on horizontal exposures of rock pile materials.

Background

Tension infiltrometers allow measurement of the hydraulic conductivity or sorptivity of the porous medium under a narrow range of unsaturated conditions, typically where the matric potential varies from near 0 to ~-30 cm [Clothier and White, 1981; Ankeny, et al., 1988; Reynolds and Elrick, 1991]. Matric potential is one of the names given to head differences caused by capillary and adhesive forces in unsaturated conditions. Applications of the tension infiltrometer include measurement of macropore and preferential flow, estimation of soil structure, and

characterization of the soil hydraulic conductivity/matric potential relationship. These properties can then be used to calculate hydraulic fluxes through the vadose zone.

Measurement locations

Two locations on top of the Goat Hill North (GHN) rock pile were successfully measured on 6/24/04 and 6/29/04 (Table D-1). The compacted area is within three-four meters of stake GP-3 and the uncompacted location is within three meters of stake GP-5. These stakes mark the locations of saturated hydraulic conductivity measurements taken by Prof. W. Wilson using a Guelph permeameter in September, 2003.

Table D- 1: Measurement locations.

Description	Easting	Northing	Elevation (ft)	Measurement date
Compacted area near the eastern tensiometer nest	453710	4062043	9786	6/24/04
Uncompacted area in the center of the western tensiometer nest close to the rim	453706	4062085	9772	6/29/04

Coordinates are UTM zone 13 NAD 27. Coordinates and elevations were collected with a handheld GPS.

Methods

Three sets of measurements were made at each location according to SOP 53 using an older model tension infiltrometer from Soil Measurement Systems (Tucson, AZ). Matric potentials were measured using calibrated pressure transducers and a datalogger. Flux rates were calculated from changes in the water tower matric potential and from visual observations of water level changes with time using a watch. Whenever possible, the flux rate was calculated in two ways: regression analysis of the time rate of change in water tower matric potential (called the regression flux rate) and from the visual observations (called the stopwatch flux rate).

The matric potential in the disk, which serves as the upper boundary condition, was determined from matric potential measurements made by a pressure transducer on either the disk or at the bottom of the water tower. Each set of measurements yields a flux rate for an applied matric potential. Hydraulic conductivity was calculated for two applied matric potential values using the procedure described by Reynolds and Elrick [1991] encoded in an Excel spreadsheet.

Results

Pressure transducer data (Figure D-1) were recovered for all three measurements at the first location, but a datalogger error allowed recovery of only the data for the last measurement at the second location (Figure D-1). However, there is excellent agreement between the calculated regression flux rates and the observed stopwatch flux rates, so where necessary the latter were used to calculate hydraulic conductivity at the second site (Table D-2). R^2 values for the regression flux were all above 0.988 with the exception of the first measurement at the first site, which has an R^2 of 0.839.

Table D- 2: Flux rates

Measurement location	Regression flux rate (cm/s)	Stopwatch flux rate (cm/s)	Mean applied matric potential (cm)	Length of measurement (min)
Compacted area near the eastern tensiometer nest	0.55	0.55	-20.3	3
	1.17	1.14	-12.2	10
	1.27	1.21	-9.7	11
Uncompacted area in the center of the western tensiometer nest close to the rim	NA	1.52	-20	3
	NA	1.85	-14	2
	2.34	2.38	-10.9	5

NA = not available.

The hydraulic conductivity values for the two areas are nearly an order of magnitude different for saturated conditions, matric potential close to 0 cm, but show relatively little difference under drier conditions, matric potential = -20 cm (Table D-3 and Figure D-2). The uncompacted area has higher hydraulic conductivity values than the compacted area.

Table D- 3. Calculated hydraulic conductivity

Measurement location	Matric potential (cm)	Hydraulic conductivity (cm/s)
Compacted area near the eastern tensiometer nest	0	*2.82 x 10 ⁻⁴
	-9.7	2.07 x 10 ⁻⁴
	-20.3	1.91 x 10 ⁻⁴
Uncompacted area in the center of the western tensiometer nest close to the rim	0	*1.69x 10 ⁻³
	-10.9	7.27 x 10 ⁻⁴
	-20	2.46 x 10 ⁻⁴

* Saturated hydraulic conductivity ($\psi = 0$ cm) is estimated by extrapolating from the nearest data point using the parameter calculated according to Reynolds and Elrick [1991].

Comparison of saturated hydraulic conductivity values from tension infiltrometer and previously collected Guelph permeameter measurements at nearby locations shows that the tension infiltrometer values are roughly an order of magnitude less than those measured by the Guelph permeameter: 2.8×10^{-4} at location 1 versus 2.3×10^{-3} cm/s at stake GP-3 and 1.7×10^{-3} at location 2 versus 1.1×10^{-2} at stake GP-5. Possible causes for these differences include spatial variability (measurements are accurate but hydraulic conductivity varies widely in space), scale (the volume of rock pile material interrogated by the tension infiltrometer is much smaller than the volume interrogated by the Guelph instrument), methodology (infiltrometer applies water directly to an undisturbed land surface whereas the Guelph permeameter

applies water to an excavated hole), and procedural (saturated hydraulic conductivity is estimated from other tension infiltrometer measurements whereas the Guelph permeameter makes measurements closer to 0 cm of matric potential). We are addressing the possible procedural cause by adding a fourth tension infiltrometer measurement to each location so that we can measure hydraulic conductivity at matric potential values closer to 0 cm. Collecting measurements at numerous locations will help determine whether there is great spatial variability in hydraulic conductivity. The importance of methodology could be estimated by collecting measurement with both instruments at the same location.

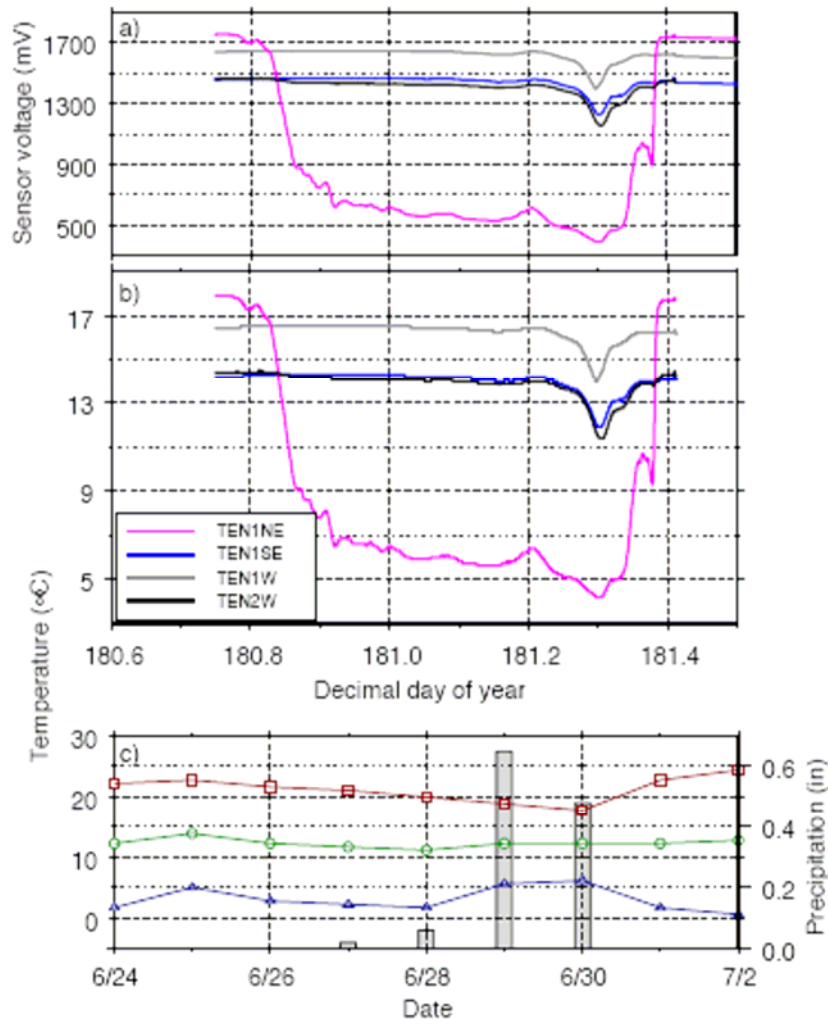


Figure D- 1. Tensiometer temperature readings and Red River meteorological data from 6/28 to 6/29/04. 6/28 = 180th day of the year 2004. a) Tensiometer temperature sensor voltages. b) Tensiometer temperature values. c) Maximum, mean, and minimum daily temperatures and daily precipitation values for Red River NWS station.

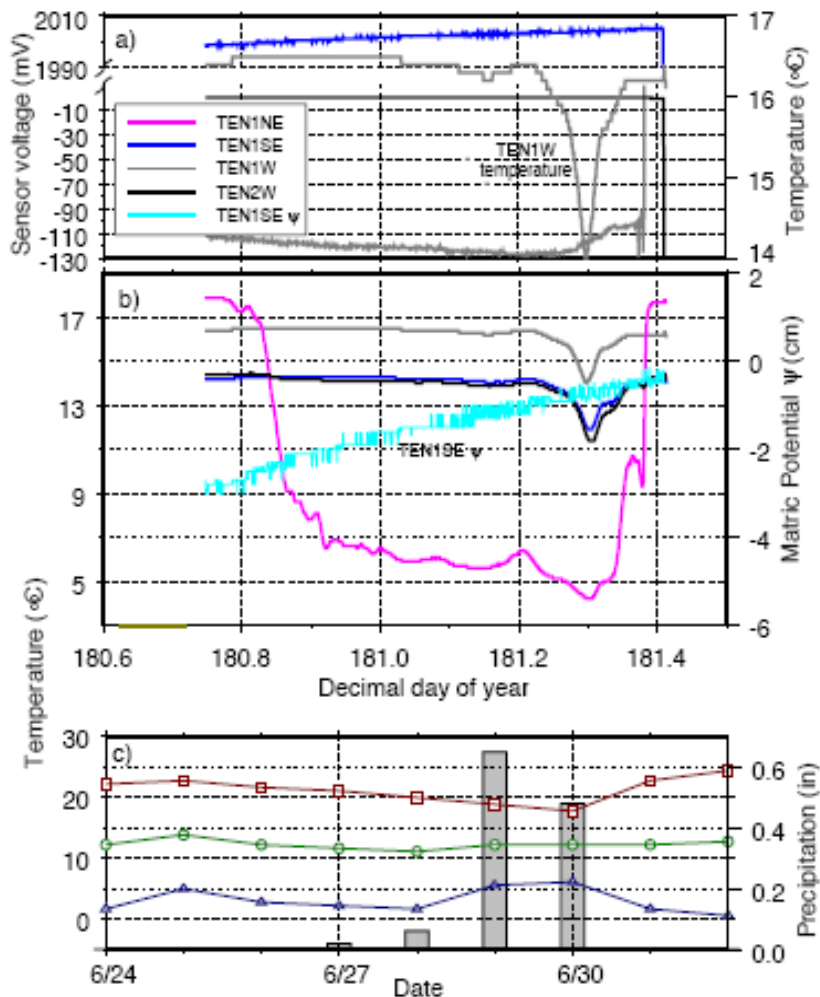


Figure D- 2. Tensiometer temperature and matric potential readings and Red River meteorological data from 6/28 to 6/29/04. 6/28 = 180th day of the year 2004. a) Tensiometer matric potential sensor voltages and TEN1W temperature. b) Tensiometer temperature and TEN1SE matric potential values. c) Maximum, mean, and minimum daily temperatures and daily precipitation values for Red River NWS station.

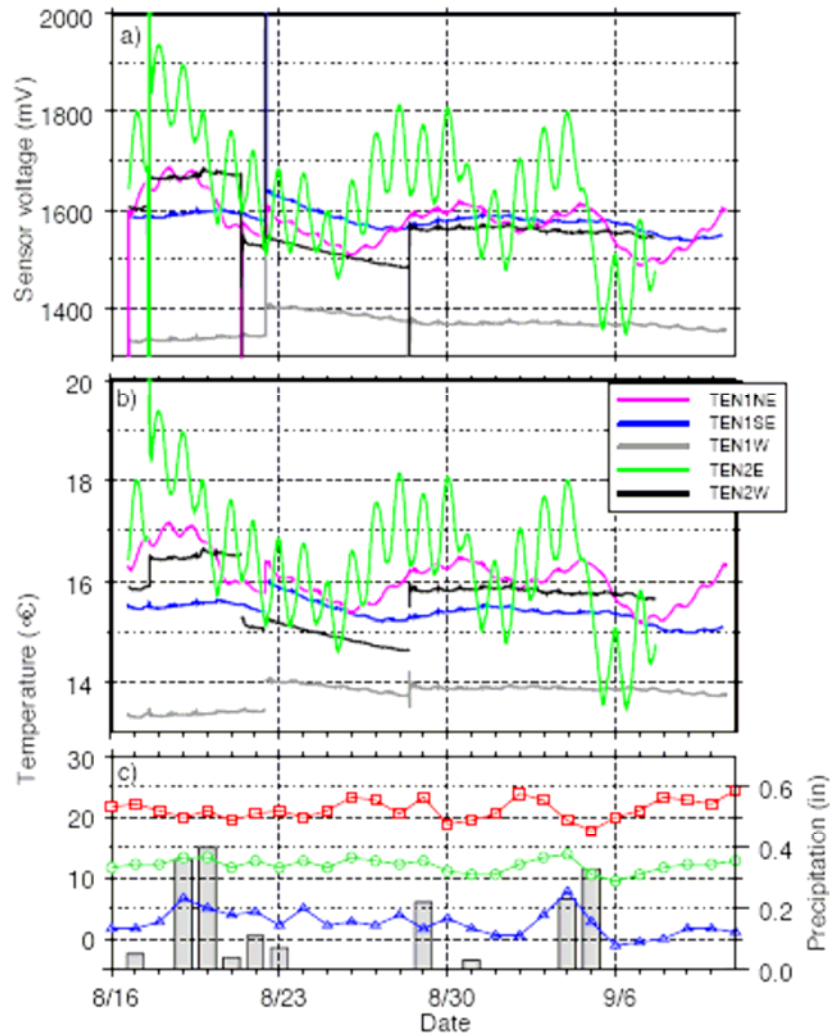


Figure D- 3. Tensiometer temperature readings and Red River meteorological data from 8/16/04 to 9/11/04. a) Tensiometer temperature sensor voltages. b) Tensiometer temperature values. c) Maximum, mean, and minimum daily temperatures and precipitation values for Red River NWS station.

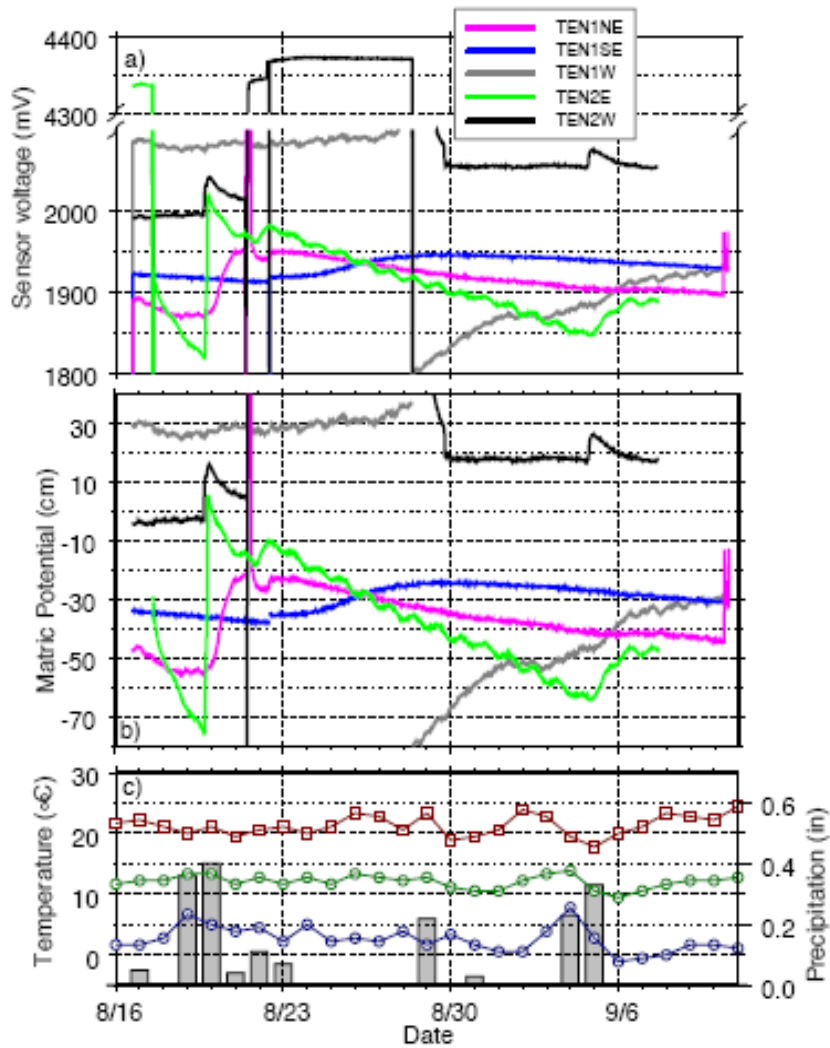


Figure D- 4. Tensiometer matric potential readings and Red River meteorological data from 8/16 to 9/11/04. a) Tensiometer matric potential sensor voltages. b) Tensiometer matric potential values. c) Maximum, mean, and minimum daily temperatures and daily precipitation values for Red River NWS station.

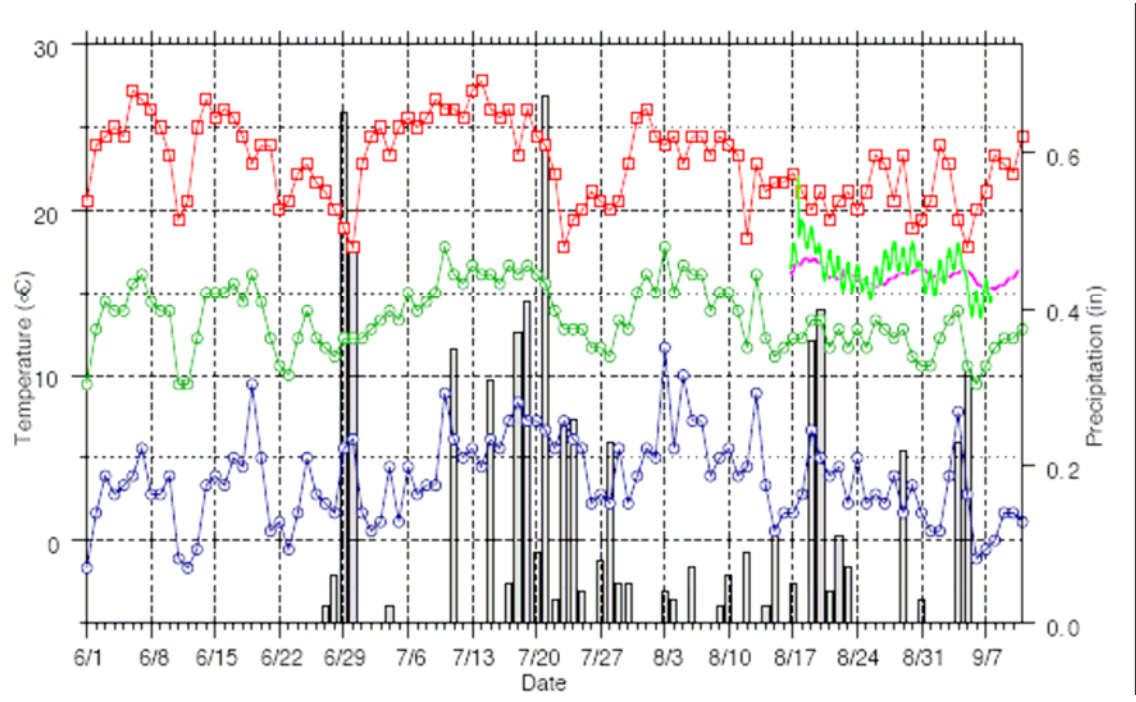


Figure D- 5. Near-surface tensiometer temperature readings and Red River meteorological data from 6/1 to 9/11/04. Temperatures for near-surface tensiometers TEN1NE and TEN2E are indicated by violet and bright green lines, respectively. Maximum, mean, and minimum daily temperatures for Red River NWS station are shown by lines with symbols, and daily precipitation values are shown as bar charts.

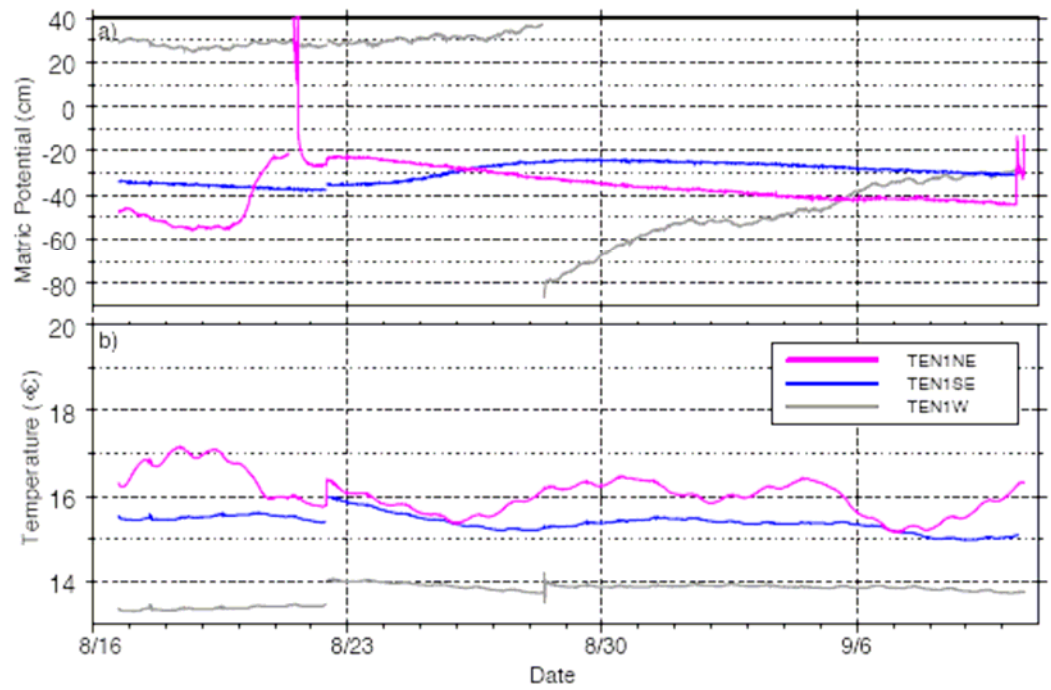


Figure D- 6. Matric potential and temperature data at station TEN1 from 8/16/04 to 9/11/04. a) Matric potential b) Temperature

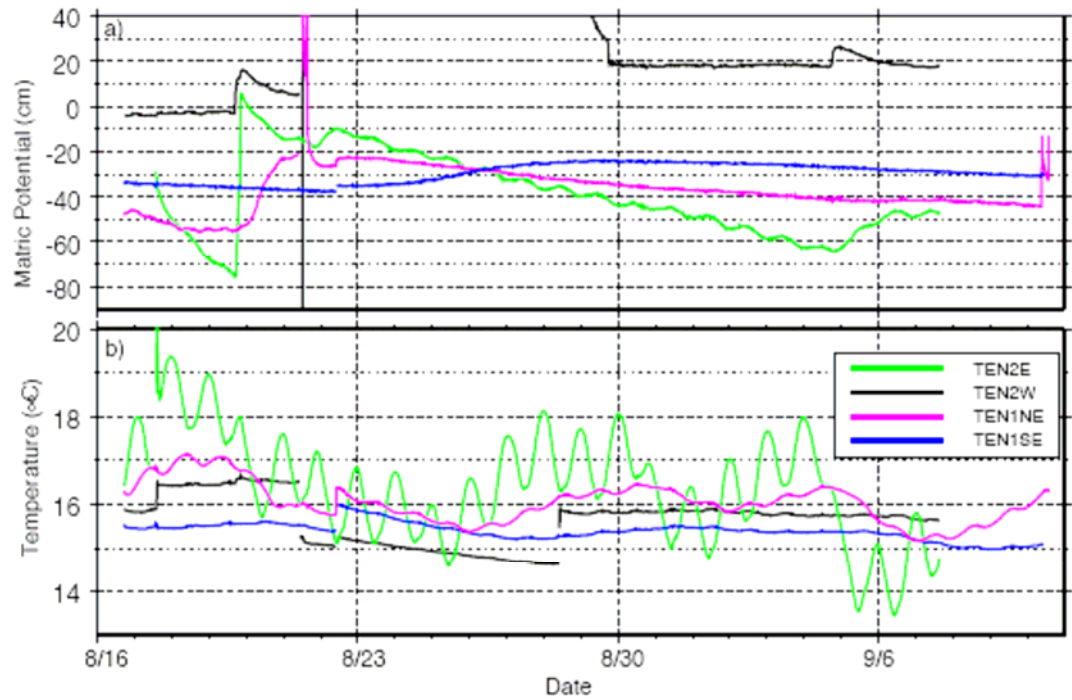


Figure D- 7. Matric potential and temperature data at station TEN2 from 8/16/04 to 9/11/04. a) Matric potential. b) Temperature. Data from station TEN1 tensiometers at similar depths are shown for comparison.

REFERENCES

Ankeny, M.D., T.C. Kaspar, and R. Horton. 1988. Design for an automated tension infiltrometer. *Soil Sci. Soc. Am.J.* 52:893-896.

Clothier, B.E. and I. White. 1981. Measurement of sorptivity and soil water diffusivity in the field. *Soil Sci. Soc. Am. J.* 45:241-245.

Reynolds, W.D. and D.E. Elrick. 1991. Determination of hydraulic conductivity using a tension infiltrometer. *Soil Sci. Soc. Am. J.* 55:633-639.

**APPENDIX E. FINAL RESULTS OF TENSION INFILTRMETER
MEASUREMENTS.**

The following appendix is a final report of the results from the tension infiltrrometer measurements made on the GHN rock pile at the Molycorp molybdenum mine in Questa, New Mexico. The report was submitted to Molycorp Inc. in January 2005.

**RESULTS OF TENSION INFILTRMETER
MEASUREMENTS, GOATHILL NORTH ROCK PILE**

TASK 1.11.2.2

Prepared by Virginia T. McLemore and Heather Shannon

Team: G. Ward Wilson, John Sigda, Joesph Marcoline, Karin Wagner, Patrick Walsh, Nate Wenner, Don Wenner, Sean Wentworth, Luiza Guitierrez, Patty Jackson Paul, Samuel Tachie-Menson

January 3, 2005

Introduction

This report presents the data obtained from guelph permeameter and tension infiltrometer measurements throughout Goathill North rock pile prior to deconstruction. This includes the guelph permeameter data collected by G. Ward Wilson as part of the Norwest's evaluation of the rockpile as well as data collected by the Utah/NM Tech/UBC Weathering Study team before and during deconstruction. The data, including raw data, are in the Molycorp database and also are summarized in Appendix 1. The measurement methods used are in SOPs 53 and 71. Samples collected by the Weathering Study team are in NAD27 coordinates. GP samples were collected by Ward Wilson and the location data was obtained from his report. The coordinate system is at this time unknown at this time. GP#A and GP#B represent

separate measurements at the same site.

The guelph permeameter measures hydraulic conductivity and the tension infiltrometer measures the hydraulic conductivity as a function of matric potential. Comparison of saturated hydraulic conductivity values at nearby locations from tension infiltrometer and Guelph permeameter measurements at nearby locations shows that the tension infiltrometer values are locally lower than those measured by the Guelph permeameter (Table E-1). Possible causes for these differences include

- different dates of measurement
- spatial variability (measurements are accurate but hydraulic conductivity varies widely)
- scale (the volume of rock pile material interrogated by the tension infiltrometer is much smaller than the volume interrogated by the Guelph instrument)
- differences in methodology
- procedural (saturated hydraulic conductivity is estimated from other tension infiltrometer measurements whereas the Guelph permeameter makes measurements closer to 0 cm of matric potential)
- some of the tension infiltrometer and Guelph permeameter measurements were conducted on disturbed surfaces where bull dozer and truck traffic compacted or loosened up the surface artificially

Additional interpretation of the data is forthcoming in future reports.

Table E- 1. Comparison of tension infiltrometer and guelph permeameter measurements.

Station id (guelph)	Ksat (cm/s)	Station id (infiltrometer)	Ksat (cm/s)
GP9-A	7.00E-03	TI01-080604	7.57E-04
GP-11A	8.40E-04	TI13-82804	6.35E-04
GP-11A	8.40E-04	TI14-82804	6.58E-03
GP5-A	1.10E+00	TI18-062404	4.96E-04
GP5-A	1.10E+00	TI19-062404	1.38E-02
GP-3A	2.30E-01	TI20-062904	1.27E-03
GP9-A	7.00E-03	TI2-080704	6.27E-04
GP-10A	7.20E-01	TI3-080704	4.60E-03
GP-11A	8.40E-04	TI4-080704	1.69E-03

Table E- 2. Results from all of the tension infiltrometer measurements.

Station_id	Ksat (cm/s)
TI7-080894	2.86E-02
TI10-080804	3.62E-04
TI9-080804	2.30E-04
TI8-080804	2.39E-04
TI6-8804	2.80E-03
TI17-101004	1.10E-01
TI20-062904	1.27E-03
TI13-82804	6.35E-04
TI14-82804	1.31E-05
TI_GHN_040624	2.82E-04
TI18-062404	4.96E-04
TI19-062404	1.38E-02
TI15-91804	5.20E-04
TI2-080704	6.27E-04
TI3-080704	4.60E-03
TI4-080704	1.69E-03
TI5-080704	1.66E-03
TI01-080604	7.57E-04
TI12-080904	3.93E-03
TI11-080904	1.37E-03
TI16-91804	9.07E-04

Table E- 3. Results from all of the guelph permeameter measurements.

<u>Station_id</u>	<u>Ksat (cm/s)</u>
GP16-A	3.00E-04
GP19-A	-8.10E-01
GP19-B	-8.10E-01
GP15-B	1.50E+00
GP15-A	1.50E+00
GP1-A	1.90E-01
GP1-B	1.90E-01
NGT 25-H2	5.15E-03
NGT 25-H1	5.15E-03
NGT 22N-H2	4.83E-04
NGT 22N-H1	4.83E-04
GP3-A	2.30E-01
GP3-B	2.30E-01
NGT 24N-H2	7.51E-03
NGT 24N-H1	7.51E-03
GP7-A	6.20E-01
GP7-B	6.20E-01
NGT 22S-H1	7.97E-03
NGT 22S-H2	7.97E-03
GP2-A	1.40E-01
GP2-B	1.40E-01
GP-4A	-1.00E+00
GP-4B	-1.00E+00
GP4A-B	2.90E-01
GP4A-A	2.90E-01
GP5-A	1.10E+00
GP5-B	1.10E+00
GP12-A	-2.50E-01
GP12-B	-2.50E-01
GP8-A	4.10E-01
GP8-B	4.10E-01
NGT 18N-H4	3.43E-03
NGT 18N-H5	3.43E-03
NGT 19N-H2	2.22E-03
NGT 19N-H1	2.22E-03
GP6-B	-2.60E+00
GP6-A	-2.60E+00
NGT 17S-H1	1.16E-04
NGT 17S-H2	1.16E-04
NGT 19N-H4	7.31E-03
NGT 19N-H3	7.31E-03
NGT 18N-H1	1.06E-02
NGT 18N-H2	1.06E-02

NGT 18S-H1	2.49E-03
NGT 18S-H2	2.49E-03
GP9-A	7.00E-03
NGT 12N-H2	1.39E-03
GP10-A	7.20E-01
GP10-B	7.20E-01
NGT 12N-H1	1.39E-03
GP11-A	8.40E-04

**APPENDIX F. “QUICK DRAW” MOISTURE PROBE AND STANDARD
TENSIO METER MEASUREMENTS.**

The following appendix contains the matric suction data collected within the trenches on the stable portion of the GHN rock pile at the Molycorp molybdenum mine in Questa, New Mexico. The measurements were collected between early September 2004 and early October 2004.

Table G- 1. Matric suction measurements made within the trenches in the stable portion of the GHN rock pile using standard tensiometers and Quick Draw tensiometers.

Date Collected	Field Id	Matric Suction (cm)
9/8/2004	GHN-LFG-0047	-163
9/8/2004	GHN-LFG-0049	-82
9/8/2004	GHN-LFG-0053	-82
9/8/2004	GHN-LFG-0050	-61
9/8/2004	GHN-LFG-0051	-41
9/8/2004	GHN-LFG-0054	-41
9/8/2004	GHN-LFG-0052	-31
9/9/2004	GHN-LFG-0062	-194
9/9/2004	GHN-LFG-0064	-102
9/9/2004	GHN-LFG-0060	-92
9/9/2004	GHN-LFG-0063	-92
9/9/2004	GHN-LFG-0061	-71
9/9/2004	GHN-LFG-0066	-71
9/9/2004	GHN-LFG-0072	-71
9/9/2004	GHN-LFG-0065	-51
9/9/2004	GHN-LFG-0069	-51
9/9/2004	GHN-LFG-0071	-51
9/9/2004	GHN-LFG-0067	-31
9/9/2004	GHN-LFG-0068	-31
9/9/2004	GHN-LFG-0070	-31
9/10/2004	GHN-LFG-0073	-61
9/10/2004	GHN-LFG-0074	-51
9/10/2004	GHN-LFG-0078	-51
9/10/2004	GHN-LFG-0075	-41
9/10/2004	GHN-LFG-0077	-31
9/10/2004	GHN-LFG-0076	-20
9/17/2004	GHN-KMD-0001	-214
9/17/2004	GHN-KMD-0002	-163
9/17/2004	GHN-KMD-0007	-71
9/17/2004	GHN-KMD-0003	-51
9/17/2004	GHN-KMD-0012	-51
9/17/2004	GHN-KMD-0004	-20
9/17/2004	GHN-KMD-0008	-20
9/17/2004	GHN-KMD-0006	-10
9/18/2004	GHN-KMD-0010	-92
9/18/2004	GHN-KMD-0011	-44
9/18/2004	GHN-KMD-0009	-25
9/19/2004	GHN-KMD-0023	-41
9/19/2004	GHN-KMD-0024	-41
9/19/2004	GHN-KMD-0025	-20
9/19/2004	GHN-KMD-0038	-20
9/19/2004	GHN-KMD-0039	-20
9/19/2004	GHN-KMD-0042	-20

9/19/2004	GHN-KMD-0043	-20
9/19/2004	GHN-KMD-0022	-10
9/19/2004	GHN-KMD-0036	-10
9/19/2004	GHN-KMD-0037	-10
9/19/2004	GHN-KMD-0041	-10
9/19/2004	GHN-KMD-0040	0
9/24/2004	GHN-KMD-0049	-122
9/24/2004	GHN-KMD-0045	-112
9/24/2004	GHN-KMD-0048	-92
9/24/2004	GHN-KMD-0044	-51
9/24/2004	GHN-KMD-0046	-31
9/24/2004	GHN-KMD-0047	-10
9/25/2004	GHN-KMD-0052	-122
9/25/2004	GHN-KMD-0051	-92
9/25/2004	GHN-KMD-0050	-82
9/26/2004	GHN-KMD-0054	-133
9/26/2004	GHN-KMD-0064	-102
9/26/2004	GHN-KMD-0063	-92
9/26/2004	GHN-KMD-0053	-82
9/26/2004	GHN-KMD-0057	-71
9/26/2004	GHN-KMD-0065	-51
9/26/2004	GHN-KMD-0055	-41
9/26/2004	GHN-KMD-0056	-31
9/26/2004	GHN-KMD-0062	-31
10/1/2004	GHN-KMD-0067	-51
10/1/2004	GHN-KMD-0069	-51
10/1/2004	GHN-KMD-0070	-51
10/1/2004	GHN-KMD-0068	-31
10/2/2004	GHN-KMD-0075	-122
10/2/2004	GHN-KMD-0076	-102
10/2/2004	GHN-KMD-0072	-82
10/2/2004	GHN-KMD-0071	-51
10/2/2004	GHN-KMD-0073	-51
10/2/2004	GHN-KMD-0077	-51
10/3/2004	GHN-KMD-0084	-71
10/3/2004	GHN-KMD-0086	-61
10/3/2004	GHN-KMD-0090	-61
10/3/2004	GHN-KMD-0082	-51
10/3/2004	GHN-KMD-0083	-51
10/3/2004	GHN-KMD-0085	-51
10/3/2004	GHN-KMD-0088	-51
10/3/2004	GHN-KMD-0093	-51
10/3/2004	GHN-KMD-0089	-41
10/3/2004	GHN-KMD-0087	-31
10/3/2004	GHN-KMD-0091	-20
10/9/2004	GHN-JRM-0020	-204
10/9/2004	GHN-JRM-0021	-143
10/9/2004	GHN-JRM-0013	-112

10/9/2004	GHN-JRM-0019	-102
10/9/2004	GHN-JRM-0001	-92
10/9/2004	GHN-JRM-0024	-92
10/9/2004	GHN-JRM-0010	-71
10/9/2004	GHN-JRM-0002	-61
10/9/2004	GHN-JRM-0008	-51
10/9/2004	GHN-JRM-0012	-51
10/9/2004	GHN-JRM-0003	-41
10/9/2004	GHN-JRM-0004	-41
10/9/2004	GHN-JRM-0005	-41
10/9/2004	GHN-JRM-0006	-41
10/9/2004	GHN-JRM-0007	-41
10/9/2004	GHN-JRM-0011	-41
10/9/2004	GHN-JRM-0014	-41
10/9/2004	GHN-JRM-0015	-41
10/9/2004	GHN-JRM-0009	-20
10/10/2004	GHN-JRM-0026	-102
10/10/2004	GHN-JRM-0025	-61

**APPENDIX G. ONE-DAY RECORD OF TENSIO METER DATA FROM
DATA LOGGER.**

The following appendix is a one-day record of matric suction and temperature recorded at TEN1NE by the data logger at the nested tensiometers station.

Table G- 2. One day record of matric suction and temperature recorded at TEN1NE by the data logger at the nested tensiometers station.

Record Id	Station Id	Year	Day of Year	Hr	Min	Sec	Matric Potential (mV)	Temp (mV)	Matric Potential (cm)	Temp (deg C)
1201	TEN1NE	2004	229	17	03	30.8	1890	1597	-47.1	16.3
2349	TEN1NE	2004	229	17	04	30.8	1890	1602	-47.1	16.3
738	TEN1NE	2004	229	17	16	16.4	1889.5	1597	-47.3	16.3
1953	TEN1NE	2004	229	17	31	16.4	1890	1596.5	-47.1	16.3
269	TEN1NE	2004	229	17	46	16.3	1890	1595.6	-47.1	16.3
468	TEN1NE	2004	229	18	01	16.3	1889.8	1594.4	-47.1	16.2
760	TEN1NE	2004	229	18	16	16.4	1889.9	1594	-47.1	16.2
1756	TEN1NE	2004	229	18	31	16.4	1889.7	1593.2	-47.2	16.2
3101	TEN1NE	2004	229	18	46	16.3	1889.4	1592.6	-47.3	16.2
449	TEN1NE	2004	229	19	01	16.3	1889.6	1592.1	-47.2	16.2
1004	TEN1NE	2004	229	19	16	16.4	1889.9	1592	-47.1	16.2
3147	TEN1NE	2004	229	19	31	16.4	1889.8	1591.8	-47.1	16.2
2602	TEN1NE	2004	229	19	46	16.3	1890.5	1592	-46.9	16.2
897	TEN1NE	2004	229	20	01	16.4	1891	1592.1	-46.6	16.2
2831	TEN1NE	2004	229	20	16	16.4	1890.8	1592.2	-46.7	16.2
300	TEN1NE	2004	229	20	31	16.3	1890.8	1592.6	-46.7	16.2
2535	TEN1NE	2004	229	20	46	16.3	1891.6	1593.3	-46.4	16.2
270	TEN1NE	2004	229	21	01	16.4	1891.8	1594	-46.3	16.2
616	TEN1NE	2004	229	21	16	16.4	1891.9	1594.6	-46.3	16.2
3237	TEN1NE	2004	229	21	31	16.3	1892.7	1595.5	-46	16.3
2378	TEN1NE	2004	229	21	46	16.3	1893.3	1596.3	-45.7	16.3
926	TEN1NE	2004	229	22	01	16.4	1893.3	1597.4	-45.7	16.3
181	TEN1NE	2004	229	22	16	16.3	1892.7	1598.6	-46	16.3
374	TEN1NE	2004	229	22	31	16.3	1892.8	1599.7	-45.9	16.3
3091	TEN1NE	2004	229	22	46	16.4	1892.6	1601	-46	16.3
2842	TEN1NE	2004	229	23	01	16.4	1892.6	1602.1	-46	16.3
2615	TEN1NE	2004	229	23	16	16.3	1892	1603.8	-46.2	16.3
1428	TEN1NE	2004	229	23	31	16.3	1892.5	1605.1	-46	16.4
2891	TEN1NE	2004	229	23	46	16.4	1892.5	1606.5	-46	16.4

APPENDIX H. PARTICLE SIZE DISTRIBUTIONS.

The following appendix presents results from the grain size analyses conducted on samples within the different regions of the GHN rock pile at the Molycorp molybdenum mine, Questa, New Mexico.

Table H- 1. The gravel, sand, silt, and clay weight percentages from grain size analyses conducted on samples from the WR1 region of the GHN rock pile.

#	Field Id	Weight Percentages				Field Description	Hole Pit Id
		Gravel	Sand	Silt	Clay		
1	GHNLF0006	5.9	60.8	20.3	13.0		LFG-0002
2	GHNLF0005	4.9	61.4	13.8	19.9		LFG-0002
3	GHNLF0004	4.5	60.0	16.5	19.0		LFG-0002
4	GHNLF0037	46.0	40.3	10.4	3.3	Unit H	LFG-0004
5	GHNLF0088	62.5	29.4	5.9	2.1	Unit O	LFG-005
6	GHNLF0085	57.0	32.3	6.7	4.0	Unit K	LFG-005
7	GHNKMD0019	53.3	37.8	5.8	3.1	Unit O	LFG-006
8	GHNKMD0028	51.5	39.0	8.1	1.5	Unit N	LFG-006
9	GHNKMD0026	61.2	28.8	5.6	4.4	Unit M	LFG-006
10	GHNKMD0016	74.8	19.6	4.7	0.9	Unit S	LFG-006
11	GHNKMD0015	63.1	29.1	6.1	1.8	Unit R	LFG-006
12	GHNKMD0018	61.7	33.6	4.4	0.3	Unit J	LFG-006
13	GHNKMD0014	69.6	25.0	3.1	2.3	Unit K	LFG-006
14	GHNKMD0027	57.6	32.8	8.2	1.5	Unit N	LFG-006
15	GHNKMD0057	59.6	31.7	5.3	3.4	Unit O	LFG-007
16	GHNKMD0062	49.1	41.1	7.7	2.2	Unit N	LFG-007
17	GHNKMD0063	49.8	41.0	8.3	0.8	Unit J	LFG-007
18	GHNKMD0053	58.8	33.3	5.1	2.8	Unit N-J	LFG-007
19	GHNKMD0052	48.0	39.5	6.8	5.7	Unit K	LFG-007
20	GHNKMD0051	49.8	39.5	6.5	4.2	Unit O	LFG-007
21	GHNKMD0056	65.1	28.1	4.6	2.2	Unit V	LFG-007
22	GHNKMD0065	58.8	33.3	5.0	2.9	Unit V	LFG-007
23	GHNKMD0055	55.7	32.3	10.9	1.1	Unit I	LFG-007
24	GHNKMD0078	87.4	9.7	1.7	1.3	Unit U	LFG-008
25	GHNKMD0100	44.9	45.8	5.5	3.8		LFG-008
26	GHNKMD0096	50.1	39.2	6.7	4.0	Unit J	LFG-008
27	GHNKMD0095	41.8	47.0	5.5	5.7	Unit C	LFG-008
28	GHNKMD0081	45.9	41.1	8.8	4.2	Unit R	LFG-008
29	GHNKMD0080	55.0	33.7	7.0	4.3	Unit S	LFG-008
30	GHNKMD0071	60.5	30.7	5.3	3.6	Unit U-V *	LFG-008
31	GHNKMD0074	60.1	32.3	4.6	3.0	Unit U	LFG-008
32	GHNKMD0073	58.4	32.0	6.1	3.6	Unit O	LFG-008
33	GHNKMD0072	77.0	19.3	2.8	0.9	Unit O **	LFG-008
34	GHNKMD0072	54.2	36.8	6.1	2.9	Unit O **	LFG-008
35	GHNKMD0072	48.5	38.9	7.8	4.9	Unit O **	LFG-008
36	GHNKMD0079	61.0	30.3	5.1	3.6	Unit U	LFG-008

* Contact of U-V

** Coarse Zone in Unit O

Table H- 2. The gravel, sand, silt, and clay weight percentages from grain size analyses conducted on samples from the WR2 region of the GHN rock pile.

#	Field_id	Weight Percentages				Field Description	Hole Pit Id
		Gravel	Sand	Silt	Clay		
1	GHNJRM0028	45.06	44.2	7.97	2.77	Unit K	LFG-009
2	GHNJRM0029	63.4	29.36	6.67	0.57	Unit J	LFG-009
3	GHNJRM0030	51.48	38.1	7.88	2.54	Unit O	LFG-009
4	GHNJRM0031	56.94	35	5.84	2.22	Unit O	LFG-009
5	GHNVTM0450	70.45	24.21	3.23	2.1	Unit O	LFG-009
6	GHNVTM0453	41.56	47.93	8.2	2.3	Unit O	LFG-009

Table H- 3. The gravel, sand, silt, and clay weight percentages from grain size analyses conducted on samples from the rubble zone region of the GHN rock pile.

#	Field_id	Weight Percentages				Field Description	Hole Pit Id
		Gravel	Sand	Silt	Clay		
1	GHNEHP0003	57.62	27.89	13.33	1.17	Rubble Zone	LFG-011
2	GHNVTM0598	86.68	11.49	1.17	0.66	Rubble Zone	LFG-019
3	GHNVTM0607	80.64	15.73	2.76	0.87	Rubble Zone	LFG-022

Table H- 4. The gravel, sand, silt, and clay weight percentages from grain size analyses conducted on samples from the colluvium region of the GHN rock pile.

#	Field_id	Weight Percentages				Field Description	Hole Pit Id
		Gravel	Sand	Silt	Clay		
1	GHNEHP0005	8.27	67.25	17.04	7.44	Colluvium	LFG-013

Table H- 5. The gravel, sand, silt, and clay weight percentages from grain size analyses conducted on samples from the traffic zone region of the GHN rock pile.

#	Field_id	Weight Percentages				Field Description	Hole Pit Id
		Gravel	Sand	Silt	Clay		
1	GHNLF0018	49.44	36.08	8.85	5.63	Traffic Zone	LFG-0003

APPENDIX I. CONSTANT FLUX SIMULATIONS.

The following pages present the output results of maximum, minimum, mean, and median pressure heads from the final time step of the four different constant flux levels.

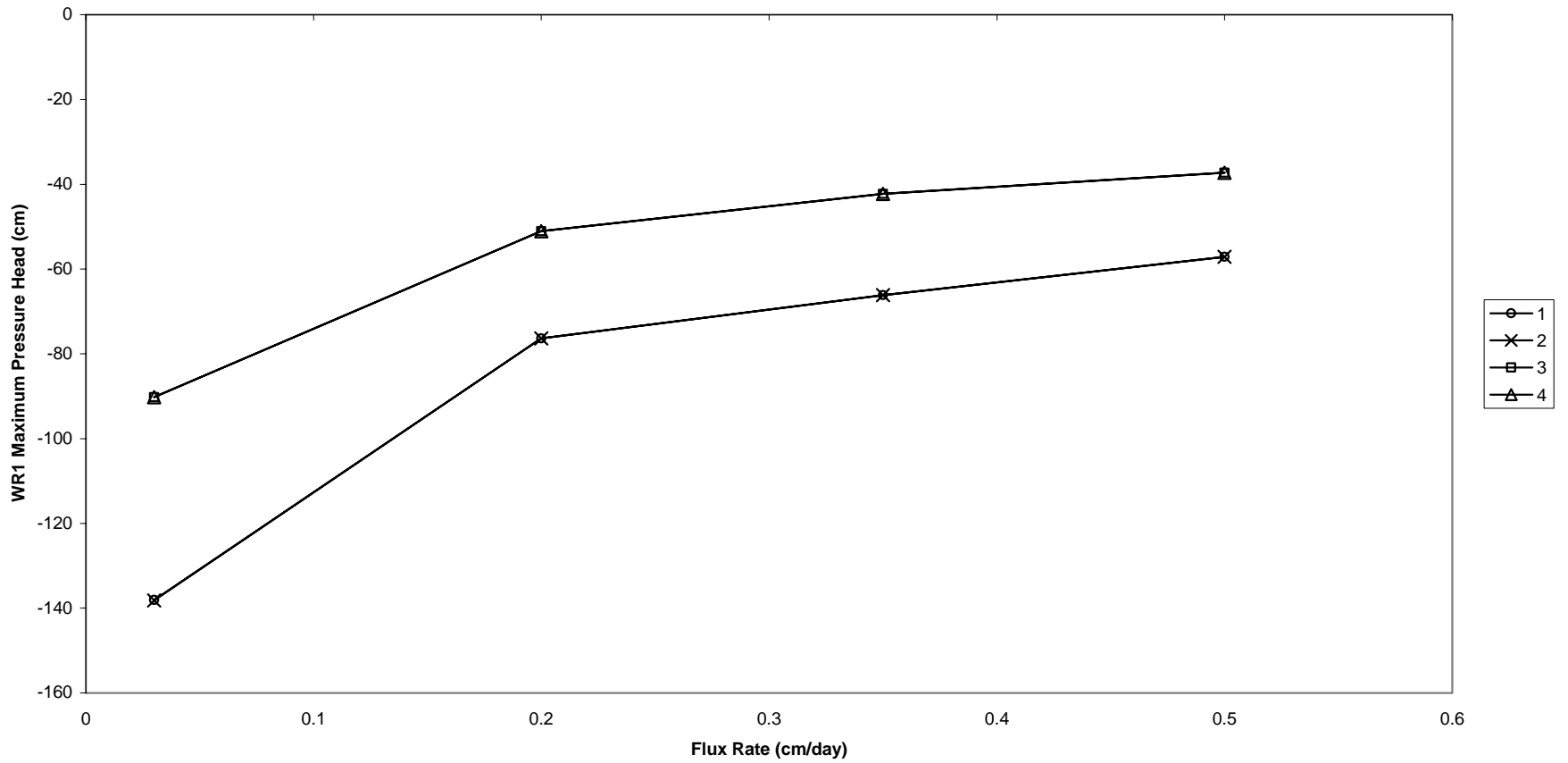


Figure I- 1. The maximum pressure head within the WR1 region of the model domain for four subsequent constant flux levels.

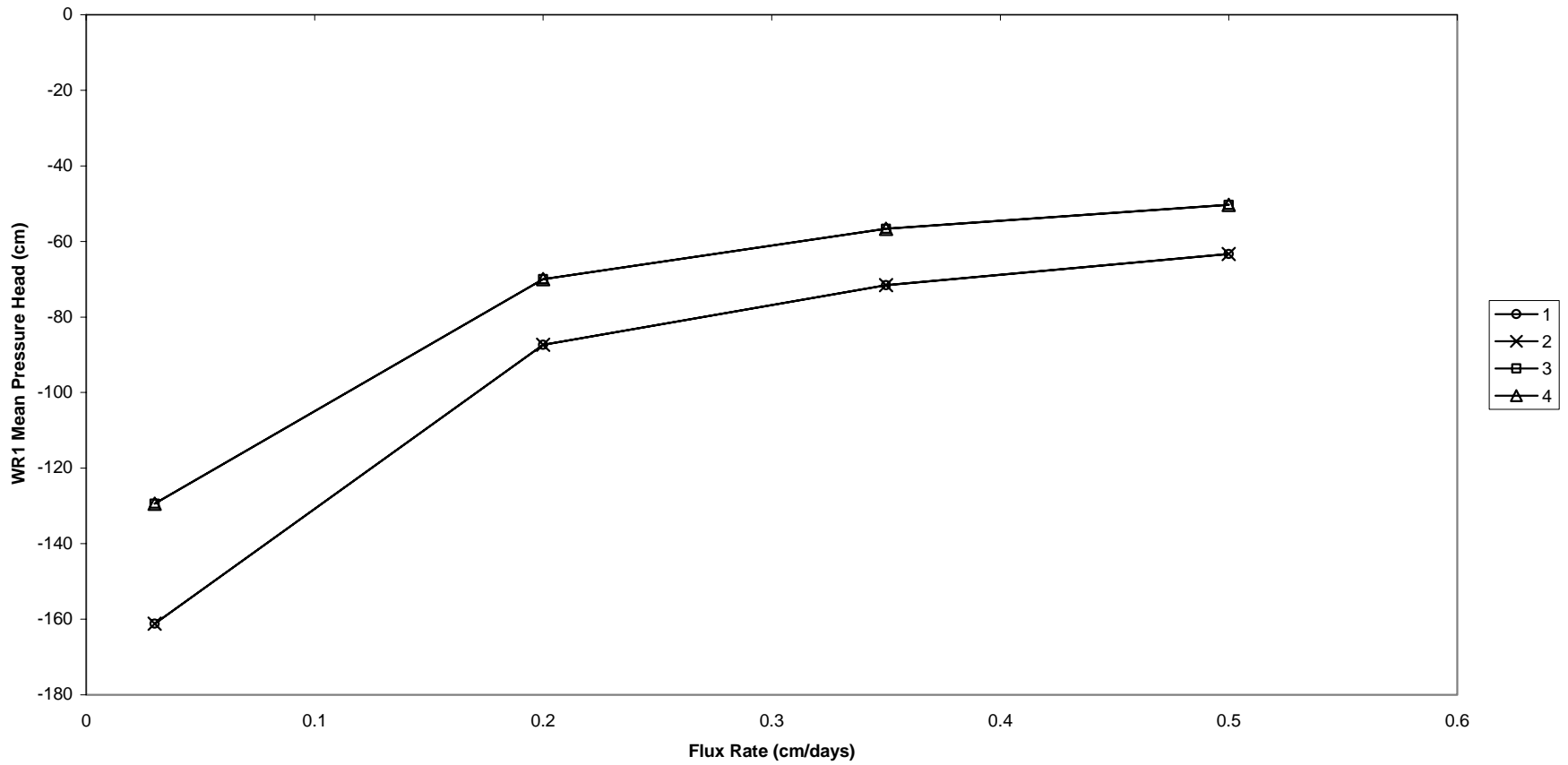


Figure I- 2. The mean pressure head distribution within the WR1 region of the model domain for four subsequent constant flux levels.

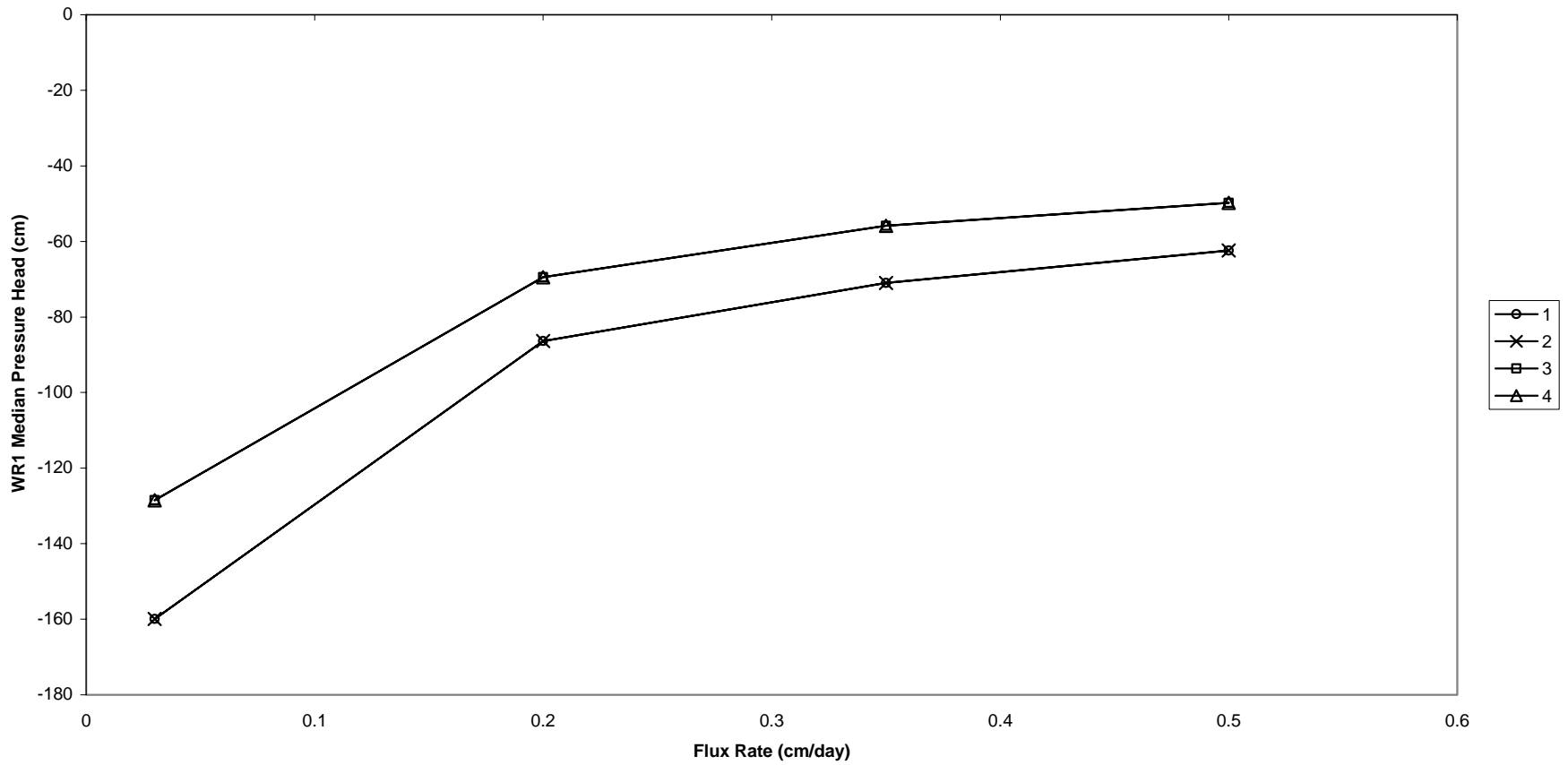


Figure I- 3. The median pressure head within the WR1 region of the model domain for four subsequent constant flux levels.

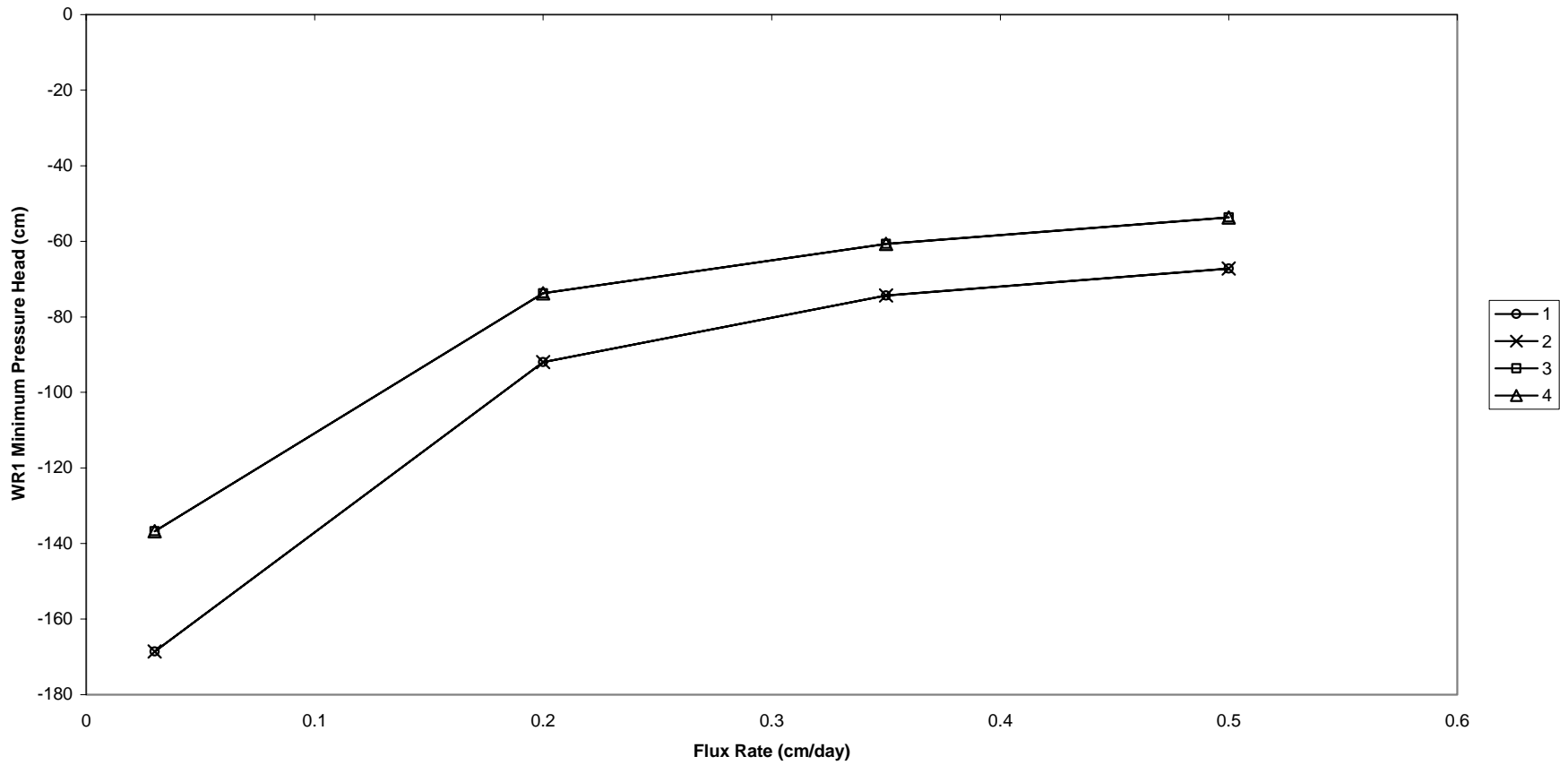


Figure I- 4. The minimum pressure head within the WR1 region of the model domain for four subsequent constant flux levels.

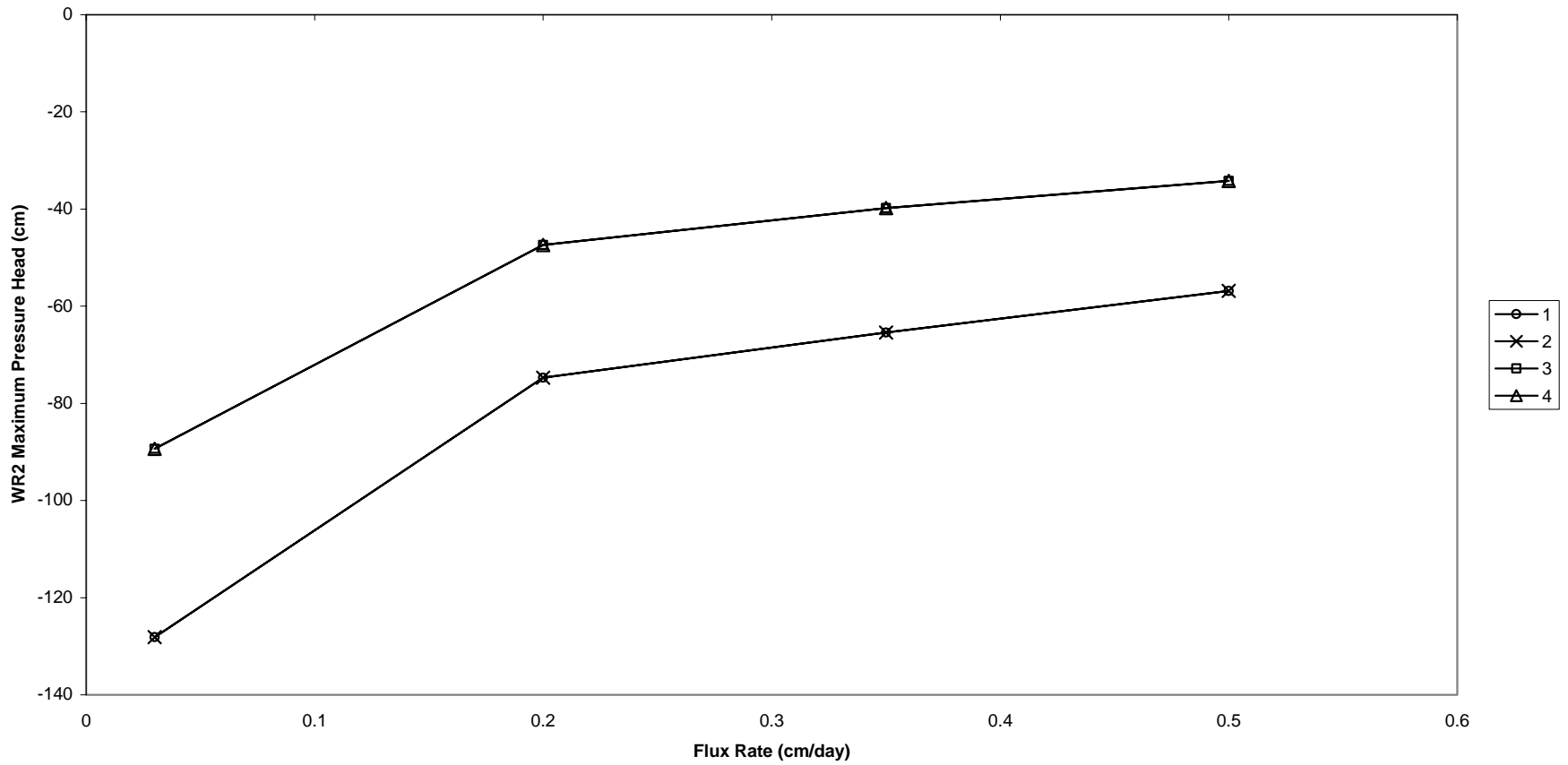


Figure I- 5. The maximum pressure head within the WR2 region of the model domain for four subsequent constant flux levels.

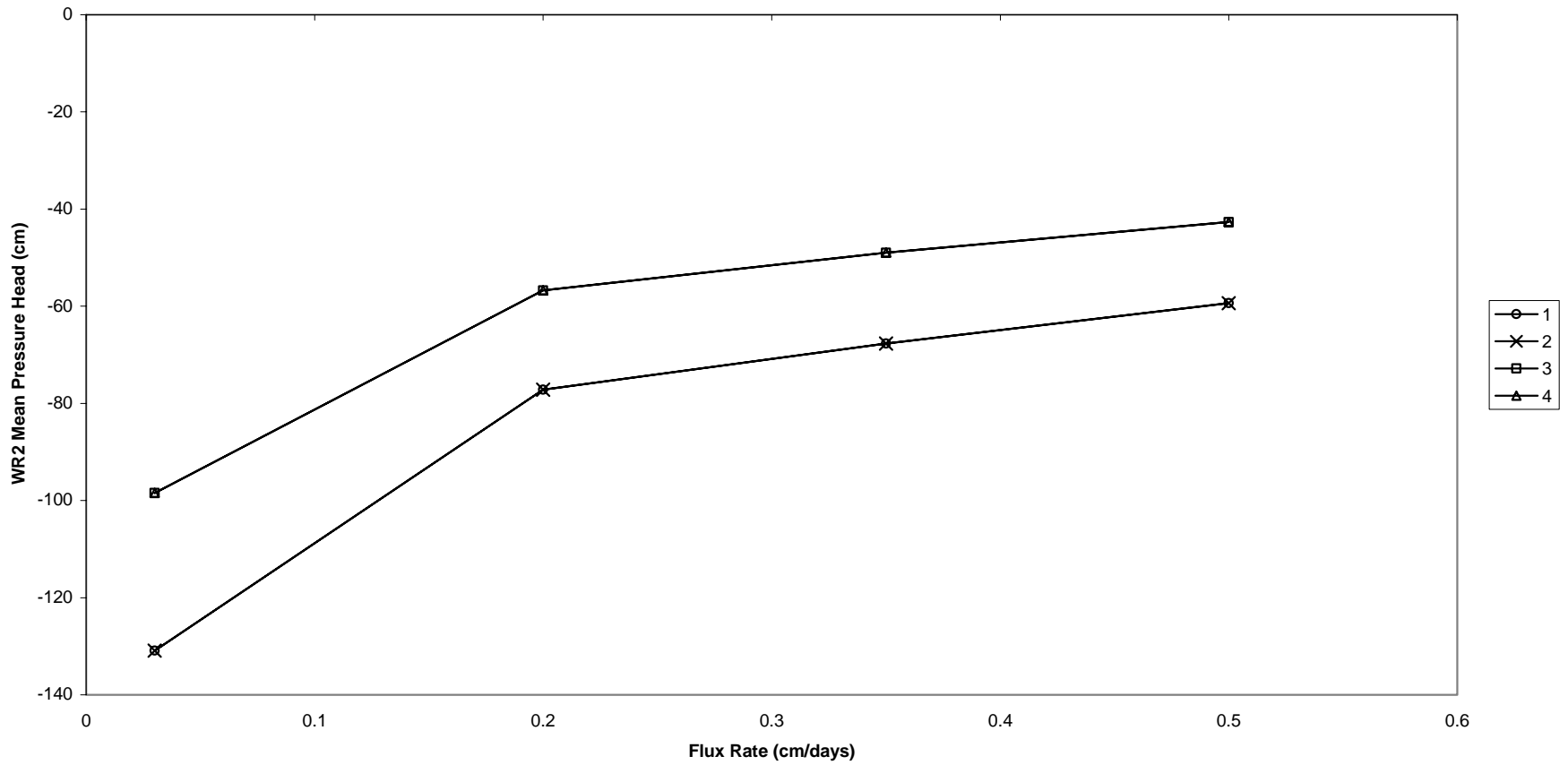


Figure I- 6. The mean pressure head within the WR2 region of the model domain for four subsequent constant flux levels.

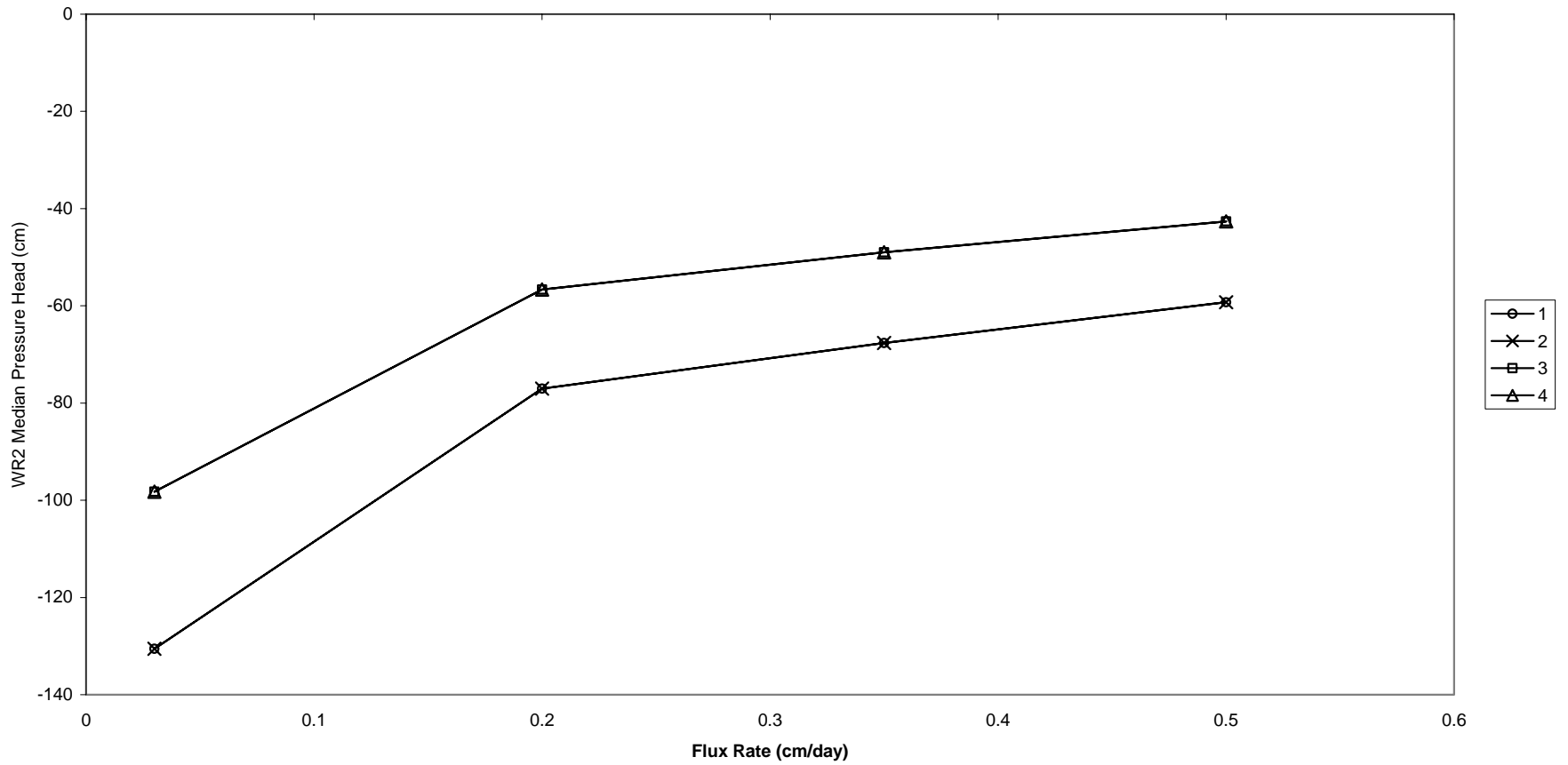


Figure I- 7. The median pressure head within the WR2 region of the model domain for four subsequent constant flux levels.

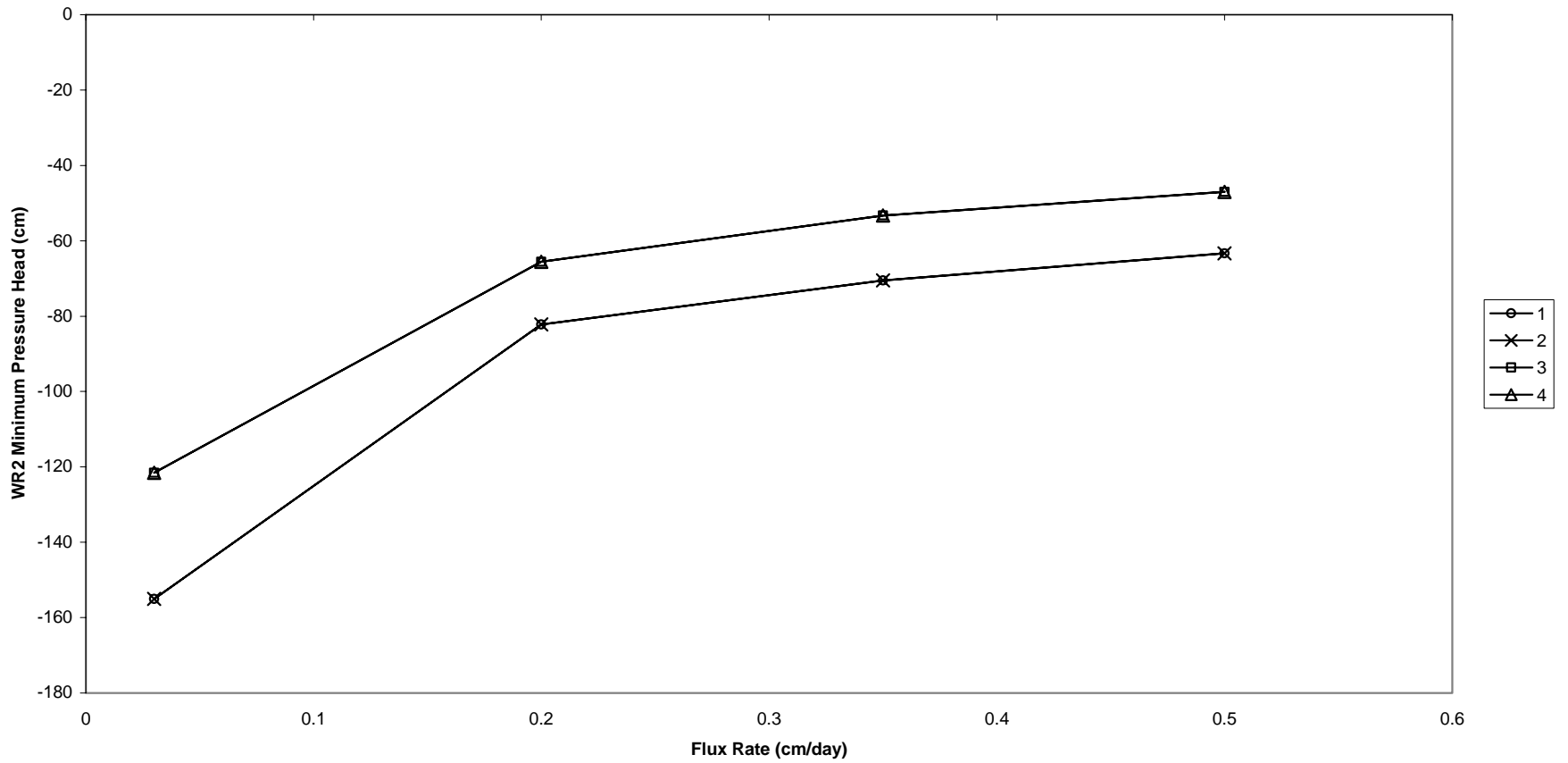


Figure I- 8. The minimum pressure head within the WR2 region of the model domain for four subsequent constant flux levels.

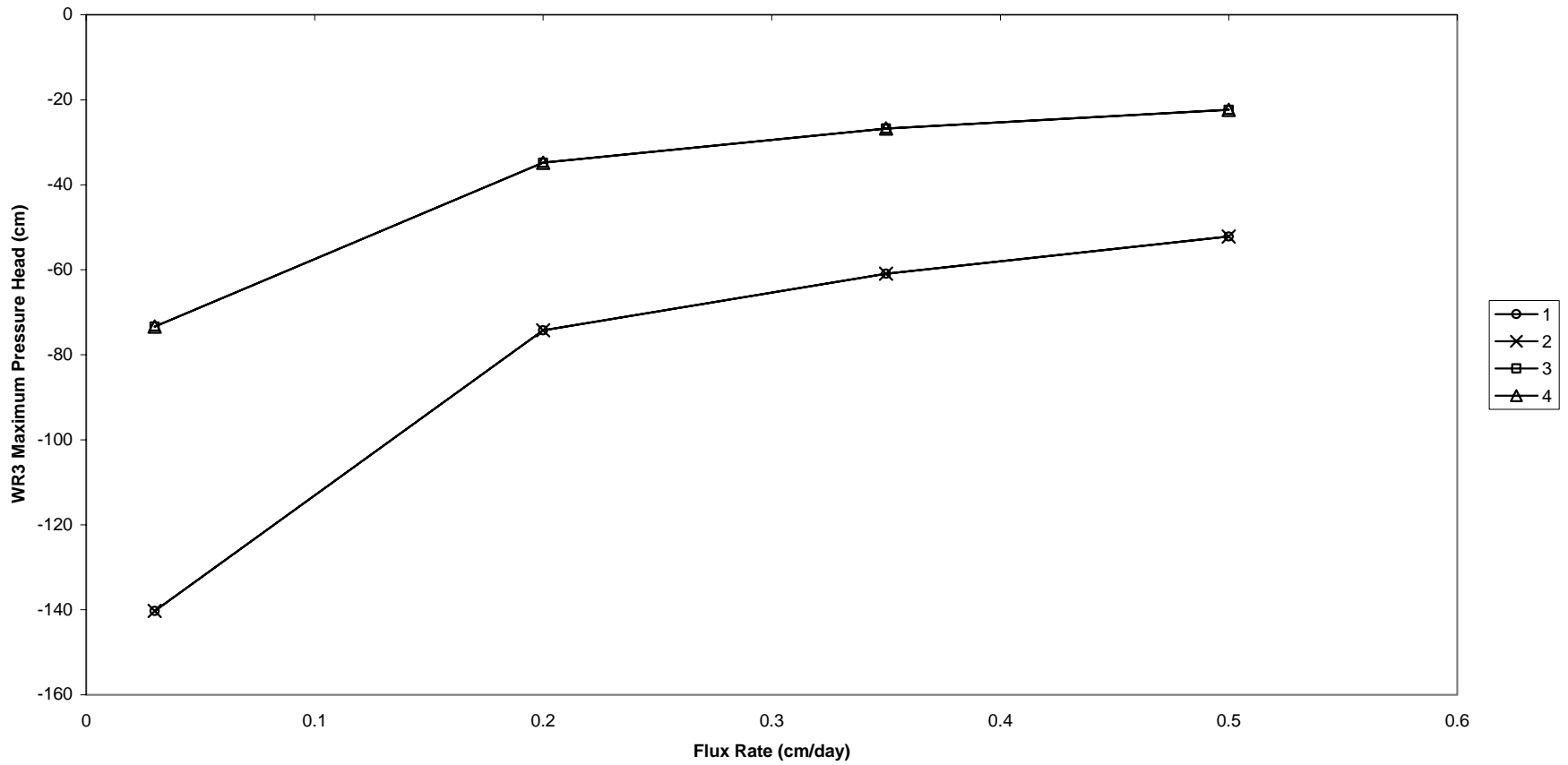


Figure I- 9. The maximum pressure head within the WR3 region of the model domain for four subsequent constant flux levels.

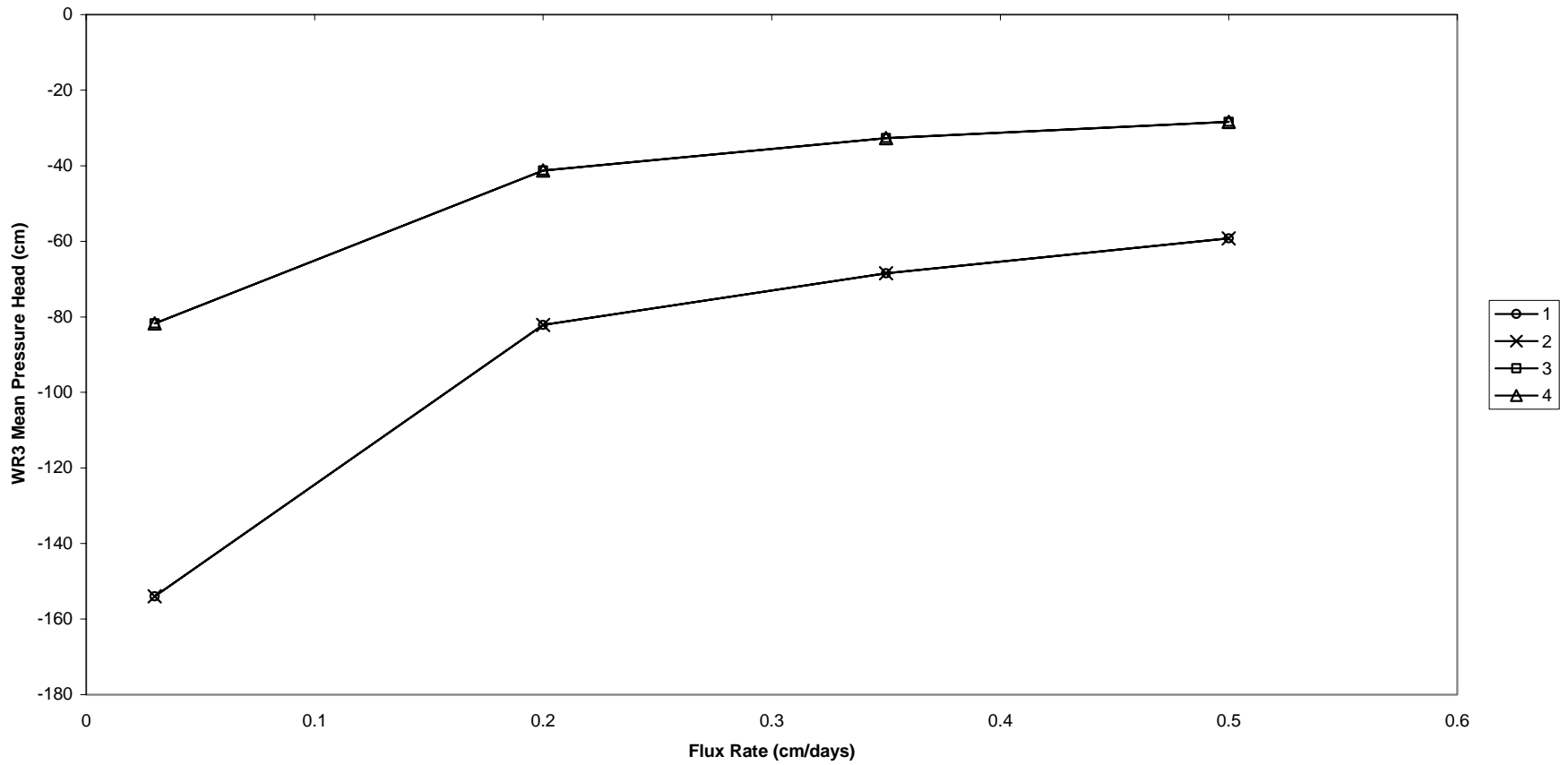


Figure I- 10. The mean pressure head within the WR3 region of the model domain for four subsequent constant flux levels.

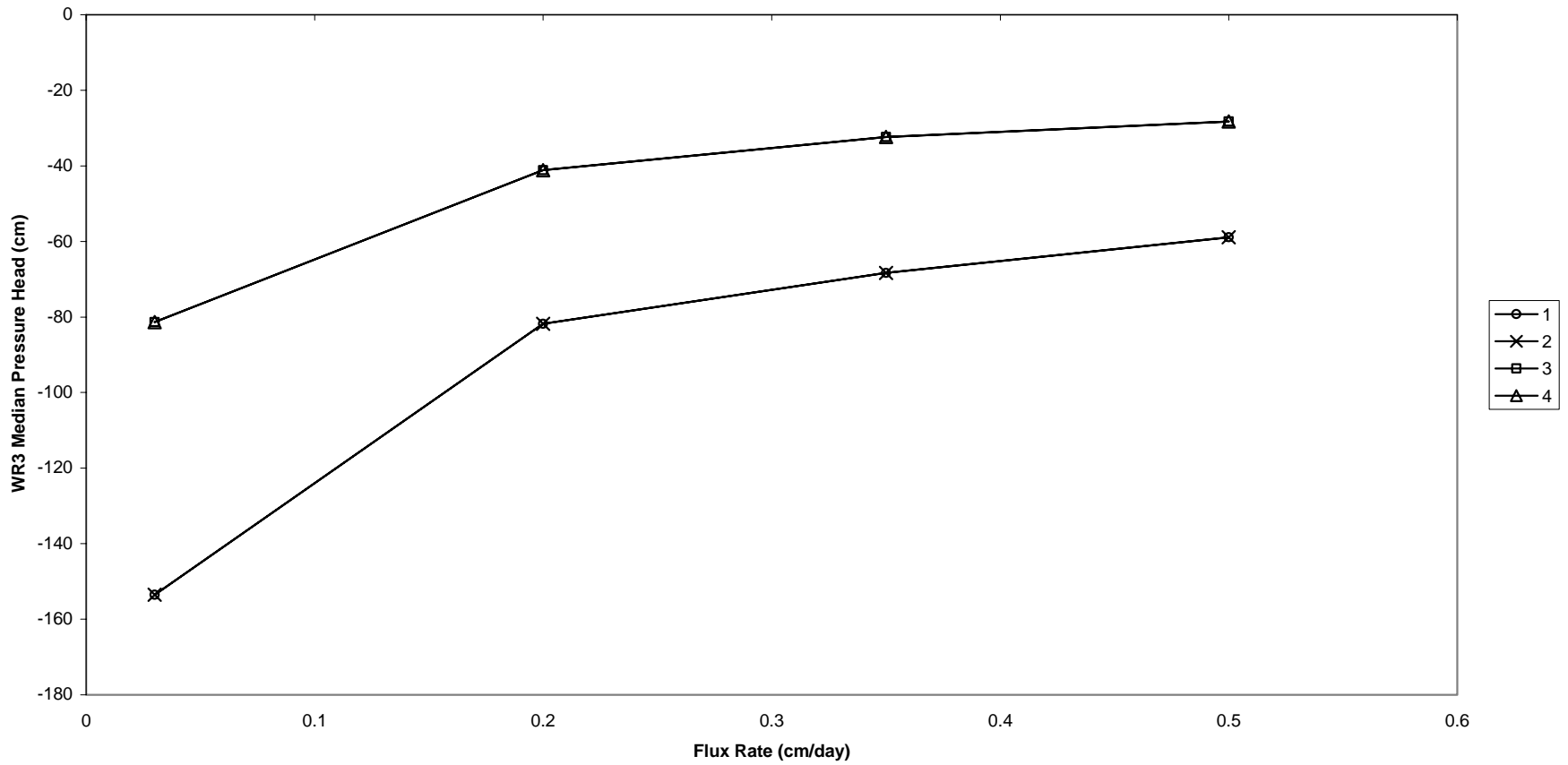


Figure I- 11. The median pressure head within the WR3 region of the model domain for four subsequent constant flux levels.

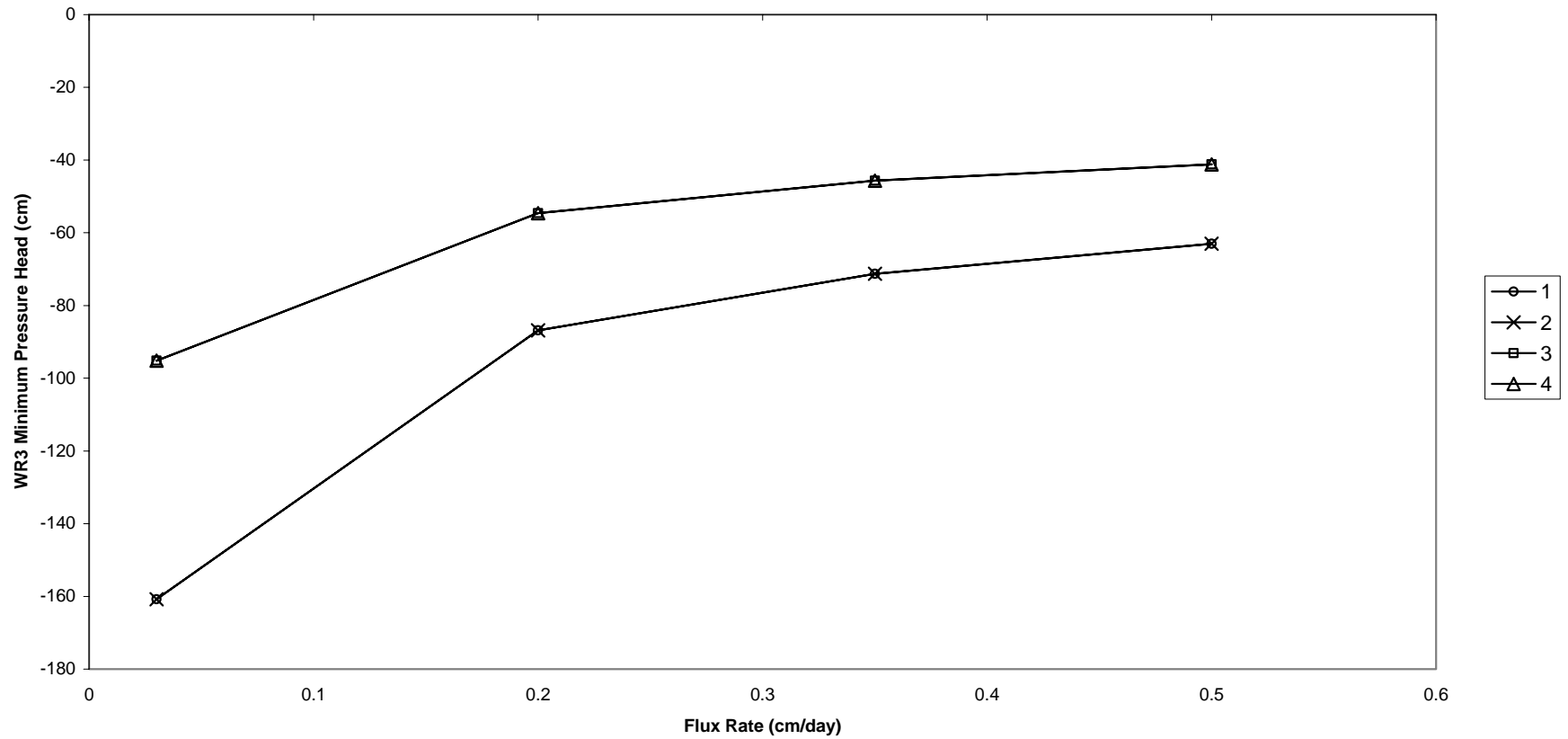


Figure I- 12. The minimum pressure head within the WR3 region of the model domain for four subsequent constant flux levels.

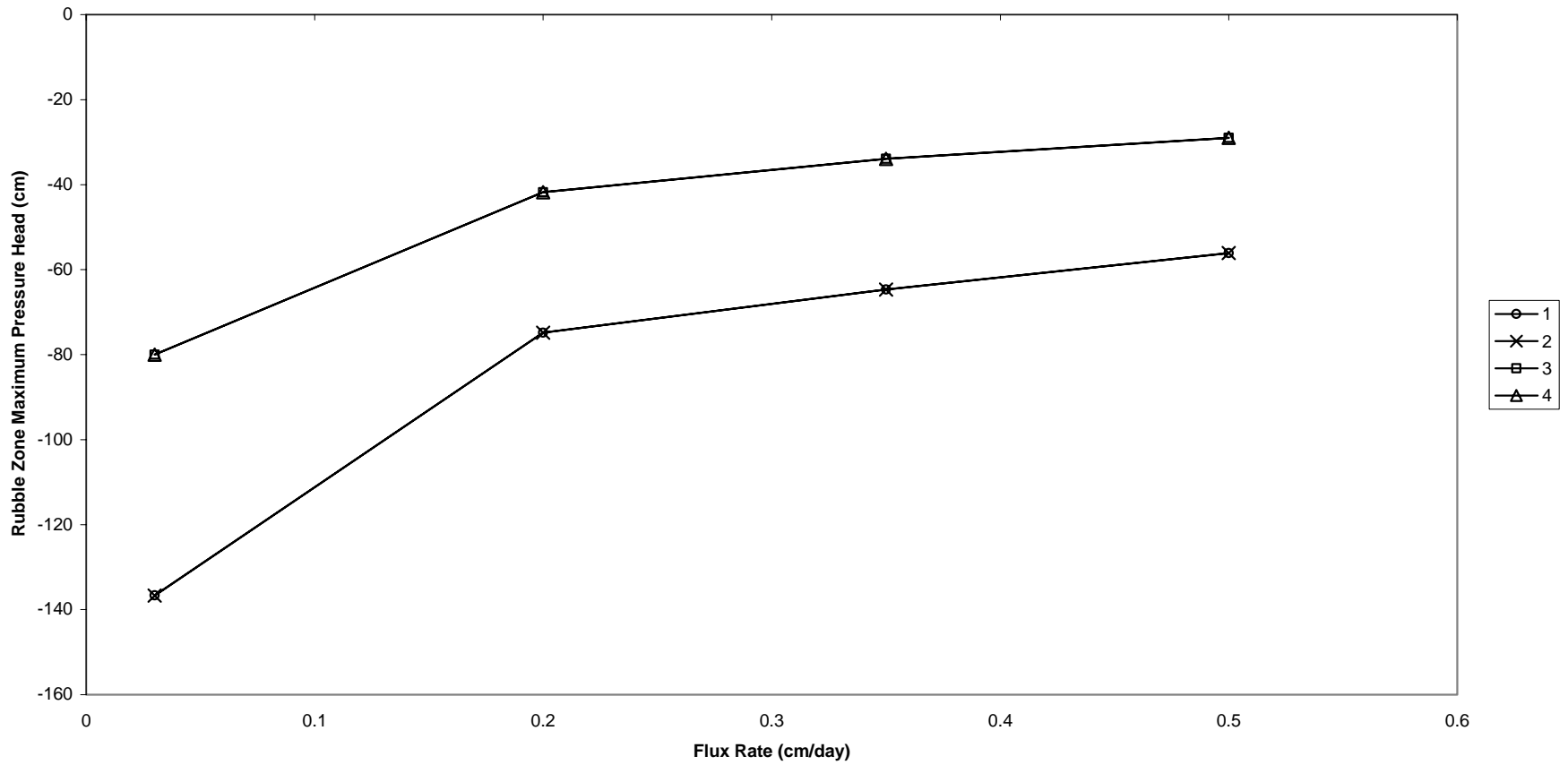


Figure I- 13. The maximum pressure head within the rubble zone in the model domain for four subsequent constant flux levels.

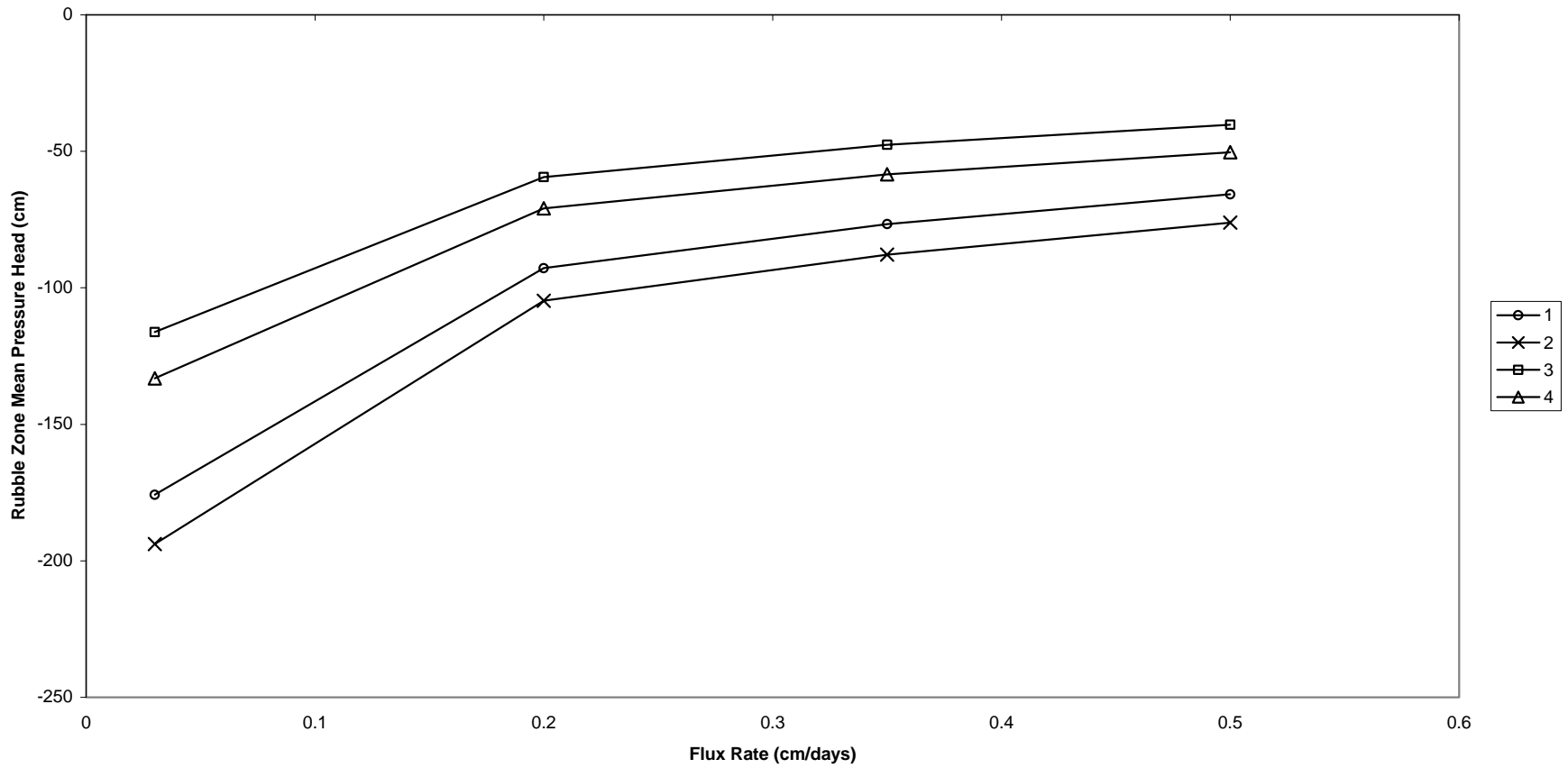


Figure I- 14. The mean pressure head within the rubble zone region of the model domain for four subsequent constant flux levels.

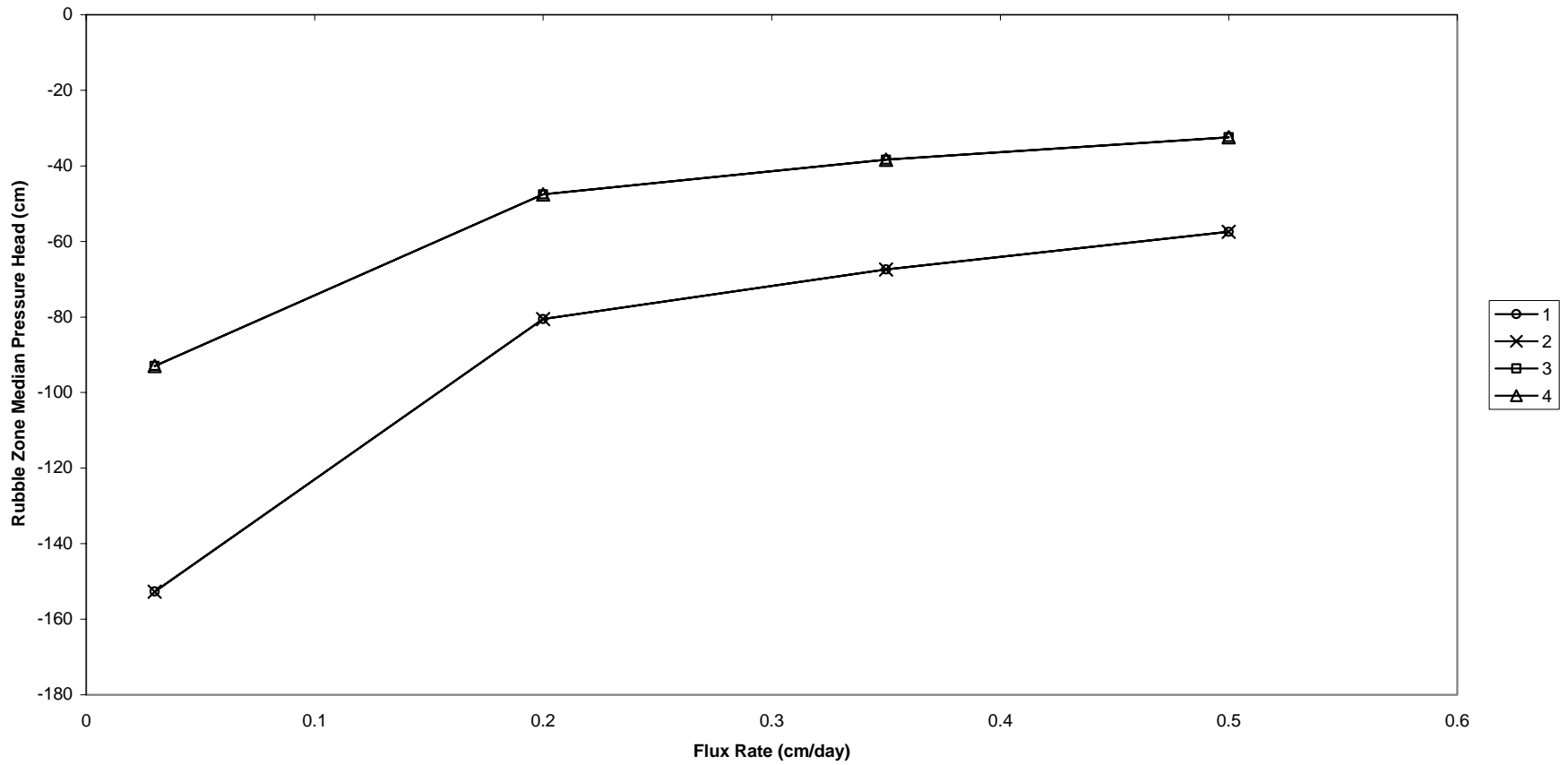


Figure I- 15. The median pressure head within the rubble zone region of the model domain for four subsequent constant flux levels.

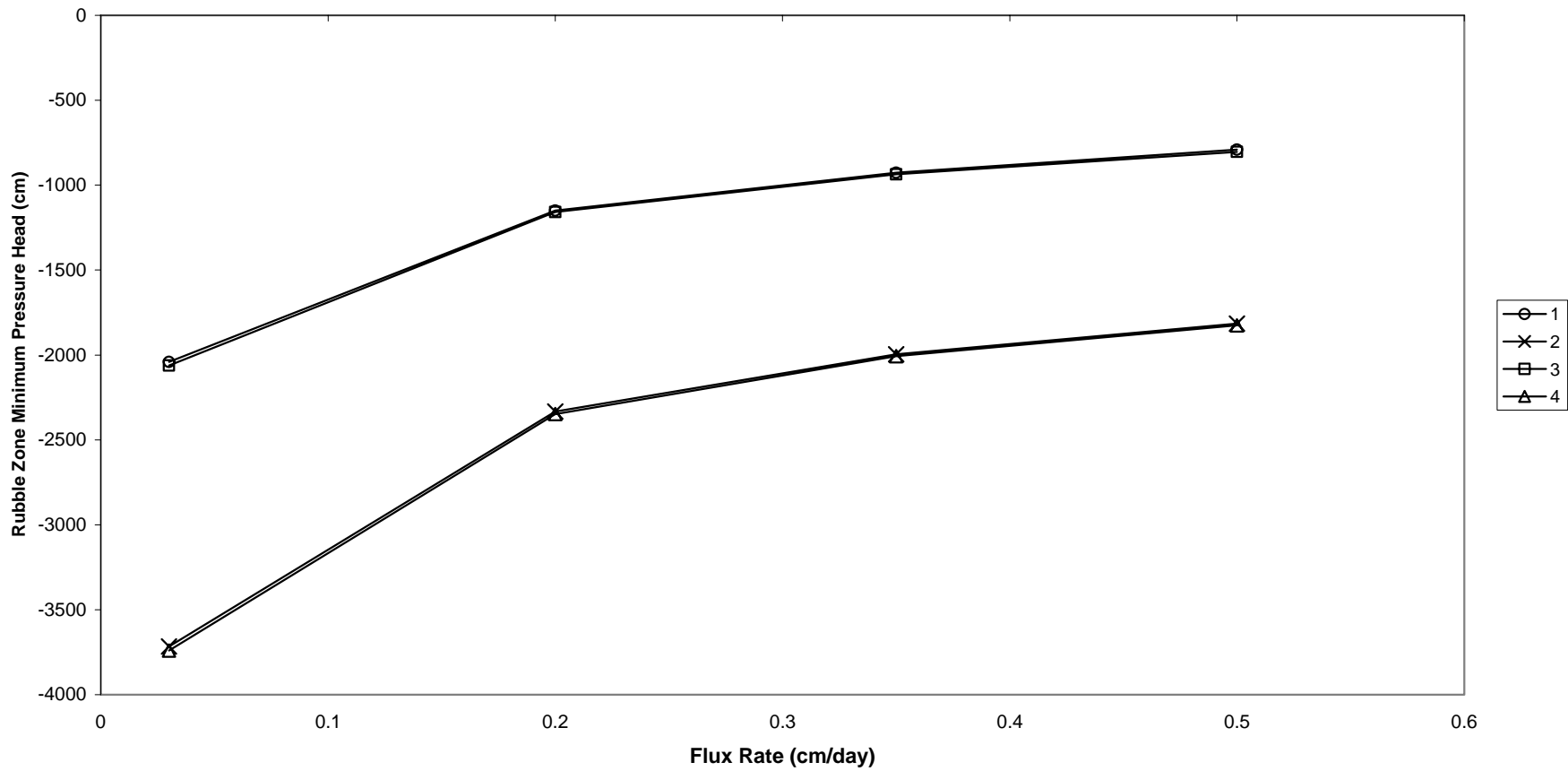


Figure I- 16. The minimum pressure head within the rubble zone region of the model domain for four subsequent constant flux levels.

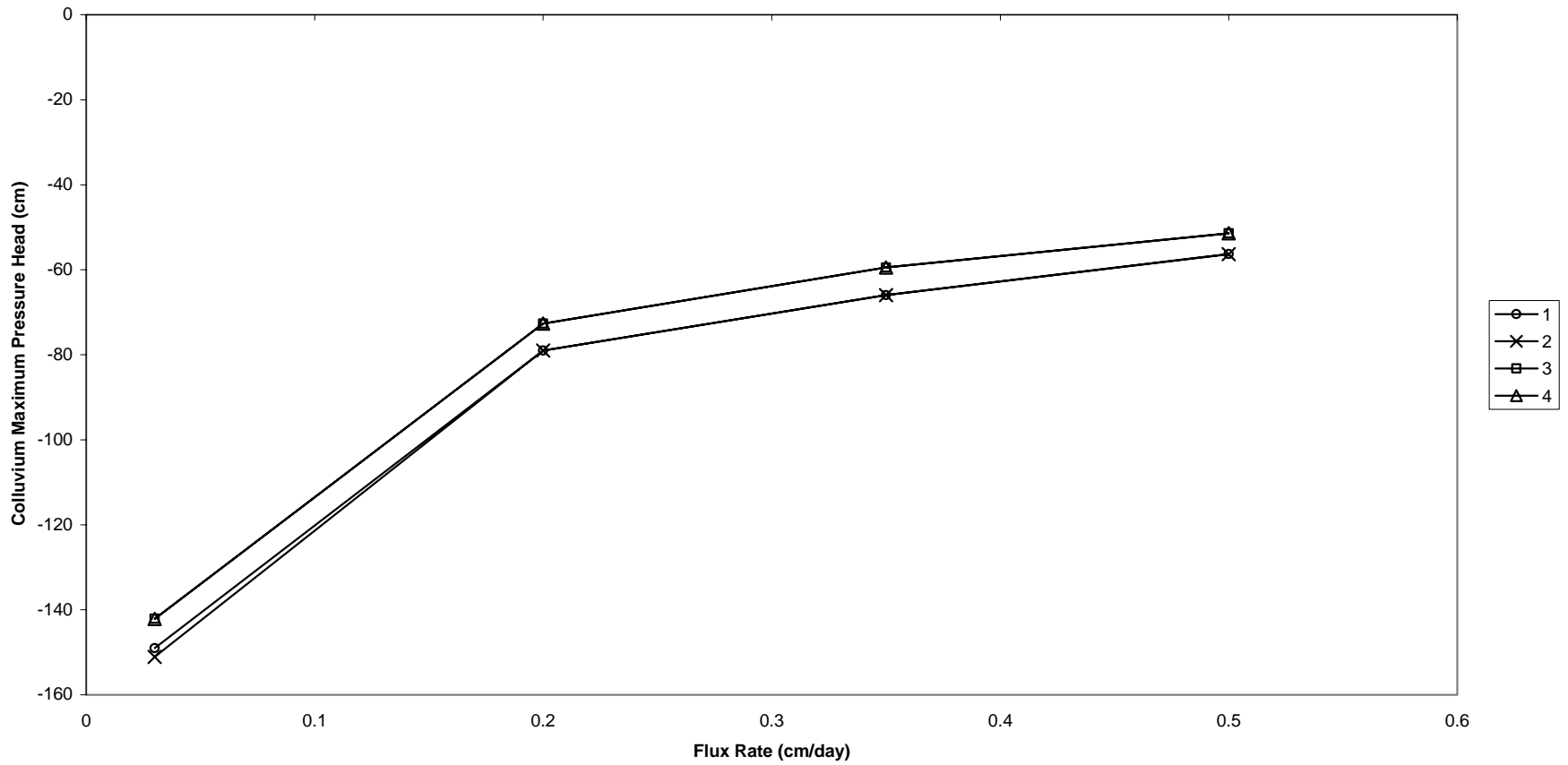


Figure I- 17. The maximum pressure head within the colluvium region of the model domain for four subsequent constant flux levels.

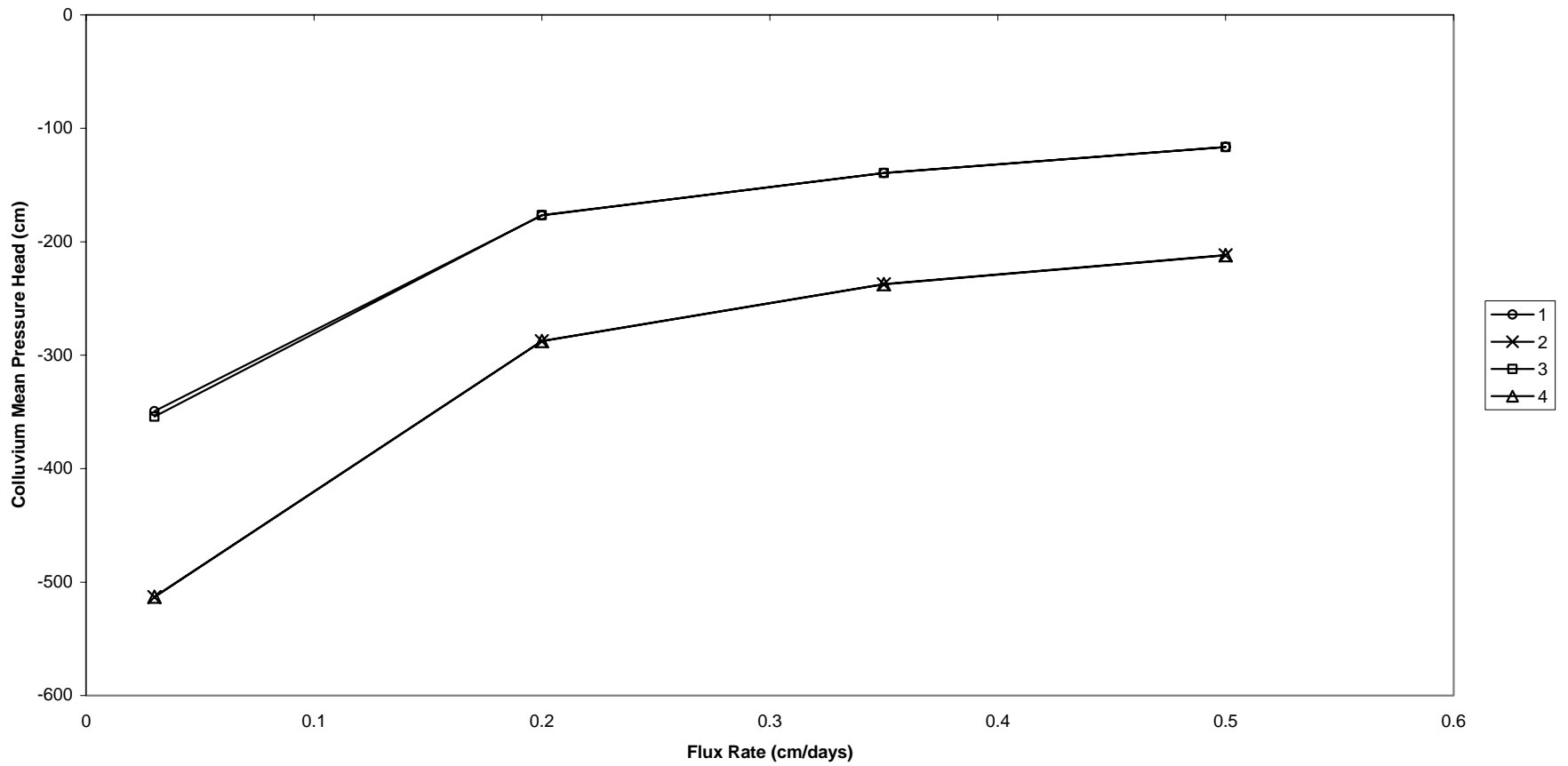


Figure I- 18. The mean pressure head within the colluvium region of the model domain for four subsequent constant flux levels.

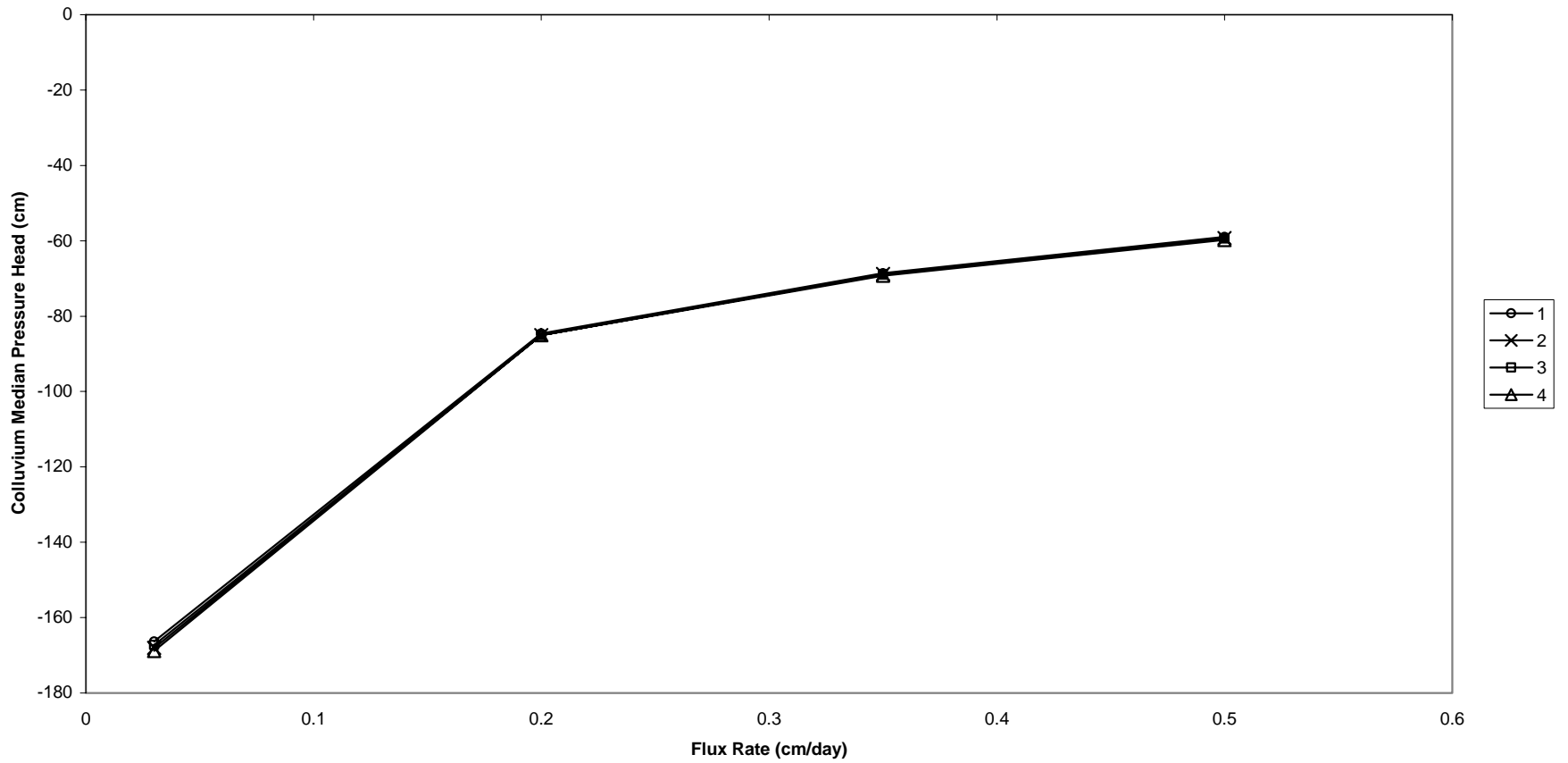


Figure I- 19. The median pressure head within the colluvium region of the model domain for four subsequent constant flux levels.

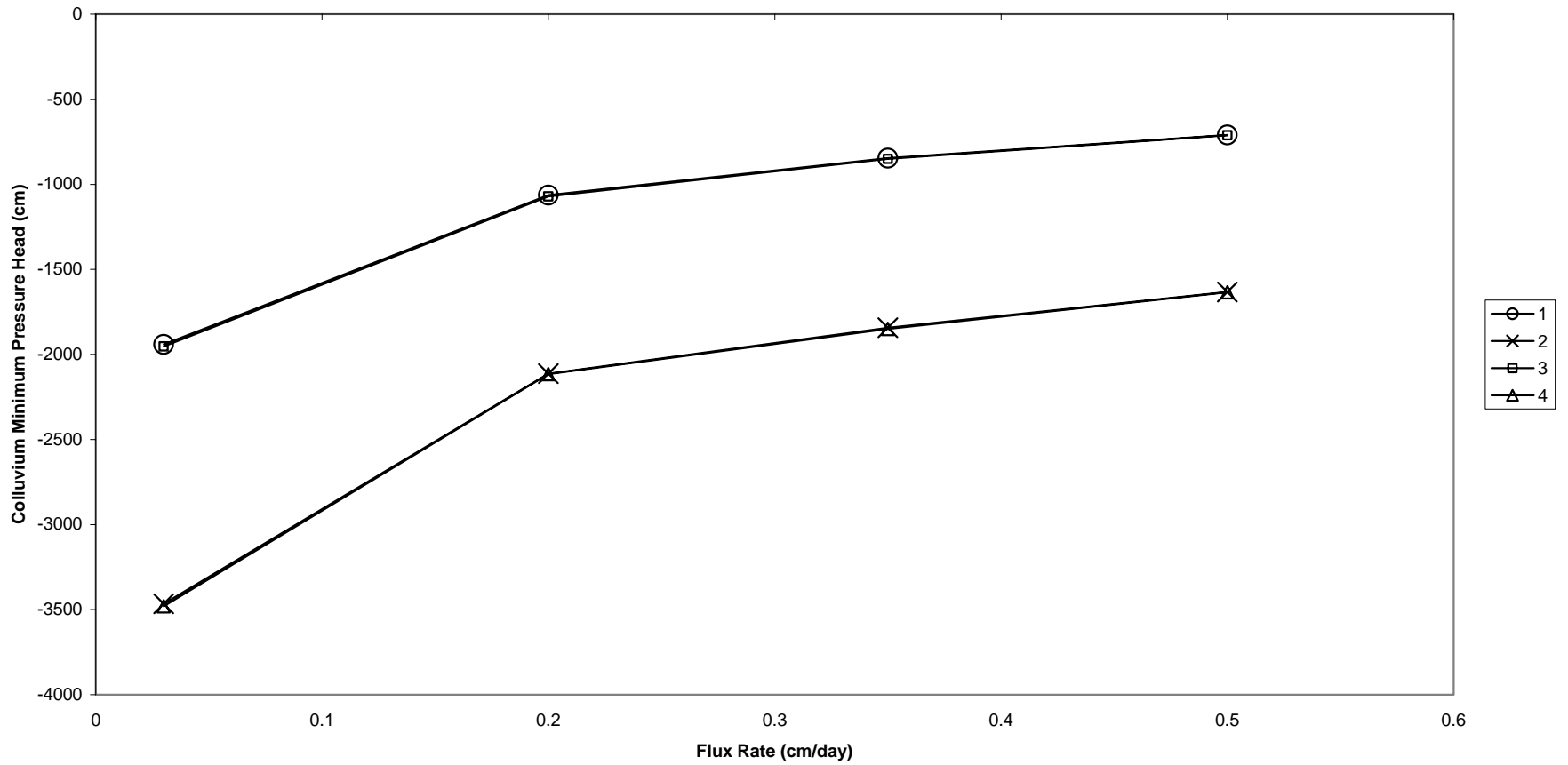


Figure I- 20. The minimum pressure head within the colluvium region of the model domain for four subsequent constant flux levels.

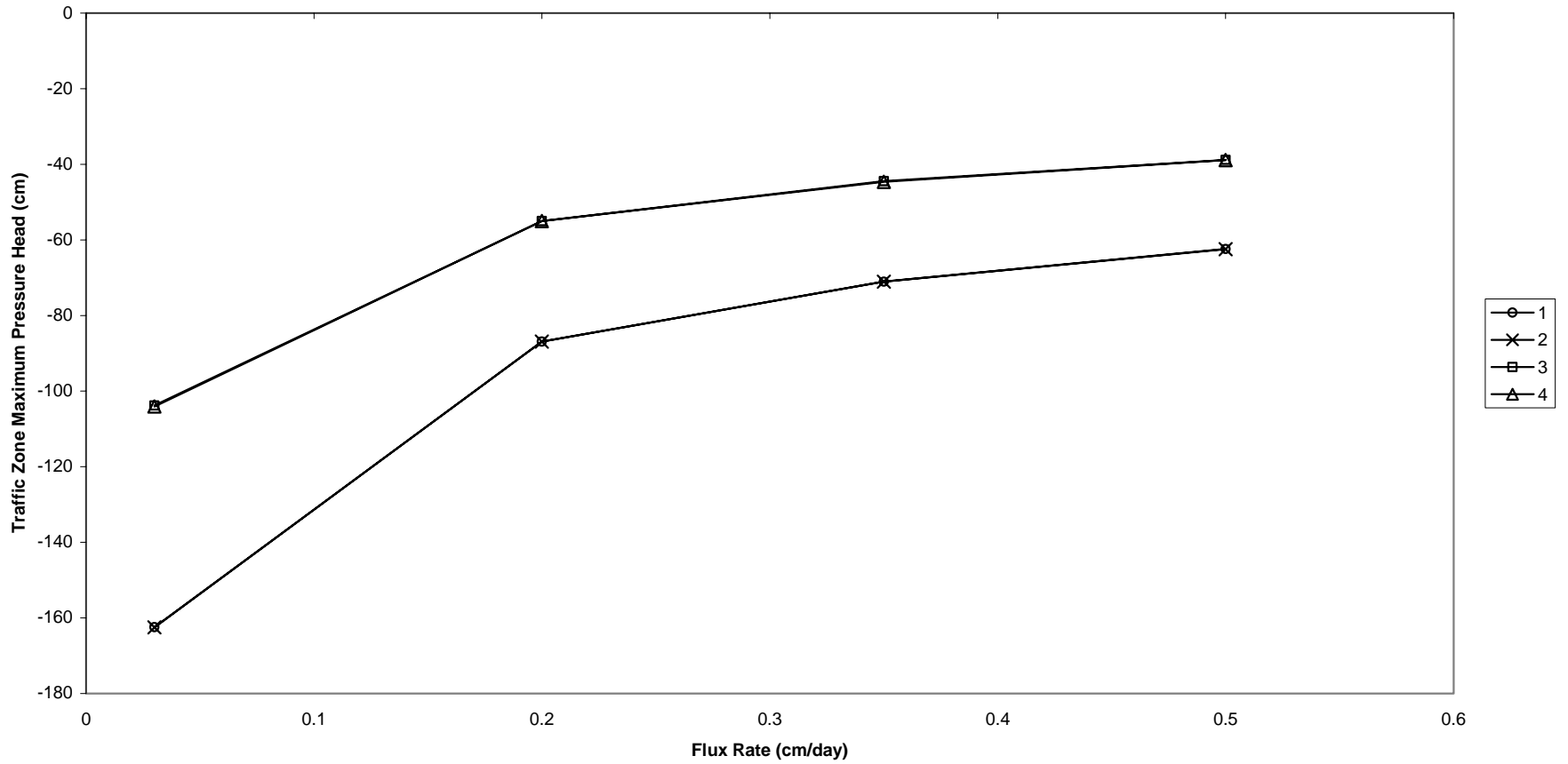


Figure I- 21. The maximum pressure head within the traffic zone region of the model domain for four subsequent constant flux levels.

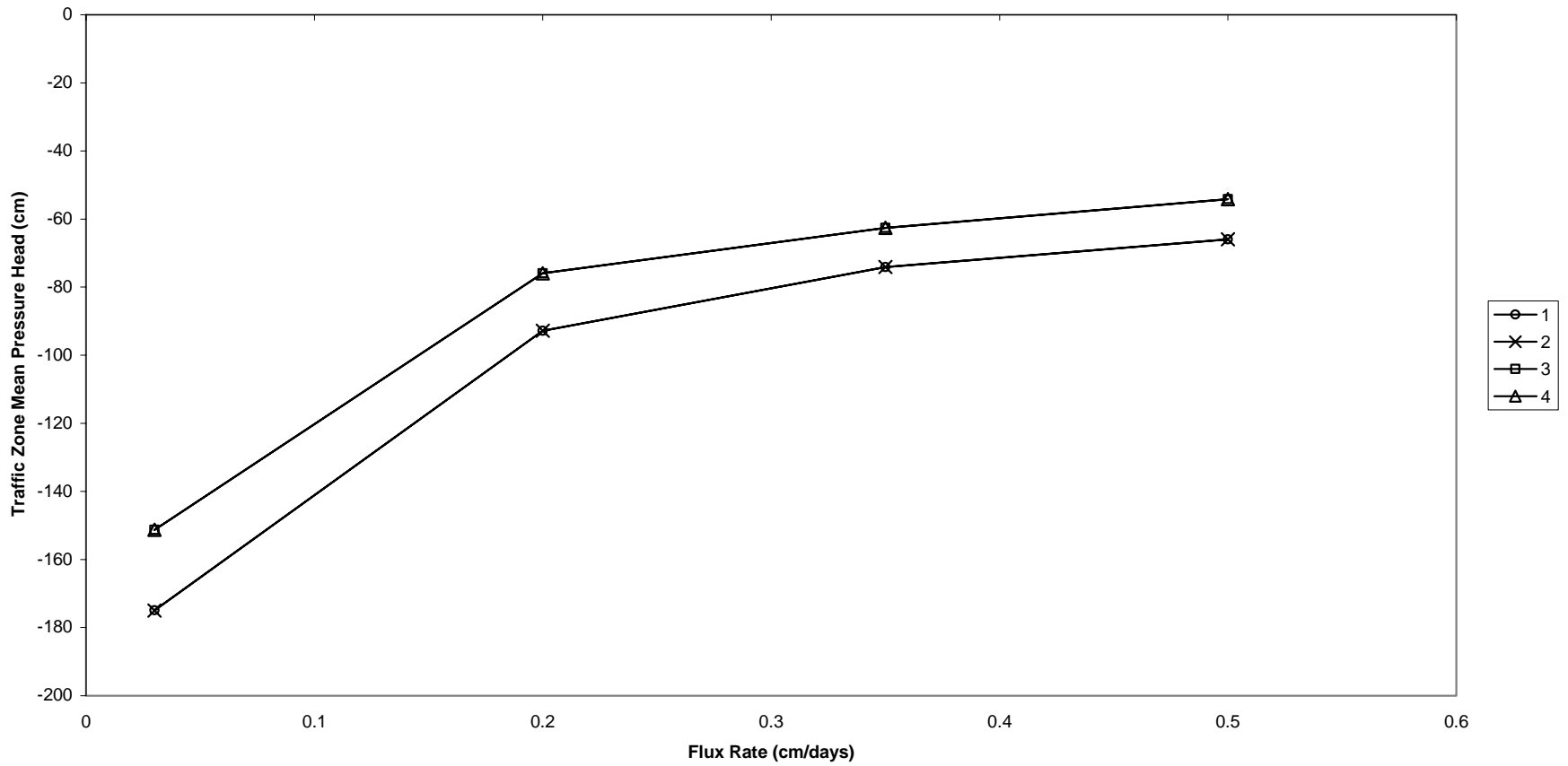


Figure I- 22. The mean pressure head within the traffic zone region of the model domain for four subsequent constant flux levels.

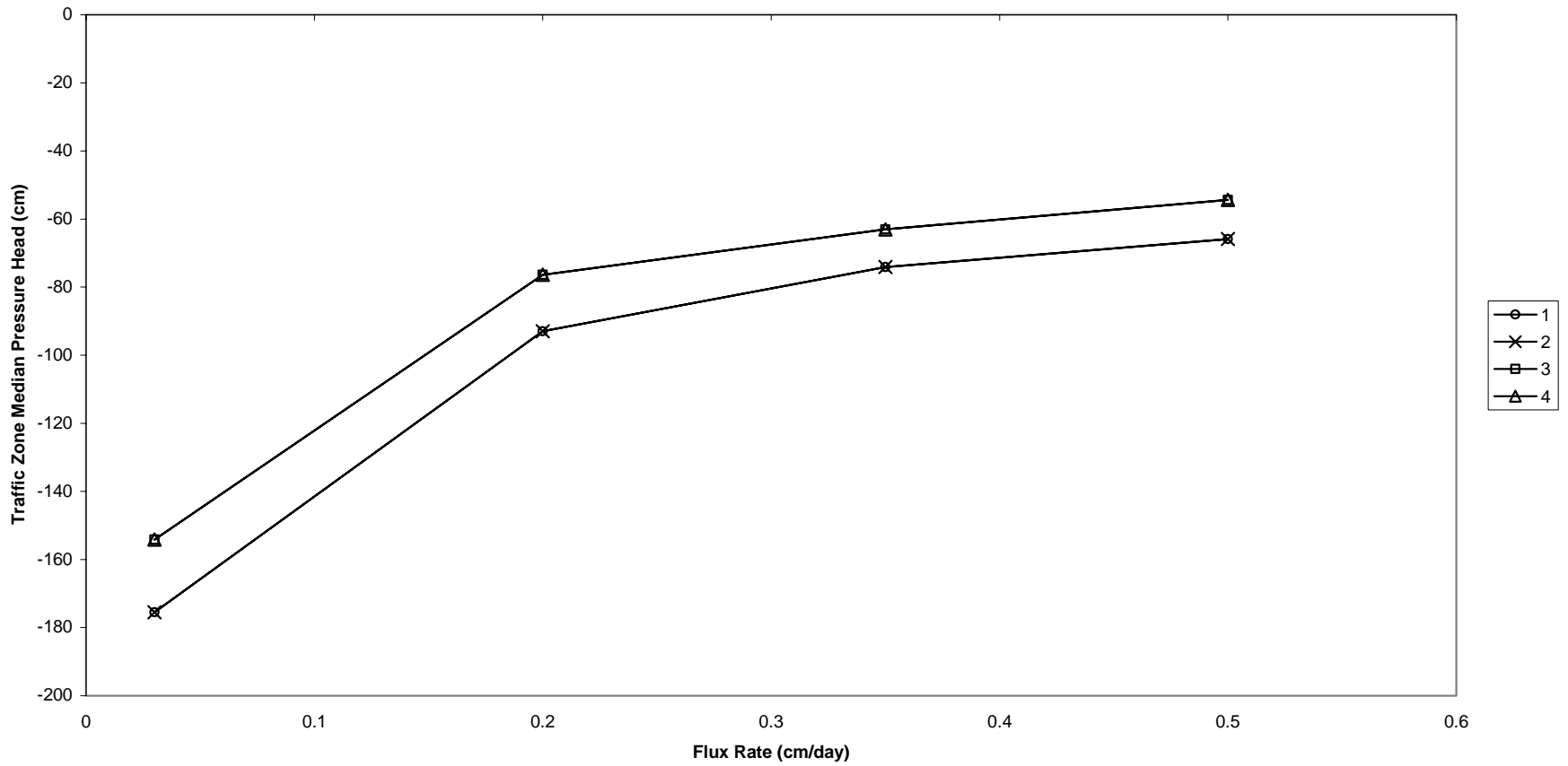


Figure I- 23. The median pressure head within the traffic zone region of the model domain for four subsequent constant flux levels.

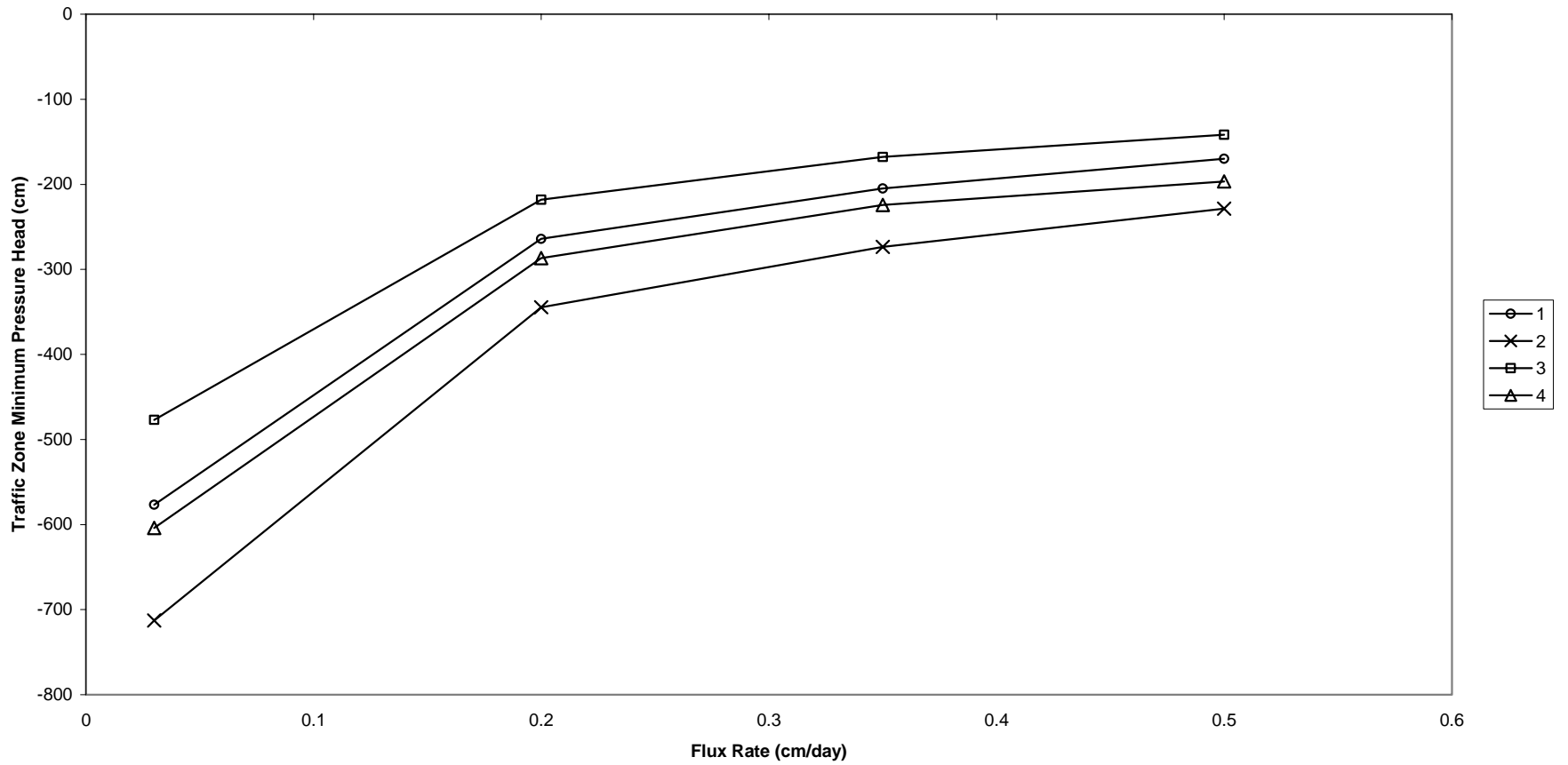


Figure I- 24. The minimum pressure head within the traffic zone region of the model domain for four subsequent constant flux levels.

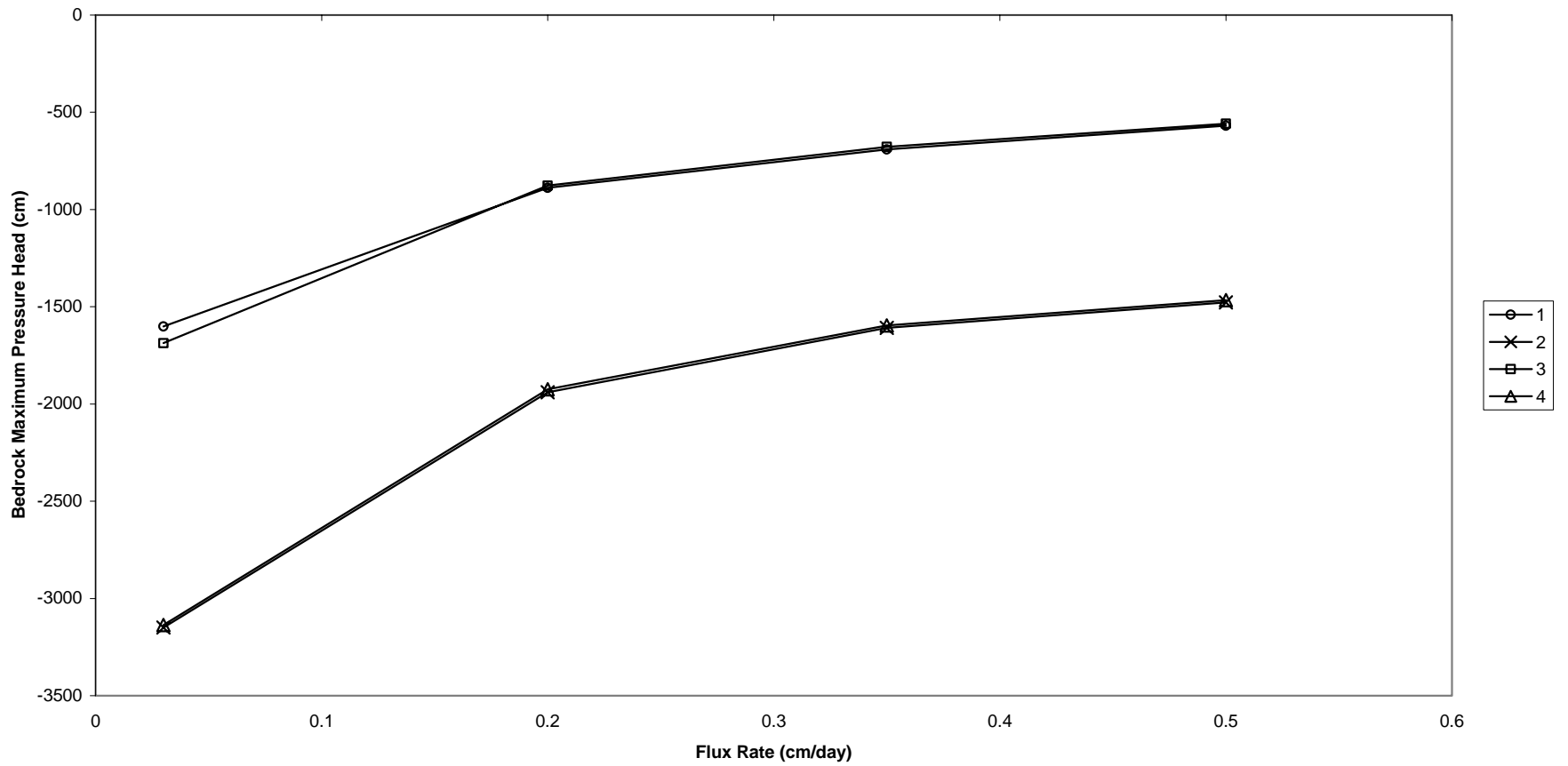


Figure I- 25. The maximum pressure head within the bedrock region of the model domain for four subsequent constant flux levels.

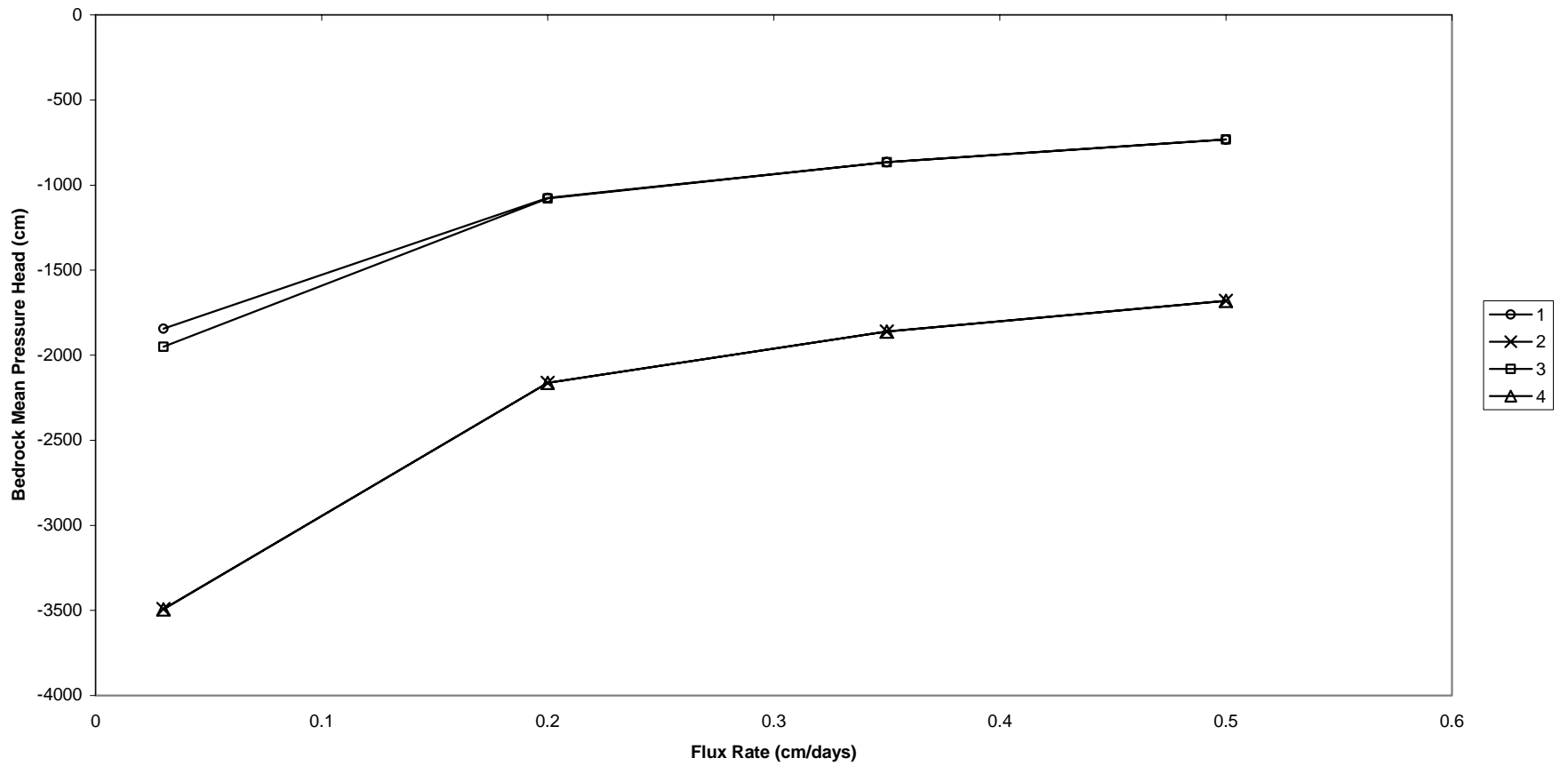


Figure I- 26. The mean pressure head within the bedrock region of the model domain for four subsequent constant flux levels.

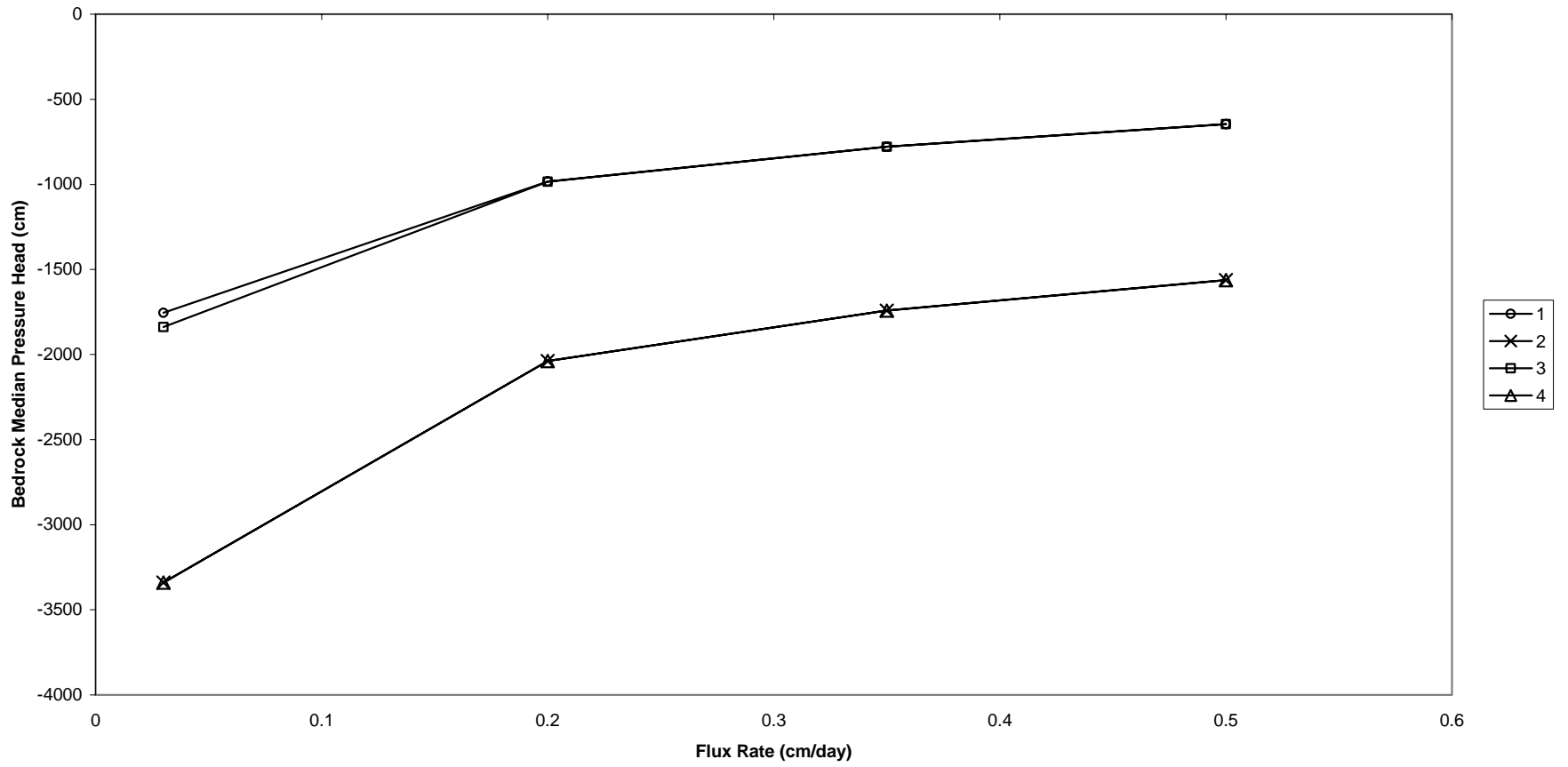


Figure I- 27. The median pressure head within the bedrock region of the model domain for four subsequent constant flux levels.

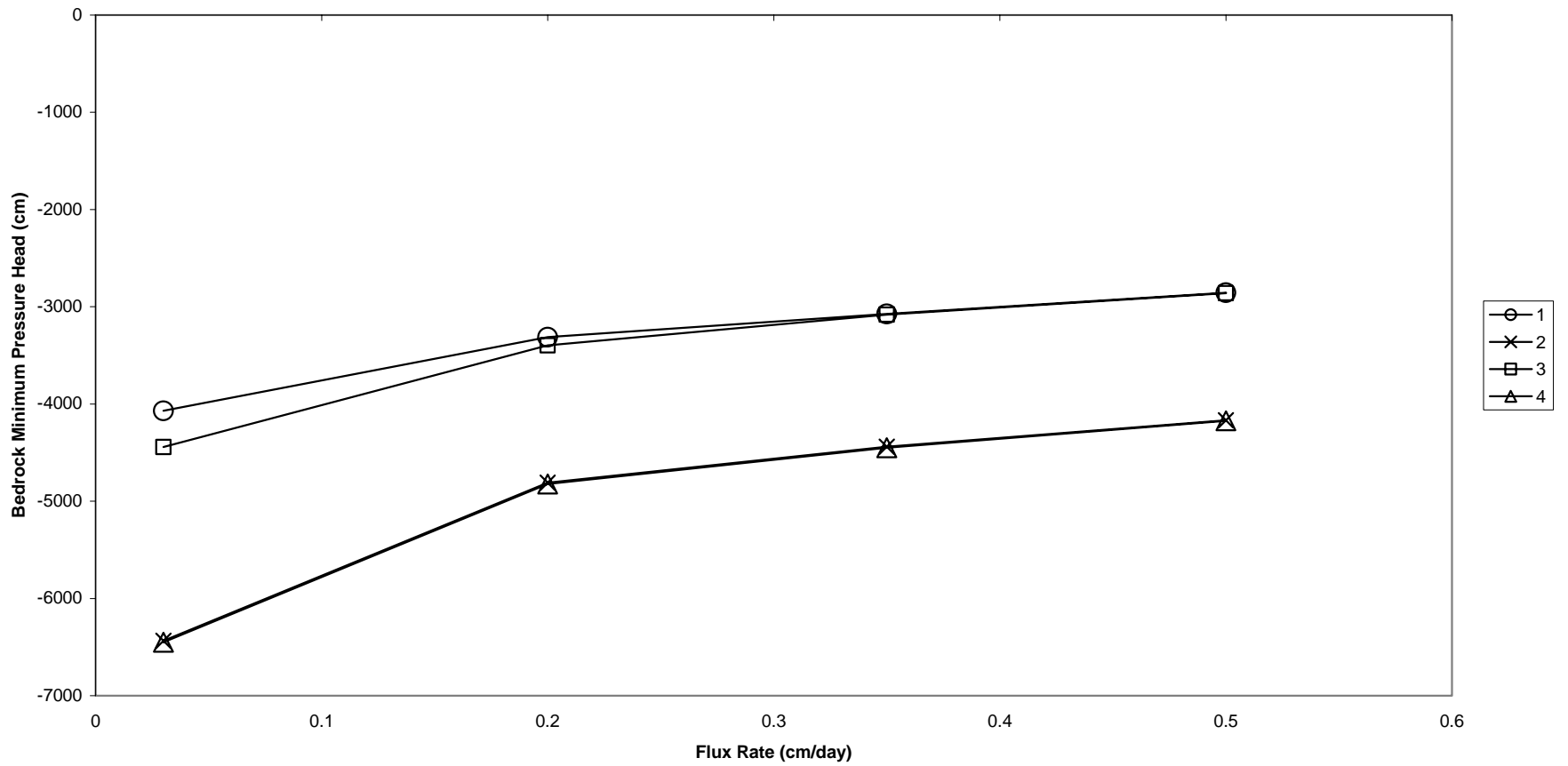


Figure I- 28. The minimum pressure head within the bedrock region of the model domain for four subsequent constant flux levels.

APPENDIX J. ATMOSPHERIC FILE

The following appendix provides the atmospheric file used in the transient time series simulations.

Pcp_File_Version=2

```
*** BLOCK I: ATMOSPHERIC INFORMATION *****
MaxAL (MaxAL = number of atmospheric data-records)
365
hCritS (max. allowed pressure head at the soil surface)
0
tAtm Prec rSoil rRoot hCritA rt ht
1 0 0 0.004592 10000 0 0
2 0 0 0.01501 10000 0 0
3 0 0 0.002033 10000 0 0
4 0 0 0.00243 10000 0 0
5 0 0 0.031266 10000 0 0
6 0 0 0.025694 10000 0 0
7 0 0 0.013794 10000 0 0
8 0 0 0.0047 10000 0 0
9 0 0 0.000237 10000 0 0
10 0 0 0.000278 10000 0 0
11 0 0 0.00051 10000 0 0
12 0 0 0.004455 10000 0 0
13 0 0 0.023373 10000 0 0
14 1.6256 0 0.012493 10000 0 0
15 0.7874 0 0.035533 10000 0 0
16 0 0 0.00022 10000 0 0
17 0 0 0.021428 10000 0 0
18 0 0 0.017608 10000 0 0
19 0 0 0.025757 10000 0 0
20 0 0 0.024729 10000 0 0
21 1.2446 0 0.037099 10000 0 0
22 0 0 0.018802 10000 0 0
23 0 0 0.024419 10000 0 0
```

24	0	0	0.013019	10000	0	0
25	0	0	0.058045	10000	0	0
26	0	0	0.036904	10000	0	0
27	0	0	0.059026	10000	0	0
28	0	0	0.039675	10000	0	0
29	0	0	0.019821	10000	0	0
30	0	0	0.036054	10000	0	0
31	0.002794	0	0.037267	10000	0	0
32	0	0	0.031474	10000	0	0
33	0	0	0.038812	10000	0	0
34	0	0	0.033418	10000	0	0
35	0	0	0.013607	10000	0	0
36	0	0	0.027172	10000	0	0
37	0	0	0.025945	10000	0	0
38	0	0	0.053396	10000	0	0
39	0.002794	0	0.038222	10000	0	0
40	0	0	0.053775	10000	0	0
41	2.8956	0	0.083799	10000	0	0
42	0.4064	0	0.076567	10000	0	0
43	0.2159	0	0.035929	10000	0	0
44	0.2159	0	0.053614	10000	0	0
45	1.3462	0	0.035618	10000	0	0
46	0.4318	0	0.038914	10000	0	0
47	0	0	0.030257	10000	0	0
48	0	0	0.030319	10000	0	0
49	0	0	0.000228	10000	0	0
50	0.13462	0	0.013724	10000	0	0
51	0.89662	0	0.062008	10000	0	0
52	0	0	0.031764	10000	0	0
53	0	0	0.070295	10000	0	0

54	3.2258	0	0.052111	10000	0	0
55	0	0	0.007341	10000	0	0
56	0	0	0.054102	10000	0	0
57	0.13462	0	0.044556	10000	0	0
58	0.762	0	0.058435	10000	0	0
59	0	0	0.021848	10000	0	0
60	0	0	0.027897	10000	0	0
61	0	0	0.040375	10000	0	0
62	0	0	0.000219	10000	0	0
63	0	0	0.000313	10000	0	0
64	5.1816	0	0.000235	10000	0	0
65	0.002794	0	0.000178	10000	0	0
66	0.16002	0	0.003529	10000	0	0
67	0	0	0.000256	10000	0	0
68	1.2192	0	0.007725	10000	0	0
69	0.0508	0	0.012229	10000	0	0
70	0	0	0.01068	10000	0	0
71	0	0	0.005461	10000	0	0
72	0	0	0.001598	10000	0	0
73	0	0	0.001033	10000	0	0
74	0.8128	0	0.000238	10000	0	0
75	0.2413	0	0.000216	10000	0	0
76	0	0	0.00018	10000	0	0
77	0	0	0.031238	10000	0	0
78	0	0	0.047939	10000	0	0
79	0	0	0.057763	10000	0	0
80	0	0	0.111893	10000	0	0
81	0.002794	0	0.143358	10000	0	0
82	7.2644	0	0.096465	10000	0	0
83	2.413	0	0.126277	10000	0	0

84	0	0	0.160481	10000	0	0
85	0	0	0.169746	10000	0	0
86	1.0541	0	0.113928	10000	0	0
87	0	0	0.210045	10000	0	0
88	0	0	0.264794	10000	0	0
89	0	0	0.237417	10000	0	0
90	0	0	0.135172	10000	0	0
91	0	0	0.10055	10000	0	0
92	0	0	0.131324	10000	0	0
93	0.1016	0	0.167645	10000	0	0
94	0.3302	0	0.286563	10000	0	0
95	0.0762	0	0.23027	10000	0	0
96	0	0	0.290492	10000	0	0
97	0	0	0.320027	10000	0	0
98	0	0	0.221913	10000	0	0
99	0.635	0	0.273108	10000	0	0
100	1.016	0	0.317713	10000	0	0
101	6.477	0	0.248354	10000	0	0
102	0.4064	0	0.204988	10000	0	0
103	0	0	0.301389	10000	0	0
104	0.4064	0	0.370976	10000	0	0
105	0	0	0.301783	10000	0	0
106	0	0	0.340867	10000	0	0
107	0.002794	0	0.351583	10000	0	0
108	0	0	0.343337	10000	0	0
109	0	0	0.277638	10000	0	0
110	4.7244	0	0.230275	10000	0	0
111	0.0508	0	0.243207	10000	0	0
112	0	0	0.148156	10000	0	0
113	0.002794	0	0.372888	10000	0	0

114	4.9022	0	0.353252	10000	0	0
115	0.9398	0	0.385744	10000	0	0
116	4.5466	0	0.297876	10000	0	0
117	0.2667	0	0.139891	10000	0	0
118	0	0	0.388982	10000	0	0
119	0	0	0.451906	10000	0	0
120	0	0	0.308827	10000	0	0
121	0	0	0.352576	10000	0	0
122	0	0	0.494573	10000	0	0
123	0	0	0.37339	10000	0	0
124	0.0508	0	0.333208	10000	0	0
125	0	0	0.433529	10000	0	0
126	0.2286	0	0.427684	10000	0	0
127	0.0762	0	0.320667	10000	0	0
128	0.1016	0	0.254877	10000	0	0
129	0.2032	0	0.353504	10000	0	0
130	3.7338	0	0.412351	10000	0	0
131	0	0	0.420627	10000	0	0
132	1.2954	0	0.392441	10000	0	0
133	2.032	0	0.458874	10000	0	0
134	5.08	0	0.381118	10000	0	0
135	0.1905	0	0.468319	10000	0	0
136	0.0762	0	0.354984	10000	0	0
137	0	0	0.493336	10000	0	0
138	0.127	0	0.496607	10000	0	0
139	0	0	0.367651	10000	0	0
140	0	0	0.347489	10000	0	0
141	0	0	0.303575	10000	0	0
142	0	0	0.458766	10000	0	0
143	0	0	0.439773	10000	0	0

144	0.8636	0	0.400494	10000	0	0
145	0.3302	0	0.441689	10000	0	0
146	0.1016	0	0.462241	10000	0	0
147	1.2446	0	0.466623	10000	0	0
148	0.3048	0	0.428921	10000	0	0
149	0.5842	0	0.397024	10000	0	0
150	0.0508	0	0.475647	10000	0	0
151	0.3048	0	0.460843	10000	0	0
152	0	0	0.486426	10000	0	0
153	0.3302	0	0.43678	10000	0	0
154	0.2794	0	0.353039	10000	0	0
155	0.4572	0	0.460892	10000	0	0
156	0	0	0.534003	10000	0	0
157	0	0	0.537082	10000	0	0
158	0	0	0.518054	10000	0	0
159	0.0508	0	0.450023	10000	0	0
160	1.4224	0	0.394673	10000	0	0
161	0.5588	0	0.367116	10000	0	0
162	0.1778	0	0.417326	10000	0	0
163	0	0	0.467503	10000	0	0
164	0.3048	0	0.514771	10000	0	0
165	0	0	0.387352	10000	0	0
166	0	0	0.463424	10000	0	0
167	0.254	0	0.471659	10000	0	0
168	0	0	0.484762	10000	0	0
169	0.3556	0	0.460568	10000	0	0
170	0	0	0.323047	10000	0	0
171	0	0	0.513397	10000	0	0
172	0	0	0.505462	10000	0	0
173	0	0	0.427523	10000	0	0

174	0	0	0.493597	10000	0	0
175	0	0	0.524919	10000	0	0
176	0	0	0.471849	10000	0	0
177	0	0	0.541129	10000	0	0
178	0	0	0.557052	10000	0	0
179	0	0	0.42828	10000	0	0
180	0	0	0.523525	10000	0	0
181	0	0	0.573004	10000	0	0
182	0	0	0.423958	10000	0	0
183	0	0	0.456653	10000	0	0
184	0.0508	0	0.450259	10000	0	0
185	0.0254	0	0.492982	10000	0	0
186	1.143	0	0.390968	10000	0	0
187	0.9652	0	0.575218	10000	0	0
188	0.3556	0	0.459049	10000	0	0
189	0.2794	0	0.478571	10000	0	0
190	0.0254	0	0.505521	10000	0	0
191	0	0	0.485903	10000	0	0
192	0	0	0.392066	10000	0	0
193	0	0	0.441399	10000	0	0
194	0	0	0.438437	10000	0	0
195	0	0	0.437451	10000	0	0
196	0	0	0.420458	10000	0	0
197	0	0	0.384402	10000	0	0
198	0	0	0.448093	10000	0	0
199	0	0	0.420846	10000	0	0
200	0	0	0.458046	10000	0	0
201	0	0	0.414326	10000	0	0
202	0	0	0.416529	10000	0	0
203	0	0	0.424696	10000	0	0

204	0	0	0.445272	10000	0	0
205	0.0508	0	0.433323	10000	0	0
206	0	0	0.486747	10000	0	0
207	0	0	0.563766	10000	0	0
208	0.3302	0	0.489329	10000	0	0
209	0	0	0.43903	10000	0	0
210	0	0	0.446907	10000	0	0
211	0.4318	0	0.446451	10000	0	0
212	0	0	0.46719	10000	0	0
213	0	0	0.459152	10000	0	0
214	0	0	0.479758	10000	0	0
215	0.0254	0	0.427663	10000	0	0
216	0.254	0	0.462091	10000	0	0
217	0.0254	0	0.391571	10000	0	0
218	0.381	0	0.460382	10000	0	0
219	0	0	0.435446	10000	0	0
220	0	0	0.39208	10000	0	0
221	0.0508	0	0.473576	10000	0	0
222	0	0	0.394041	10000	0	0
223	0.2032	0	0.40239	10000	0	0
224	0.381	0	0.460217	10000	0	0
225	0.3556	0	0.432876	10000	0	0
226	0.508	0	0.455857	10000	0	0
227	1.27	0	0.382872	10000	0	0
228	0.7874	0	0.473767	10000	0	0
229	1.27	0	0.284987	10000	0	0
230	0.0508	0	0.463437	10000	0	0
231	0	0	0.492342	10000	0	0
232	0.5588	0	0.396329	10000	0	0
233	0.2286	0	0.340196	10000	0	0

234	0	0	0.34895	10000	0	0
235	0	0	0.271913	10000	0	0
236	0	0	0.366537	10000	0	0
237	0.635	0	0.435664	10000	0	0
238	0.8636	0	0.455568	10000	0	0
239	0.0508	0	0.431994	10000	0	0
240	0.635	0	0.354512	10000	0	0
241	0.508	0	0.46894	10000	0	0
242	0.4572	0	0.415034	10000	0	0
243	0	0	0.476231	10000	0	0
244	0	0	0.408204	10000	0	0
245	0	0	0.392749	10000	0	0
246	0.1016	0	0.387218	10000	0	0
247	1.6256	0	0.466804	10000	0	0
248	0.1778	0	0.363032	10000	0	0
249	0	0	0.37922	10000	0	0
250	0	0	0.383901	10000	0	0
251	0.3302	0	0.415622	10000	0	0
252	0.1016	0	0.376731	10000	0	0
253	0.7874	0	0.395592	10000	0	0
254	0	0	0.440995	10000	0	0
255	0	0	0.227143	10000	0	0
256	0.4064	0	0.347654	10000	0	0
257	0	0	0.355362	10000	0	0
258	1.3208	0	0.395219	10000	0	0
259	0.9906	0	0.433133	10000	0	0
260	0	0	0.384902	10000	0	0
261	0.4064	0	0.260312	10000	0	0
262	0.2286	0	0.388473	10000	0	0
263	0.2794	0	0.4298	10000	0	0

264	0	0	0.374373	10000	0	0
265	0	0	0.296748	10000	0	0
266	0	0	0.326466	10000	0	0
267	0	0	0.363357	10000	0	0
268	0	0	0.281906	10000	0	0
269	0	0	0.311693	10000	0	0
270	0	0	0.319567	10000	0	0
271	0.2794	0	0.282752	10000	0	0
272	1.0414	0	0.33006	10000	0	0
273	0	0	0.303607	10000	0	0
274	0	0	0.35703	10000	0	0
275	0	0	0.296348	10000	0	0
276	0	0	0.283194	10000	0	0
277	0.1016	0	0.350058	10000	0	0
278	0.0254	0	0.356116	10000	0	0
279	0.3302	0	0.302902	10000	0	0
280	0	0	0.364089	10000	0	0
281	0	0	0.309532	10000	0	0
282	0	0	0.342512	10000	0	0
283	0	0	0.300868	10000	0	0
284	0	0	0.296133	10000	0	0
285	0	0	0.299178	10000	0	0
286	0	0	0.318393	10000	0	0
287	0	0	0.302859	10000	0	0
288	0.0762	0	0.286207	10000	0	0
289	0.4572	0	0.310505	10000	0	0
290	0.0508	0	0.299339	10000	0	0
291	0	0	0.137177	10000	0	0
292	0.1778	0	0.267111	10000	0	0
293	0	0	0.343126	10000	0	0

294	1.8796	0	0.31211	10000	0	0
295	0.2794	0	0.220529	10000	0	0
296	1.524	0	0.242052	10000	0	0
297	0	0	0.246772	10000	0	0
298	0	0	0.244552	10000	0	0
299	0	0	0.265573	10000	0	0
300	0	0	0.202285	10000	0	0
301	0	0	0.293624	10000	0	0
302	0.2032	0	0.251488	10000	0	0
303	3.048	0	0.176213	10000	0	0
304	2.9464	0	0.162541	10000	0	0
305	3.4798	0	0.209821	10000	0	0
306	0	0	0.187691	10000	0	0
307	0	0	0.184776	10000	0	0
308	0	0	0.179676	10000	0	0
309	0	0	0.142323	10000	0	0
310	0	0	0.129735	10000	0	0
311	0	0	0.173746	10000	0	0
312	0	0	0.188598	10000	0	0
313	0	0	0.119612	10000	0	0
314	0	0	0.171748	10000	0	0
315	0	0	0.113773	10000	0	0
316	0	0	0.105494	10000	0	0
317	0	0	0.074523	10000	0	0
318	0	0	0.100306	10000	0	0
319	0	0	0.108829	10000	0	0
320	0	0	0.110457	10000	0	0
321	0	0	0.136812	10000	0	0
322	3.6068	0	0.103884	10000	0	0
323	3.4798	0	0.105414	10000	0	0

324	0	0	0.066873	10000	0	0
325	0	0	0.065115	10000	0	0
326	0	0	0.119683	10000	0	0
327	0.3048	0	0.103728	10000	0	0
328	0.0762	0	0.125671	10000	0	0
329	0	0	0.093447	10000	0	0
330	0.508	0	0.024854	10000	0	0
331	2.4384	0	0.041571	10000	0	0
332	0.9525	0	0.016634	10000	0	0
333	0.002794	0	0.033709	10000	0	0
334	0	0	0.049784	10000	0	0
335	0	0	0.075371	10000	0	0
336	1.8796	0	0.044021	10000	0	0
337	0	0	0.025827	10000	0	0
338	0	0	0.04921	10000	0	0
339	5.6642	0	0.034216	10000	0	0
340	0	0	0.060101	10000	0	0
341	0	0	0.040629	10000	0	0
342	0	0	0.024147	10000	0	0
343	0	0	0.03594	10000	0	0
344	0	0	0.023615	10000	0	0
345	0	0	0.048052	10000	0	0
346	0.5461	0	0.051534	10000	0	0
347	0	0	0.047209	10000	0	0
348	0	0	0.042441	10000	0	0
349	0	0	0.060796	10000	0	0
350	0	0	0.049492	10000	0	0
351	0	0	0.020032	10000	0	0
352	0	0	0.021123	10000	0	0
353	0	0	0.019266	10000	0	0

354	0.0254	0	0.021765	10000	0	0
355	0.5207	0	0.035502	10000	0	0
356	0.4064	0	0.033367	10000	0	0
357	0.028194	0	0.049358	10000	0	0
358	0	0	0.028637	10000	0	0
359	0	0	0.025854	10000	0	0
360	0	0	0.012994	10000	0	0
361	0	0	0.027433	10000	0	0
362	0	0	0.017998	10000	0	0
363	0.1905	0	0.01863	10000	0	0
364	0	0	0.000248	10000	0	0
365	0	0	0.01937	10000	0	0

*** END OF INPUT FILE 'ATMOSPH.IN' *****

APPENDIX K. “WET YEAR” SIMULATIONS.

The maximum, mean, median, and minimum pressure heads within each zone for the “wet year” simulations are presented in the following appendix.

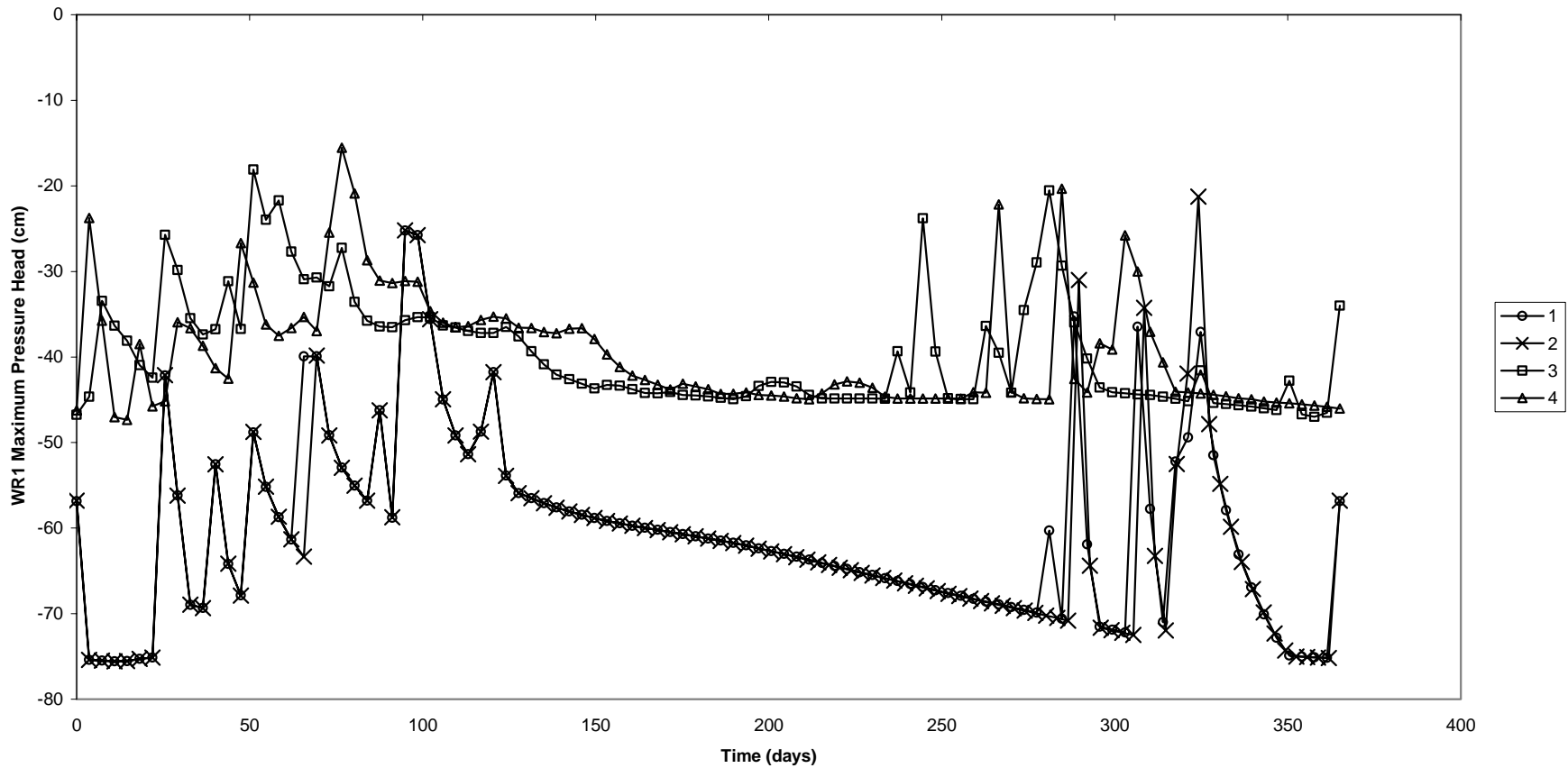


Figure J- 1. The maximum pressure head within the WR1 region of the model domain for the four “wet year” simulations.

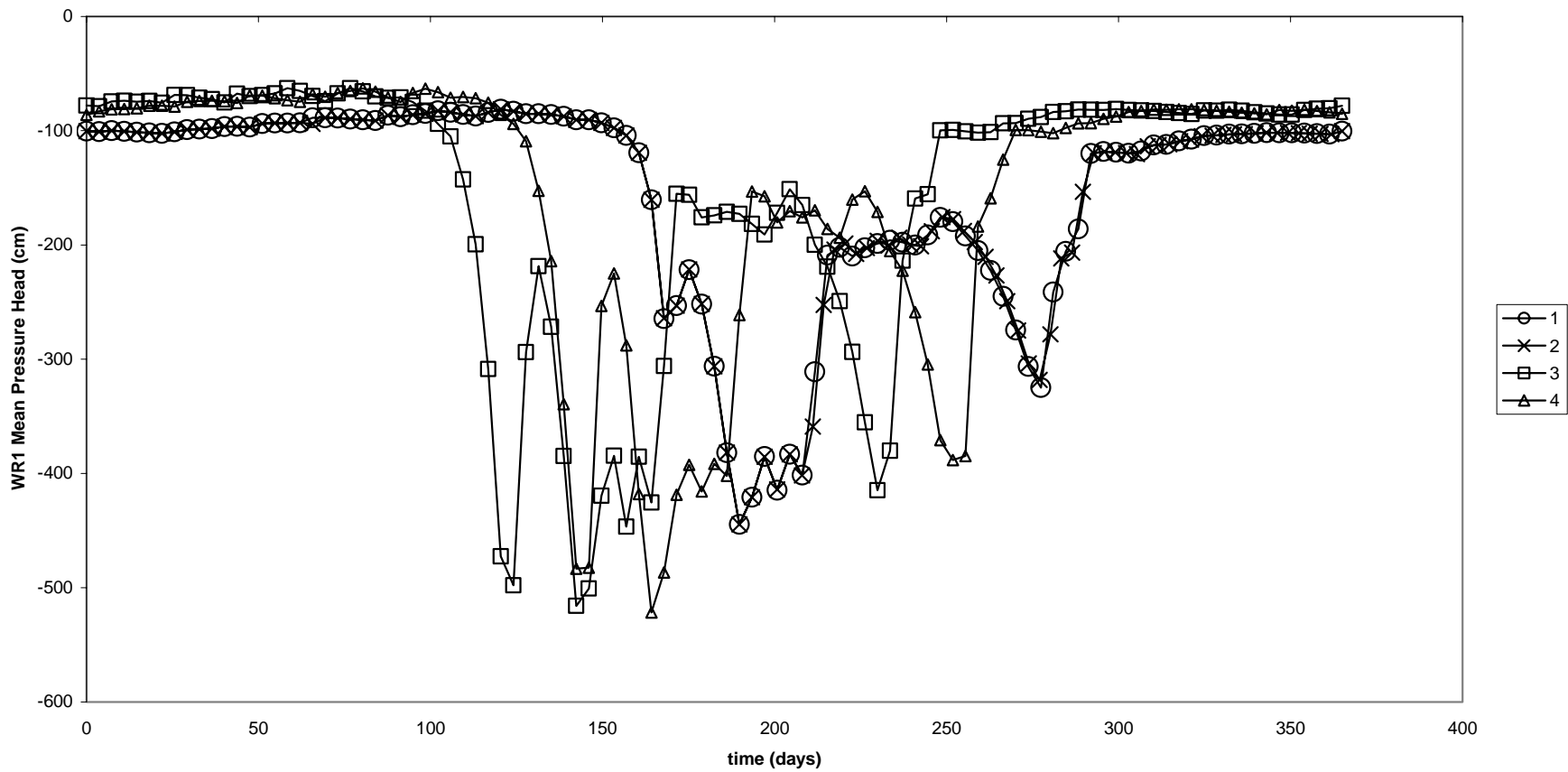


Figure J- 2. The mean pressure head within the WR1 region of the model domain for the four “wet year” simulations.

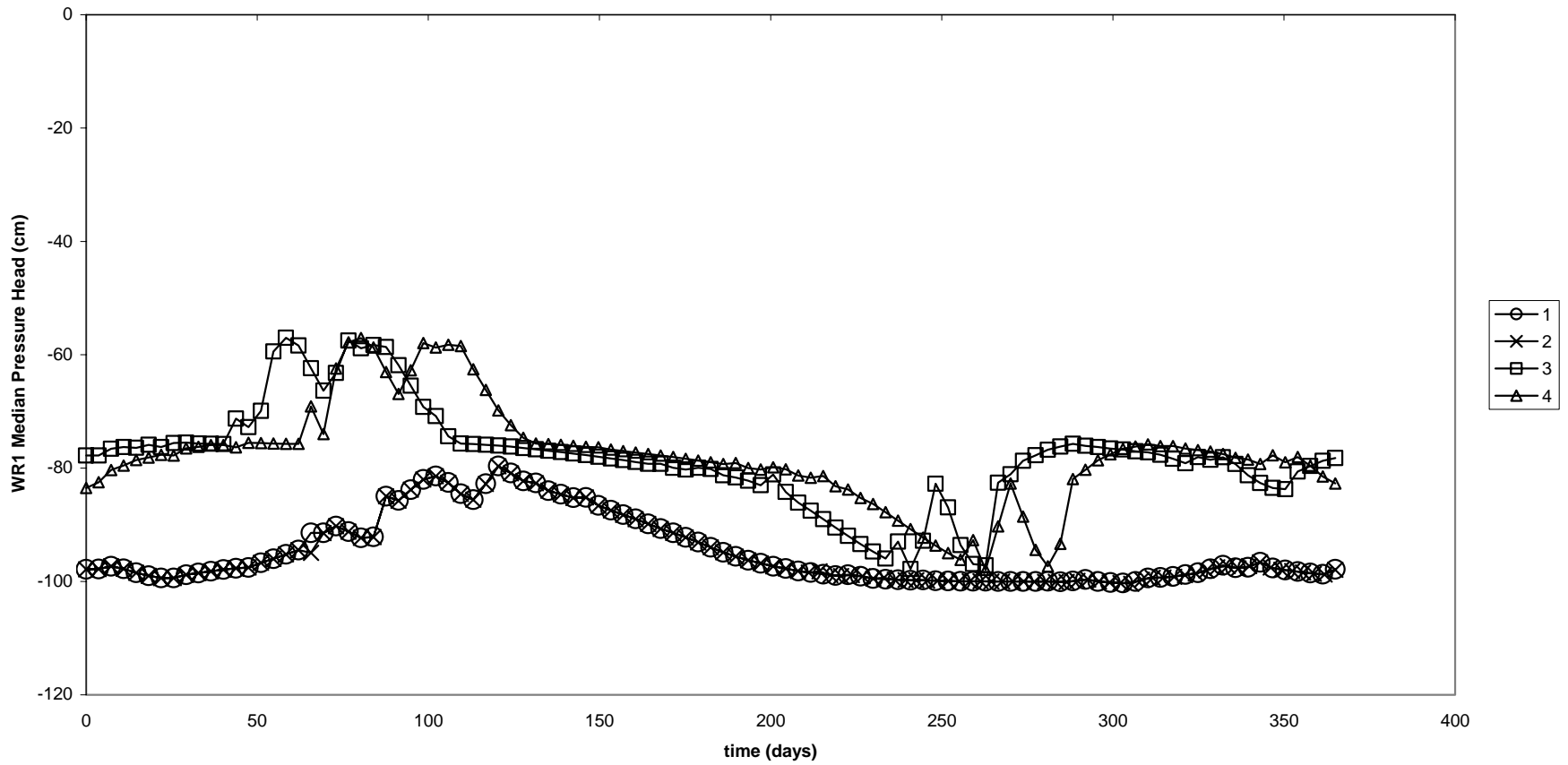


Figure J- 3. The median pressure head within the WR1 region of the model domain for the four “wet year” simulations.

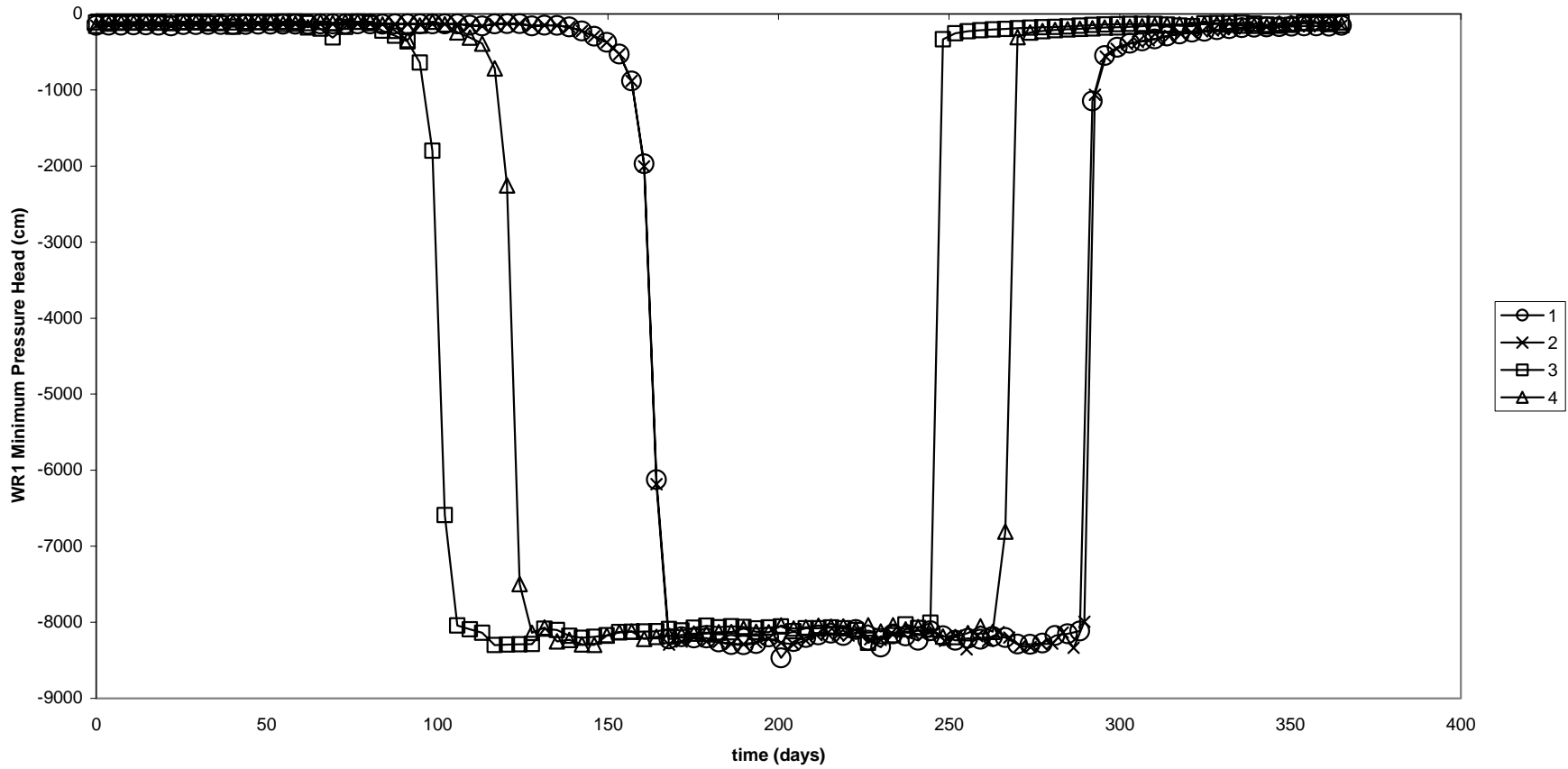


Figure J- 4. The minimum pressure head within the WR1 region of the model domain for the four “wet year” simulations.

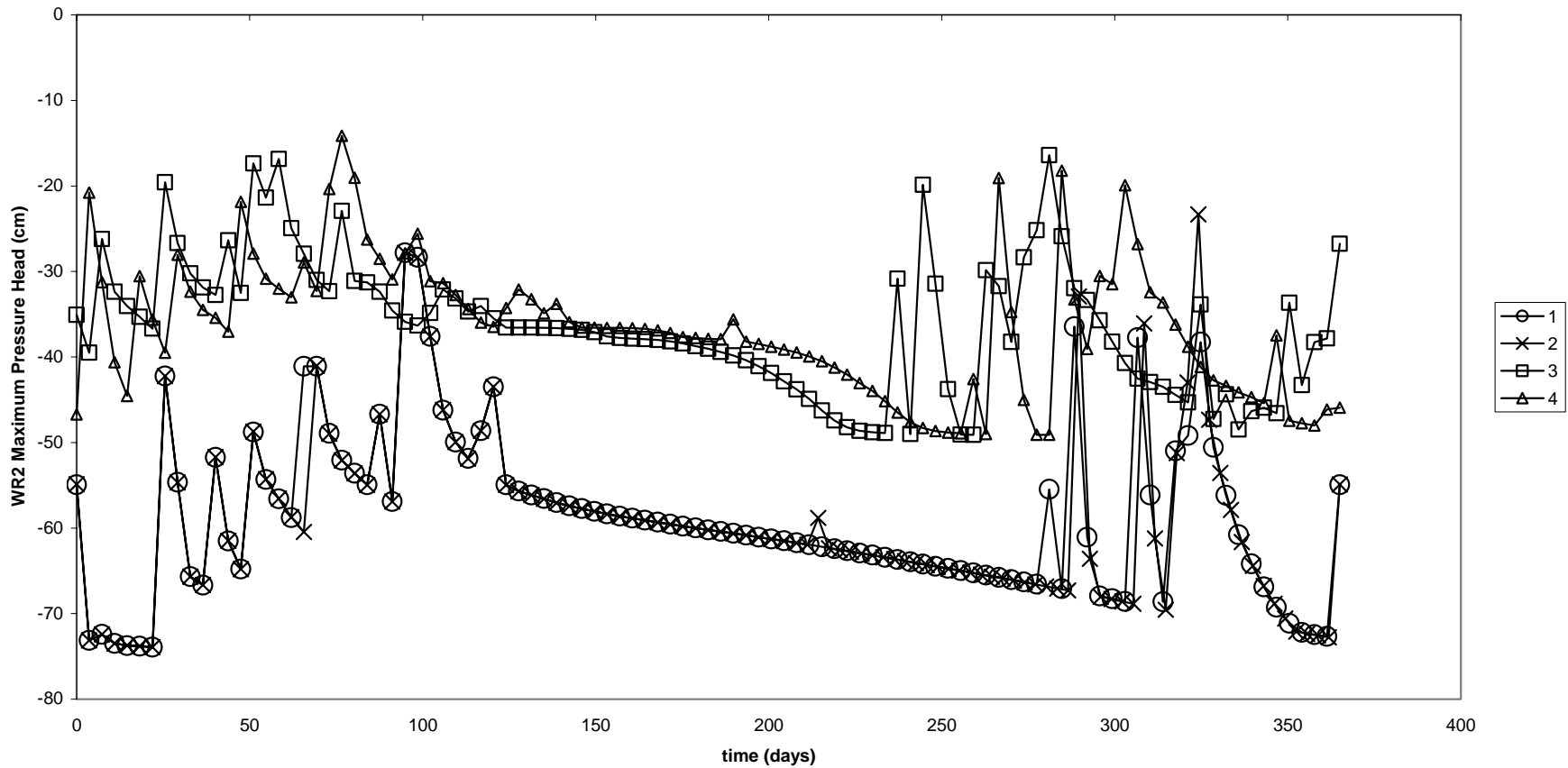


Figure J- 5. The maximum pressure head within the WR2 region of the model domain for the four “wet year” simulations.

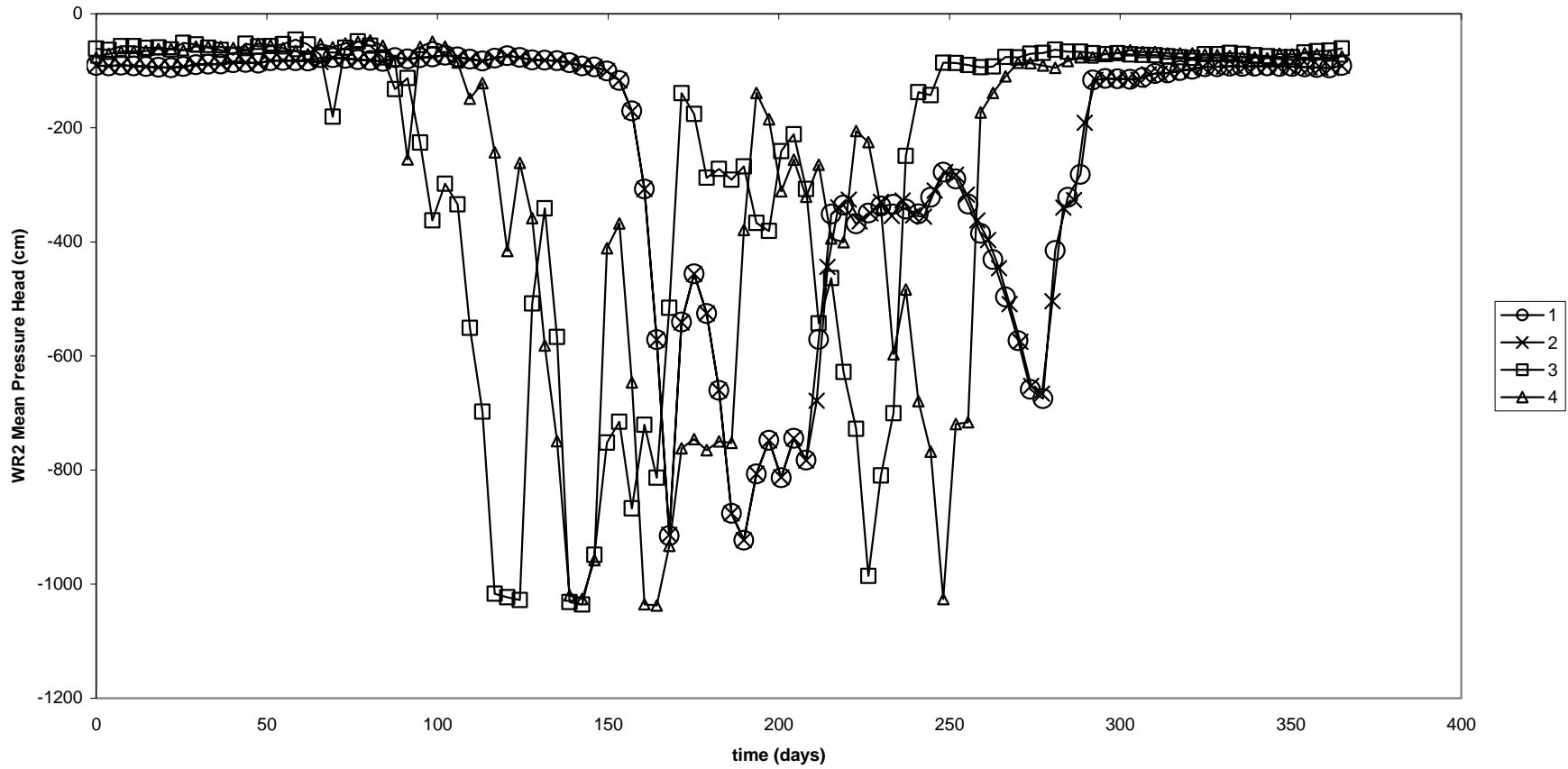


Figure J- 6. The mean pressure head within the WR2 region of the model domain for the four “wet year” simulations.

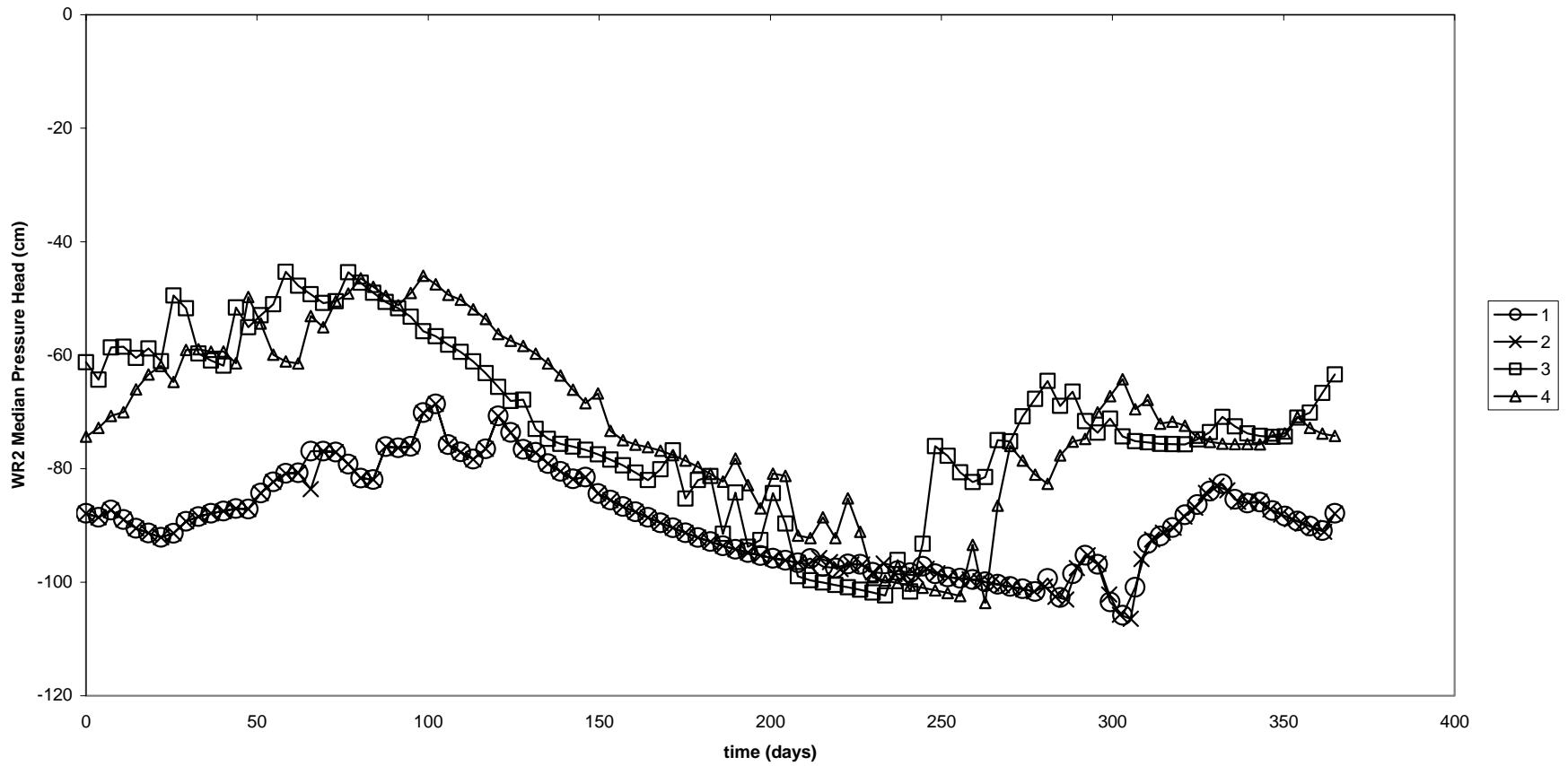


Figure J- 7. The median pressure heads within the WR2 region of the model domain for the four “wet year” simulations.

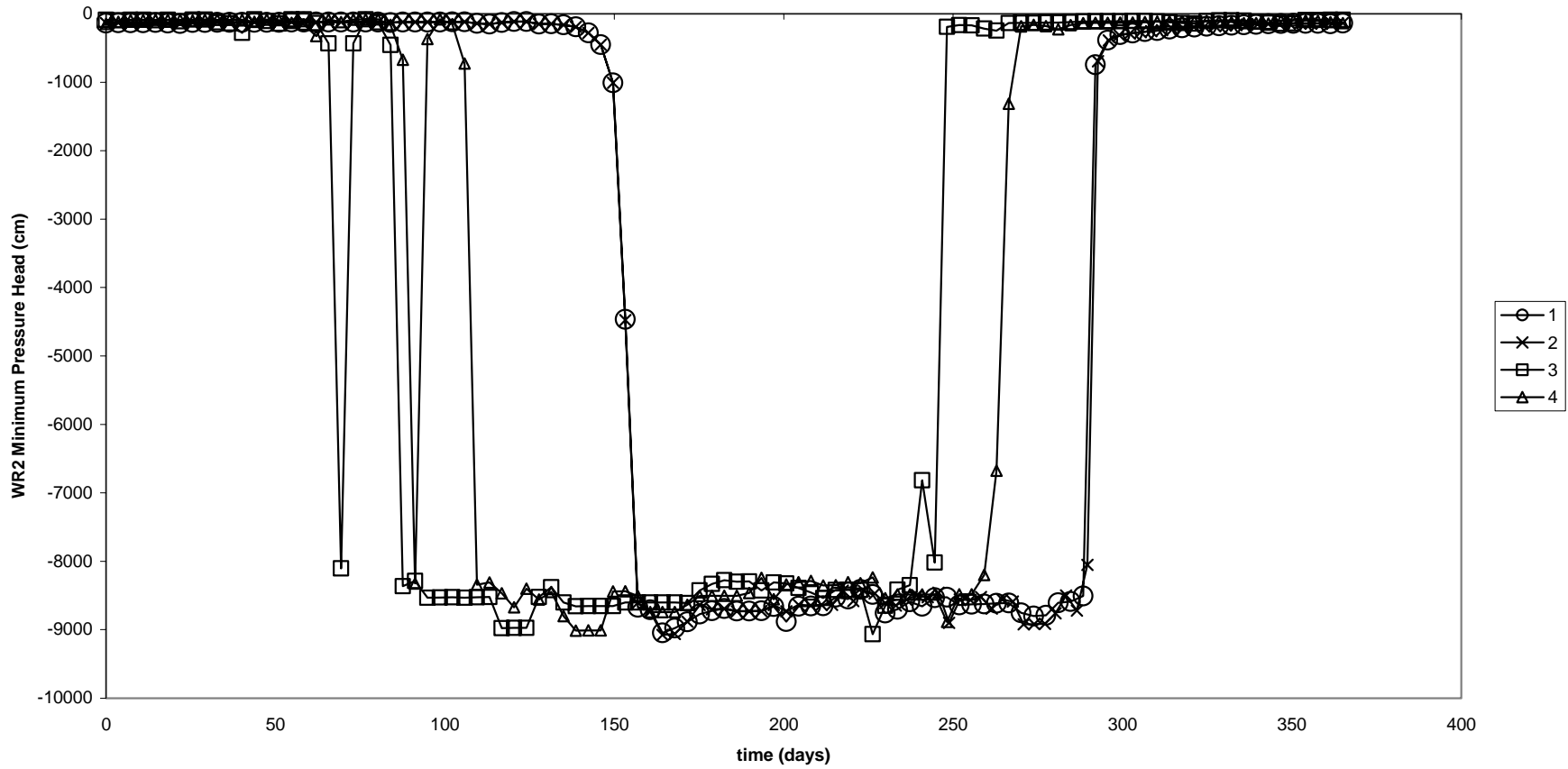


Figure J- 8. The minimum pressure heads within the WR2 region of the model domain for the four “wet year” simulations.

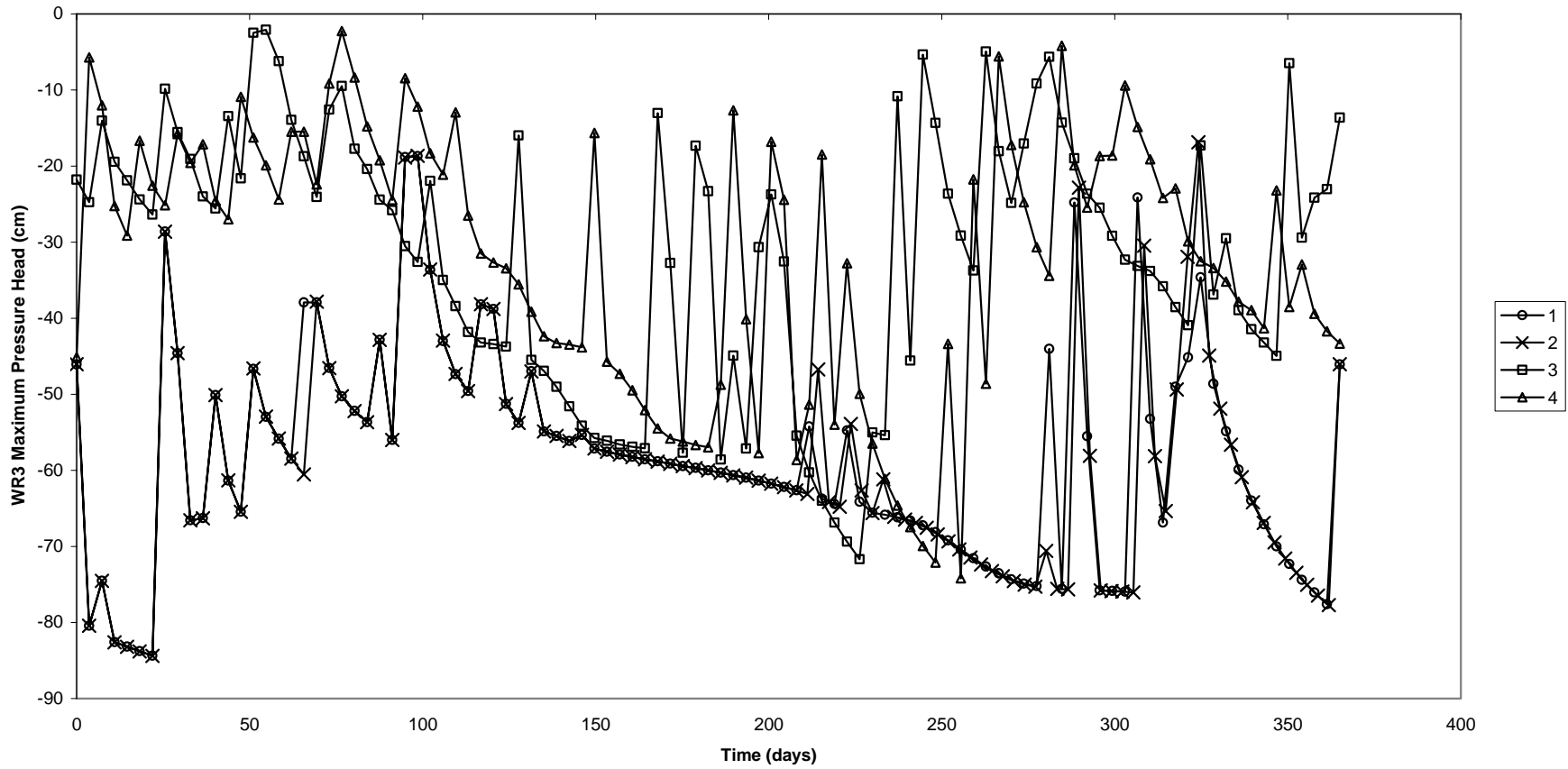


Figure J- 9. The maximum pressure head within the WR3 region of the model domain for the four “wet year” simulations.

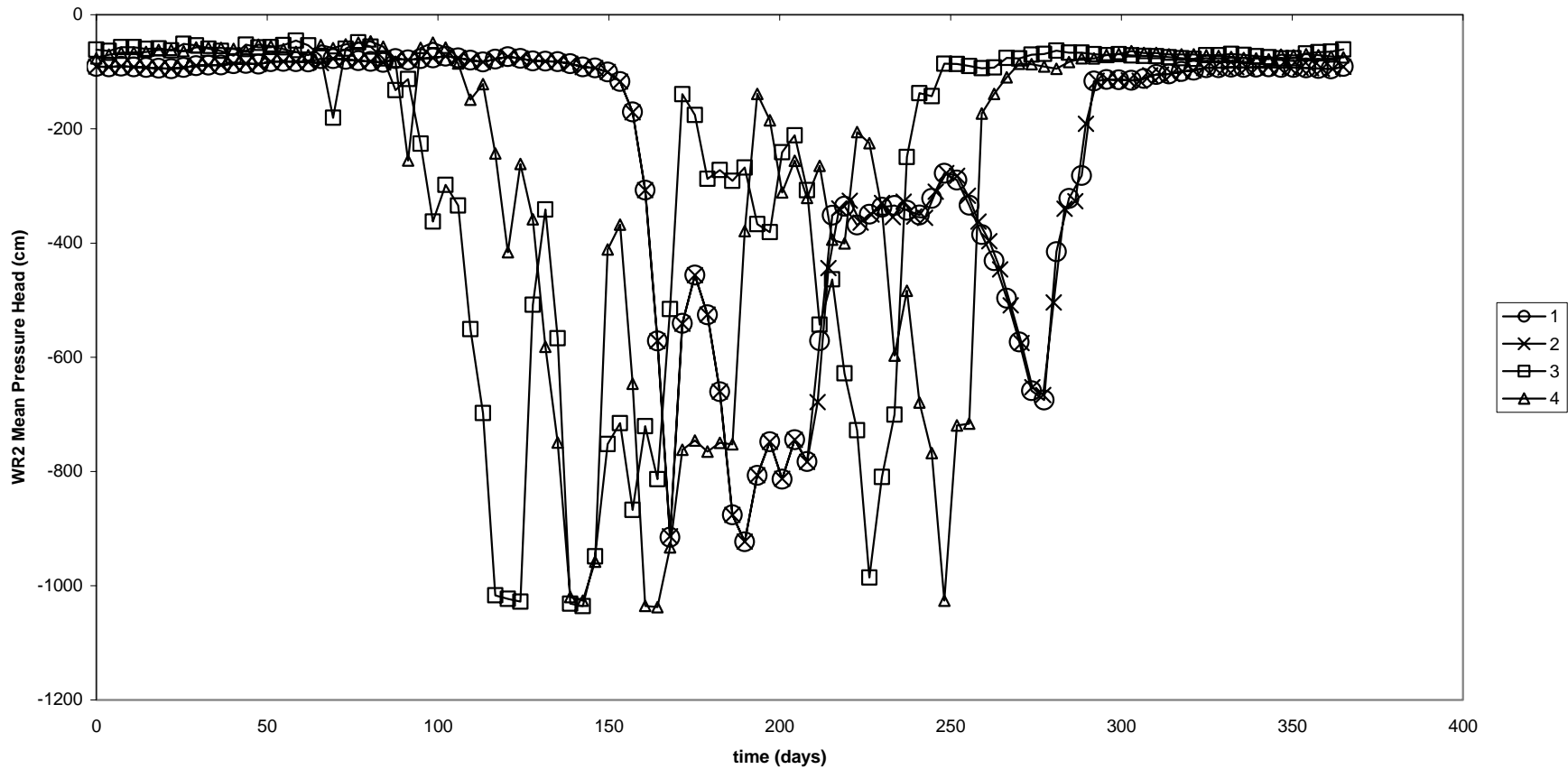


Figure J- 10. The mean pressure head within the WR3 region of the model domain for the four “wet year” simulations.

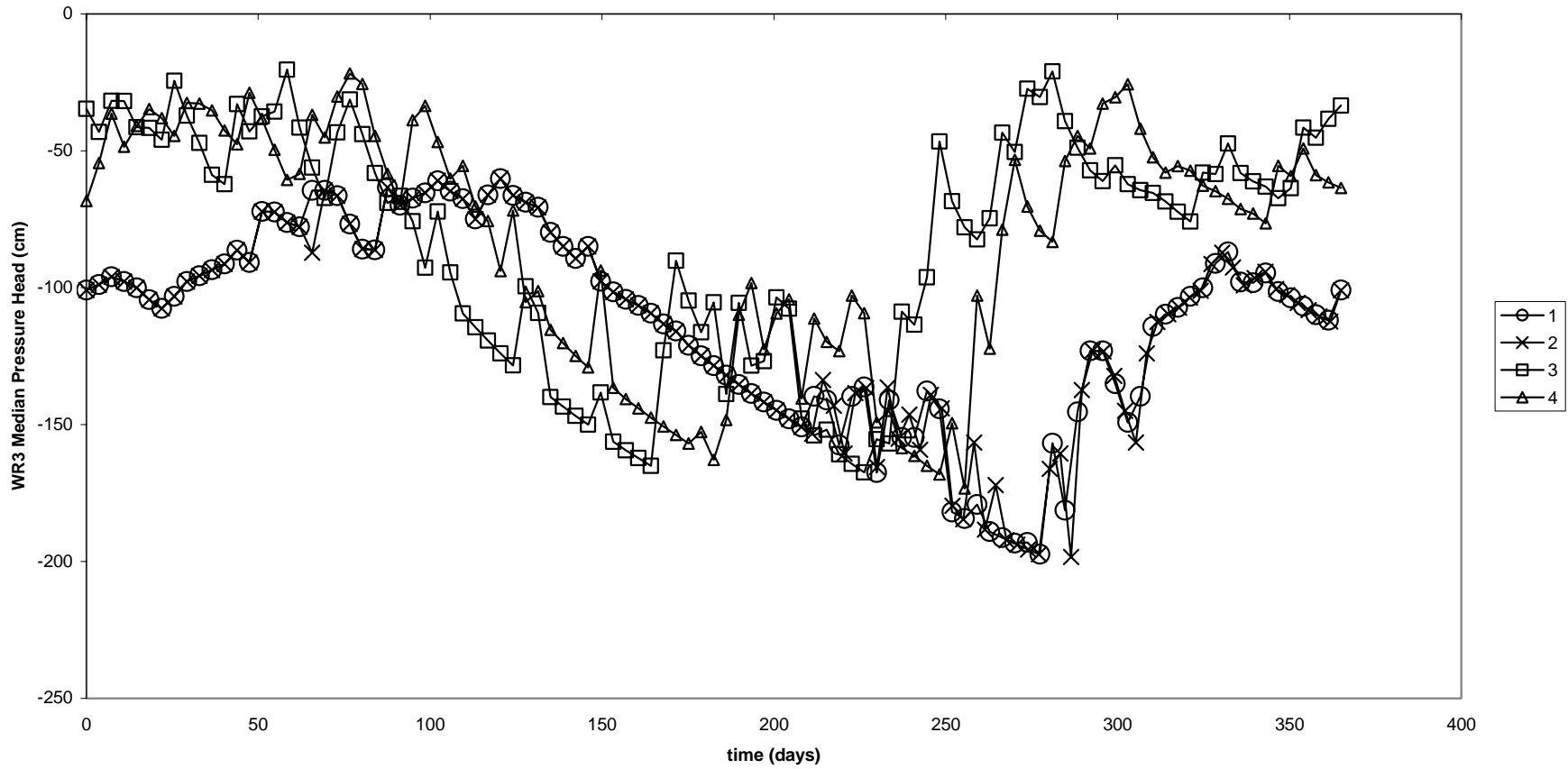


Figure J- 11. The median pressure head within the WR3 region of the model domain for the four “wet year” simulations.

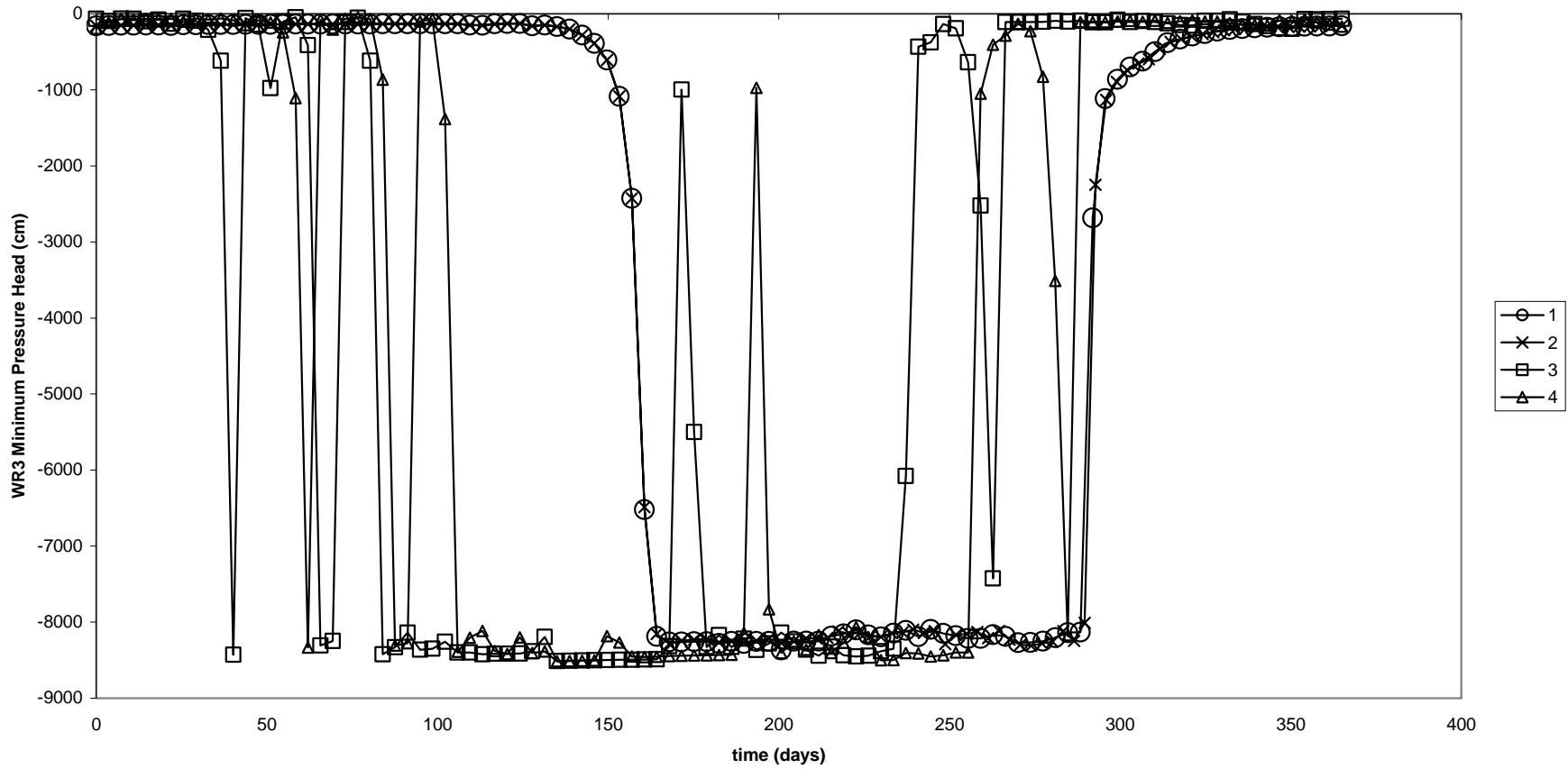


Figure J- 12. The minimum pressure head within the WR33 region of the model domain for the four “wet year” simulations.

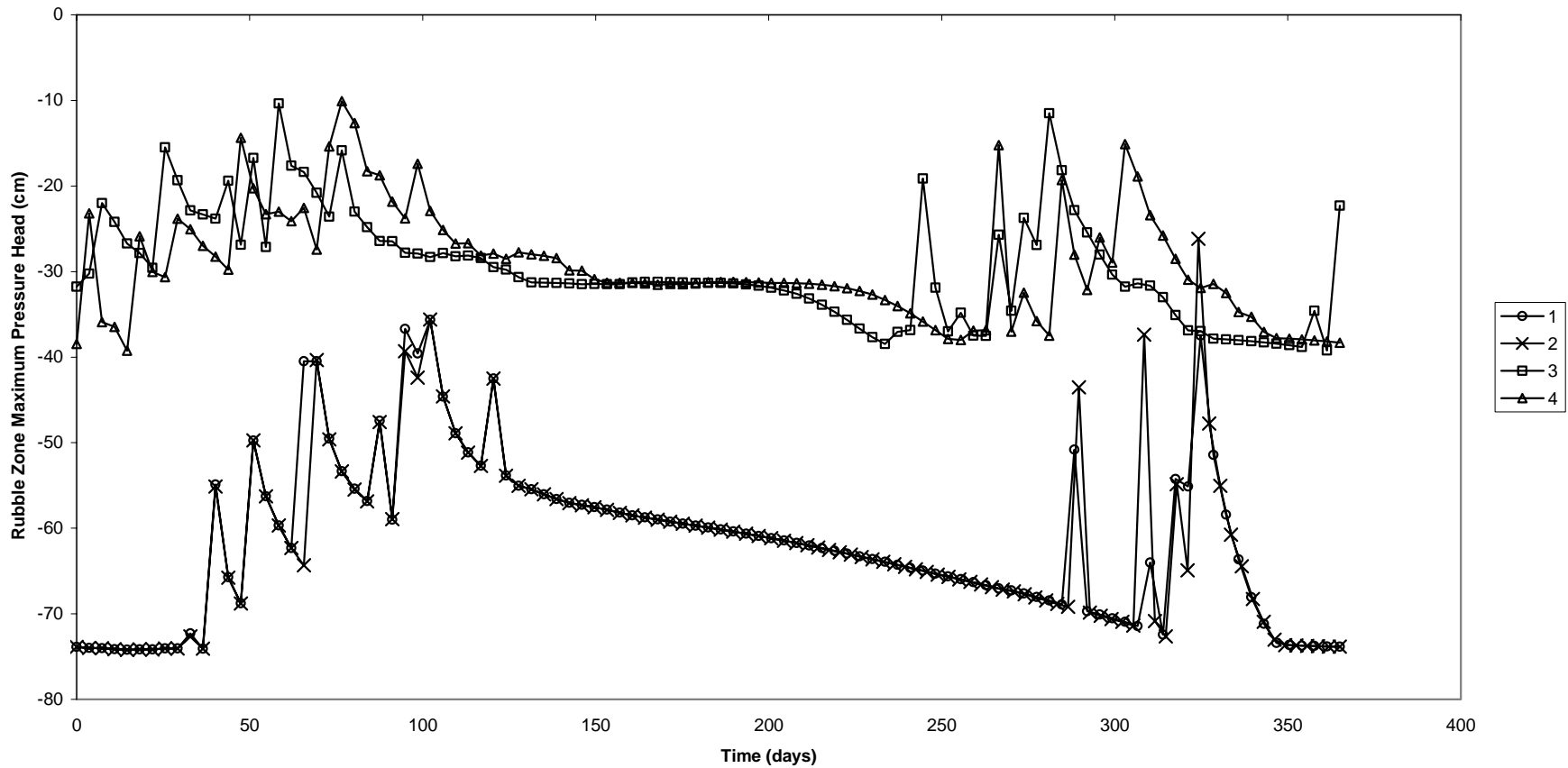


Figure J- 13. The maximum pressure head within the rubble zone region of the model domain for the four “wet year” simulations.

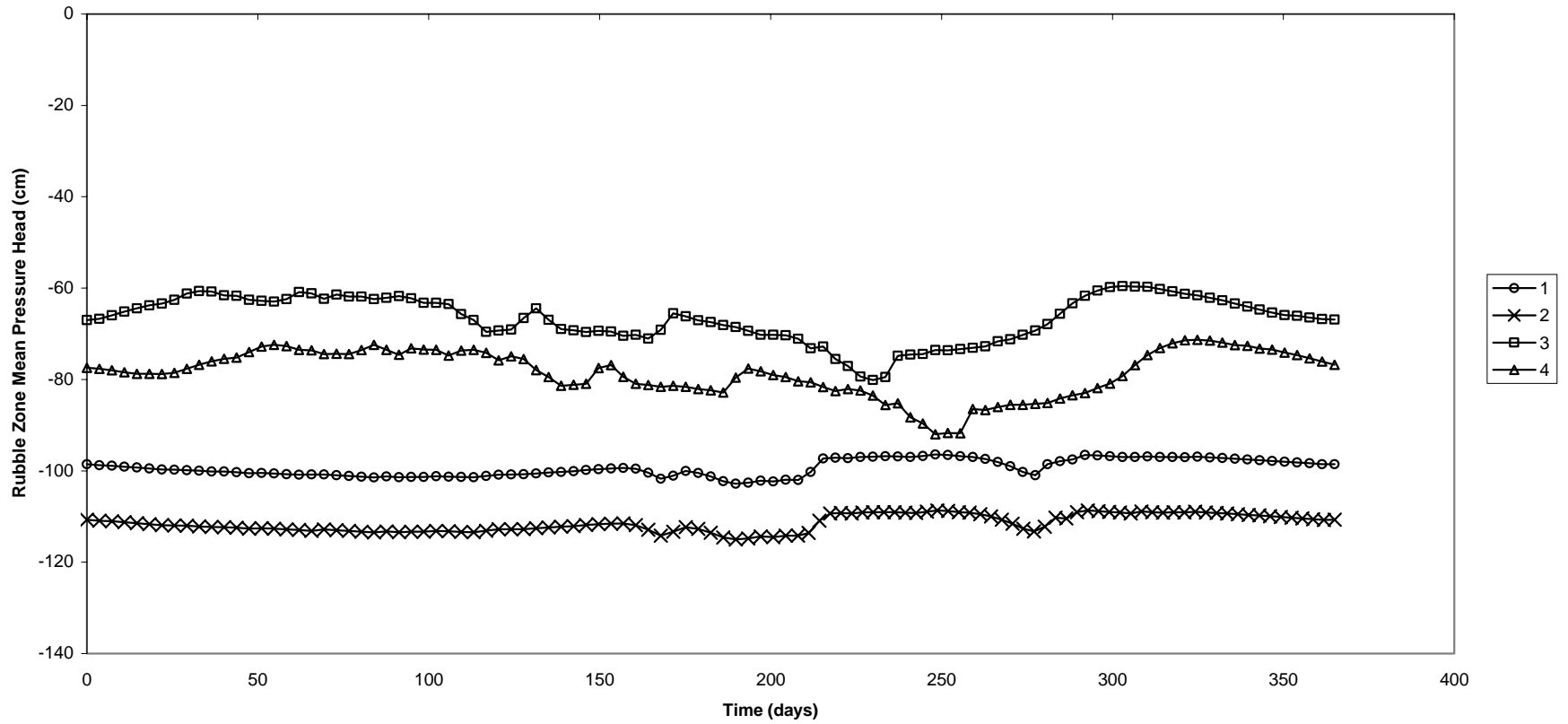


Figure J- 14. The mean pressure head within the rubble zone region of the model domain for the four “wet year” simulations.

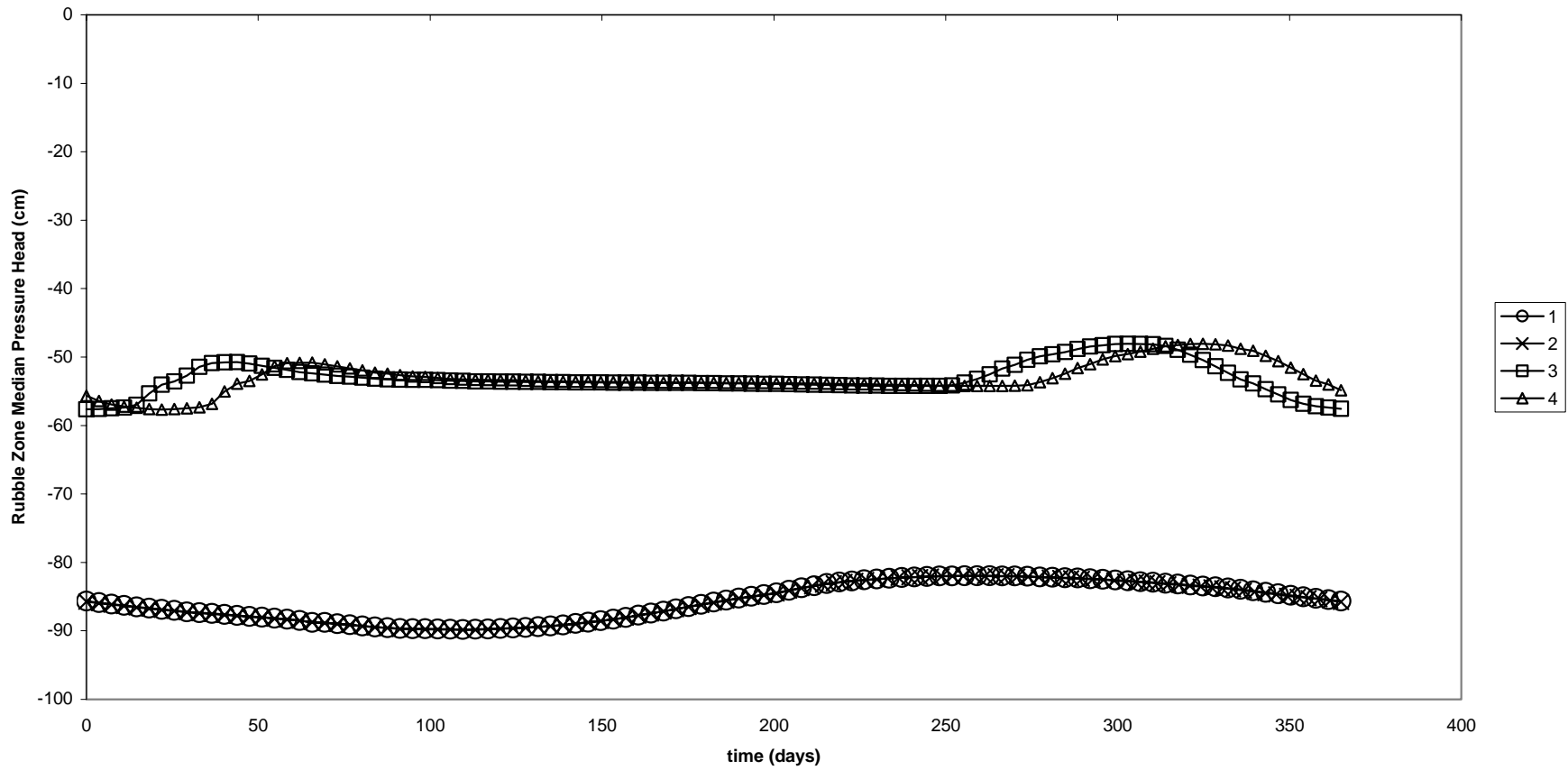


Figure J- 15. The median pressure head within the rubble zone of the model domain for the four “wet year” simulations.

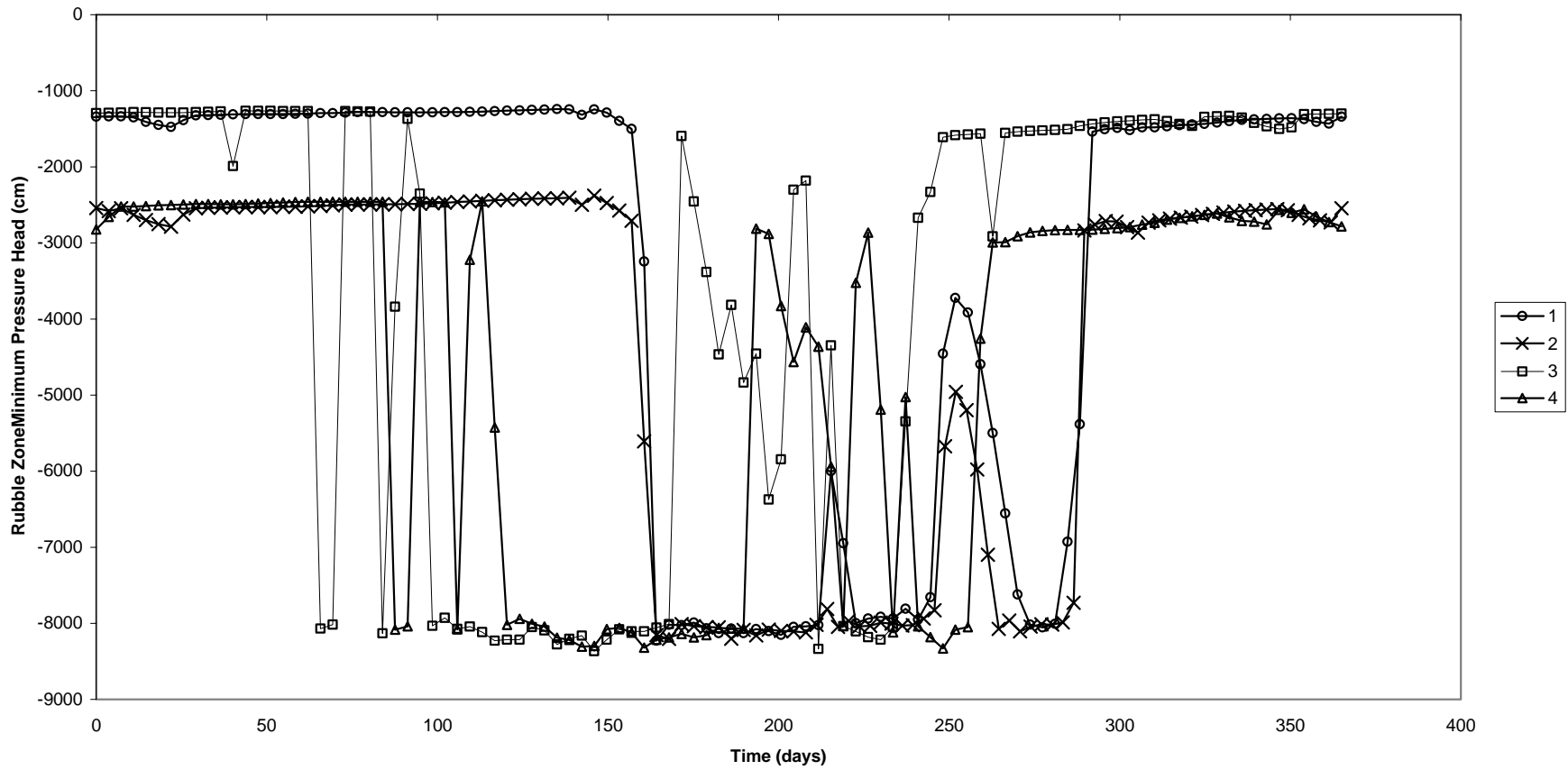


Figure J-16. The minimum pressure head within the rubble zone region of the model domain for the four “wet year” simulations.

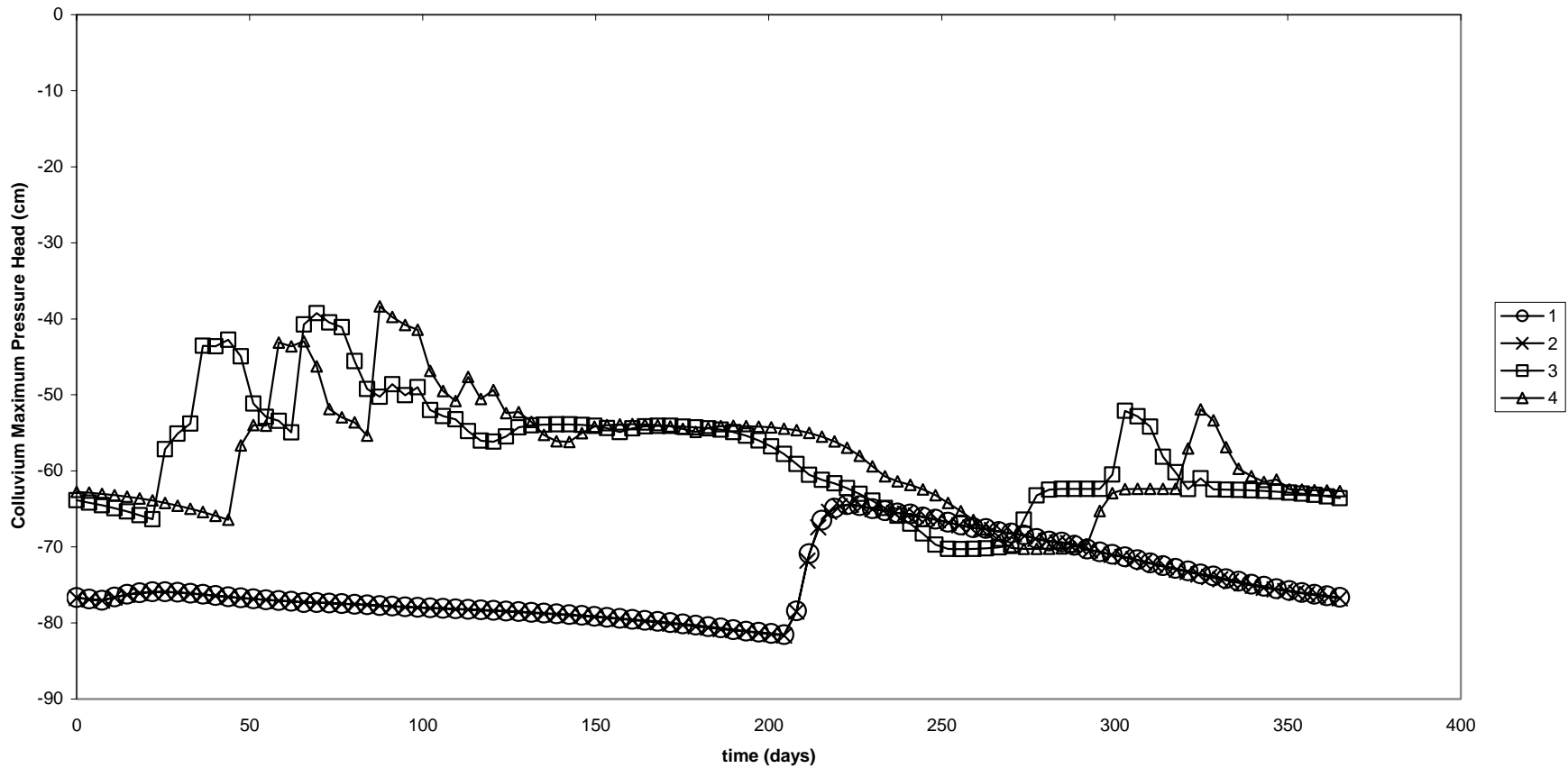


Figure J-17. The maximum pressure head within the colluvium region of the model domain for the four “wet year” simulations.

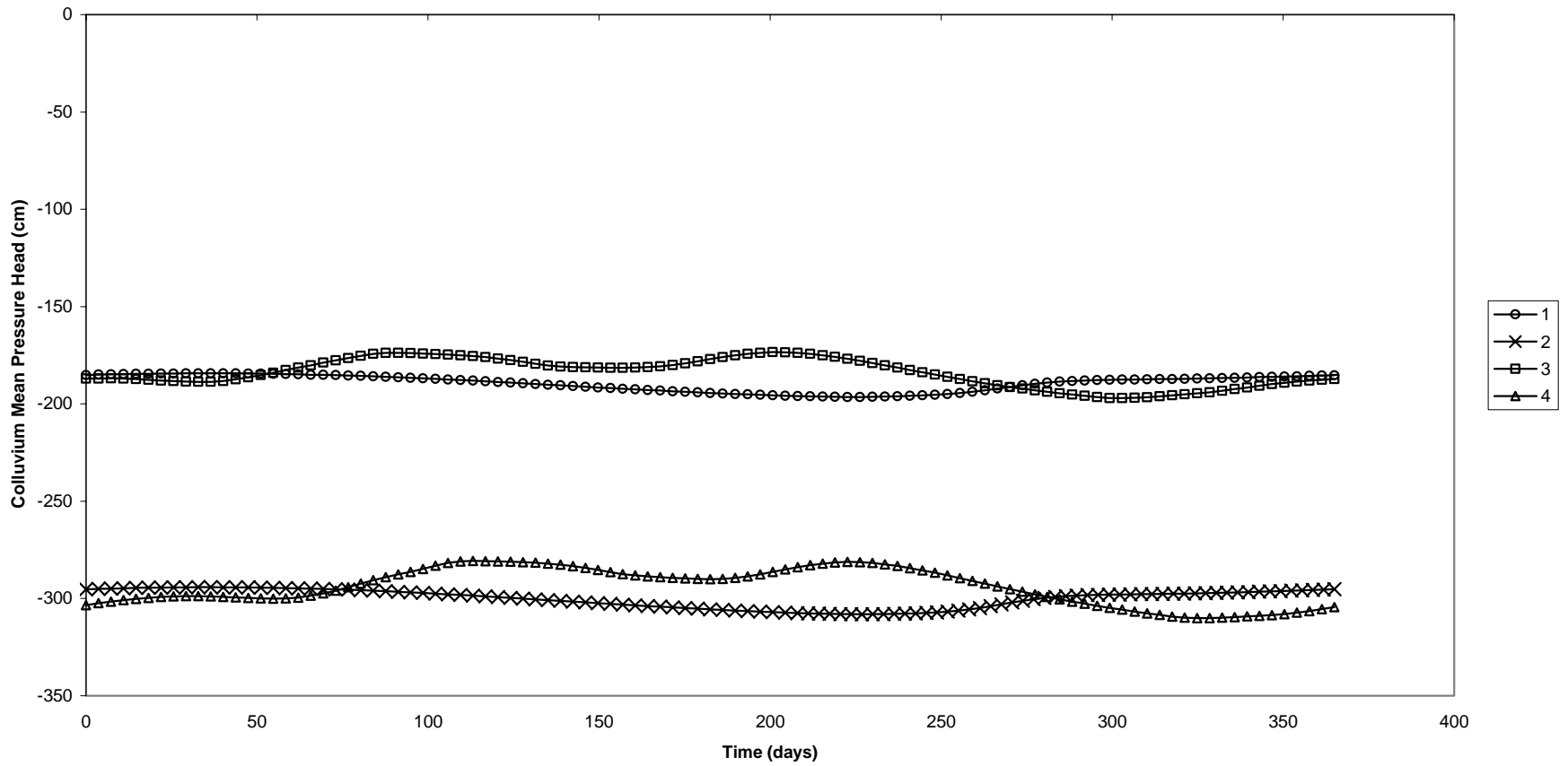


Figure J- 18. The mean pressure heads within the colluvium region of the model domain for the “wet year” simulations.

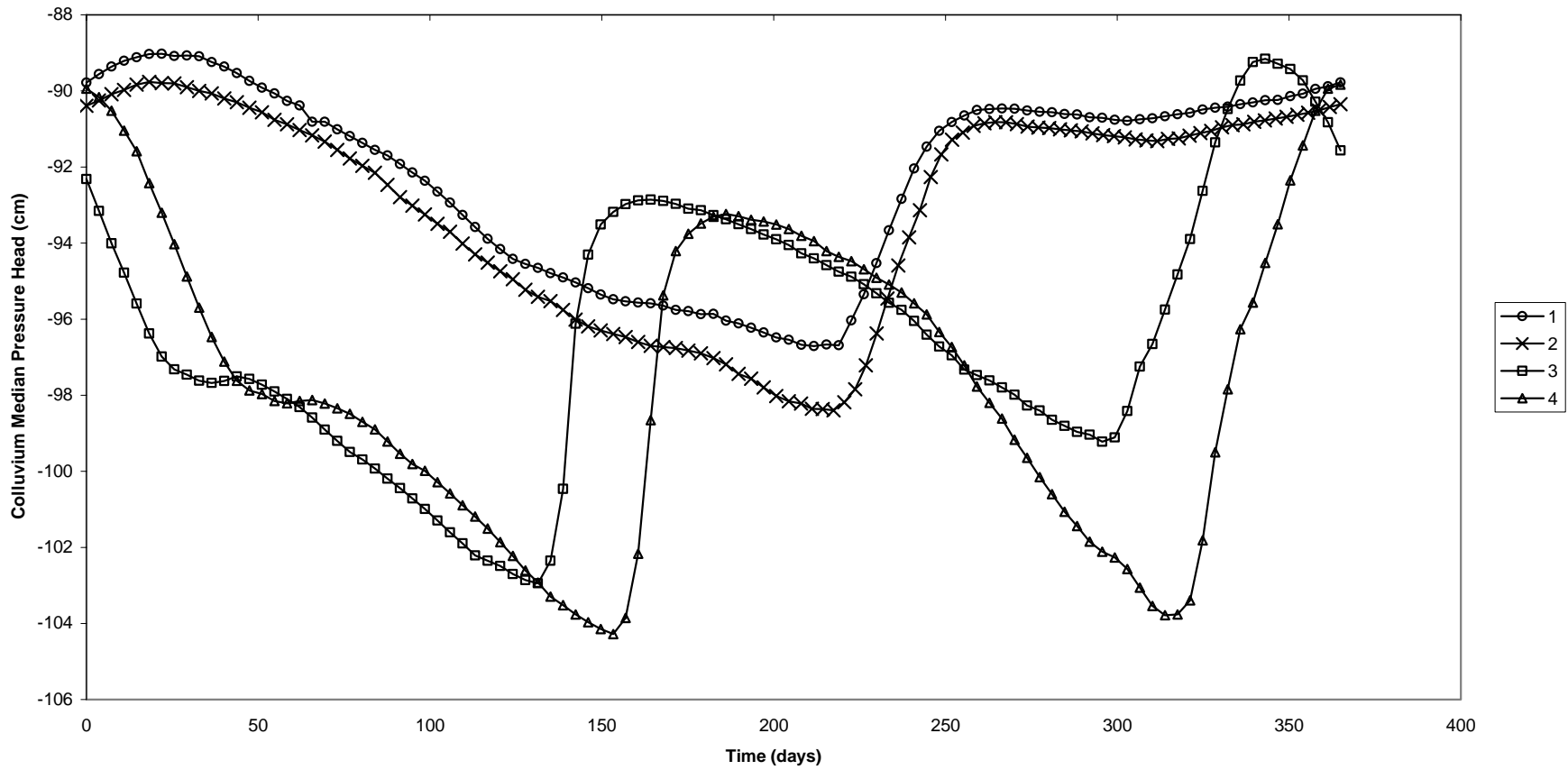


Figure J- 19. The median pressure head within the colluvium region of the model domain for the four “wet year” simulations.

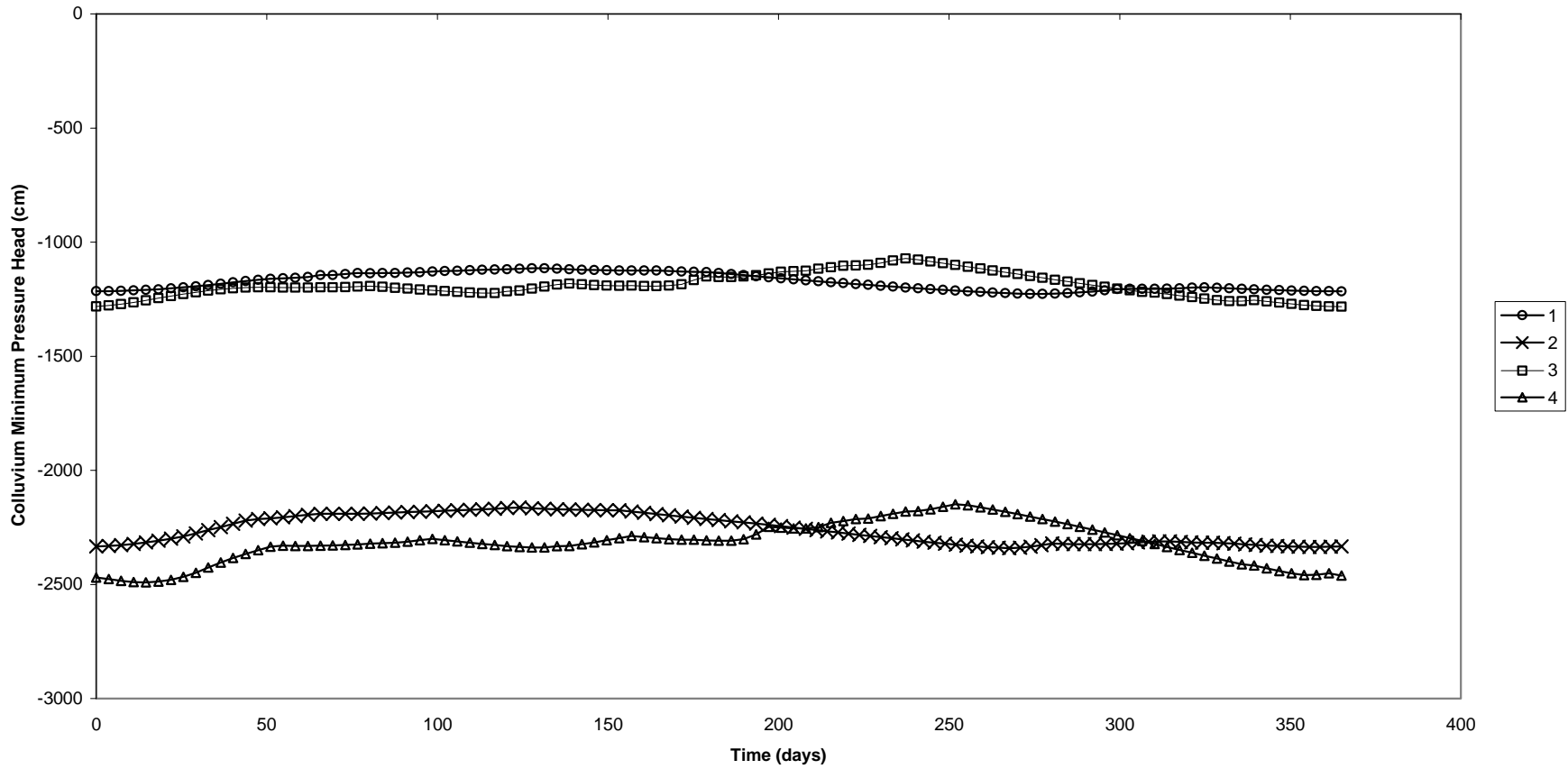


Figure J- 20. The minimum pressure head within the colluvium region of the model domain for the four “wet year” simulations.

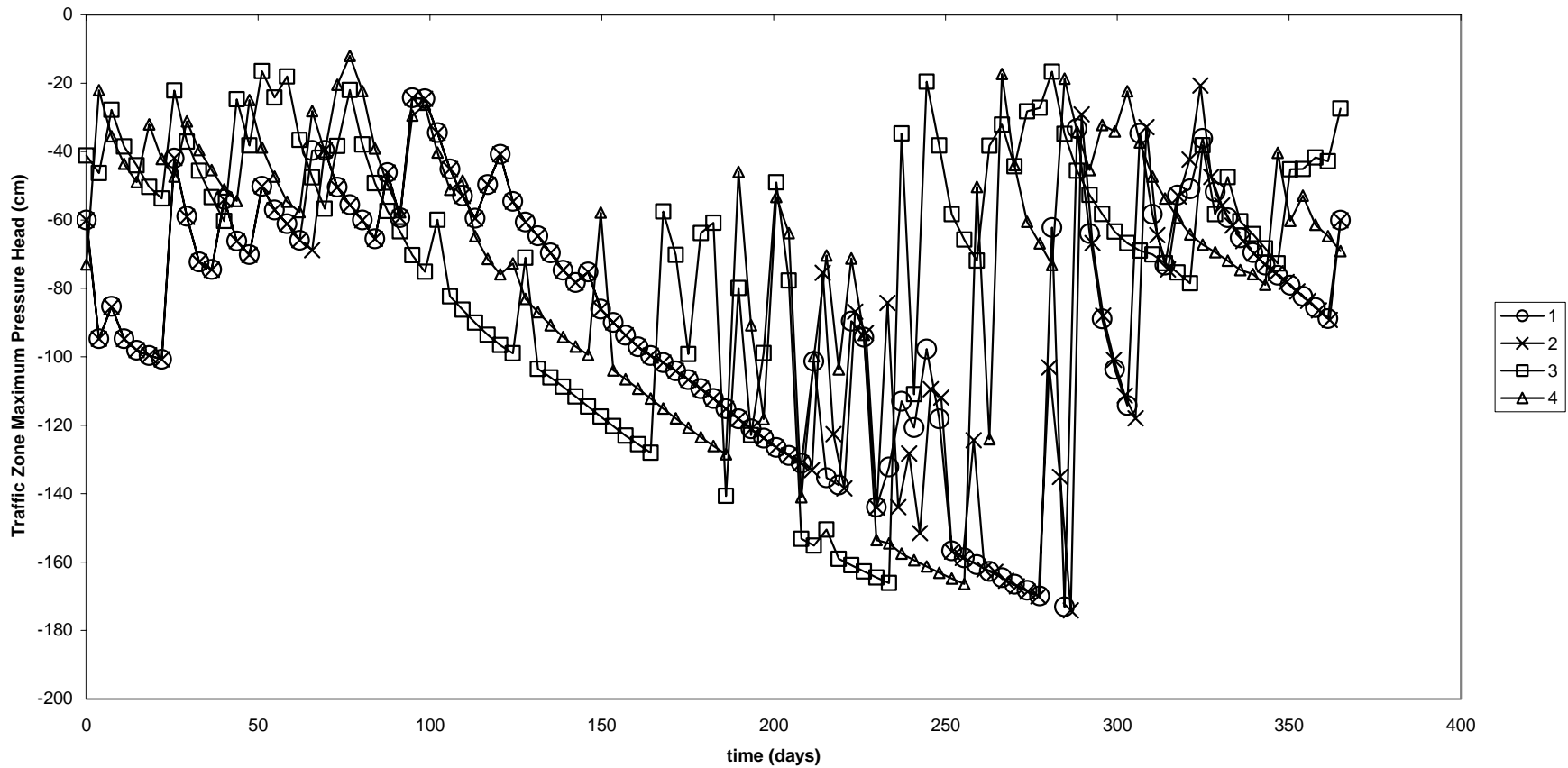


Figure J- 21. The maximum pressure head within the traffic zone region of the model domain for the four “wet year” simulations.

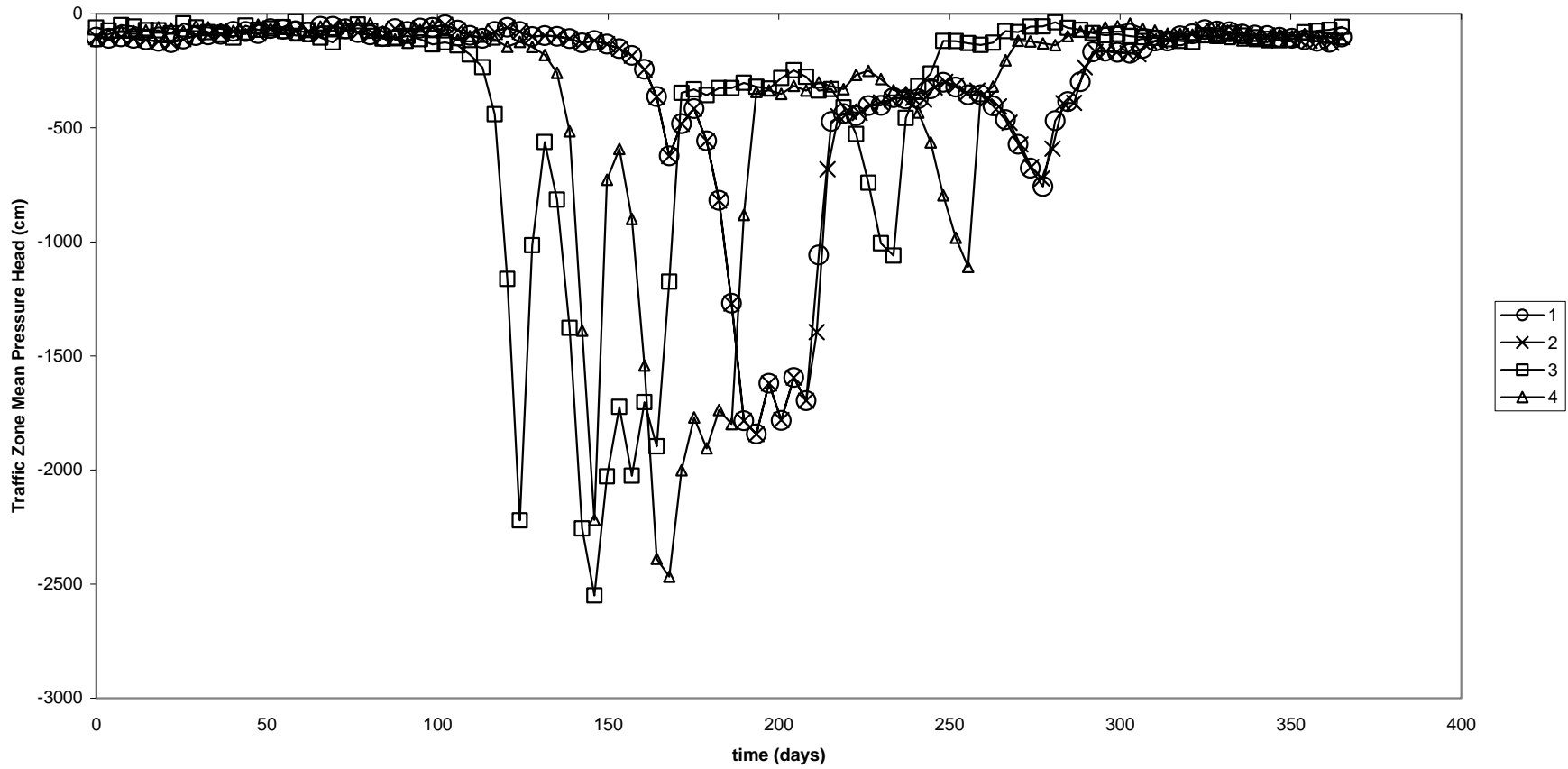


Figure J- 22. The mean pressure head within the traffic zone region of the model domain for the four “wet year” simulations.

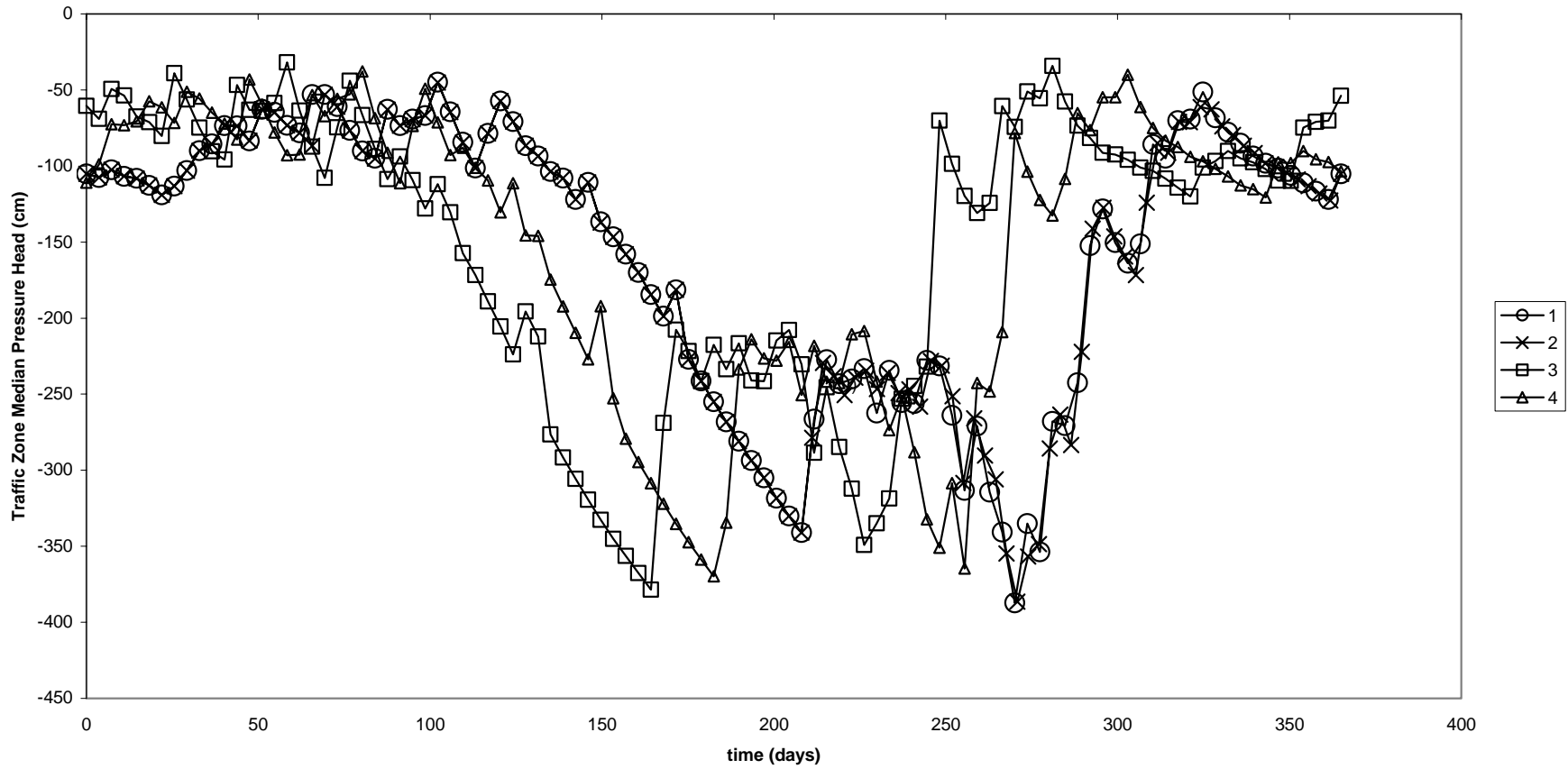


Figure J- 23. The median pressure head within the traffic zone region of the model domain for the four “wet year” simulations.

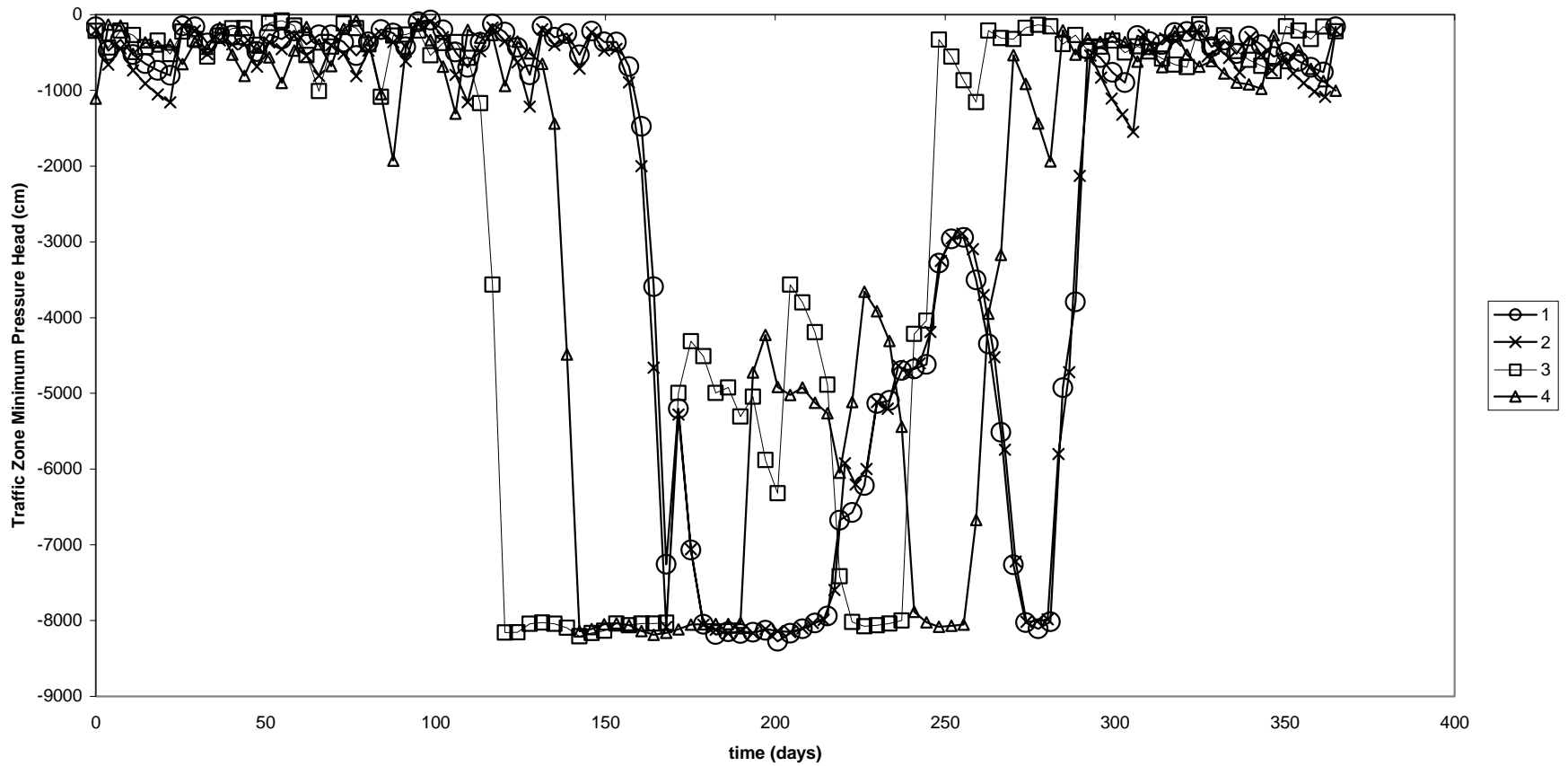


Figure J- 24. The minimum pressure head within the traffic zone region of the model domain for the four “wet year” simulations.

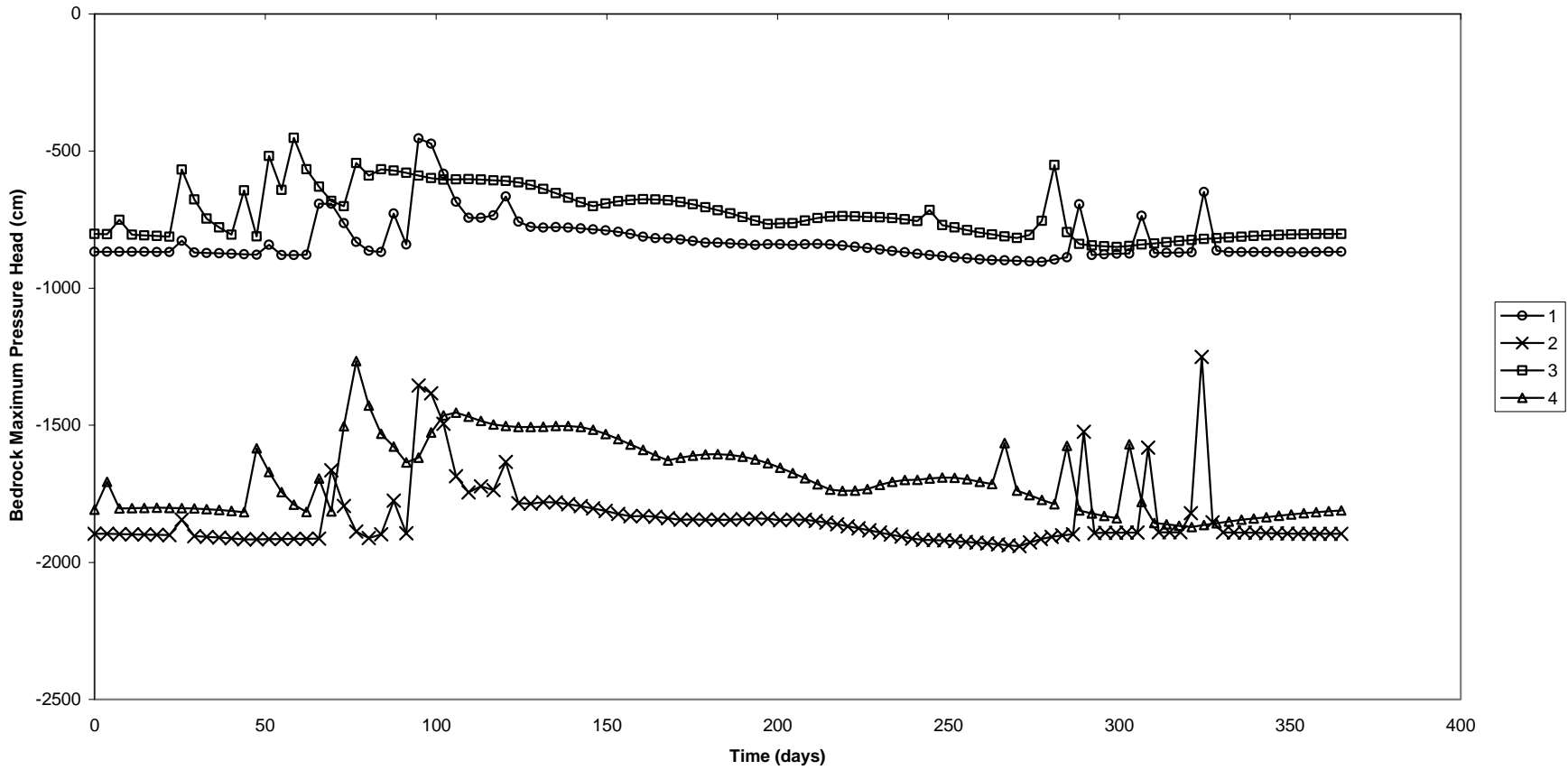


Figure J- 25. The maximum pressure head within the bedrock region of the model domain for the four “wet year” simulations.

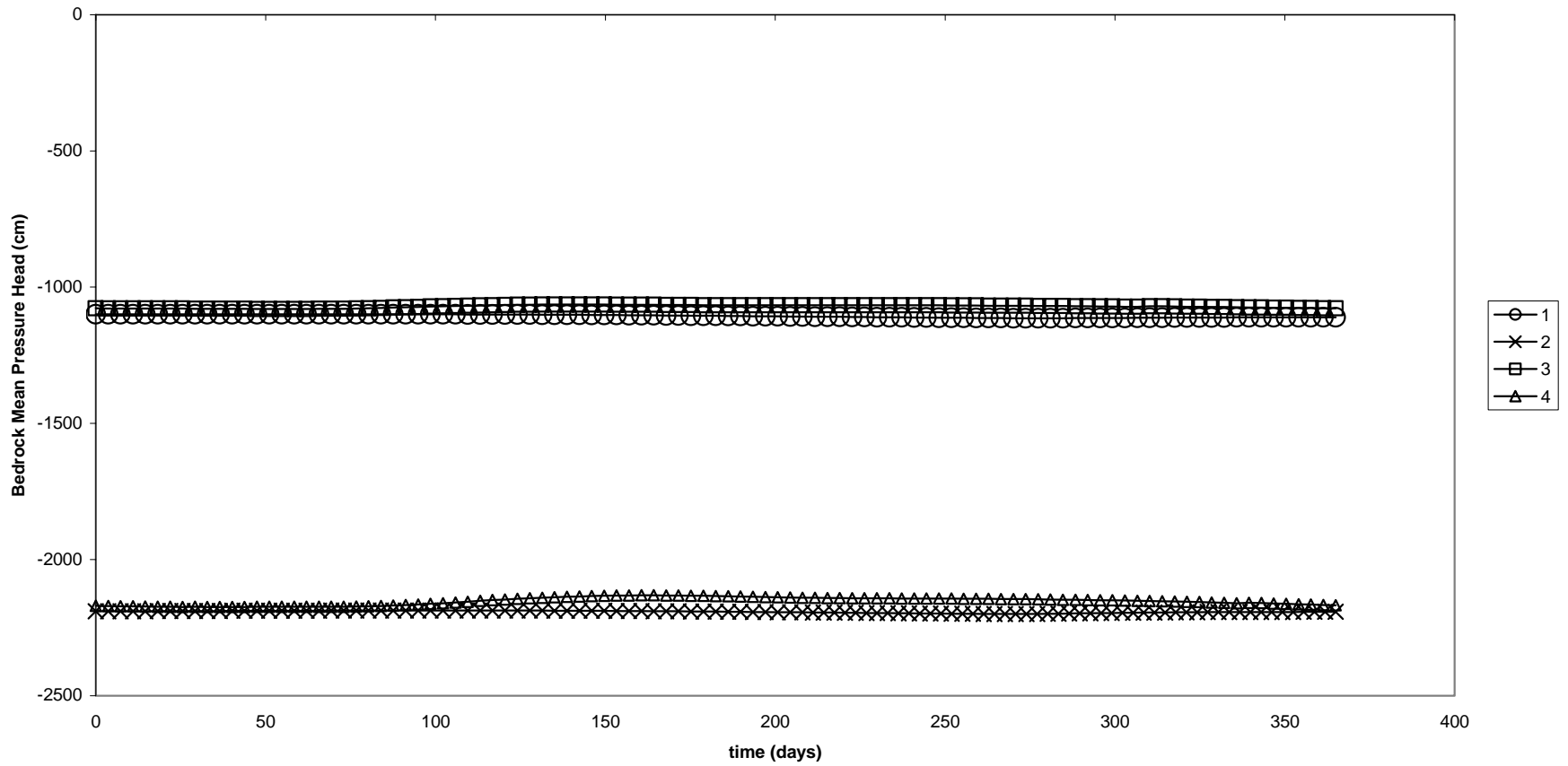


Figure J- 26. The mean pressure heads within the bedrock region of the model domain for the four “wet year” simulations.

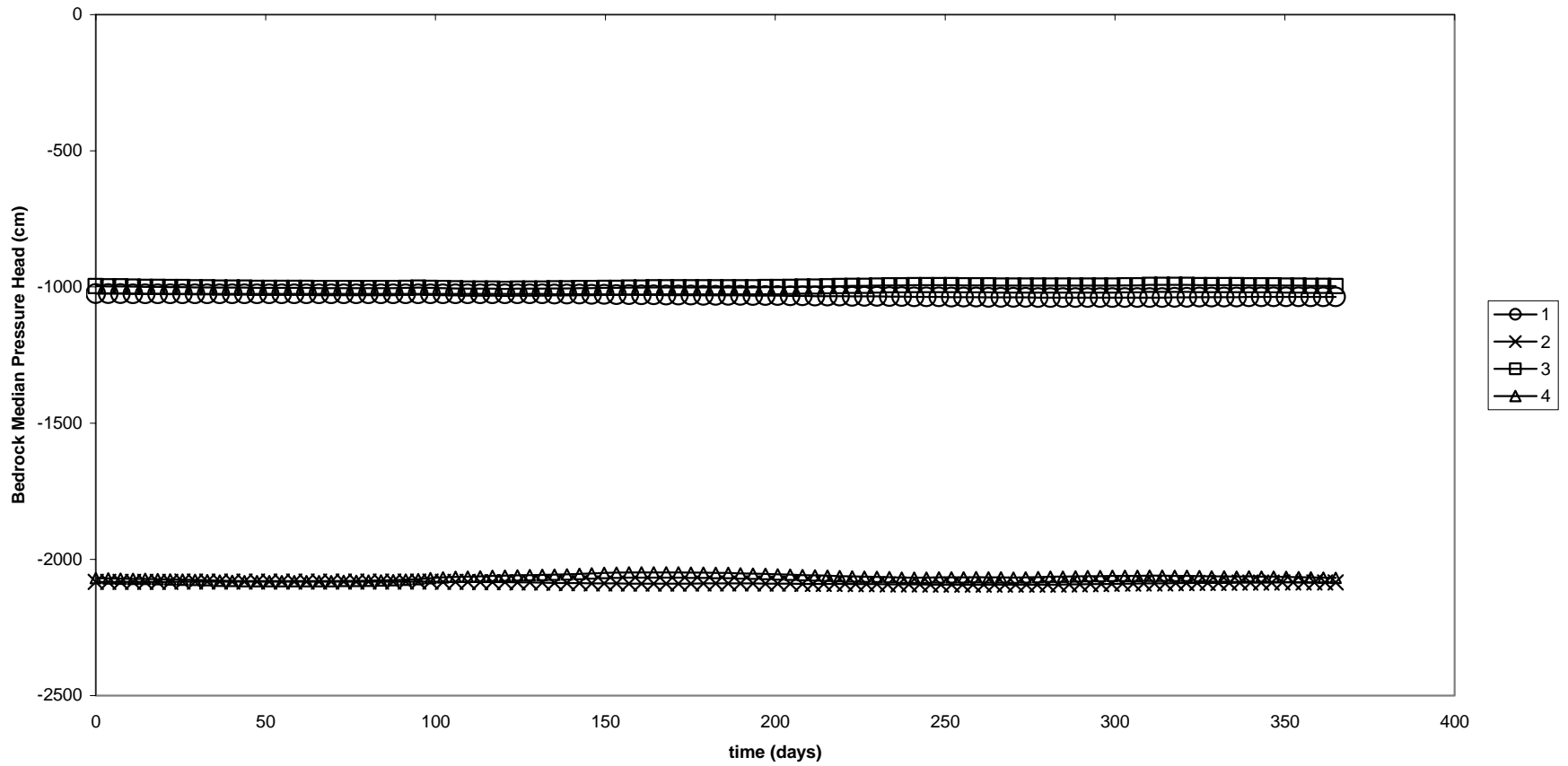


Figure J- 27. The median pressure heads within the bedrock region of the model domain for the four “wet year” simulations.

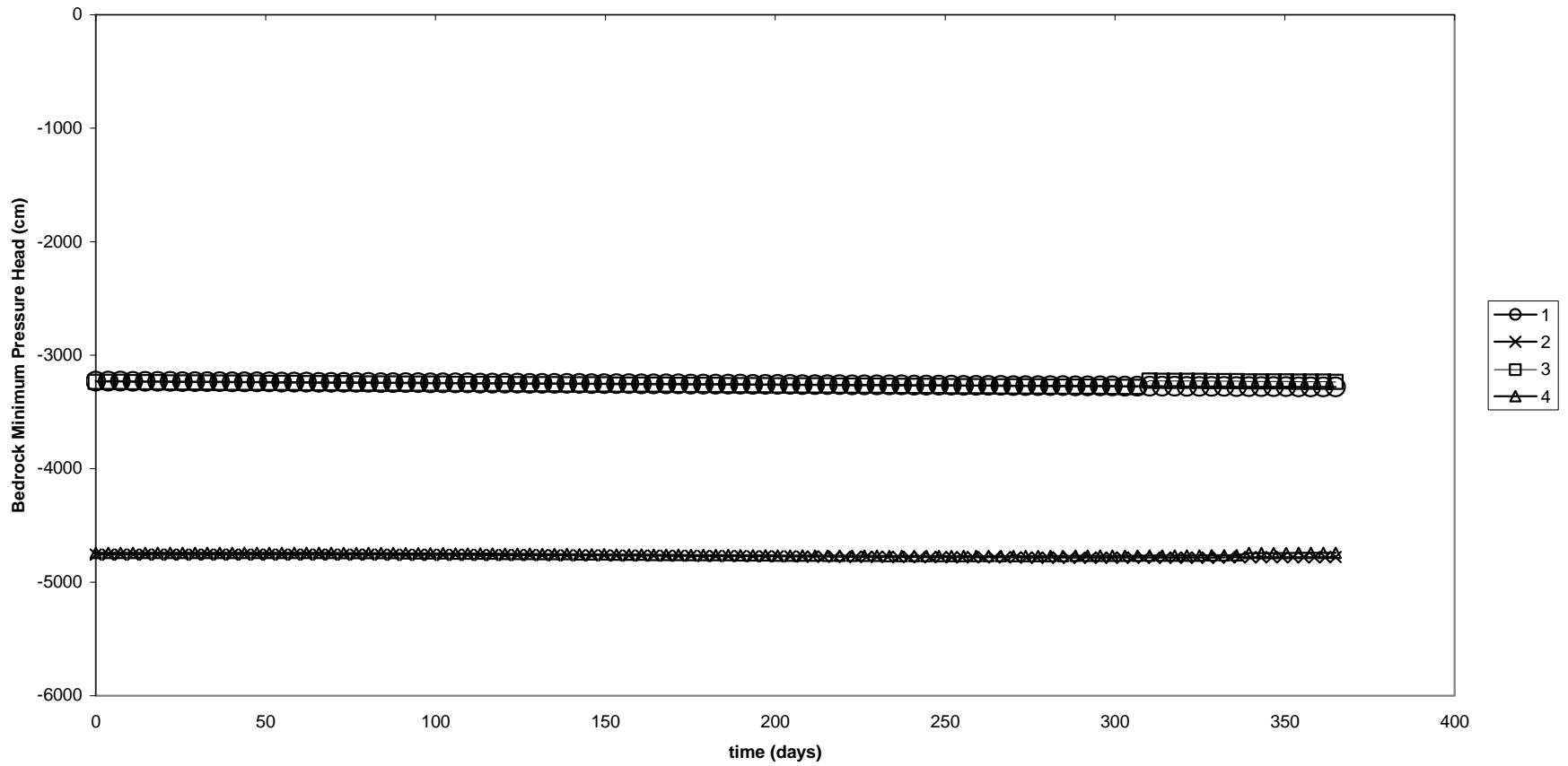


Figure J- 28.The minimum pressure heads within the bedrock region of the model domain for the four “wet year” simulations.

